Western Australian School of Mines: Minerals, Energy and Chemical Engineering

Faculty of Science and Engineering

The Effect of Supercritical CO_2 on Shaly Caprocks

Pooya Hadian

0000-0001-6192-3317

This thesis is presented for the Degree of

Doctor of Philosophy

of

Curtin University

January 2020

Declaration

To the best of my knowledge and belief, this thesis contains no material previously published by any other person except where due acknowledgment has been made.

This thesis contains no material which has been accepted for the award of any other degree or diploma in any university.

Pooya Hadian

20 January 2020

This work is dedicated to

My wife and son, Taktoom and Niak

for their continuous support,

encouragement and motivation to me

during my PhD research.

Summary

Geosequestration of anthropogenic carbon dioxide (CO_2) has been suggested as a solution for resolving the problem of increasing greenhouse gas emissions which contributes to global warming. Carbon dioxide is the major greenhouse gas which results from fossil fuel combustion for domestic and industrial purposes. Saline aquifers are the most common target for injection of CO_2 for their abundancy and proximity to the emission source. Interaction between rock-forming minerals, brine, and injected CO_2 in deep brine aquifers alter natural petrophysical properties of CO_2 geosequestration sites. The effect of supercritical CO_2 ($scCO_2$) after being injected under the shaly caprocks is one of the critical issues to be considered to address the safety and efficiency of the geosequestration process. There have been few studies to address the caprock sealing properties' variation during geosequestration of CO_2. This study is to assess the shale-$scCO_2$ interactions and their effect on petrophysical properties of the caprock via experiments and simulations at in situ conditions.

Several core samples were selected from The Jurassic Eneabba Basal Shale and claystone rich facies of the Triassic Yalgorup Member (725-1417 m) from the Harvey CO_2 sequestration site, Western Australia. Shale samples were saturated with NaCl brine and exposed to $scCO_2$ under reservoir conditions (T=60°C, P=14.1MPa) for nine months and then tested to determine their altered mineralogical, petrophysical and geochemical properties. The work presented in this thesis is based on the results from the various experimental and modelling studies on the collected shale samples. A series of measurements were conducted to evaluate the caprock mineral alteration and the pore structure properties through the $scCO_2$ injection process. X-ray Diffraction (XRD) and Scanning Electron Microscopy (SEM) results of samples are reported here to examine the alteration of the mineralogical composition before and after exposure to $scCO_2$. Nuclear Magnetic Resonance (NMR), Low-Pressure Nitrogen Adsorption (LPNA), and Mercury Injection Capillary Pressure (MICP) results are reported here to assess changes to pore size distribution, surface area, and capillary threshold pressure of samples before and after being exposed to $scCO_2$.

The experimental results show that long term exposure to $scCO_2$ causes porosity increase in most of the samples, except for relatively tighter, clay-rich samples. Pore size distribution charts show that the increase in porosity is a result of larger pore sizes being expanded because of CO_2-induced mineral dissolution. In this study, experimental results describing the mineral reactions showed alteration of rock-forming minerals after exposure to a mixture of

brine and $scCO_2$. These reactions include dissolution of feldspars, kaolinite, and quartz and precipitation of muscovite in most samples. Exposure to CO_2 in the long term also has a substantial drying-out effect on the samples, and precipitation of NaCl crystals has been observed. This process changes the pore structure of the samples even further.

The low-pressure nitrogen adsorption results demonstrated that the mesopore (2-50 nm) volume of the samples is mainly responsible for the pore size variation. LPNA results also showed changes in specific surface area, pore size distribution, and pore diameter which is related to the chemical reactions between some authigenic minerals and the CO_2.

For caprock sealing efficiency, a range of capillary entry pressure of 412psi to 8350psi was measured for these caprock materials, which may indicate fair capillary sealing efficiency. However, capillary entry pressures and height of the CO_2 column were reduced after exposure to CO_2 up to 83% in one sample, with an average of 38% reduction.

Geochemical modelling incorporating reaction rates of dissolution and precipitation, and the surface area was applied to reproduce long-term trends. Simulations were run under experimental condition (NaCl brine and 60°C and 14.1 Mpa) and reservoir condition (sampled brine composition and samples' temperature and pressure). The geochemical models could not account for brine evaporation into the $scCO_2$. In modelling under the reservoir conditions, dissolution of kaolinite, chlorite, goethite, microcline, and plagioclase was dominant in samples and participation of muscovite, magnesite, hematite, nontronite-k, gibbsite, and alunite were observed. Indication of porosity enhancement and pH reduction in 100-years period was also observed in the simulations. In model indications of experiments, quartz precipitation was dominant in all samples, and kaolinite, muscovite, goethite, microcline, and plagioclase dissolution were observed too.

Acknowledgments

I would like to convey my sincere gratitude to my supervisor Prof. Reza Rezaee for his expertise and generous support through this study. I would like to thank my co-supervisor Dr Ali Saeedi and Dr Stephanie Vialle, for their help in the experimental and modelling part of this study, respectively. I also should acknowledge Veronica Avery for helping XRD sample preparation induction and running the samples in XRD machine, Ellaine Miller for SEM sample preparation, induction, and hands-on training. My heartfelt gratitude goes to my colleagues and the excellent staff of the petroleum engineering department who made this experience a pleasant and fruitful one. I would like to warmly thank Robert Webb for technical support, Mohsen Ghasemi for helping me with setting up the exposure apparatus, Jie Zou who ran the Low-Pressure Nitrogen Adsorption tests for me, and Nadia Testamanti for the tips on NMR method.

I owe my profound gratitude to my beloved family for their continued support. My parents, Jamshid and Zakieh, who are the reason behind all my achievements, and my lovely sister Dena, I will always be in your debt. My amazing wife, Taktoom, and my adorable son, Niak, whose great love, limitless support, and understanding made this dream possible. I would like to dedicate this thesis to my cherished family without whom none of my success would be possible.

The authors wish to acknowledge the Department of Mines, Industry Regulation and Safety for providing the rock samples (Approval No. S32833). The authors would like to acknowledge the contribution of an Australian Government Research Training Program Scholarship in supporting this research. This study was also supported by a Curtin Research Scholarship (CRS). Part of this research was undertaken using the EM/XRD instrumentation (ARC LE0775553/LE0775551) at the John de Laeter Centre, Curtin University.

Table of Contents

List of Figures

List of Tables

List of Acronyms

CPMG: Carr-Purcell-Meiboom-Gill

DFT: Density Functional Theory

HPLC: High-performance Liquid Chromatography

IFT: Interfacial Tension

IPV: Incremental Pore Volume

ISA: Incremental Surface Area

LPNA: Low-pressure Nitrogen Adsorption

MICP: Mercury Intrusion Porosimetry

NMR: Nuclear Magnetic Resonance

PSD: Pore Size distribution

PVT: Pressure-Volume-Temperature

XRD: X-ray Diffraction

Chapter 1. Introduction

To address the increasing amount of greenhouse gasses, especially CO_2 being emitted to the atmosphere, geosequestration is identified as a key solution (IPCC Working Group III, 2005). Injection of anthropogenic CO_2 deep underground instead of releasing it to the atmosphere is the basic concept in this method. CO_2 under the storage condition of target reservoirs is in the critical state. The excessive amount of CO_2 in the geologic formation, which also contains water, modifies the chemical equilibrium of the existing system and induce a series of reactions that alter the host rock mineralogy and properties. The chemical reactions that follow the disequilibrium between rock and fluids are characterised qualitatively in previous studies (De Silva et al., 2015). The extent and direction of changes induced by these chemical reactions to the petrophysical properties of the sealing shale strata need to be evaluated quantitatively based on the condition of the target reservoir and solid and liquid phases at play for each scenario. Chemical reactions cause dissolution or precipitation of minerals, which may alter the porosity or permeability of caprocks. Such changes could in turn lead to deterioration or improvement of seal (J. Pearce et al., 2018).

In this research, we evaluated the mineralogical and petrophysical changes of several shaly samples after undergoing exposure to supercritical carbon dioxide ($scCO_2$) via experimental and simulation methods. Samples were in contact with supercritical CO_2 in a batch reactor for nine months under the in-situ conditions of 60°C and 14.1 MPa. The primary emphasis of this investigation is on the identification and characterisation of the effects of reactions between $scCO_2$, minerals in the shale samples and brine. To achieve this objective, samples were analysed with several experimental methods before and after exposure. The mineralogical characterisation was achieved by X-ray diffraction (XRD) and scanning electron microscopy with Energy Dispersive Spectroscopy (SEM+EDS) methods. Petrophysical characterisation of samples was achieved by Low-Pressure Nitrogen Adsorption (LP-NA), Nuclear Magnetic Resonance (NMR), and Mercury Injection Capillary Pressure (MICP). The simulation predicted the fate of the system after hundreds of years via Geochemical Reaction Path Modelling. Geochemist workbench (GWB) was used to interpret and extrapolate laboratory experiments on CO_2-brine-minerals reactions to more extended periods. This program incorporates kinetic rate laws in its calculations (Gunter et al., 1997).

There are several related studies of CO_2 sequestration system performed by other researchers which lack the inclusive methods applied here (Castaneda-Herrera et al., 2018; Credoz et al., 2009; Dawson et al., 2013; Farquhar et al., 2015; Kaszuba et al., 2003, 2005;

Kharaka et al., 2006; Kirste et al., 2019; Liu et al., 2012; Liu, 2013; Lu et al., 2012; J. Pearce et al., 2018; Rezaee, 2014; Rezaee et al., 2017; Rosenbauer et al., 2005; Schlomer et al., 1997; Wollenweber et al., 2010; Yin et al., 2016). They were usually applied under higher than in-situ temperature or pressure, or for a brief period of reaction time. This study aims to provide a comprehensive assessment of the effect of $scCO_2$ on shaly caprock in a geosequestration project using an integrated approach. In other words, the chemical interactions of primary phases and resulting secondary phases were estimated via experimental and modelling approach, and their effect on petrophysical properties was assessed.

The most applied experimental strategy to investigate potential geochemical reactions is to put rock samples in CO_2-saturated brine. CO_2 solubility is much less in the higher temperature and higher salinity as observed by Gunter et al. (1997). The reduction of the solubility of CO_2 in solution would cause lower potential participation of secondary phases. In a sand reservoir capped with shale caprock, the injected CO_2 into the reservoir migrates upward due to buoyancy force and accumulates under the overlying shale layer. For the above reasons, in the present study, the caprock interactions were investigated with H_2O saturated CO_2. To achieve the water-saturated CO_2, 50 cm^3 of water was added CO_2 accumulator. Then wet supercritical CO_2 from accumulator was injected into the batch reactor containing saturated core samples. The amount of water dissolved in $scCO_2$ is determined by temperature and pressure in the accumulator cell.

1.1 Geosequestration

The link between increasing atmospheric CO_2 concentration and increasing global temperature has become one of the most significant concerns of the past decades (Kharaka et al., 2011). Earth's temperature has increased by around 0.85°C from 1880 to 2012 (IPCC, 2014), and an assessment in Australia has suggested a forecast rise of 1- 6°C in average annual temperatures in the period of 1990- 2070 (Preston, 2006; Shukla et al., 2010). Burning fossil fuels, the primary source of greenhouse gasses is still the major source of energy due to their low cost, high energy density and abundant supply (Kweon et al., 2017). CO_2 is a significant greenhouse gas, as it accounts for over 60% of the greenhouse gases emissions. Its atmospheric concentration has intensely increased in the last fifty years (IPCC, 2013). The CO_2 atmospheric concentration has risen by around 32% since the Industrial Revolution, half of which has been released to the atmosphere during the past few decades (De Silva et al., 2015). Mitigating climate change requires a reduction in greenhouse gas emissions (Szabó et al., 2016). CO_2 Capture and Storage (CSS) is proposed as the key method for reducing

anthropogenic CO_2 emissions into the atmosphere, which will lead to modifying the global rise in atmospheric temperature (IPCC, 2013).

In carbon capture and storage (CCS) projects, CO_2 is normally captured at stationary industrial sources, such as power plants and then injected into deep underground strata (below 800 meters) with a known seal. Carbon dioxide exists as a supercritical fluid when stored at depths greater than about 800 m and temperatures above 31°C. The efficiency of the seal along with reservoir storage evaluation, and other vital issues such as injectivity, migration, and trapping of CO_2 are the crucial scientific and technical challenges in a CCS project. If injected CO_2 can migrate back into the atmosphere the process of carbon storage for climate abatement will fail. Even if the Injected CO_2 would not release to the atmosphere, it still could lead to serious suffocation of surface creatures and acidification of groundwater (Li et al., 2019).

Yang et al. (2008) reviewed carbon separation and capture processes which is the main operation before disposal. The challenges facing the capture phase in CCS projects are the amount of energy required to capture the CO_2 from the plant's fume and the vast amount of water required for the process. The technology for CO_2 transport and injection is well established, being already used in Enhanced Oil Recovery (EOR) (Bachu et al., 1994). Carbon dioxide is also found in natural occurrences which offer ideal analogues for disposal of CO_2 (Pearce et al., 1996). Shukla et al. (2010) summarised other options for reducing the amount of CO_2 emissions as using less carbon-intensive fuels, improving energy efficiency, and developing alternative energy resources.

The most common methods to store large volumes of CO_2 are geosequestration and ocean sequestration. The largest sink capacity to store anthropogenic carbon dioxide is available in ocean sequestration. It is, however, a more challenging method mainly due to the insufficient safe storage life span, high operational and transportation costs and many environmental issues such as ocean acidification (De Silva et al., 2015), making ocean storage a socially and economically unacceptable option for commercial volumes of anthropogenic CO2. Therefore, we now focus on geosequestration. Geosequestration in deep saline aquifers is the most abundant and economical method due to the large volume of pore space available and long term hydrodynamic trapping of CO_2, when compared to other options of depleted oil and gas reservoirs, coal seams, and even ocean sequestration (Bachu et al., 1994; Gunter et al., 1997). The second reason making saline aquifers more economical than other options is their common proximity of most existing CO_2 capture sites to saline aquifers. These

aquifers are often not suitable to supply potable water due to being highly mineralised (De Silva et al., 2015). Three of the trapping mechanisms (structural, solution, and mineral trapping) discussed in the next paragraph are active in saline aquifers. Presented in Table 1-1 are the advantages and disadvantages of various geological media that can be used for CO_2 storage.

Table 1-1. Advantages and disadvantages of the various geological media (Bachu, 2008; Bachu et al., 1994; Celia et al., 2015; Holloway, 2001).

	Capacity (Gt-CO_2)	***Advantages***	***Disadvantages***
Deep saline aquifers	250- 900	• Most abundant and economical • Large capacity • Proximity to sources • Not a source of potable water • Different trapping mechanisms	• Greatest geological uncertainty
Depleted oil and gas reservoirs	25- 30	• Proven caprocks • Minimal environmental risk • Potential EOR to offset the cost	• Limited capacity • Cost of transport • Possible leakage pathway from drilled wells
Coal seam	5- 10	• Potential methane recovery to offset the cost	• Minimal capacity
Ocean	1000- 10,000	• Largest capacity	• Short life span • High operational and transportation costs • High environmental risk

Four main CO_2 trapping mechanisms are responsible for capacity, performance, and integrity of the reservoir (Benson and Cook 2005; Friedmann 2007; Benson and Cole 2008):

- Structural and stratigraphic trapping, where a caprock or an impermeable barrier keep the undissolved injected CO_2 stored as a supercritical and buoyant fluid.
- Residual trapping, where high capillary entry pressures and low permeability in the water-wet pores of reservoir rocks, away from the supercritical plume, traps CO_2 completely.
- Solution trapping, where the dissolution of CO_2 in formation-water is trapping it in aqueous species such as H_2CO_3, HCO_3^-, and CO_3^{2-}.
- Mineral trapping, where the CO_2 reacts with host minerals in an aqueous medium, and precipitates as calcite, magnesite, siderite, and dawsonite (Bachu et al., 1994; Gunter et al., 1993; Kharaka et al., 2011).

Structural and residual trapping are categorised as geological trapping and solution, and mineral trapping are sub-categories of geochemical trapping. Mineral trapping is often considered the safest and most permanent trapping, and more economical in the long term

(De Silva et al., 2015). In mineral trapping, reactions between CO_2 and formation rock minerals and brine form stable minerals that precipitate in pores. Although mineral trapping provides the most permanent form of CO_2 storage, it takes hundreds to thousands of years to complete because the reactions are prolonged (De Silva et al., 2015; Gunter et al., 2004). Reactions between the CO_2 gas, brine and minerals of the system, and in particular the kinetics of these reactions, are less understood (Shukla et al., 2011).

Another trapping mechanism identified in the literature is sorption onto organic material in coals and shales. The very low permeability of coal and its swelling behaviour in the presence of CO_2 has abandoned this trapping concept to be operational to this date (Celia et al., 2015). Transforming shale gas formations into CO_2 storage targets has been suggested as the shale gas production has increased over the last decade (Khosrokhavar et al., 2014). An estimate of up to 28 Gt of storage capacity in the Devonian shale has been reported (Yin et al., 2016). The CO_2 can be stored in shale either as adsorbed gas or free gas. Gas is adsorbed on the organic matter or clay surface in the adsorbed state or is accumulated in the natural crack in the free state. Previous studies have shown the preferable CO_2 adsorption over the CH_4, and greater adsorption capacity of CO_2 than CH_4.

Advantages of CO_2 storage in shale formations is the enhanced methane recovery due to potential fracturing and methane desorption, water usage reduction, and formation damage prevention in CO_2 enhanced shale gas recovery (CO_2-ESGR) (Yin et al., 2016). However, low permeability of shales limits the amount of injected CO_2 and increases the number of wells required for the storage. Another disadvantage is CO_2 adsorption which leads to shale swelling and a further reduction in permeability. As a result, commercial-scale carbon storage in shale or coal has been deemed prohibitively expensive and technically impractical.

Shukla et al. (2010) introduced the major geological sequestration projects in operation. The first commercial project was at Sleipner in the North Sea, which was launched in 1996 in a Norwegian offshore aquifer. Approximately 1 million tonnes (Mt) of CO_2 per year is being injected. The reservoir is a 200-300m thick sandstone (Utsira Formation), and caprock is the 250 m thick Nordland shale, which is 1000m below the surface. The In-Salah Gas project in Algeria injects CO_2 into the Krechba Carboniferous sandstone at a depth of 1800 meters. It was operational from 2004 to 2011 and injected approximately 0.5 Mt CO_2 per year (Rutqvist et al., 2009). Other major injection operations include the Weyburn project in south-central Saskatchewan, Canada started in the year 2000. Here, the Midale carbonate reservoir consists of two aquifers: Vuggy (limestone dominated) and the Marly bed (Dolostone unit)

(Burrowes, 2001). A total of 1.8 Mt of CO_2 per year has been injected into a depleted oil reservoir at a depth of 1400m. In the Snohvit gas project, the North Sea, Injection into Tubaen formation and then Sto formation began in 2008. Approximately 0.5 Mt per year is injected (Celia et al., 2015). Other smaller projects in the United States has been carried out such as Decatur project in Illinois (1 MT CO_2) (Celia et al., 2015).

In southeast Australia, the Otway basin pilot project includes several pilot-scale experiments across various geological reservoirs and sealing layers. The Cooperative Research Centre for Greenhouse Gas Technologies (CO2CRC) initiated the injection of CO_2 into the saline aquifer at a depth of about 2000m underground. 65,445 t of CO_2-rich gas were stored between March 2008 and August 2009. The storage reservoir consists of Waarre-C formation porous sandstone, while the cap-rock/seal is a thick layer of low-porosity Belfast mudstone (Jenkins et al., 2012; Sharma et al., 2011). Gorgon project in northwest Australia is the world's largest commercial-scale CO_2 injection project. Gorgon field contains on average 14% naturals occurring CO_2 which is injected and stored in the Dupuy formation more than 2 kilometres beneath Barrow island (https://australia.chevron.com/).

A saline aquifer suitable for CO_2 storage must preferably be capped by a low permeable rock stratum above to obstruct upward buoyant migration and contain the mobile and buoyant CO_2 within the reservoir. Tight caprocks, such as shale, anhydrite, and salt beds In sedimentary basins would impede the upward buoyant migration in the permeable rocks such as sandstones and carbonates (Celia et al., 2015). Basal caprock in carbon storage projects will be in contact with either $scCO_2$ if the entire reservoir thickness is filled with injected CO_2, or dissolved CO_2 since the density of formation water saturated with CO_2 is higher than when under-saturated. The prediction of CCS project success chiefly depends on the long-term integrity of such caprock for hundreds to thousands of years to come (De Silva et al., 2015).

Shaly caprocks are identified to compromise more than 60% of hydrocarbon reservoir seals (Olabode, 2012). Shale layers act as a barrier in a storage formation. Due to their extremely low permeability, typically less than 1,000 nD (Labus et al., 2017), they either completely stop the upwards leakage of CO_2 or significantly reduce the leakage rate (IPCC Working Group III, 2005).

1.2 Supercritical CO_2

Carbon dioxide (CO_2) is an odourless, colourless gas which is denser than air. High concentrations of CO_2 (>4%) can be dangerous due to suffocation, although it exists in the air in minor amounts. Carbon Dioxide was identified by Joseph Black around the middle of the 18th century. He demonstrated that a hydroxycarbonate of magnesium, when heated, produced a gas and magnesium oxide (Luigi, 2007a):

$$4MgCO_3.\ Mg(OH)_2.\ 4H_20 \rightarrow 5MgO + 5H_20 + 4CO_{2(g)}$$

Equation 1-1

The same gas (CO_2) is also produced plus $MgCl_2$ salt when hydroxycarbonate of magnesium is attacked by HCl acid (Luigi, 2007a):

$$4MgCO_3.\ Mg(OH)_2.\ 4H_20 + 10HCl \rightarrow 5MgCl_2 + 10H_20 + 4CO_{2(g)}$$

Equation 1-2

Black named the gas *fixed gas* due to its ability to be fixed by magnesia and calcium oxide. He also observed the production of carbon dioxide with calcium oxide when similar experiments were carried out with limestone. So Black is considered the first man to both produce and sequestrate CO_2 through his experiments. The results were interesting in that it showed it is possible to trap a gas into a solid phase through chemical reactions. John Robinson, Black's colleague, later showed that marble is made up of CaO for half of its weight and CO_2 for the rest (Luigi, 2007a).

Over the short term, the atmospheric carbon concentration is buffered by its interaction with vegetation, soils and the ocean, whereas over longer geological timescales, it has been balanced by fluxes in and out of rocks, the weathering of Ca-Mg-silicate rocks, the burial and weathering of sedimentary organic matter, and degassing of volcanoes. As silicates weather, they release cations such as Ca and Mg, which can combine with dissolved CO_2 to form carbonate minerals (Kharaka et al., 2011).

The triple point of CO_2 in the P-T diagram is at -56.57°C, and 5.185 bar (≈75.2 psi), and the critical point is close to 31.8°C and 7.38 MPa (≈1070 psi) (Luigi, 2007b). It is evident that CO_2 is a supercritical fluid at temperatures and pressures above its critical point. Most of the candidate CO_2 storage sites will be sufficiently deep that the temperatures and pressures will exceed the CO_2 critical point, making the CO_2 supercritical (J. Pearce et al., 2018).

The density of CO_2 increases with depth as a result of formation fluid pressure. Between 500m and 1000m, the CO_2 density may dramatically increase from 200 kg/m^3 to 900 kg/m^3

and after that reach a more stable value (De Silva et al., 2015). Supercritical CO_2 takes up much less space when injected into deep reservoirs (Holloway, 2001) because of its liquid-like density and gas-like compressibility (Perera et al., 2011). This means that supercritical CO_2 also exerts less buoyancy forces than gaseous CO_2, and a larger number of CO_2 molecules occupies the aquifer's pore space (Bachu, 2002). All this would lead to an increase in the suitability of aquifers for CO_2 storage with increasing depth (De Silva et al., 2015).

Because of only slight solubility of CO_2 in the saline formation water, and its minor buoyancy regarding formation water, the injected CO_2 will eventually rise and accumulate as a separate fluid phase in a significant period of time, years to tens of years. The low-permeability caprock depending on wettability and relative permeability impedes or stops upward migration by buoyancy (Celia et al., 2015). The integrity of caprock in contact with supercritical CO_2 plume can be altered due to its interactions with shale layers (Rezaee et al., 2017).

1.3 scCO_2, Brine and Caprock Interactions

The reactions induced by injection of scCO_2 into a deep aquifer could alter the caprock or trap CO_2 in the form of stable minerals. The former act to deteriorate the seal integrity, while the latter would improve the storage capacity and certainty. The importance of geochemical studies devoted to CO_2 disposal in deep aquifers is two-fold. First, is assessing long-term interactions to predict the permanent CO_2 trapping capacity of the reservoir in a mineral phase. Second is the case of caprock, where assessing induced changes to petrophysical and transport properties, especially in its lower part of caprock, which is in contact with CO_2 is of much interest (Gaus, 2010).

Gaus (2010) categorised the reactions based on their locations: 1. interactions in the well vicinity during the injection phase, 2. interactions between CO_2 and caprock, 3. interactions along leakage pathways such as abandoned wells, caprock and faults, 4. potable aquifer contamination related to leakage of sequestrated CO_2 and, 5. brine movement into aquifers due to pressurised injection of CO_2. The second interactions are favourable when a considerable amount of clay minerals (Kaolinite, Illite, Smectite, Chlorite) are present in the caprock. This case is the focus of this study as CO_2 will be contacted with caprock for very long periods. However, only a limited number of studies have been reported on the CO_2-caprock interactions under geosequestration conditions.

It is doubtful that CO_2-rock interactions open a leakage pathway as no evidence has been reported so far. Creating a leakage path would require an excessive amount of dissolution at a specific site over a very long time which is unlikely to happen in the absence of a flow regime. However, in case of a leakage, CO_2-rock interactions can potentially improve leakage through minerals dissolution and clay minerals shrinkage, or prevent it through precipitation minerals that can react rapidly (Gaus, 2010).

Early investigations on geological CO_2 storage considered only the hydrodynamic trapping under a low-permeability caprock and solubility trapping, without considering the reactivity of the aquifer rock (Luigi, 2007e). Mineral trapping as a result of chemical reactions can be significant, especially in the long term, due to slow kinetics of reaction involving CO_2 entrapment. It strongly depends on the in-situ pressure and temperature, the availability of reactive minerals, such as feldspars, magnesium and iron-rich clays, micas and Fe-oxides, and their reactive surface area (Gunter et al., 2000; Palandri et al., 2005). Mineral trapping, together with solubility trapping can permanently trap over 90% of injected CO_2 in the aquifer for geological time-scales (Gunter et al., 1997). Solid precipitates are immobilised mainly as carbonates, such as calcite, magnesite, dolomite, dawsonite, and siderite (Lagneau et al., 2005; Palandri et al., 2005).

Geochemical reactivity of the seals must be qualified to determine their long-term effectiveness, as they act as a physical barrier to CO_2 migration. Fluid-rock interactions play a significant role in the success of CO_2 sequestration in deep saline aquifers, which include chemical reactions and interfacial interactions. The dissolution of minerals that form the caprock takes place under the acidic condition of the aquifer induced by increased CO_2 content. The amount of minerals dissolved or precipitated, subsequent pH buffering, pore volume changes and arrangement are crucial parameters for the investigation of seal integrity. Interfacial interaction altering interfacial tension is also very important. Changes to Interfacial Tension (IFT) and rock wettability can induce variations to caprock capillary-sealing efficiency and transport properties (relative permeabilities and residual saturations) concerning CO_2 (Chalbaud et al., 2009).

Although it is assumed that these geochemical interactions occur in the context of CO_2 storage in an aqueous environment, some reactions may occur in the pure $scCO_2$-rock setting. For instance, in the vicinity of the injection well, where the CO_2 concentration is almost 100%, because the brine in this region would dissolve in supercritical carbon dioxide (Gaus, 2010). Other possible interactions in a non-aqueous environment are the chemical

interactions between water dissolved in $scCO_2$ and rock. Some processes are identified as the drive for CO_2 and rock interactions such as the dissolution of CO_2 in brines, desiccation of clays, reactions triggered by brine concentration, acid-induced reactions, interactions of pure CO_2 and minerals, and reactions induced by other gases than CO_2 (Gaus, 2010).

The injection of CO_2 into the saline aquifer triggers the chemical reactions that alter the mineralogical assembly and thermodynamic equilibrium of the aquifer (De Silva et al., 2015). Although CO_2 solubility is lower in higher concentrated brine and higher temperature, it still has considerable solubility in high-pressure aquifer brine up to 1-1.5 mol/kg, and this is critically higher for $scCO_2$ in deep saline aquifers (De Silva et al., 2015). Upon injection, CO_2 would dissolve into the in-situ brine, forming a reactive solution (carbonic acid). Both dissolved CO_2 in brine and acidification of the brine will trigger the interaction with the formation rock and, for example, cause mineral dissolution. H_2CO_3 partially dissociates in the brine into hydrogen and bicarbonate ions, and consequently, bicarbonate ions partially dissociate into H^+ and carbonate ions (De Silva et al., 2015; Gunter et al., 1997):

$$CO_{2\,(g)} + H_2O_{\,(l)} \leftrightarrow H_2CO_{3\,(aq)}$$

Equation 1-3

$$H_2CO_{3\,(aq)} \leftrightarrow H^+_{\,(aq)} + HCO^{3-}_{\,(aq)}$$

Equation 1-4

$$HCO^{3-}_{\,(aq)} \leftrightarrow H^+_{\,(aq)} + CO_3^{2-}{}_{(aq)}$$

Equation 1-5

This will cause an imminent drop in pH of the brine and cause an acid attack on the minerals. Carbonate minerals, which are generally a constituent of sedimentary rocks, interact with the proton and rapidly buffer the pH, reducing the acidity of the brine. According to Liu et al. (2011), injection of CO_2 drops the aquifer pH to around three and eventually raised to around five due to the reactions initiated among the CO_2 and carbonate minerals.

$$CaCO_3(s) + H^+_{\,(aq)} \rightarrow Ca^{2+}_{\,(aq)} + HCO_3^-{}_{(aq)}$$

Equation 1-6

$$CaMg(CO_3)_2\,(s) + 2H^+_{(aq)} \rightarrow Mg^{2+}_{(aq)} + HCO_3^-{}_{(aq)}$$

Equation 1-7

Even after carbonate dissolution buffers the pH, the brine is still acidic enough to attack aluminosilicate minerals (clays and feldspars). Dissolution of formation rock minerals may occur as a result of the acid attack. A significant increase in porosity and permeability could

happen, especially near the injection well, which also improves the trapping process by increasing injectivity. Precipitation of carbonate minerals as an outcome of such reaction, in contrast, would decrease the aquifer permeability in the later stages of the geochemical reactions, and therefore decrease injectivity and trapping capacity (Bachu et al., 1994).

While the main expected carbonate products are Ca-, Mg-, and Ca-Mg-carbonates, Fe-carbonates such as siderite ($FeCO_3$) and ankerite ($Ca(Fe, Mg, Mn)(CO_3)_2$), as well as dawsonite ($NaAlCO_3(OH)_2$) are also important (Luigi, 2007d). The presence of either a Na/K or Ca/Mg cation in the basic aluminosilicate mineral determines how the formation water will evolve. If Na/K-bearing minerals are present, CO_2 is neutralised, and bicarbonate brines develop. On the other hand, in case of Fe/Ca/Mg-bearing minerals, neutralisation of CO_2 results in precipitation of siderite, calcite, magnesite or dolomite, with brine ionic strength remaining relatively constant. A substantial amount of CO_2 is trapped and immobilised in both paths, so the chance of CO_2-charged brine reaching the surface is minimised (Czernichowski-Lauriol et al., 2006; Gunter et al., 1997):

$$Fe^{2+}_{(aq)} + CO_2{}^{-3}{}_{(aq)} \rightarrow FeCO_3(s)$$

Equation 1-8

$$Ca^{2+}_{(aq)} + CO_2{}^{-3}{}_{(aq)} \rightarrow CaCO_3(s)$$

Equation 1-9

$$Mg^{2+}_{(aq)} + CO_2{}^{-3}{}_{(aq)} \rightarrow MgCO_3(s)$$

Equation 1-10

De Silva et al. (2015) summarised all the possible dissolution and precipitation reactions and their resulting secondary minerals. Feldspar reactions with CO_2 are considerable and are categorised to two groups: calcium-rich feldspar such as anorthite and labradorite, which provide divalent cations (Ca^{2+}); and alkaline feldspar or potassium and sodium-rich feldspars, which provide monovalent cations (Na^+ or K^+) for the mineral trapping process (De Silva et al., 2015). According to Gunter et al. (1993), the complex reactions between clay and feldspar minerals and brine-CO_2 can generally be presented as:

$$\text{Feldspars} + \text{Silicastic clays} + CO_2 \rightarrow \text{Kaoline} + \text{Calcite} + \text{Dolomite} + \text{Quartz}$$

Equation 1-11

It is observed experimentally that small anorthite amounts induce fast reactions with CO_2, resulting in carbonate precipitation and significant porosity increase of the reservoir rock.

The complete reaction for the dissolution of Ca-feldspar, which precipitates calcite and kaolinite, is as follows (De Silva et al., 2015):

$$CaAl_2Si_2O_{8(s)} + CO_{2(g)} + 2H_2O_{(l)} \rightarrow CaCO_{3(s)} + Al_2Si_2O_5(OH)_{4(s)}$$

Equation 1-12

The presence of any alkaline feldspar in the formation rock causes precipitation of a sodium alumino-carbonate mineral $NaAl(CO_3)(OH)_2$, called dawsonite, although the rate is slower than in Ca-feldspar. The $Na^+(aq)$ ions are essential for dawsonite precipitation, as they cause the CO_2 to precipitate in the form of dawsonite, even when K-feldspar exists (De Silva et al., 2015):

$$NaAlSi_3O_{8(s)} + CO_{2(g)} + 2H_2O_{(l)} \rightarrow NaAl(CO_3)(OH)_{2(s)} + 3SiO_{2(s)}$$

Equation 1-13

$$KAlSi_3O_{8(s)} + Na^+_{(aq)} + CO_{2(g)} + 2H_2O_{(l)} \rightarrow NaAl(CO_3)(OH)_{2(s)} + 3SiO_{2(s)} + K^+_{(aq)}$$

Equation 1-14

Gunter et al. (1997) reported the precipitation of Na-Smectite as a result of albite dissolution:

$$7\ NaAlSi_3O_{8(s)} + 6\ H_2O + 6\ CO_2 \rightarrow 6HCO_3^- + 6Na^+ + \text{Na-Smectite} + 10\ \text{Quartz}$$

Equation 1-15

Apart from the dissolution of feldspar, clay minerals dissolve at low pH. Dissolution of kaolinite and illite provides cations to the aquifer fluid (De Silva et al., 2015; Yang et al., 2010).

$$Al_2Si_2O_5(OH)_{4(s)} + 6H^+_{(aq)} \rightarrow 5H_2O + 2SiO_{2(aq)} + 2Al^{3+}_{(aq)}$$

Equation 1-16

$$\text{Illite} + 8H+_{(aq)} \rightarrow 5H_2O_{(l)} + 0.6K^+_{(aq)} + 0.25Mg^{2+}_{(aq)} + 3.5SiO_{2(aq)} + 2.3Al^{3-}_{(aq)}$$

Equation 1-17

Chlorite dissolution is an example of alteration of clay minerals. Iron and magnesium are the donor cations in the reaction and siderite and dolomite trap CO_2 permanently (Gaus, 2010):

$$Fe_{2.5}Mg_{2.5}Al_2Si_3O_{10}(OH)_8 + 2.5\ CaCO_3 + 5\ CO_2$$
chlorite *calcite*

Equation 1-18

$$\rightarrow 2.5\ FeCO_3 + 2.5\ MgCa(CO_3)_2 + Al_2Si_2O_5(OH)_4 + SiO_2 + 2H_2O$$
Siderite *dolomite* *kaolinite* *chalcedony*

Equation 1-19

Another example is the reaction between annite ($KFe_3^{2+}AlSi_3O_{10}(OH)_2$) and CO_2, which results in siderite ($FeCO_3$) precipitation plus K-feldspar (De Silva et al., 2015; Lagneau et al., 2005):

annite + 3 CO_2 → 3siderite + K-feldspar

Equation 1-20

In another path of reactions, Gunter et al. (2000) showed precipitation of muscovite as a result of albite, K-feldspar, kaolinite, and annite dissolution:

$3\ NaAlSi_3O_8 + 2\ CO_2 + 2\ H_2O + K^+ \rightarrow KAl_3Si_3O_{10}(OH)_2 + 6\ SiO_2 + 3\ Na^+ + 2\ HCO_3^-$

Equation 1-21

$3\ KAlSi_3O_{8(s)} + + 2\ CO_2 + 2\ H_2O \rightarrow KAl_3Si_3O_{10}(OH)_2 + 6\ SiO_2 + 2\ K^+ + 2\ HCO_3^-$

Equation 1-22

$3\ Al_2Si_2O_5(OH)_4 + 2\ K^+ + 2\ HCO_3^- \rightarrow 2\ KAl_3Si_3O_{10}(OH)_2 + 5\ H_2O + 2\ CO_2$

Equation 1-23

$3\ KFe_3^{2+}AlSi_3O_{10}(OH)_2 + 11\ CO_2 \rightarrow KAl_3Si_3O_{10}(OH)_2 + 9\ Siderite + 6\ SiO_2 + H_2O + 2\ K^+ + 2\ HCO_3^-$

Equation 1-24

Xu et al. (2004) provided a list of minerals whose alteration would lead to carbonates precipitation after surveying different classes of rock-forming mineral. Based on their data, the minerals that can potentially sequestrate the maximum quantity of CO_2, assuming the complete alteration of primary minerals, are olivine (2014.7-1896.3 kg/m^3), pyroxene group-enstatite (1404.2 kg/m^3), augite (1306.3 kg/m^3), serpentine (1232.7 kg/m^3), amphibole group and hornblende (1169.5-1000.4 kg/m^3), chlorite group (923.4 kg/m^3), mica group-phlogopite and biotite (881.8- 671 kg/m^3), and plagioclase-anorthite (436.4 kg/m^3). Clay minerals- illite and smectite have a lower capacity of 78.4 and 161.2 kg/m^3.

A geochemically suitable caprock for CO_2 storage contains both clay minerals and carbonates as suggested by several studies (Izgec et al., 2008; Lagneau et al., 2005; Rosenbauer et al., 2005; Szabó et al., 2016). Siliciclastic aquifers that contain a collection of basic aluminosilicate minerals such as feldspars, zeolites, illites, chlorites, and smectites were identified as the best option for trapping CO_2, by precipitating carbonates (Gunter et al., 2000; Gunter et al., 1993; Law et al., 1996). When reacted with CO_2, the basic aluminosilicate minerals break down to form kaolinite. Their metallic cations are released and replaced the protons from the H_2CO_3 aqueous complexes in the brine, and the CO_2 is neutralised. Although the potential for CO_2 sequestration is significantly higher in case of silicate mineral reactions than carbonate

mineral dissolution, the faster kinetic rates of carbonate minerals would lead to more CO_2 uptake at the beginning of the sequestration process (Gunter et al., 1997).

Although the scCO_2-brine-rock system is a complex multi-component multi-phase system, some simple physical explanations such as buoyancy and capillary pressure can define most of the system. For example, a relatively fast buoyant separation relative to the overall time scale of the project is expected due to the density difference between injected CO_2 and brine, assuming vertical equilibrium is reasonable (Celia et al., 2015).

Carbon dioxide is normally the nonwetting fluid relative to brine in sedimentary rocks (sandstones and carbonates) that do not contain organic material. Upon injection, CO_2 displaces the formation water under the pressure up to the point of irreducible water saturation in a drainage cycle. Upon the completion of the injection phase, the buoyant CO_2 rises to form a plume under the seal. Water invades back up to the point of irreducible CO_2 saturation in an imbibition cycle. CO_2 becomes immobile at this stage, and capillary trapping is achieved (Celia et al., 2015).

The non-wetting CO_2 under the seal in inhibited to flow through by the capillary forces up to the capillary entry pressure. If the pressure of the underlying CO_2 plume exceeds the capillary entry pressure of the caprock, CO_2 can penetrate the seal and eventually leak when an interconnected flow path is formed across the caprock. Capillary entry pressures for CO_2 of 0.5 to 5 MPa (72.5 to 725 psi) is known to restrict the penetration of CO_2 (Kampman et al., 2017). To create the buoyancy pressure large enough to overcome the capillary entry pressure, a certain height of fluid phase is necessary under the hydrostatic conditions.

The sealing efficiency of the caprock crucially depends on its wettability. In cases when the seal is CO_2-wet, CO_2 will spontaneously imbibe into the shale and flow through it, given enough time (Naylor et al., 2011; Schlomer et al., 1997). Mixed-wet or oil-wet storage rock are reported in previous measurements to be CO_2-wet (Yang et al., 2008).

In cases where the seal rock properties are altered as a result of chemical interaction between the caprock and scCO_2/brine, a potential leakage is possible. This could occur if CO_2-rich brines penetrate more permeable pathways and fractures and penetration of CO_2 is further enhanced by the mineral dissolution reactions (Kampman et al., 2017). The capillary entry pressure and the relevant CO_2 column height must be assessed to indicate the possible breakthrough and leakage (Olabode, 2012).

1.4 The Effect of Chemical Reactions on Porosity and Permeability

The effect of chemical reactions on flow and mechanical properties of caprock is a significant point of study in sequestration projects as they play an essential role in the selection of the appropriate aquifer for CO_2 injection and seal integrity studies. The mineralogical reactions induced by CO_2 interaction with water and caprock are highly complex and depend on the thermodynamic, kinetic, flow and transport processes. They can have either beneficial or deleterious impacts on porosity and permeability (J. K. Pearce et al., 2018). The result of such reactions is determined by factors such as reservoir pressure and temperature and its host rock mineralogy and composition of the brine. They are also time-dependent, due to very slow reaction kinetics of most minerals involved in such reactions. Several mechanisms are believed to contribute to the alterations of rock properties such as dissolution and precipitation of mineral phases, compaction, and fines migration (Czernichowski-Lauriol et al., 2006).

The relationship between mineralogy, pore structure and permeability in shales is still not fully understood. Chemical reactions that lead to an increase in porosity and therefore permeability are usually attributed to the dominance of the primary minerals' dissolution mechanism (carbonates, feldspars, and micas), while Chemical reactions that lead to a decrease in this property may reveal secondary minerals' precipitation (carbonates, anhydrite, kaolinite, and dawsonite) alongside with other mechanisms such as physical compaction, and fines migration (Shiraki et al., 2000).

1.5 Previous Studies

Most of the studies on CO_2-brine-rock interactions have focused on the host reservoirs that store the CO_2, and geochemical reactions of the caprock associated with CO_2 sequestration have been much less studied (Liu et al., 2012). However, caprock alteration, which can lead to CO_2 storage failure and mineral trapping as a safe and permanent CO_2 storage method, has received substantial consideration in recent research studies (A. Olabode et al., 2017)Appendix I). There are some experimental methods and a few modelling software applied in this regard to examine and quantify the extent of changes imposed by CO_2 injection into the reservoir.

Experimental methods usually Include total impact experiments (also: batch-soak reactors/autoclaves) where powdered samples, small rock pieces, or plugs are reacted with $scCO_2$ injected into the aqueous environment under the pressures and temperatures usually

higher than of existing in deep saline aquifers for a known period (see Section 1.5.1). At the end of the experiment, rock samples are extracted from the cell and carefully observed to determine the changes in their mineralogy and petrophysical properties. The goal of such studies is to investigate the role of elevated CO_2 fugacity on mineral dissolution and precipitations, brine chemistry evolution, as well as the accompanying impact on porosity/permeability. These experiments are usually based on real rock samples and brine compositions, but synthetic rock material and brine concentration have been used for several reasons. The studies on the caprock minerals reported to date have been carried out under temperatures and pressures higher than that of actual reservoirs to fast-track the slow-occurring reactions (Appendix I). Nevertheless, experiments under extreme laboratory conditions (temperatures up to 200°C and pressures up to 30 MPa) have provided valuable insights into the possible brine-CO_2-rock reactions and their long-term influence on rock properties (Appendix I.A) (De Silva et al., 2015).

To support the results of geochemical lab experiments, the performance of reference experiments in CO_2 free brine and coupled geochemical modelling is preferential (Szabó et al., 2016). However, there are several such coupled experimental-modelling geochemical caprock studies (Alemu et al., 2011; Czernichowski-Lauriol et al., 2006; Gunter et al., 1997; Kaszuba et al., 2003; Knauss et al., 2005; Liu et al., 2011; Julie K. Pearce et al., 2019; Sass et al., 2001).

Several reviews on caprock and CO_2-saturated brine interactions have been published so far, e.g., De Silva et al. (2015). Shukla et al. (2010) reviewed the caprock integrity after CO_2 injection with a focus on stress field perturbation as a result of injection pressure and upward pressure, caprock stability during and after injection, the effect on pre-existing fracture and faults and reopening them. Griffith et al. (2011)'s review presented a detailed characteristic of proposed CO_2 storage sites in the US, including their structural petrophysical and chemical data. They gathered several common features in the caprocks, such as the existence of frequent minerals of calcite, quartz, dolomite, illite, feldspar (potassium or sodium), glauconite, and kaolinite. Liu et al. (2012) reviewed the geochemical aspects of laboratory experiments and summarised several experimental studies. Among these, one can find batch experiments (Alemu et al., 2011; Credoz et al., 2009; Kaszuba et al., 2005; Kohler et al., 2009; Navarre-Sitchler et al., 2011), CO_2 diffusion experiments (Aplin et al., 2006; Berthe et al., 2011; Busch et al., 2008; Wollenweber et al., 2010; Wollenweber et al., 2009), as well as CO_2 breakthrough and flow experiments (Angeli et al., 2009; Soldal, 2008).

1.5.1 Previous experimental studies

After being injected, CO_2 will be in contact with caprock in different forms, as predicted by several studies (Liu et al., 2012; Lu et al., 2012): dissolved in brine (saturated or under-saturated) and wet CO_2. Laboratory studies have been carried out by several authors to investigate the potential for mineral trapping that is summarised here. Most of such studies are related to the host reservoirs (sandstone and carbonate units) which contain the injected CO_2. Fewer studies have been focused on the interaction of the caprock with CO_2 in geosequestration projects (Pearce et al., 2020). Studies related to caprock samples are difficult because of practical difficulties mainly related to low permeability of the samples which introduce several problems. Low permeability core plugs are problematic in the saturation process because they take longer to be saturated, and they could collapse in the process. Also, penetration of CO_2 or CO_2-saturated water is prevented by their low permeability.

The overall outcome of the experiments designed at assessing the interactions between CO_2-brine-rocks show apparent changes in the fluid composition as well as carbonate dissolution but less obvious aluminosilicate interactions that either trap the CO_2 or cause large porosity or permeability changes. This is not surprising as the kinetic rates for carbonates are much higher than of alumino-silicates, and the slow pace reaction would not contribute much in the limited time span of these types of experiments as they would in the geologic timescale required for a CO_2 storage context (Gaus, 2010). A reduction of the caprock capillary sealing efficiency has also been observed, in most studies on geochemical and petrophysical properties of post-experiment samples, but in limited magnitude (Liu et al., 2012).

Experimental conditions and results of several studies have been reported in Appendix I.A. Pearce et al. (1996) and Rochelle et al. (1996)'s batch experiments on supercritical CO_2, with sandstone and mudstone, showed substantial alteration of primary calcite and dolomite, as well as the dissolution of anhydrite. They also reported precipitation of calcite and possible corrosion of detrital feldspars. The precipitation of Na-smectite was reported here, although not enough convincing evidence supporting this last process was presented.

Gunter et al. (1997), in one of the earliest batch-soak reactor studies on glauconitic sandstones, chose biotite as a proxy for glauconite and labradorite as a proxy for anorthite. Under these conditions, there were no new major reaction products observed. They related this to increased formation pH due to the excessive alkalinity of the brine solution, which neutralised the acidity in the media and prevented the water-rock reactions. Sass et al.

(2001)'s experiments with anorthite and glauconite did not show any carbonate precipitation either. In the experiments run with anorthite, sodium increased in the solid solution, and a corresponding amount of Ca was released to the aqueous solution, in case of glauconite, also the Na content of the solid phase increased, but K, Fe and Si decreased, whereas Al, Mg and Ca did not change.

Schlomer et al. (1997) investigated sealing efficiency of caprocks via geochemical and mineralogical analysis, mercury porosimetry and specific area measurements (nitrogen adsorption). They calculated maximum sustainable gas column heights in the range of 20 to 2000m. Busch et al. (2011) evaluated relative permeability and capillary threshold pressures (or column height) techniques to study their effect on plume migration, residual CO_2 trapping and CO_2 dissolution in the brine.

Kaszuba et al. (2003, 2005) simulated an arkose aquifer and shaly caprock system in a flexible cell hydrothermal reactor, in one of the first attempts to study seal integrity of a geologic carbon repository. They attained a steady state in a first step, at 200°C, 200bar for several days and then injected CO_2 to the reactor in a second step under the same conditions but for longer periods. In 2004, The results of experiments include precipitation of clay minerals on oligoclase, precipitation magnesite on biotite grains, precipitation of analcime. In 2005, they also performed a CO_2-free reference experiment with the same pressure and temperature conditions and time. Kaszuba et al. (2005) observed magnesite precipitation followed by magnesite dissolution and precipitation of siderite, clay minerals and analcime. However, they did not observe any dawsonite as a precipitating phase suggested by reactive transport models (James W. Johnson, 2001; Knauss et al., 2005). They attributed this to undersaturation state of dawsonite in the aqueous solution. Equilibrium reaction between dawsonite and analcime in the experiments of Kaszuba et al. (2005) is worth considering as follow:

$$Na_{0.96}Al_{0.96}Si_{2.04}0_6.H_20 + 0.96\,CO_{2(g)} \leftrightarrow 0.96\,NaAlCO_3(OH)_2 + 2.04\,SiO_2 + 0.04\,H_2$$

Equation 1-25

Brine chemistry also showed significant variations (Kaszuba et al., 2005). The significant increase in SiO_2, K^+ and Ca^{2+} and decrease in Na^+ and Cl^- concentrations verified the existence of primary silicate minerals dissolution through reaction with CO_2 and brine.

The fugacity of CO_2 and ionic strength of the brine play an important role in the fate of reactions. In their study on the effects of CO_2 concentration on the mineral dissolution and precipitation processes, Moore et al. (2005) reacted 1×10^{-8} mol of each selected mineral with

CO_2 and recorded the required CO_2 amount to saturate the solution with by-products (Appendix I.A). Full saturation of kaolinite, a by-product of orthoclase dissolution, occurred at a CO_2 concentration of 0.03 mol/kg (pH = 6), with dawsonite under-saturated. While, full saturation of dawsonite was achieved at a CO_2 concentration of 0.07 mol/kg, with kaolinite under-saturated. When CO_2 concentration was increased to 1 mol/kg (pH = 5), alunite was formed and some of the precipitated kaolinite was dissolved.

Bertier et al. (2006) carried out a long-term experimental study with sandstone, saline water, and CO_2 over eight months. According to their results, a large dissolution of carbonates and some dissolution of feldspar and significant precipitation of kaolinite, siderite, and calcite took place. This large dissolution and precipitation, which significantly modify the reservoir properties, can facilitate injection or increase CO_2 storage capacity respectively. Wigand et al. (2008) used SEM analysis to identify the minerals in the mineral trapping process in saline aquifers. They reported dissolution of dolomite just after CO_2 injection and dissolution of albite, and K-feldspar in the later stage of their experiments. Precipitation of montmorillonite was observed as a result of albite dissolution. In 2009, Ketzer et al. (2009) also observed the dissolution of calcite, feldspar, and pyrite in their SEM analysis. Precipitation of kaolin during their 100-hours batch experiment was observed for the first time.

One reason for reactions not taking place is the lack of ions in a CO_2-brine-rock system. In a study by Rimmelé et al. (2010) with distilled water in the presence of $scCO_2$, no significant changes in the mineralogy of the rock samples were observed, as a result of a lack of ions in the solution. Lu et al. (2011) selected 0.2 mol/kg KCl as their brine for $scCO_2$ interaction with sandstone. Due to the non-availability of Na+ ions in the aqueous medium, no dawsonite was precipitated, as explained in Section 1.3. The high temperature of the system caused only a conversion of smectite into illite. These conditions are not typical of the temperature range of CO_2 geosequestration projects (35–75°C).

Marbler et al. (2013) observed a reduction in sandstone strength through their experiments due to CO_2-brine–rock interactions. Dissolution of calcite due to precipitation of carbonates induced weak spots and micro-fractures in the cement, which weakened the bonds between cement and detritus minerals.

Mito et al. (2008) executed field-scale experiments on the chemical composition of aquifer fluid and reported an increase in $HCO3^-$ concentration which was attributed to the dissolution of CO_2. The increases in Ca, Mg, Fe, Al and Si concentrations were mainly due to chlorite and

plagioclase dissolution, which revealed the initiation of considerable geochemical reactions from the initial stage of CO_2 injection.

$$\text{Plagioclase} + 2\,H^+ + 3\,H_2O \rightarrow Ca^{2+} + 2\,Al(OH)_3 + 2\,H_4SiO_4 + NaAlSi_3O_4$$

Equation 1-26

$$\text{Chlorite} + 20\,H^+ \rightarrow 5\,Fe^{2+} + 5\,Mg^{2+} + 4\,Al(OH)3 + 6\,H_4SiO_4$$

Equation 1-27

Wollenweber et al. (2010)'s experiments on shaly caprock plugs showed an increase in permeability and decrease in capillary entry pressure, although not reported any detectable mineral alterations. The diminution of shaly caprock is due to carbonate dissolution and reprecipitation. In their study on shaly caprock, Liu et al. (2012) reported only a limited caprock interaction which was only to the vicinity of the CO_2-caprock interface. Minor dissolution of K-feldspar and anhydrite, along with precipitation of illite, smectite, and siderite in the vicinity of pyrite were found in this case. Armitage et al. (2013) study on mudstone samples from In Salah, Algeria showed chlorite and siderite dissolution which caused an increase in porosity and permeability of the caprock.

Yin et al. (2016) studied the effects of shale-scCO_2 reaction on the physical and structural properties of shale samples from a CO_2 enhanced shale gas recovery (CO_2-ESGR) site in China with several different methods. They found that the influence on the micropores is much stronger than mesopores. XRD results showed increased quartz content and decreased calcite and clay contents. The same trend was also observed by Wang et al. (2016). However, Rathnaweera, Ranjith, Perera, et al. (2016)'s 1.5-year study on sandstone exposed to brine-scCO_2 showed quartz dissolution as well as calcite, siderite, and barite dissolutions.

Rathnaweera, Ranjith, Perera, et al. (2016) studied the interaction between injected CO_2, brine, and rock and their geochemical and mineralogical effects, particularly on flow characteristics of the reservoir rock (Appendix I.A). Permeability changes and their impact on flow in deep saline aquifers were investigated.

Rezaee et al. (2017) conducted a study on shale alteration after exposure to scCO_2 on samples from Gippsland Basin, Australia. They examined mineralogical changes by XRD and SEM and reported dissolution and precipitation of several authigenic minerals such as kaolinite, natrojarosite, silica, and gypsum. The also applied NMR and MICP methods to examine capillary threshold pressure, and pore size distribution which indicated a reduction in the

capillary threshold pressures and an increase in pore volume for most of the samples exposed to $scCO_2$.

Kweon et al. (2017) investigated the impact of reactive surface area on reaction rates with the same temperature and pressure as this study (14.1MPa and 60°C) for two weeks under CO_2 reservoir conditions. They also used different type of samples (cores, rock chips, and powder). They found that iron and other dual valance minerals (magnesium and calcium) play an important part in mineral dissolution reactions.

1.5.2 Previous modelling works

The fate of CO_2 in deep geological formations is determined by the reactions between CO_2, brine and mineral phases. Previous work suggested the dissolution of primary phases, mainly silicates and aluminium-silicates, and the precipitation of secondary phases, mainly carbonates, silica minerals, and clay minerals (Luigi, 2007d). The minerals react at different rates determined by their rate constants and mineral surface area (Kweon et al., 2017). Different surface area values, such as geometric and BET, have been used in previous studies. Some authors selected the BET surface area, while others calculated the surface area based on a relationship between mineral density, grain diameter, and roughness factor. The reactive surface area then comes into play by some authors to incorporate the amount of surface area involved in the reaction process. The previous attempts to interpret the experimental results using geochemical models have not always been successful. The species concentrations of the two approaches cannot be matched clearly, and all processes occurring in the experiments are not captured in the models or vice versa (Wigand et al., 2008).

In their reaction path modelling of geological CO_2 sequestration using the PATHARC.94 computer code, Gunter et al. (1997) chose the geometrical surface area as the reactive surface area. They assumed a constant-volume sphere with an average diameter of 100 microns for individual mineral grains in the calculation of the geometrical surface area. The average temperature, pressure, and chemical composition of the aquifer are reported in Appendix I.B.

Gunter et al. (1997) simulation predicted substantial precipitation of siderite and subordinate calcite. Mineral trapping of CO_2 and solubility trapping was predicted to take place in around 6–40 years. The required time for these reactions to come to equilibrium is much longer (hundreds to thousands of years) according to recent studies (Miller et al., 2016). The main occurring reaction was considered to be (Luigi, 2007f):

$$3\ KFe_3^{2+}AlSi_3O_{10}(OH)_2 + 11\ CO_2 \rightarrow KAl_3Si_3O_{10}(OH)_2 + 9\ FeCO_3 + 6\ SiO_2 + H_20 + 2K^+ + 2\ HCO_3^-$$

Annite *muscovite* *siderite*

Equation 1-28

In their second study, Gunter et al. (2000) chose to dissolve a finite amount of CO_2, one molal at the beginning of the simulation instead of buffering it to simulate the condition after CO_2 injection had ceased. After the equilibrium was attained in a hundred years, CO_2 pressure dropped from 87 to 0.02 bar. Precipitation of 1 mol of siderite alongside the minor amount of calcite and dolomite was reported here, confirming the high capacity of Fe(II) minerals for CO_2-trapping. However, Xu et al. (2000a, 2004) questioned these results. They modelled the same glauconitic sandstone aquifer using TOUGHREACT. They recognised that the overestimation of precipitating siderite and consequently, the CO_2-sequestration capacity is because of selecting annite [$KFe(II)_3A1Si_30_{10}(OH)_2$] as a proxy for glauconite [$K_{0.75}Mg_{0.25}Fe(II)_{0.25}Fe(III)_{l.25}\,Al_{0.5}Si_{3.75}O_{10}(OH)_2$]. Therefore, they considered glauconite instead of annite, oligoclase instead of albite + anorthite, and illite instead of muscovite in reaction path modelling. The presence of some Mg in illite [$K_{0.6}\,Mg_{0.25}\,Al_{1.8}\,(Al_{0.5}\,Si_{3.5}\,O_{10})\,(OH)_2$] which is absent in muscovite determines a moderate increase in the CO_2-sequestration capacity. The initial aqueous solution, CO_2 injection pressure, and temperature are reported in Appendix I.B. The main trapping minerals were found to be ankerite and siderite. In 100,000 years, the total CO_2 sequestration capacity was approximately 140 g/kg, and porosity decreased from the initial value of 12% to 11.6%.

In another reaction path modelling investigation, Xu et al. (2003, 2005) used TOUGHREACT code and a total surface area of 10 $m^2\ dm^{-3}$ of the medium. Mineralogy, porosity, brine type, injection pressure, and temperature are reported in Appendix I.B. Here, dawsonite, ankerite, and siderite trapped CO_2 in a solid phase but siderite was later re-dissolved. Siderite and ankerite are Fe^{+2} -bearing minerals which are associated with the dissolution of chlorite and hematite. The Na^+ required for dawsonite precipitation was supplied by oligoclase. So the availability of these ions from the dissolution of chlorite and oligoclase determines the CO_2 mineral-trapping capacity. Owing to the abundance of oligoclase and chlorite minerals, also precipitation of carbonate minerals in these sediments compared to glauconitic sandstones of the previous study, sequestration capacity was significantly higher. In this case, a porosity decrease of about 4% was also observed after 100,000 years.

Permian White Rims Sandstone over-lied by shale and evaporite layers as the seal was investigated by White et al. (2005). They measured the sealing properties of potential caprocks through mercury injection porosimetry and found that a CO_2 column of the order

of 500-900 m in thickness was withheld by caprock (Mancos Shale). The reservoir rock mineralogy is reported in Appendix I. B. They simulated a 30-years CO_2 injection followed by 1,000 years reaction path modelling and considered dolomite, siderite, and dawsonite as possibly precipitating solid phases in their modelling, although not initially present in the reservoir. The results suggested that calcite and dawsonite trapped 21% of the injected CO_2, 52% remained as a separate gas phase or dissolved in ground-waters, and the remaining 17% had leaked to the ground surface.

Gaus et al. (2005) implemented reaction path modelling and reactive transport modelling using code PHREEQC v2.6 (Parkhurst and Appelo, 1996) to examine the effect of CO_2 injection on the porosity of the caprock. The mineral compositions of the caprock considered in geochemical modelling and thermodynamic conditions are reported in Appendix I.B. They chose three different compositions for plagioclase in separate runs. First with albite, second with albite/anorthite 50-50, and third with oligoclase (An_{20}). They also considered dawsonite, disordered-dolomite, and magnesite as possible secondary minerals in addition to primary minerals. In all three runs, calcite accompanied by a limited amount of dawsonite precipitated. Small changes in porosity (<0.05% and 2.8%) were calculated in the case of albite and albite/anorthite. About 2.8% decrease in porosity is attributed to the dissolution of anorthite and the subsequent precipitation of calcite and kaolinite.

Lagneau et al. (2005) modelled the CO_2 sequestration with conditions reported in Appendix I.B. Dissolution of annite and K-feldspar was the main geochemical reactions. A small degree of calcite dissolved and then re-precipitated to pH buffering from 5.1 to 7.7. The increase in pH was related to the precipitation of siderite, taking Fe^{+2} ions in the formation fluid.

Ranganathan et al. (2011) modelled the CO_2 mineralisation and movement in a 3000m deep, 50km*50km*50m section for 10,000 years. The reported that injected CO_2 moved upward in the reservoir and accumulated beneath the caprock. The CO_2 plume then spread laterally or downward due to reactions with surrounding minerals. According to this model, the first evidence of any noticeable mineralisation came after around 200 years. After considering 10,000 years, precipitation of kaolinite, dolomite, and illite trapped only up to 10% of injected CO_2. 60% of CO_2 was trapped through solubility trapping

Liu et al. (2011) model incorporated a 10m thick sandstone layer located at 2km depth. The CO_2 was introduced into the model with an injection rate of 31,526 ton/year. The duration of simulations was 10,000 years which saw the hydrodynamic and solubility trapping processes completed. At the end of this period, a CO_2 plume with over a 3300m radius from

the injection well existed. The acidic environment (pH about 3-5) caused the feldspar to dissolve. High K^+, Al^{3+} and Ca^{2+} ion concentrations around the wellbore reacted with SO_4^{2-} ions present in the pore fluid and precipitated some alunite and anhydrite.

$$K^+_{(aq)} + 3\ Al^{3+}_{(aq)} + 2\ SO_4^{2-}{}_{(aq)} + 6\ H_2O_{(l)} \rightarrow \underset{\textit{Alunite}}{KAl_3(SO_4)_2(OH)_{6\ (S)}} + 6\ H^+_{(aq)}$$

Equation 1-29

$$Ca^{2+}_{(aq)} + SO_4^{2-}{}_{(aq)} \rightarrow \underset{\textit{Anhydrite}}{CaSO_{4\ (S)}}$$

Equation 1-30

The results of reaction path modelling by Kirste (2013), however, involved the initial dissolution of chlorite, and K-feldspar and precipitation of kaolinite, siderite, magnesite, and SiO_2. Smectite appeared only in the case of most reactive mineralogies and conditions. The used two series of reactive surface area for mineral phases and even for the higher reactive surface area, the total dissolution did not exceed 0.7% in 100 years. Only a very slight decrease in porosity was reported. The temperature sensitivity was the highest among the parameters analysed such as pH and CO_2 content.

1.6 Objectives

This research is designed to give a better understanding of fate and efficacy of shaly caprocks in a CO_2 storage system. The injection of CO_2 into deep aquifers ultimately modifies the geochemical conditions of the host and cap-rocks, but the effect and extent of $scCO_2$ on the physical properties of the caprock are not completely understood. The primary goal of this study has been to examine the dynamic seal capacity of shaly intervals in Yalgorup Member of Lesueur Formation and Eneabba Formation in South West Hub CCS project and to characterise their caprock sealing efficiency before and after exposure to supercritical CO_2.

This study is a coupled experimental and modelling research program incorporating several core and cuttings analysis methods and geochemical reaction path modelling. In this research, selected shale samples were exposed to $scCO_2$ under reservoir conditions for nine months, and petrophysical changes (surface area, porosity, pore size distribution, and capillary pressure) in samples were monitored from a suite of experiments. Several analysis methods including x-ray diffraction (XRD), scanning electron microscopy (SEM) associated with energy dispersive spectrometry (EDS), nuclear magnetic resonance (NMR), and low-pressure nitrogen adsorption were used in this study to achieve the earlier outlined

objective. The results of XRD analysis and SEM examinations before and after reacting the samples indicate whether chemical reactions occur between rock-forming minerals and the brine/scCO_2 system. NMR, and surface area measurements results can show changes in pore volume and capillary threshold pressures. These results determine if shale samples after being exposed to supercritical CO_2 lose their original integrity as a caprock and if their sealing efficiency is reduced.

1.7 Significance

It is crucial to evaluate the viability of any CO_2 storage system regarding injectivity, containment and long-term safety for both humans and the environment, before implementing. The sealing efficiency of the caprock plays an important role in this matter and must be assessed beforehand. The success of geologic CO_2 sequestration is related to the restraint of the injected CO_2 under the caprock for hundreds to thousands of years by a trapping mechanism. Interaction between scCO_2 and shale minerals and the following alteration of shale sealing properties can cause seal failure and leakage of CO_2 to upper formations and atmosphere (Gaus, 2010). The geochemical reactivity of shales to CO_2 and their effect on microstructure and composition of shale are the most important factors in seal characterisation. Initial capillary entry pressure, which determines the seal capacity may be changed as a result of alteration in shale microstructure and composition. This study aims to study the significance of shale alteration and its effect on seal efficiency.

In case of leakage from the geosequestration site, a substantial quantity of CO_2 will be released back to the atmosphere. Such release would refute the benefits of geologic CO_2 sequestration, introduce health, safety, and environmental risks, and have adverse ecological effects. The leakage of CO_2 could happen into overlying resource-bearing strata, protected groundwater aquifers, shallow soil zones, and the atmosphere which would damage some hydrocarbon or mineral resources, contaminate drinking water resources, have lethal effects on vegetation and sub-soil animals, and lead to increased atmospheric emissions (Celia et al., 2015; Nelson et al., 2005; Oldenburg et al., 2002). Although the changes to the chemical composition of the deep saline aquifer is not a concern as they are considered minor compared to the high salinity of brine, and saline aquifers will not be exploited for drinking water, but same changes to a shallow aquifer is a major concern as they can alter the potable character of the water. The acidification of potable aquifers' water as a result of leaked CO_2 dissolution triggers metal mobilisation and trace metals and bitumens transport (Gaus, 2010).

Leakage through pathways such as transmissive faults and fractures or defective wells should be avoided through careful site selection, storage site characterisation, and monitoring. Over-pressurization on the injection formation should be avoided to reduce the risk of fracture creations and faults re-opening. Fractures could also be developed in the caprock as a result of thermal stress induced by significantly colder injected CO_2 than the in-situ formation temperature (Celia et al., 2015).

Geochemical alteration of the caprock can also play a significant role in its sealing efficiency in addition to the geomechanical defects. In this study, we assessed the potential changes in seal rock characteristics to determine their importance to seal integrity. The reactive geochemistry at the reservoir seal interface may become critical to the success of a carbon storage project.

Supersaturated subsurface fluids can influence the sealing ability of the defective caprocks. In deep micro-fractured formations, the fluid flow is governed by the fracture geometry. Mineralisation in favourable geochemical and thermodynamic conditions can lead to flow impedance. This is more common within clay-based rocks, where micro-fracture networks could be closed because of mineral dissolution/precipitation reactions. Mineral dissolution/ precipitation and other mineral alterations such as reorganisation of clay minerals in the fracture, and Illitisation of primary clay minerals can induce porosity and permeability changes (A. O. Olabode et al., 2017). When such reactions lead to fracture opening or widening the integrity of the seal could be compromised.

This research is of interest at present because it leads to a better understanding of the effect of supercritical CO_2 on shale layers as seals. Assessing $scCO_2$-rock interactions is an integral part of CCS seal characterisation due to direct contact of the $scCO_2$ plume to caprock due to buoyancy forces. This research examined aspects of physical and chemical alteration of shale formations when they are exposed to $scCO_2$ under reservoir conditions. The results of this research contribute to comprehend $scCO_2$/brine/shale interactions via experimental investigations and simulations. Investigation of long-term CO_2 injection is always accompanied by some numerical modelling of geochemical reactions because the rate of reactions of aluminosilicates is so low, that makes them impossible to be amended in an experimental study timescale.

1.8 Geological setting and caprock samples

There has been a focus on Carbon Capture and Storage (CCS) program in Australia in recent years as the country is one of the top twenty countries in CO_2 emissions per person. With its stationary energy-intensive industries, Australia is predicted to be contributing up to 20% of CO_2 emission by the end of 2020. Currently, several projects have been proposed or already established in Australia for CCS purposes such as Southwest Hub (WA), CarbonNet, Otway (VIC), Surat (QLD), Gippsland (VIC), and Gorgon (WA) (Alajmi, 2015; Gibson-Poole et al., 2007; J. K. Pearce et al., 2019).

Suitable mainland locations in Western Australia for the geosequestration of carbon dioxide have been identified. The Gorgon project in the North West represents a massive investment in Carbon Capture and Storage on Borrow Island. South West Hub project is being investigated by the Department of Mines and Petroleum and National Geosequestration Library (NGL). Lesueur Formation of the Southern Perth Basin is being assessed for storage of industrial-scale CO_2 emissions (National Geosequestration Laboratory, 2015).

The South West Hub project has been introduced as a potential mainland location for the geosequestration of carbon dioxide. This potential CCS system has suitable storage capacity in its saline aquifer and efficient seal properties in the shaly caprock. Also, the area is located relatively close to the biggest CO_2 emitter of the state, the Kwinana Power Plant. It is planned to collect CO_2 from several industrial emitters, where the injection mass is expected to be in the order of 6.5 million tons per year for the 40 years of project activity (Delle Piane et al., 2013). These numbers were changed later to 800,000 tons per year over 30 years (Sharma et al., 2018).

The potential geosequestration site is in a deep saline aquifer within the Lesueur Sandstone. A total of 4 wells have been drilled in the Harvey region to investigate the suitability of the Lesueur Sandstone of Southern Perth Basin for storage of industrial-scale CO_2 emissions. The results have identified significant differences between the Upper and Lower Members of the Lesueur Sandstone in terms of sedimentology, petrophysical, geomechanical and elastic properties. The Lower Member of the Triassic Wonnerup is a laterally extensive and thick layer of sandstone which represents the targeted reservoir, whereas the Upper Member, Yalgorup is far more heterogeneous, due to mixed nature of the mudstone intervals and thick continuous clean sandstone succession. A series of rock baffles in Triassic Yalgorup Member and a thick interval of paleosol section (Jurassic Basal Eneabba Shale) correspond to the targeted seals. The Yalgorup Member consists of mixed-thickness, interbedded high to low

energy channel-fill facies, and swampy /overbank deposits, and paleosols. The Wonnerup Member consists of thick, continuous, high energy channel-fill facies, with minor intercalations of moderate to low energy channel-fill/stacked rippleforms and rare swampy deposits. This is an ideal lithology for a CO_2 reservoir (Delle Piane et al., 2013).

Primary containment is provided through a non-conventional seal called "Migration Assisted Trapping" (MAT sometimes referred to as Migration Assisted Storage or MAS) in the Wonnerup Member of the Lesueur Formation. The top seal at the site is not a classic thick marine shale. The overlying paleosol packages in the Yalgorup Member of the Lesueur Formation as the lower confining layer and the basal shale part of the Eneabba Formation as the upper confining layer provide the secondary containment (Sharma et al., 2018).

1.9 Structure of the thesis

There are two main approaches used in this thesis to determine the impact of $scCO_2$ on the shale samples. First, the laboratory experiments, reacting several samples of the shale caprock with $scCO_2$ under the simulated reservoir conditions. Second, the indirect observations of the reactions through numerical modelling. Geochemical models were applied here to overcome the shortcomings of laboratory experiments being limited in scale and timeframe. The methodology of both these methods is described in Chapter 2. The results of experimental methods applied to the samples are summarized in Chapter 3. Chapter 4 covers the results of geochemical modelling reproducing the experiments for a longer period and modelling the reactions under the reservoir conditions and water chemistry. Chapter 5 discusses the results and gives a conclusion.

Chapter 2. Methodology

Relatively fresh samples of shale intervals were selected from the Harvey-3 cores in Perth's Core library, Western Australia, to achieve the objectives of this study, as outlined in Chapter one. A total of fifteen core samples from the Eneabba Basal Shale and claystone rich facies of the Yalgorup Member (Lesueur Sandstone), depth ranging from 741m to 1218m, were collected in September 2016. The experiments implemented in this study are two types: the exposure of the shale samples to $scCO_2$ and the characterisation methods performed to analyse the samples before and after the exposure phase. The exposure part is explained in section 2.3, and the detailed methodology of the characterisation part is explained in section 2.4. An additional modelling study is performed to complement the experiments. The methodology of the modelling study is described in section 2.5.

In this study, an exposure period of nine months was selected, based on the reaction time required to complete the kinetically slow reactions of observed minerals with CO_2 and brine. It is known that each mineral has a specific kinetics reaction rate (Table 4-1). However, the timescales required to complete the reactions are certainly more than one year, up to hundreds or even thousands of years (Davis et al., 2011). Therefore, considering the time frame available for this PhD study and in order to record the maximum impact possible, nine months was selected as being a reasonable period for the CO_2-brine-rock interactions. However, this period is not nearly enough to capture all the possible mineral reactions that occur in CO_2 and brine environment such as precipitation of feldspars and secondary precipitation of calcite and quartz. Therefore, it would be possible to see the dominant reactions such as the initial dissolution of quartz and kaolinite and the salt drying-out effect (Rathnaweera, Ranjith, & Perera, 2016). Injection of CO_2 may dissolve the water in the sample and cause the sample dry-out. Precipitation of salt occurs as a result of this CO_2 induced drying-out (Mouzakis et al., 2016).

Shale samples were characterised with a full suite of non-destructive petrophysical methods. The samples were analysed before and after they were dynamically exposed to supercritical CO_2 under in-situ reservoir conditions. X-ray diffraction (XRD) analyses were used to examine the compositional changes of the seal rock mineralogy. Scanning Electron Microscopy (SEM) images were taken before exposure to $scCO_2$ to see the original texture and the microstructure of the seal rock surface. XRD and SEM analysis indicate whether any dissolution or precipitation has taken place (Soldal, 2008). Pore size distributions were measured using low-pressure nitrogen adsorption (Busch et al., 2008), and nuclear magnetic

resonance (NMR) (Manalo et al., 2003; Matteson et al., 1998; Prammer et al., 1996) methods. Low-pressure nitrogen adsorption measured the surface area and pore volume to check the occurrence of any changes to this critical rock parameter (Amann et al., 2011; Labani et al., 2013). The pore size distribution was also obtained from Mercury Injection Capillary Pressure (MICP) method. MICP also provide more data such as threshold pressure and the equivalent height of the column of CO_2.

To estimate the fate of a system when CO_2 is injected to a saline aquifer, evaluation of pressure and temperature conditions is needed. They can be determined by local geothermal gradient and pressure gradient and the depth of the aquifer (Luigi, 2007b). Taking a surface temperature of 22°C and an average geothermal gradient of 28°C/km, the temperature will be 42°C at 700m and 64°C at 1.5 km. Assuming a hydrostatic pressure gradient of 10 MPa/km, the pressure will be around 1015psi at 700m and 2175psi at 1.5 km (Wollenweber et al., 2009). The estimated pressure and temperature for the samples are reported in Table 2-1. We adopted the values relative to the highest pressure and temperature. For this study, the temperature of 60°C and pressure of 14.1 MPa (2050 psi) relative to a maximum depth of 1417 m was used for exposure. The equivalent circulating densities (ECD) from the Harvey-3 final well report shows an equivalent pressure of 2233 psi at the depth of 1400 meters (Mouzakis et al., 2016). HSFT Formation Tester log reported a test pressure of 2118 psi and temperature of 56.4°C at depth of 1472.5 meters which agrees with the selected values based on calculations. Selection of higher in-situ temperature would increase the rate of reaction contributing to more significant changes but also would result in different pH values for the fluid (Armitage et al., 2013). Instead, a more extended exposure period was selected to make sure adequate changes have been observed.

We adopted the pore classification system developed by Rouquerol et al. (1994) for materials that contain nanometre-scale porosity. According to this pore classification, pores smaller than 2nm are micropores, between 2 and 50nm are mesopores, and larger than 50nm are macropores. Mesopores and micropores have a significant contribution to porosity and storage capacity in shales. Most important parameters for the description of shale's pore system are pore size distribution, pore shape, effective porosity, and specific surface area (Labani et al., 2015). The surface area has a reverse relationship with the pore size. Micropores have the most contribution on the surface area, according to a study by Labani et al. (2013) on the potential gas shales from Western Australia (WA), while mesopores and macropores contributions come next accordingly.

2.1 Sample Data

Harvey-3 was cored continuously from 584 to 1550m (966 metres). A moderate correlation between core gamma response and lithofacies were reported by Delle Piane et al. (2013). After reviewing core photographs and gamma-ray logs, the Eneabba Basal Shale and claystone rich facies of the Yalgorup Member were selected for core viewing and sampling. A total of 15 samples, mainly shale and mudstone, were collected from Harvey-3 well cores from Perth core library in 2016. Specific data for the core samples used in this study are listed in Table 2-1 and Table 2-2. The materials consist predominantly of shale constituents with depths ranging from 725 to 1417m. Core samples photos are illustrated in Appendix II.

Table 2-1. Core sample interval data relative to Kelly Bushing (KB) and estimated T and P from Harvey-3.

Sample ID	***Depth (m)***	***Formation***	$T_{estimated}$ ***(°C)***	$P_{estimated}$ ***(MPa)***
H1	1417.50	Yalgorup Mbr.	62	14.16
H2	1412.00	Yalgorup Mbr.	62	14.11
H3	1332.80	Yalgorup Mbr.	59	13.33
H4	1326.60	Yalgorup Mbr.	59	13.27
H5	1187.60	Yalgorup Mbr.	55	11.87
H6	1169.30	Yalgorup Mbr.	55	11.69
H7	1046.60	Yalgorup Mbr.	51	10.47
H8	940.65	Yalgorup Mbr.	48	9.40
H9	916.30	Yalgorup Mbr.	48	9.16
H10	887.15	Yalgorup Mbr.	47	8.87
H11	859.50	Yalgorup Mbr.	46	8.59
H12	823.10	Yalgorup Mbr.	45	8.22
H13	766.10	Yalgorup Mbr.	43	7.66
H14	738.20	Eneabba shale	43	7.38
H15	725.20	Eneabba shale	42	7.25

Samples H14 and H15 belong to Eneabba Formation and samples H1 to H13 belong to Yalgorup Member of Lesueur Formation according to the defined stratigraphy of Harvey-3 well (Labus et al., 2017). The overlying Eneabba Formation is a Claystone/mudstone rich shale formation. Yalgorup Member of the Lesueur Sandstone contains mixed sandstone/siltstone/claystone characterised by highly variable porosity and permeability. Samples were selected from the palaeosols facies (D) which is the dominant lithology and are interbedded with very coarse-grained and poorly sorted moderate-energy channel barforms (facies B) (Labus et al., 2017). Facies D are clay-dominated and also contain 30%-40% quartz, feldspar and albite (Olierook et al., 2014), while facies B contain primarily quartz, K-feldspar,

with minor clays, framework carbonates and rare opaque minerals, micas, organic carbon and heavy minerals (Piane et al., 2018).

The original cores were cut to 1.5-inch plugs for NMR tests. For the remaining of the research methods, pebble-sized core chips and crushed/powdered rock particles were used (Table 2-2). Given the heterogeneity of the shales, the same samples must be used before and after the exposure to $scCO_2$. The same plugs for NMR measurements. XRD and LPNA test require powdered samples. To ensure that samples are identical, samples were crushed to a powder, and then they were mixed and homogenised. The crushed samples were then divided into two aliquots, one of which was analysed in its initial condition and the other of which was examined after exposure to $scCO_2$. For MICP and SEM applications, the samples were broken in half, one of which was analysed in its initial condition and the other of which was examined after exposure to $scCO_2$. This approach helped reduce the effects of microscopic heterogeneity on the results of the tests (Rezaee et al., 2017).

All received samples were analysed by XRD method initially. For exposure to $ScCO_2$ samples H1, 2, 4, 5, 8, 9, 10, 13, 14, and 15 were selected. Samples H3, 6, 7, 11, 12, and 14 were excluded from further studies because no plugs or disks were recoverable from them. Small amounts of samples H1, 2, 4, 5, 8, 9, 10, 13, 14 and 15 were powdered and used in XRD and Low-pressure Nitrogen Adsorption (LPNA) tests. Samples H1, 2, 5, 8, 9, and 13 were examined by SEM in their initial state at the beginning of the study. For samples H1, 2, 5, 8, 9, 10, 13, plugs were recovered to be used for the NMR test. However, the core plug for sample H10 failed after saturation before exposure and sample H8 plug failed after four months' exposure. A summary of methods applied for the study of each caprock samples is summarised in Table 2-2. The details of different methods are provided in the following chapters.

Table 2-2. Summary of samples used for different testing methods.

Sample #	***Depth (m)***	***Condition***	***XRD***		***LPNA***	***SEM***	***NMR***	***MICP***
			Before	After				
H1	1417.50	Plug+ Disk	Y	Y	Y	Y	Y	Y
H2	1412.00	Plug+ Disk	Y	Y	Y	Y	Y	Y
H3	1332.80	Broken	Y					
H4	1326.60	Broken	Y	Y	Y			
H5	1187.60	Plug+ Disk	Y	Y	Y	Y	Y	Y
H6	1169.30	Broken	Y					
H7	1046.60	Broken	Y					
H8	940.65	Plug	Y	Y	Y	Y	failed	
H9	916.30	Plug+ Disk	Y	Y	Y	Y	Y	Y
H10	887.15	Plug	Y	Y	Y		failed	
H11	859.50	Broken	Y					
H12	823.10	Broken	Y					
H13	766.10	Plug+ Disk	Y	Y	Y	Y	Y	Y
H14	738.20	Broken	Y	Y				
H15	725.20	Broken	Y	Y	Y			

2.2 Brine chemistry

Selected shale samples were required to be saturated with synthetic brine before being placed into the Pressure-Volume-Temperature (PVT) cell at storage conditions and exposed dynamically to $scCO_2$ for nine months. Simplified artificial pore water (brine) of 30,000 ppm (512 mmol/L NaCl) was prepared from ROWE ultrapure water and ROWE NaCl (CS10307) and used for all the batch reactions. This concentration was chosen equivalent to sodium and potassium chloride in available groundwater data of the Harvey-3 Lesueur Formation Fluid Sampling form Rockwater Hydrological and Environmental Consultants Report (Rockwater, 2015). This synthetic water chemistry was selected so that there would be minimal risk of damage to the core material before exposing them to scCO2. Also, the dissolution process is encouraged by simple NaCl brine as it lacks the divalent cations, which have a pH-buffering effect and decrease the acid-induced reactions (Wang et al., 2016). On the other hand, cations needed for mineral precipitation can only be derived from the reactions with rock-forming minerals, instead of brine (Kaszuba et al., 2005). Selected shale samples were pressure-saturated at 14.1MPa with 30,000 ppm NaCl solution before being placed into the PVT cell (Figure 2-2). The pressure inside the saturation cell was increased gradually in 48 hours to a maximum of 14.1 MPa. To ensure full saturation of the samples, the pressure

drops were monitored and compensated for the next 48 to 72 hours until the pressure remained constant for 12 hours.

The initial water chemical data estimates were based on the formation fluid sampling data. Samples were taken from six meters interval below the casing (total depth about 1,548 m) by flushing the open-hole with fresh water and then undertaking a "wet pull", whereby the base of the drill string is sealed off, and the volume of water retained in the rods is removed as they are pulled from the well. Then the well was pumped until casing interval and at least three times the volume of the aquifer interval (approximately 12,000 L) had been extracted, or until salinity and pH had stabilised. Sample B1 was collected after 265 minutes, and ALS (3A) at the end of pumping. Results of chemical analyses for Harvey-3 samples prior to CO_2 injection show that the brine is a Na-K-Cl type water, with a salinity of approximately 30,100 mg/L (Table 2-3), with relatively high concentrations of SO_4^{2-}, calcium, and magnesium, but low values for iron, manganese, aluminium, and zinc (Rockwater, 2015).

Table 2-3. Chemical Analyses Results for Water Samples (Rockwater, 2015)

Analytes	Units	B1	3A (ALS)
Field pH	pH	7.04	7.02
Field EC	µS/cm	77,000	72,500
Field Temperature	°C	37.6	38.4
pH	pH	6.97	6.8
Electrical Conductivity @ 25°C	µS/cm	93,700	82,600
Total Dissolved Solids @180°C	mg/L	62,600	59,900
Total Hardness as $CaCO_3$	mg/L	8,200,	7,220
Total Alkalinity as $CaCO_3$	mg/L	227	219
Sulphate as $SO4^{2-}$	mg/L	1,660	1,420
Chloride	mg/L	30,100	28,400
Calcium	mg/L	2,270	1,960
Magnesium	mg/L	616	565
Sodium	mg/L	11,400	9,960
Potassium	mg/L	13,600	9,830
Aluminium	mg/L	5.12	1.29
Manganese	mg/L	10.0	10.7
Zinc	mg/L	1.78	1.47
Iron	mg/L	16.5	3.58
Reactive Silica	mg/L	18.2	22.7
Ammonia as N	mg/L	5.86	5.57
Total Nitrogen as N	mg/L	11.3	8.40
Total Phosphorus as P	mg/L	1.59	1.25
Reactive P as P	mg/L	0.32	0.32
Total Anions	meq/L	888	835
Total Cations	meq/L	1010	829
Ionic Balance	%	6.34	0.33

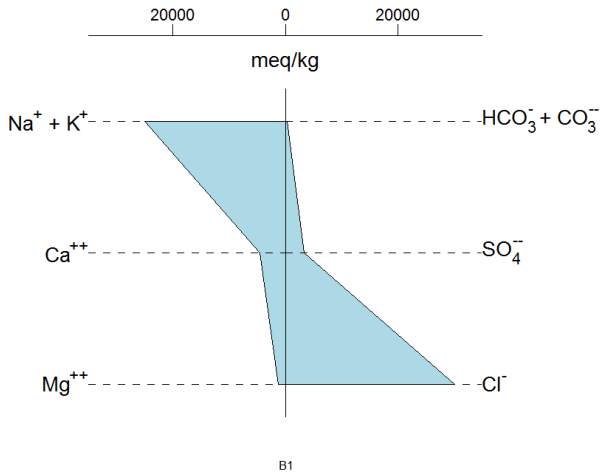

Figure 2-1. Stiff diagram showing concentrations of major cations and anions before CO_2 injection

2.3 Exposure Phase Apparatus

Shale samples in various forms of core-plugs, small rock fragments and crushed rock were tested in this study for pore accessibility and conformance reasons (Comisky et al., 2011). We placed selected shale samples into a PVT cell under the reservoir condition of 14.1 MPa (2050 psi) and 60°C (maximum in Table 2-1), related to the deepest sample recovered from the depth of 1400 m, for nine months. Figure 2-2 and Figure 2-3 provide, respectively, a schematic and a photo of the exposure apparatus used in this study. During the exposure, high-purity (99.9 mole %) $scCO_2$ mixed with deionised water was injected continuously using a high-accuracy continuous pump with constant rate into the PVT cell. To make the CO_2 fluid saturated with water, 50 cm^3 of water was added to accumulator before filling it up with Supercritical CO_2. The amount of water dissolved in $scCO_2$ is determined by temperature and pressure in the accumulator cell. The High-performance liquid chromatography (HPLC) injection pump (SHIMADZU LC-20AT) allowed the pressure, and flow-rate values to be set at 14.1 Mpa and 0.7 cm^3/h (i.e. 0.01 mL/min) which could be controlled and recorded with the accuracies of 1 psi, and 0.001 mL/min, respectively. The injection rate must be realistic so that we can expect the same experimental results as the real-life injection process. We adopted the same method of rate calculation as Rezaee et al. (2017). They used the time measured for the CO_2 mixture to reach from an injection well to the observation well, 300m apart, in the Otway project. Then, they calculated the velocity of 0.07 m/h and considering the cell dimensions, and converted it to the flow rate of 0.7 cm^3/h. The accumulator connected to the input of the samples cell was filled with CO_2 and pressurised with an air-driven compressor about every 40 days. To make the CO_2 saturated with water, 50 mL of

water was injected inside the accumulator initially. Under the high pressure and temperature of the cell, water dissolves in the $scCO_2$ and makes it wet. The outlet end of the PVT cell was connected to a Swagelok KPB back-pressure regulator which maintained the pressure inside the cell equal to 14.1 MPa (in-situ pore pressure). The temperature inside the cell was set to 60°C and maintained using a PID temperature controller (Omega CSi8DH) and heating jackets (Omega SRFG series) with an accuracy of 0.04°C. The accumulator and exposure cell with the attached heating jackets were wrapped in insulation pads to minimise the temperature fluctuation. All wetted parts of the apparatus are made from Hastelloy, super duplex stainless steel or titanium to minimise any fluid contamination or damages caused by corrosion when exposed to highly corrosive materials (e.g., carbonated water or high salinity brine) under high pressures and temperatures for a prolonged period. At the end of the exposure, pressure and temperature were reduced gradually to room conditions and samples were examined again to assess any rock chemical and petrophysical alterations.

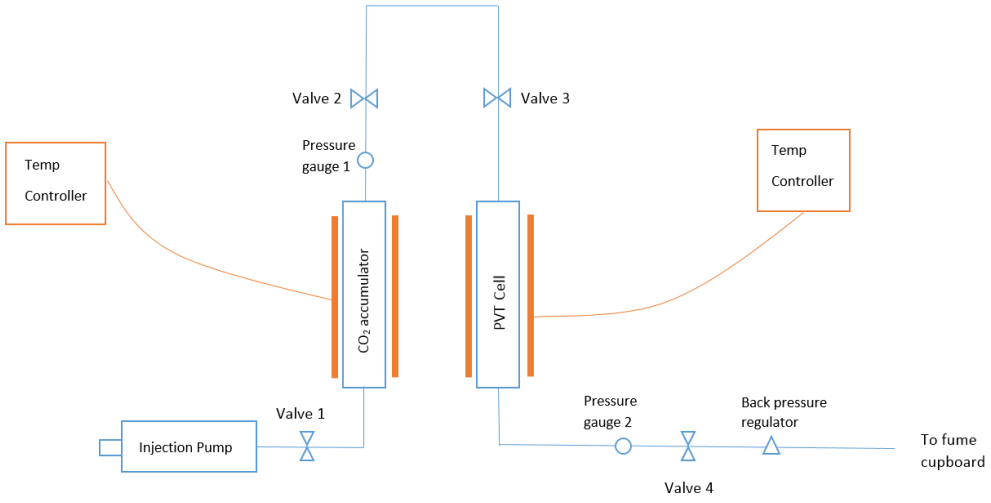

Figure 2-2. Schematic of exposure set-up

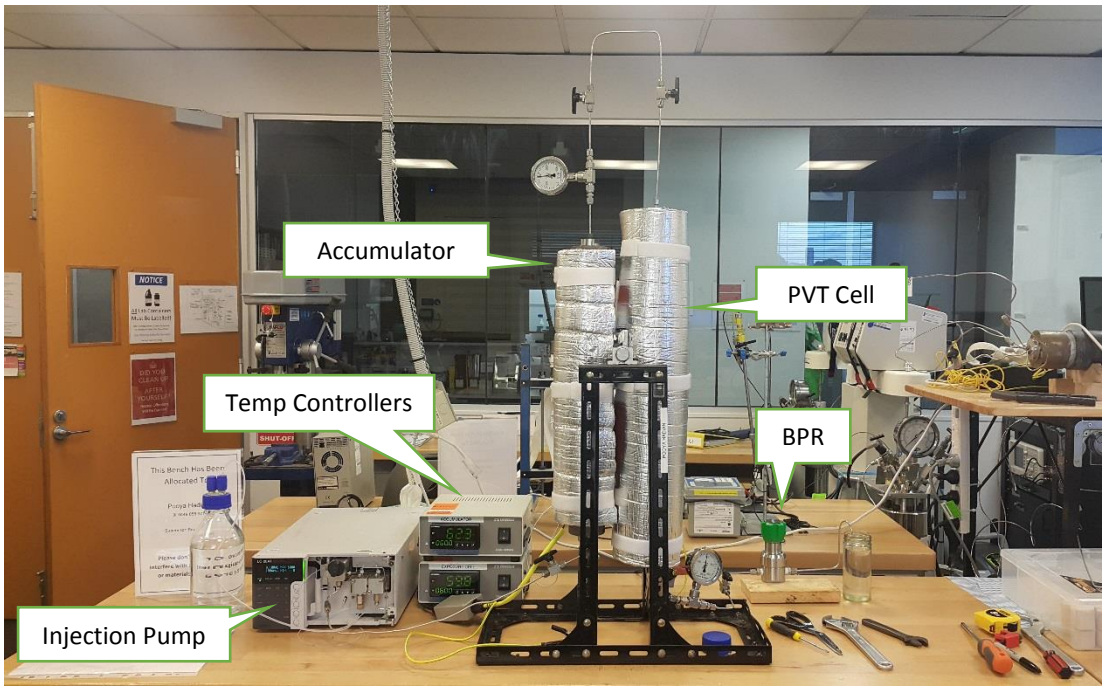

Figure 2-3. A photo of exposure set-up used in this study

The same numbers of samples undergo the same thermodynamic condition of exposure for the same period but in the absence of pressurised CO_2. This group was selected as the observation samples were placed in the same brine inside an oven (60°C) for nine months to see the changes without the effect of $scCO_2$. They were tested with XRD and LP-NA after treatment.

2.4 Experimental Methods

2.4.1 X-Ray Diffraction (XRD) Analysis

The mineralogical composition of shales was studied with the X-ray diffraction (XRD) technique to estimate the mineralogy of all fifteen samples as received and on the selected ten samples after an exposure period of four and nine months. Laboratory tests were conducted on powdered samples at the John de Laeter Centre, Curtin University. The received samples were crushed and homogenised and then were divided into two batches, the first patch was analysed in their initial condition, and the second batch was examined after exposure to $scCO_2$.

Proper sample preparation is a crucial step in the analysis of powder samples by X-ray diffraction, especially in the case of soils and clays that contain finely divided colloids, which are poor reflectors of x-rays. Sample preparation of clays includes appropriate techniques to obtain desired particle size, orientation, and thickness. Extremely fine-grained samples are required to achieve an excellent signal-to-noise ratio to avoid fluctuation in intensity and

spottiness and minimise preferred orientation. Another benefit of reduction of particles size is to have enough particle participation in the diffraction process. The recommended size range for the quantification of various phases is around 1-5µm. First stage grinding is accomplished either manually with pestle or mortar or mechanically with ring mills. Excessive grinding can result in lattice distortion and the possible formation of an amorphous layer outside the grains. A second stage grinding with a set 5-minutes time in micronising mill and pellets would help maintain the required size and avoiding the excessive grinding. The ground particles are then packed into a flat sample holder assuming random orientations in a random mount method. This method ensures reflections from various h-k-l planes from emitted x-rays when the identification of phases in a specimen is required. A second type is oriented mounts suitable for analysing clay minerals which rarely show strong diffraction effects from Bragg planes other than the (00l). To prepare the oriented mounts a slurry of the sample with distilled water is allowed to evaporate until the slurry is smeared into a sample holder.

In this study, samples were first cleaned of visible contaminants and disaggregated in a mortar and pestle and then reduced to the required size using a McCrone® micronising mill for whole-rock XRD mineral analyses. To ensure samples are not contaminated with each other, ring-mill and micronising mill sample holders were cleaned with ethanol and run with quartz powder after each sample. Before measurements, the samples were air-dried overnight at 40°C. Approximately three grams of each sample were selected initially to be added with standard material (Corundum) to the exact amount of 10% for quantification. The resultant powders are dried, disaggregated, and packed into sample holders to produce random whole-rock mounts.

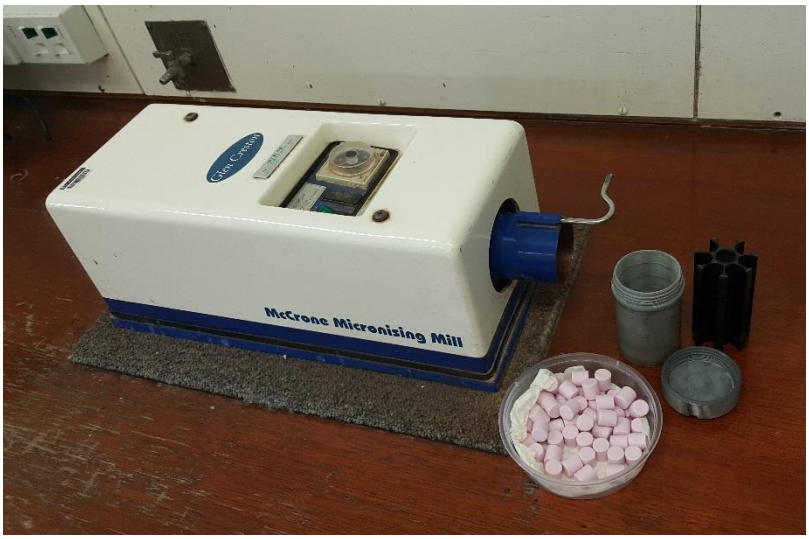

Figure 2-4. Micronising mill used to powder samples to the required size.

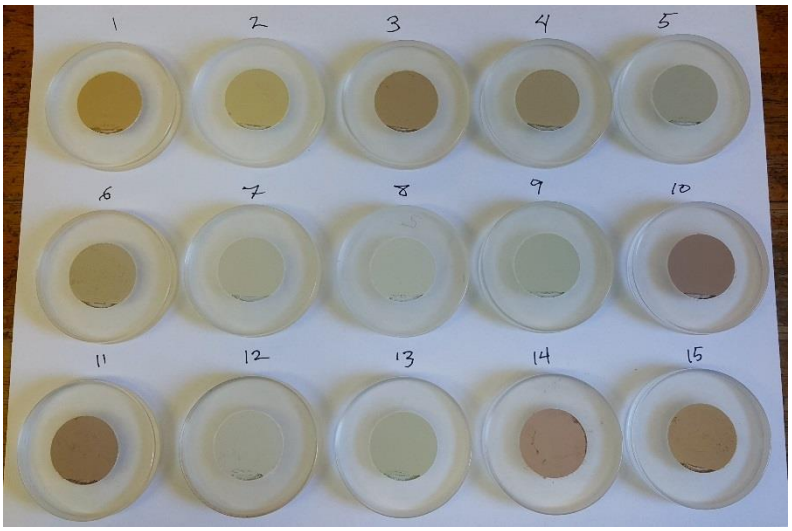

Figure 2-5. XRD power samples packed in Sample holders.

X-ray Diffraction (XRD) analyses of the samples are performed using a Bruker D8 Advance automated powder diffractometer with Bragg-Brentano configuration at John de Laeter Centre of Curtin University. It uses a LynxEye detector and a copper x-ray tube at 20 kV and 5mA. The whole-rock samples are analysed over an angular range of 7 to 120 degrees 2Θ. The instrument is complemented with Bruker DIFFRAC EVA software for search/match analysis, and the XRD quantitative results were calculated using the Rietveld method in comprehensive full pattern data analysis programme, TOPAS.

It should be mentioned due to some factors affecting the results of XRD analysis; the resulted weight percentage data are considered semi-quantitative. There are a number of limitations that affect the qualitative X-ray diffraction method. Only the crystalline material can be detected by this method. A search match routine gives a list of possible minerals in the sample based on the diffraction patterns compiled in a database which is subject to the user for selection of correct phases. Rietveld method of analysis of powder diffraction gives the quantitative amounts. Detection limits of this method are about 1-5% and differ for each mineral species. The actual minerals analysed in the samples are different from the database entry minerals for several reasons. Feldspars which are usually solid solutions of three end members are especially problematic in quantifications. Clays are another source of uncertainties due to their wide range crystallinities and similar matrix indices of different mineralogies.

Figure 2-6. Bruker D8 Advance automated powder diffractometer

Mineralogy plays a significant role in controlling shale properties. Clays can affect the shale pore structure while the non-clay minerals, especially quartz content, is essential for estimating the brittleness index of the rock (Labani et al., 2015).

2.4.2 Scanning Electron Microscopy (SEM)

Scanning electron microscopy technique is commonplace in the investigation of geological samples and has many applications. SEM can image the morphology of the samples by using the secondary electrons, and compositional differences by using backscattered electrons. Analysis of morphology can inform about any phases being participated or dissolved. A typical SEM image has a resolution higher than 10nm (typically 5 nm). A high resolution at high magnification is an advantage of SEM over the light microscopy (LM) along with the depth of field and microanalysis. Depth of filed in SEM is 300 times higher than LM, which means images have a 3D appearance and show great topographical details. Secondary electron and backscattered electron signals were used. Microanalysis of the samples gives elemental composition information, which is further enhanced with EDS mode (energy-dispersive X-ray spectroscopy). SEM operates under vacuum and samples must be rendered conductive before viewing to avoid electron charge build-up on the surface. The high vacuum condition is applied to minimise the electron beam scattering and higher electron collection efficiency. Minimising the attenuation of the electron beam is important to decrease the probe size and achieve better resolution. Samples were coated with 10nm of carbon and were placed on the stubs using double-sided carbon tapes; then carbon paint was applied to samples edges to make a conductive path from the surface to the stub for the electron to

current. Due to high vacuum operating condition, any moisture would be sucked out of the samples which can enter the electron beam column and contaminate it. After the preparation phase, samples were stored in a desiccator so that any moisture would be sucked out of the samples.

SEM studies were carried out for six broken rock surfaces before and after exposure to $scCO_2$ to study the texture and the microstructure of the seal rock surface, formation of authigenic minerals and any other changes due to exposure to $scCO_2$. The samples were prepared using relatively small and flat samples. Samples were coated with carbon, to prevent charging of electron on the surface of nonconductive rock samples. EDS was performed to determine the elemental composition of minerals. SEM studies were performed using a Zeiss EVO 40XVP controlled pressure electron microscope associated with energy dispersive spectrometry analysis (EDS). The SEM instrument was operated with an accelerating voltage of 20 and 15kV in the controlled pressure mode, with a chamber pressure of 0.5 mBar, to prevent the charging of non-conductive materials. The images were collected with both a secondary electron detector and a backscattered electron detector which shows atomic number contrast. Appendix IV displays SEM images. Images from the secondary electron detector show the surface of the samples and are more similar to photograph as the show the topography of the samples' surface. In a backscattered image low atomic numbered material such as carbon appear black and high atomic numbered materials such as lead appear brighter, as they penetrate deeper into the sample and bounce back from the deeper atoms. The Bruker EDS was used to collect and analyse spectra from selected points. The spectra collected were used for the identification of the elements present in the minerals without quantification.

EDS mode identifies the chemical elements present in the samples. Energy-dispersive X-ray spectroscopy can be applied as a qualitative or quantitative method. It is a method that compliments SEM. An Energy Dispersive detector detects x-rays produced as a result of electrons from the primary beam interacting with the sample's surface. These characteristic X-rays are displayed in a spectrum of intensity versus X-ray energy. Elements making up the samples are identified base on the energies of the characteristic X-rays, while their concentrations are given by the intensities of the characteristic X-ray peaks. The detection limit of EDS analysis in the SEM is in the range of 0.1-0.5 wt. %. This method is considered non-destructive and can be repeated many times. However, it is susceptible to clay minerals. When applied as quantitative analysis, EDS samples need to be flat and polished.

SEM method provides high-resolution images to study the nanopore structure of the shales. However, this is not a suitable method for $scCO_2$ exposure method because it required a surface coating with a conductive matter such as carbon to eliminate the electron charging on the surface of the samples. The coated samples are not suitable for the analyses of changes in the shale surface morphology as they act as a barrier between the actual mineral surface and the $scCO_2$ and significantly influence the CO_2-mineral interactions. In this study, samples were broken into two similar pieces for the before and after SEM analyses to avoid the mentioned shortcoming.

2.4.3 Nuclear Magnetic Resonance (NMR)

Low-field NMR is a non-destructive technique that is performed under room conditions. It assumes that the sample is fully or partially water-saturated as it measures the hydrogen content of the pores. The application of NMR measurements is to determine porosity, pore size distribution and to estimate the permeability of shale core plugs using a bench-top laboratory NMR spectrometer. In contrast with MICP-PSD that provides only effective porosity, NMR PSD provides a full experimental characterisation of pore geometry, the size of the pore body, and the isolated pores (Hinai et al., 2015).

Figure 2-7. 2 MHz Magritek bench-top laboratory NMR spectrometer

In nuclear magnetic resonance spectrometer, an external magnetisation field is applied, and the protons within the hydrogen atoms aligned parallel to the magnetic field orientation (Figure 2-8). Protons exhibit behaviour like spinning magnets which enable them to interact with the external magnetic field and produce a measurable response. Once the protons align, an oscillating magnetic field (B1) at a frequency of about 2.3 MHz (optimum frequency for hydrogen atoms) is applied. The application of this secondary field causes the protons to change orientation to 90°. Then amplitude and relaxation time of hydrogen protons is measured every time the field oscillates. The signal amplitude is proportional to the number of hydrogen atoms present which, when calibrated, gives porosity. This method requires a

material containing hydrogen. Hydrogen is the dominant atom found in reservoir fluids, so the desk-top laboratory equipment like the downhole NMR tools is tuned to measure the response of the protons within the hydrogen nucleus (McPhee et al., 2015b).

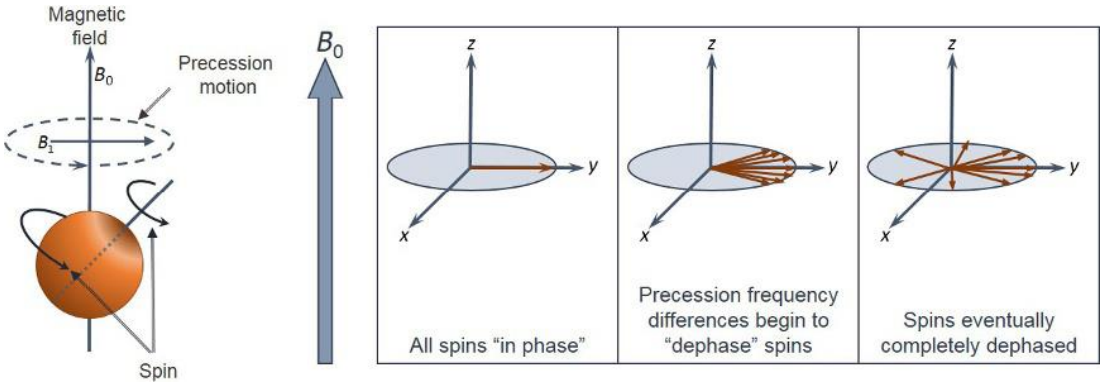

Figure 2-8. Precession of the hydrogen nuclei after application of the B_1 magnetic field (left). T_2 relaxation process (right). McPhee et al. (2015b)

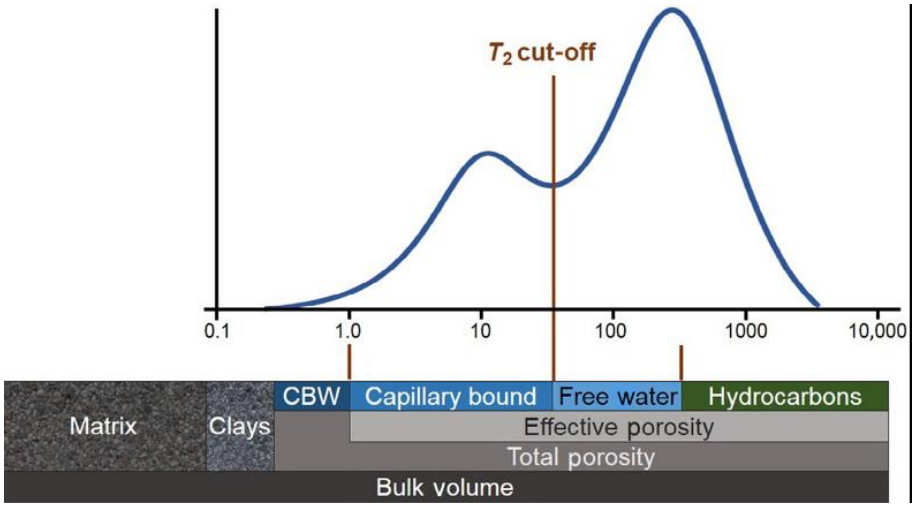

Figure 2-9. A typical NMR T_2 distribution trace and how this corresponds to the volume of fluids in place. From McPhee et al. (2015b)

The relaxation time is dependent on the pore sizes and so generates data on the distribution of pore sizes. This distribution can be used to extrapolate the amount of clay- and capillary-bound water as well as free water and hydrocarbons (Figure 2-9).

The measurement of longitudinal and transverse relaxation has traditionally been the primary application of NMR in the petroleum industry. Transverse relaxation (T_2) is governed by the contribution of bulk ($1/T_{2B}$), surface ($1/T_{2S}$) and diffusion processes ($1/T_{2D}$):

$$\frac{1}{T_2} = \frac{1}{T_{2B}} + \frac{1}{T_{2S}} + \frac{1}{T_{2D}}$$

Equation 2-1

T_{2B} is the relaxation time of pore fluid as it would be measured in a container so large that container effects would be negligible. T_{2S} is the surface relaxation time of the pore fluid resulting from surface relaxation. T_{2D} is the relaxation time of pore fluid induced by diffusion in the magnetic field gradient.

$$\frac{1}{T_2} = \frac{1}{T_{2B}} + \rho_2 \left(\frac{S}{V}\right) + \frac{D(\gamma\ G\ TE)^2}{12}$$

Equation 2-2

where ρ_2 is the surface relaxivity related to mineral interaction with fluid (Pm/s), *S/V* is the ratio of pore surface to pore fluid volume and is defined as pore geometry index (1/Pm), *D* is the molecular diffusion coefficient (cm^2/s), Υ is a constant of the gyromagnetic ratio of a proton (MHz/T), *G* is the field-strength gradient (G/cm), and *TE* is the inter-echo spacing used in the CPMG (Carr-Purcell-Meiboom-Gill) sequence. Since no static magnetic gradient field was applied during the CPMG sequence, this equation can be simplified to the second part of the equation as a function of the pore geometry and surface relaxivity (Hinai et al., 2015).

To calculate the T_2 spectrum, a pulse sequence is used. This sequence generates a train of echoes where the echo amplitude decreases exponentially with the time constant T_2. The most used one is the CPMG (Carl-Purcell-Meiboom-Gill) sequence, here a 90° radiofrequency pulse is applied, followed by successive 180° pulses applied at a fixed time interval.

The 2 MHz Magritek bench-top laboratory NMR spectrometer was applied to record T_2 relaxation time spectrum of shale core plug samples before and after exposure to CO_2 to estimate the porosity and pore size distribution. The magnet operates at a stable temperature of 30°C and atmospheric pressure, with a frequency of approximately 2 MHz. Shale core plugs of 1.5-inch diameter and about 1.5-inch length were measured using a P54 probe, which allows a minimum CPMG echo-spacing of 100 µs.

In this work, T_2 relaxation time measurements were conducted on six types of samples. Dry samples, as received from the core library, and then the samples saturated with 30,000ppm NaCl brine were measured. T_2 relaxation time measurements were conducted again after samples were exposed to $scCO_2$ for four and nine months, both in a dry and saturated state.

Table 2-4. The common parameters used for NMR measurements

Parameter Name	***Value***	***Parameter Name***	***Value***
B1 Frequency (MHz)	2.00054	Inter-expt. Delay (ms)	1000
90 Degree Pulse Amplitude (dB)	-12	Dummy Scans	1
180 Degree Pulse Amplitude (dB)	-6.5	Number of echoes	3000
Pulse Length (μs)	20	Tau (μs)	50
Damping Time (μs)	15	Point per echo	64
Receiver Gain (dB)	40	Echo shift (μs)	15
Minimum SNR	200	Dwell Time (μs)	0.5

In preparation for the NMR measurements, all samples were pressure-saturated with the previously prepared deaerated brine using the Vinci Manual Saturator (Figure 2-10). The 30,000 ppm NaCl brine was prepared in the lab using distilled water and appropriate amounts of analytical grade sodium chloride. The samples were loaded into the cells and then connected to a vacuum pump to evacuate any trapped air in their pore space for 24 hours. Subsequently, brine entered the cell under the vacuum pressure, and the cell was isolated from the vacuum pump. The pressure was increased to a maximum of 14.1 MPa via the hand pump gradually to avoid plug failure. The full saturation of the samples was achieved by operating the hand pump to compensate for the lost pressure, due to the penetration of brine into the samples' pores, until the pressure remained constant for 12 hours. The excess fluid on the surface of the core plug was removed to avoid overestimation of porosity by rolling the sample on white printing paper. A paper towel is not suitable for this case, as it could draw out some of the water in the pores close to the surface of the plugs. To avoid fluid spreading through the container and keep the fluids intact with the plugs, they were then wrapped tightly with transparent plastic wrap.

Figure 2-10. Vinci Manual Saturator and vacuum pump

It is also worth noting that, to be able to calculate the porosity of a sample, the NMR signal was calibrated by running an experiment on a glass vial containing a known volume of the formation brine. The procedure is summarised below:

1. Run a calibration sample using a brine sample of known volume (i.e., 20 ml). The brine sample used in the calibration was the same brine used to saturate the rock samples.
2. Run a calibration to collect the background signal from a cling wrap used to cover the samples to prevent evaporation of the saturating water during the tests and thereby increase the accuracy of the results obtained from the main NMR test.
3. Pressure saturate the samples with formation brine using high-pressure cells.
4. Remove the samples from the high-pressure cells and weigh them.
5. The exterior of the samples was wiped from excess brine and then quickly covered with the cling wrap referred to before.
6. Insert the warped sample into the probe (P54) to start the test.
7. Enter the required data/information about the rock sample into the acquisition software (ProspaRCA) from the control computer machine and then follow a series of steps and processes in the software to measure and extract the T_2 data.
8. After the T_2 experiment has finished, analyse the T_2 results using the 'Analyse' button to define the relaxation spectrum.

2.4.4 Low-Pressure Nitrogen Adsorption (LP-NA)

Low-pressure gas adsorption methods using nitrogen and carbon dioxide are generally used to quantify the surface area and pore size distribution of shales. Low-pressure adsorption of CO_2 is useful for characterising micro-porosity, while nitrogen adsorption can provide useful results for characterising meso- and part of macro-porosity, with open-pore sizes in the 2–300 nm range (Labani et al., 2015). Overall, the low-pressure gas adsorption technique can detect pore sizes in the 0.3–300 nm range depending on the gas employed, and it is regularly used in combination with high-pressure mercury intrusion porosimetry (MICP) to evaluate a wider range of pore sizes. Before conducting the tests, the solids must be degassed to ensure a clean surface that will allow the adsorption of molecules. This is usually achieved by heating the adsorbent under vacuum, at the maximum temperature allowed by the solid without altering its nature (Sing, 1985).

The following parameters resulted from this method: pore size and their distribution, surface area distribution, BET surface area (total surface area per mass of the sample expressed as m^2/g), specific pore volume (total pore volume per mass of the sample expressed as cm^3/g), average pore throat size.

About one gram of each sample was crushed to <250 µm to be used for low-pressure isotherm analysis. Samples need to be crushed to less than 250 µm to reach the vacuum threshold to begin the gas adsorption analysis. Since the pore sizes of the gas shale vary between nanometre and micrometre scale, crushing the samples in millimetre size range does not affect the pore structure, and the crushed sample porosity can be considered as representative of the matrix porosity (Labani et al., 2015). Crushed samples were mixed and homogenised then divided into two patches. The first series were tested in the original condition received from the core library, while the second series was exposed to $scCO_2$ inside a pressure vessel under the reservoir condition of 14.1 Mpa and 60 °C related to the deepest sample recovered from the depth of 1400 m. The third set of samples containing eight out of the original ten samples were tested after being exposed to the same temperature, brine composition, and period without the parameter of $scCO_2$. This set of samples served as the observation samples to investigate the role of $scCO_2$ in the changes induced to studied samples.

Figure 2-11. Micromeritics® TriStar II 3020 apparatus

To ensure a surface free of traces of gas and water molecules, it is necessary to remove moisture content and degas the samples before pore structure analysis (Bustin et al., 1998). The samples were degassed for 8 hours at 110°C before starting the main analysis. Finally, the nitrogen adsorption and desorption isotherms were collected at a constant temperature of 77°K (-196°C) using a Micromeritics® TriStar II 3020 apparatus (Rezaee et al., 2013). Adsorption and desorption isotherm curves were measured using between 40 and 60 points. The amount of gas adsorbed depend on the adsorbent and the temperature and pressure and is measured by the instrument at different relative pressures (P/P0) where P is the gas vapour pressure in the system and Po is the saturation pressure of adsorbent. The adsorption isotherm is the point by point measurement of the quantity of nitrogen adsorbed against the equilibrium pressure, while desorption isotherms are the measured quantity of nitrogen from the sample as the relative pressure is lowered (Rezaee et al., 2013).

A quick calculation of the pore surface area is achieved after the rapid equilibrium of physical adsorption. Among the methods to calculate the surface area, BET Method (Brunauer-Emmett-Teller) is the most widely adopted one. Isotherms are initially adjusted to the linear form of the BET equation:

$$\frac{P}{n(P_o - P)} = \frac{1}{n_m C} + \frac{C-1}{n_m C}\frac{P}{P_o}$$

Equation 2-3

where n is the amount adsorbed at the relative pressure P/Po, n_m is the monolayer capacity, and C is an empirical constant related to the shape described by the isotherm (Rouquerol et al., 1994). The term specific surface area (SSA) of pores in the solid may be calculated as:

$$SSA_{BET} = n_m a_m L$$

Equation 2-4

where a_m is the molecular cross-sectional area (i.e., the area occupied by each adsorbate molecule in the complete monolayer), and L is the Avogadro constant (Rouquerol et al., 1994).

Total pore volume is determined from the amount of vapour adsorbed at a relative pressure close to one, assuming the pores are then filled with a liquid adsorbate. The average pore size is calculated from the total pore volume and surface area, assuming the pores which would not be filled below a relative pressure of 1 have a negligible contribution to the total pore volume (Rezaee et al., 2013). Pore diameter has been calculated from adsorption data by assuming a cylindrical pore shape using the following formula:

$$D = \frac{4V_{ads}}{S}$$

Equation 2-5

where V_{ads} is the total amount of adsorbed nitrogen at maximum pressure and S is the BET surface area.

Pore size distribution is the distribution of pore volume with respect to pore size and is best calculated by BJH (Barrett-Joyner-Halenda) and DH (Dollimore and Heal) methods in the mesopores. Classical models such as BJH and DH are based on using the thickness of the adsorbed layer and Kelvin equation assuming cylindrical-shaped pores (Sing et al., 1985) to calculate pore size from isotherm data. BJH and DH models underestimate pore sizes of micropores and even smaller mesopores because these theories do not give a realistic description of micropore's filling. Alternatively, the density functional theory (DFT) model provides a much more accurate approach for pore size analysis even in in the micropore area as well as the mesopore (Rezaee et al., 2013). Pore size distributions (PSD) were obtained based on the DFT model assuming slit-shaped pores in this study.

The actual pore size in both models is calculated using the thickness of the adsorbed layer and the Kelvin equation:

$$\ln\left(\frac{P}{P_0}\right) = \frac{2\gamma V_m}{RTr_K}cos\theta$$

Equation 2-6

where γ is the surface tension of nitrogen at its boiling point (77 K), θ is the contact angle between the adsorbate (liquid nitrogen) and the adsorbent, V_m is the molar volume of liquid

nitrogen, R is the gas constant, T is the boiling point of nitrogen (77 K), and r_K is the Kelvin radius of the pore.

2.4.5 Mercury Injection Capillary Pressure (MICP)

The High-Pressure Mercury Intrusion (MICP) porosimetry technique involves injecting mercury into an evacuated and dry core sample under controlled pressures (capillary pressure). Mercury is the non-wetting phase fluid, which forces air (mercury vapour) to be the wetting phase. Due to its high surface tension, mercury cannot enter pores in the absence of external forces. As the pressure in the system increases, the mercury will intrude the smallest pore throats, as narrow as approximately 3 nm. The volume of mercury injected at each pressure step determines the non-wetting phase saturation (Shg). 1-Shg defines the wetting phase saturation (McPhee et al., 2015a).

Figure 2-12. Micromeritics Autopore IV 9500 apparatus.

Mercury porosimetry is a destructive technique that provides PSD, pore diameter, total pore volume or porosity of connected pores, the skeletal and apparent density, and specific surface area (Giesche, 2006). Mercury intrusion is useful for characterising meso- and macro-porosity. Therefore, combining mercury data with low-pressure gas adsorption data allows for the determination of full pore size spectrum of gas shale reservoirs (Labani et al., 2015).

The MICP technique is particularly useful in shales for quantifying the portion of macropores and mesopores outside the reach of LP-GA measurements. At a maximum pressure of 60,000 psi, pore sizes as narrow as 3 nm may be intruded by mercury, providing valuable information about the rock's resistance to the passage of non-wetting fluids through multiple pore scales. The cumulative mercury volume up to this point is then used for deriving porosity.

The MICP experimental data were measured using a Micromeritics Autopore IV 9500. Capillary pressure curves were collected for pressure points in the range 0.5–60,000 psi, which allows the assessment of equivalent pore sizes between 3 and 3.5e5 nm approximately. Ten small rock fragments weighing 1.8-4.1g for five samples were used for tests. Like low-pressure adsorption measurement, the samples should be evacuated before the test to remove moisture and possible gas content. Before mercury was injected into the chamber, shale samples were degassed at a 25 μmHg vacuum pressure for 10 minutes. In all cases, the experimental data were collected using a reference equilibration rate of at least 0.001 μL/g/s with mercury filling pressure of 0.53 psia. Pore throat sizes were calculated based on the Washburn equation for a mercury surface tension of 485 dynes/cm, with an advancing contact angle of 130°.

The equivalent pore diameter (d) was computed according to the capillary pressure equation (Washburn, 1921):

$$d = -\frac{4\gamma \cos\theta}{P_C} \times \mathrm{C}$$

Equation 2-7

P_C = capillary pressure [psi], ϒ = interfacial tension [dynes/cm], Θ = wetting angle, d-pore diameter (microns), C=0.145 (constant to convert to psi)

Considering $\Upsilon_{Hg/air}$ = 485 dynes/cm and $\Theta_{Hg/air}$ = 130°, we have the following equation:

$$d = \frac{180.8}{P_C}$$

Equation 2-8

Pore size distributions were approximated from the linear pore volume per unit radii distributions (dV/dr), based on a cylindrical pore model. The surface area of the intruded pores (dS) may be estimated as a function of the cumulative volume (dV) injected up to a certain pressure.

$$dS = -\frac{\mathrm{P\ dV}}{\gamma|\cos\theta|}$$

Equation 2-9

The specific area of pores is calculated at the first maximum point (or peak value) identified in the incremental area curve to procure comparable values across the whole sample set.

The maximum column heights of the non-wetting lighter phase are calculated from mercury injection capillary pressure data. This method is discussed by several researchers such as Berg

(1975) and Schowalter (1979). The buoyancy pressure of the injected CO_2 column determines the capillary pressure of the CO_2-brine. To calculate the maximum column heights of CO_2, the following steps are taken. First capillary pressure from an air/mercury system is converted to the CO_2/brine system. Then the maximum height of the CO_2 column that can be supported by the caprock can be calculated as follows (Rezaee et al., 2017; Schlomer et al., 1997):

$$h_{CO2} = P_{C_{air-Hg}} \frac{\gamma_{CO2-brine}.cos\theta_{CO2-brine}}{\gamma_{air-Hg}.cos\theta_{air-Hg}} \times \frac{1}{g(\rho_{brine} - \rho_{CO2})}$$

Equation 2-10

$$h_{CO2} = P_{C_{air-Hg}} \frac{\gamma_{CO2-brine}}{0.485(-0.64)} \times \frac{1}{g(\rho_{brine} - \rho_{CO2})}$$

Equation 2-11

A contact angle (θ) of zero is assumed for CO_2-brine in this study. Where h_{CO2} is the maximum column height, P_C is threshold pressure, ϒ is interfacial tension, θ is contact angle, and ρ is density. Calculation of CO_2-brine interfacial tension is based on the following equation suggested by Chalbaud et al. (2009):

$$\gamma_{b,Co2} = \gamma_{W_{plateau}} + \lambda * \chi_{NaCl} + \left[\frac{P}{M}(\Delta\rho)\right]^{\eta} * T_r^{\beta}$$

Equation 2-12

where λ, β, η are regression coefficient and P, M and $\gamma_{Wplateau}$ are constant values set to 1.255, 1.0243, 4.7180, 82, 44.01 (g/mol), 26 (mN/m). Tr is the relative temperature (T/Tc) (Chalbaud et al., 2009).

$$\gamma_{b,Co2} = 26 + 1.255 * \chi_{NaCl} + \left[\frac{82}{44.01}(\Delta\rho)\right]^{4.7180} * T_r^{1.0243}$$

Equation 2-13

2.5 Modelling Methodology

The injection of CO_2 into a deep aquifer disturbs the chemical equilibrium of the aqueous solution stored in the deep aquifer with existing minerals, both primary and authigenic.

The chemical composition of an aqueous solution depends on several factors. Two main thermodynamic parameters of temperature and pressure need to be determined. The concentration of each component in the mineral assembly, the brine composition in terms of ions present, and the fugacity of CO_2 are also essential too (Luigi, 2007e).

To have a better understanding of the observed experimental changes in mineralogy, geochemical reaction path modelling was applied for all samples. The modelling was done using the Geochemist Workbench (Bethke, 2010) software applying the EQ3/6 thermodynamic database. In geochemical reaction modelling, numerical consequences of a formation brine and CO_2 reacting with caprock minerals is simulated. A quantitative analysis of initial mineral amounts in the samples is required.

Static reaction path models (as opposed to reactive transport models) are used in determining the reactivity of the system and the potential product mineral phases; they are capable of providing an understanding of the potential for porosity enhancement or loss through the relevant mechanism (Gaus, 2010). Static modelling is limited by the batch type reaction modelling the software is capable of, for examples, evaporation of the water into the supercritical CO_2 and the subsequent precipitation of salts cannot be modelled. The sensitivity of the model to input parameters is tested in this type of modelling, so the key sensitive parameters (mineral reactive surface area, water to rock ratio, choice of secondary minerals) are identified to ensure the validity of assumptions and simulations.

In reaction path modelling a basis is chosen as water, a set of aqueous species, minerals, and gases. The compositions of the basis are expressed, and chemical reactions are written for. The numbers of basis entries are the number of components in the system, which is fixed by the laws of thermodynamics. The existence of water, as a reaction medium, is crucial in the basis, allowing mineral components to be transported and to interact with one another. It is well-known that nothing much would happen if there isn't a fluid, as early as the mid-16th century. In the CO_2 sequestration aquifers, the effective reaction media is the aqueous electrolyte solutions. It is comprised of solvent water, ionic and neutral solutes.

The geochemical modelling consists of two parts: equilibrium modelling (reactions that proceed quickly over the time span of the calculation) and kinetics-based reaction path

modelling (reactions that proceed slowly but measurably). Equilibrium modelling is applied first to correct analytical values for brine chemistry by assuming equilibrium with formation minerals at in-situ temperature. Kinetics modelling is then applied to evaluate the potential reactions and products of combining mineral phases with brine and $scCO_2$ as a function of time.

Here we used *SpecE8* module of GWB software to model equilibrium states and geochemical processes in systems that contain an aqueous fluid. Modelling reaction that takes place in gaseous media even supercritical gaseous CO_2 as we did in our experiment is out of aspects of such modelling programs. *React,* and *SpecE8* of GWB calculate the equilibrium distribution of aqueous species in a fluid, based on saturation state concerning minerals, and the fugacity of gases dissolved in a fluid. *React* also trace the evolution of the system as it undergoes reaction at a given temperature while integrating kinetic rate laws and simulating the fractionation of stable isotopes in a reacting system (Bethke et al., 2016).

In equilibrium modelling, distribution of aqueous chemical species is governed by Local equilibrium. Here, the aqueous electrolyte solutions are solved for mass balance, charge balance and equilibrium relations involving the activities of relevant solutes and the solvent water. A Newton–Raphson iterative method is applied to solve the chemical reaction equations. It is a quite complex exercise as it requires the correct computation of the activity coefficients of solutes and water activity (Luigi, 2007c).

The activity of aqueous species is the product of the activity coefficient and molar concentration. Activity coefficients of aqueous species except for $CO_{2\,(aq)}$ are calculated from the extended Debye-Huckel equation. $CO_{2(aq)}$ activity coefficient and fugacity coefficient are functions of pressure, temperature and salinity. Activities of pure minerals phases and H_2O are assumed to be unity (Xu et al., 2004).

The Debye-Huckel function can compute activity coefficients of electrolytes in dilute solutions with ionic strengths up to 0.1 mol/kg. In this technique, the solvent is considered as an ideal dielectric fluid without any structure. Also, the solute ions are considered as spheres with their charges situated at their centres. Peter Debye and Erich Huckel (1923) recognised that the most important interactions were long-range Coulombic forces. In contrast, the much weaker van der Waals forces, which are felt over shorter distances, governs the interactions acting between the neutral molecules of the solvent and non-electrolytes. This difference in the range of the acting forces introduces a large departure

from ideality in electrolyte solutions even at low concentrations, where the particles of ionic solutes are far apart (Luigi, 2007c):

$$\log \gamma_{\pm} = \frac{-A_{\gamma}|Z_{+}.Z_{-}|\sqrt{I}}{1 + \dot{a}B_{\gamma}\sqrt{I}}$$

Equation 2-14

where ϒ is the activity coefficient, Z is the electrical charge, $\dot{a}$ is the ion size parameter, A and B are functions of temperature, and I is the solution ionic strength defined as half sum of the product of each species molality (m) and the square of its charge (z):

$$I = \frac{1}{2}\sum_{i} m_i z_i^2$$

Equation 2-15

For dilute to slightly concentrated aqueous solutions of NaCl composition use of the B-dot equation is acceptable, whereas for very concentrated electrolytes use of the Pitzer's model is compulsory (Luigi, 2007c). *SpecE8* can employ both these methods. The B-dot equation, an extended form of the Debye-Huckel equation is used for ionic strengths of up to about three mol/L to calculate activity coefficients for the aqueous species:

$$\log \gamma_{\pm} = \frac{-A_{\gamma}.|Z_{+}.Z_{-}|.\sqrt{I}}{1 + \dot{a}.B_{\gamma}.\sqrt{I}} + \dot{B}.I$$

Equation 2-16

$$\dot{B} = \frac{1}{I}.\left[\log \gamma_{\pm} + \frac{A_{\gamma}.|Z_{+}.Z_{-}|.\sqrt{I}}{1 + \dot{a}.B_{\gamma}.\sqrt{I}}\right]$$

Equation 2-17

Some software packages such as PHREEQC use Davies equation, which is similar to the B-dot method. *SpecE8* module of GWB can emulate the activity coefficient calculation by this method:

$$\log \gamma_{\pm} = \frac{-A_{\gamma}.|Z_{+}.Z_{-}|.\sqrt{I}}{1 + \sqrt{I}} + 0.3\ A_{\gamma}.|Z_{+}.Z_{-}|.I$$

Equation 2-18

The Viral methods (the Pitzer equations) employ similar expressions as Debye-Huckel method but with an extra term for interaction among the solution components to calculate

activity coefficients in concentrated water. A Viral method known as Harvie-Moller-Weare (HMW) is used in *SpecE8* only for very high ionic strength.

In kinetics modelling, kinetic rate data are incorporated to simulate changes in composition with time, instead of local equilibrium. Under-saturated phases dissolve, and super-saturated phases precipitate at rates defined in the kinetic rate data input so that equilibrium between mineral and fluid composition is achieved. The kinetics modelling of rock-water-scCO_2 usually considers the following important factors: Kinetics of chemical reactions between minerals and brine, CO_2 solubility dependence on pressure, temperature, and salinity of the brine, redox processes that could affect the deep acquirer environments (Xu et al., 2004).

2.5.1 Notes for implementation

A *basis* is chosen at the beginning of geochemical model construction so that a combination of its components would form each species and phase in the model. The *basis* is also written with the minimum necessary number of components which are linearly independent of one another. This last condition is to make sure that no component can be formed in a balanced reaction in terms of the others. A straightforward way to choose a basis is to select elements as components and include oxidation state to incorporate the electron for redox reactions. Since any species or phase is composed of elements, the following species and phases are chosen as the components to satisfy the rules mentioned above: water, each mineral in equilibrium with the system of interest, each gas species set at known fugacity in the external buffer, and enough aqueous species abundantly present in solution to complete the basis set. The mass of initial phases is calculated in correct proportion to the 1kg water using the measured porosity. The basis species are the aqueous species included in the basis, while the secondary species are the remaining species in solution (Bethke, 2010).

The initial system is the equilibrated result of the formation water chemistry and coexisting formation minerals in equilibrium with the formation water. The reactant phases are introduced as CO_2 and those phases that are initially present in the aquifer before injection of CO_2, their surface area and kinetic parameters. It should be mentioned that for possible secondary phases, a small positive value must be set for the concentration of species or fugacity of gases in the Basis pane. A zero value would prevent the software to solve for the distribution of mass kinetic rate laws are set for minerals swapped into the initial system and thus initially in equilibrium with the fluid, as well as for the minerals set as reactants (Bethke et al., 2016).

2.5.2 Kinetics of Dissolution & Precipitation

In a dissolution and precipitation processes, five major steps have been identified (Bethke, 2010): 1-diffusion of reactants from the bulk fluid to the mineral surface, 2- adsorption of the reactants onto reactive sites, 3- a chemical reaction involving the breaking and creation of bonds, 4- desorption of the reaction products, and 5- diffusion of the products from the mineral surface to the bulk fluid. A reaction is "transport controlled" if its rate is dependent on aqueous diffusion (steps 1 and 5). On the other hand, the reaction is termed "surface controlled" if its rate is controlled by the speed of surface reaction (step 3). The adsorption and desorption processes (steps 2 and 4) are almost certainly rapid. For many import cases, reactions tend to be surface controlled, except under acidic conditions. For this reason and because of relative simplicity, the surface controlled rate law is majorly considered (Bethke, 2010). The general form of rate law (Lasaga et al., 1981; Lasaga et al., 1994) for kinetically-controlled mineral dissolution and precipitation is used:

$$r_m = A_m \, k(T)_m \left[1 - \left(\frac{Q_m}{K_m}\right)^p\right]^q$$

Equation 2-19

where r_m: dissolution/precipitation rate, A_m: specific reactive surface area per kg H_2O, $k(T)_m$: temperature-dependent rate constant (moles/unit surface area and unit time), K_m: equilibrium constant, Q_m: ion activity product, p and q: orders of rate law determined by experiments, usually assumed one to get a linear rate law.

A more complex form of Equation 2-19 is used when the effects of an inhibiting or catalysing species must be considered.

$$r = A_s \sum_i \left[k_{+i} \prod_j (a_j)^{n_j} \left(1 - \left[\frac{Q}{K}\right]^{p_i}\right)^{q_i}\right]$$

Equation 2-20

where a_j: the activity of the catalysing or inhibiting species, n_j: power for species j, derived empirically, often consider one at higher temperatures

The activity of catalysing are typically related to those of hydrogen ions and hydroxide ions. So, the equation is re-written for acidic, neutral and basic conditions. However, the basic rate would not be important in CO_2 disposal as the high pressures of CO_2 would force the formation water to remain on the acidic side of neutrality (Gunter et al., 1997).

The product of the reactive surface area and the kinetic rate (As K_+) brings much uncertainty as the values reported ranges to vary widely based on the experiment used to determine them. Consequently, in a well-implemented model with known parameters, the predicted long-term changes include uncertainties up to several orders of magnitude. These two are discussed in the following sections. Two other factors that have received much attention have been temperature and solution pH. Considering activation energy of 62.8 kJ/mol, Berner et al. (1983) estimated that silicate weathering rates increase by an order of magnitude with each 10°C increase in temperature (Kharaka et al., 2011). The temperature dependence of the rates is discussed in the Arrhenius equation (Section 2.5.2.2).

2.5.2.1 Kinetic rates of dissolution and precipitation

A thermodynamically favourable chemical reaction could take considerably long periods to complete. The rate at which the reactions occur would determine its impact on the trapping capacity, porosity, or permeability in a CO_2 storage scenario. Therefore, incorporating kinetic rate laws into a reaction model is the necessary tool for tracing reaction paths describing precipitation and dissolution using the time (Gaus, 2010). Kinetic rates for most carbonates and certain sulphates are high and can be measured directly in the laboratory (rate constants between 10^{-5} to 10^{-8} moles/m^2s). Feldspars and clay minerals reactions are slow at low temperatures (rate constants as low as 10^{-12} to 10^{-13} moles/m^2s) and take up to the order of several thousands of years as modelled in multiple papers (Audigane et al., 2007; White et al., 2005). Quartz and the inert group have the smallest rate constants (10^{-14} to 10^{-16} moles/m^2s) (Gunter et al., 1997; Palandri et al., 2004). Using the kinetics rate laws determined by laboratory experiment brings the uncertainties entailed in applying laboratory measurements to model reaction processes in nature (Bethke, 2010).

The dissolution rate of salts, minerals, and basaltic glass normalised to BET surface area at 25–30°C as a function of pH is presented in Figure 2-13. The dependence of the dissolution rate of albite on temperature and pH is shown in Figure 2-14. Temperature dependence of quartz dissolution rate data in pure H_2O using BET surface area and geometric surface area is illustrated in Figure 2-15.

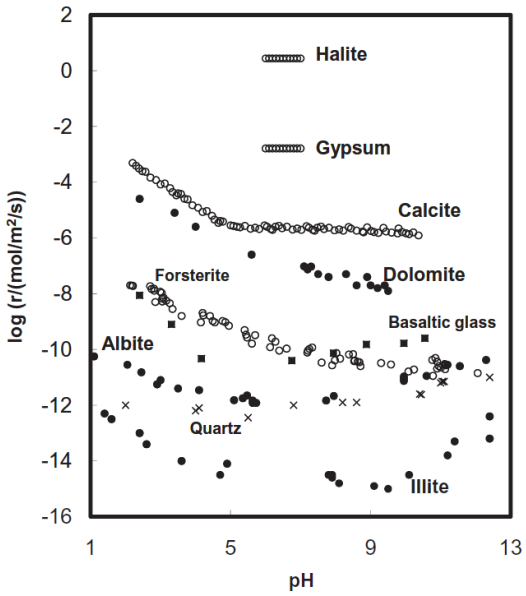

Figure 2-13- Dissolution rate of salts, minerals and basaltic glass, normalised to BET surface area at 25–30°C as a function of pH (Kharaka et al., 2011).

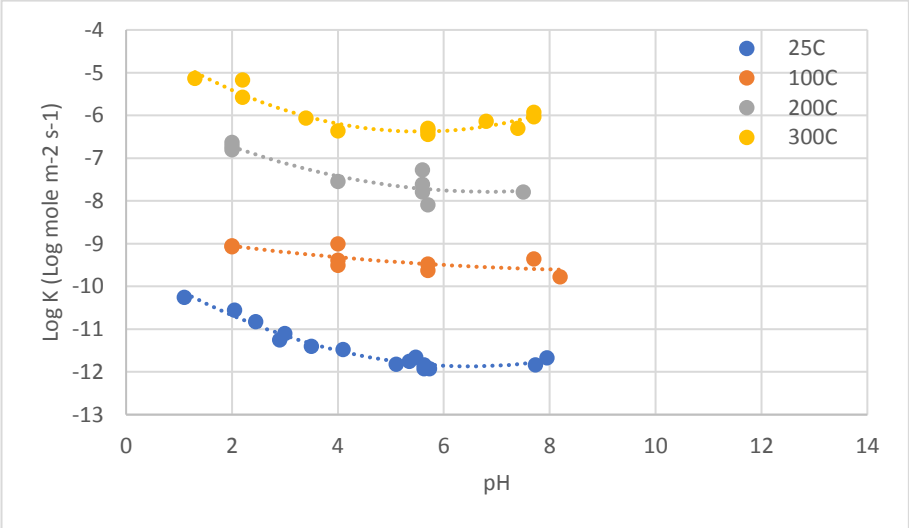

Figure 2-14. pH dependence of dissolution rates of Albite, data from (Palandri et al., 2004).

Different rate constants are reported for a single mineral under acidic, neutral, or alkaline conditions. Species in the solution can promote or inhibit the reaction mechanism, so different reaction mechanisms are found to be predominant in fluids of differing composition. Furthermore, rate law measured for reaction with deionised water is different from that of electrolyte solutions (Bethke, 2010).

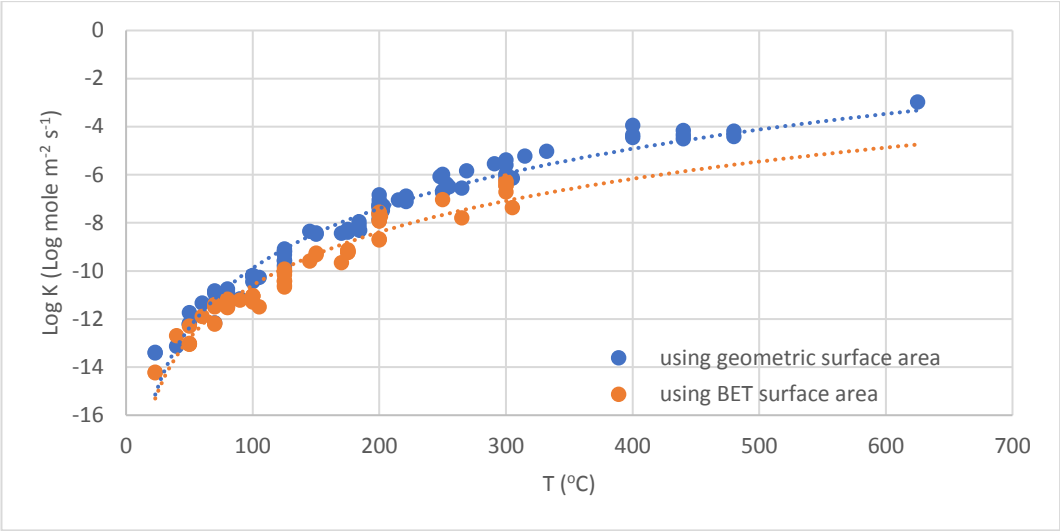

Figure 2-15.Quartz dissolution rate data in pure H_2O, data from (Palandri et al., 2004).

2.5.2.2 Arrhenius equation

The reaction rate constant can be related to temperature by the phenomenological Arrhenius equation (Lasaga et al., 1981; Lasaga et al., 1994):

$$k_+ = A\, e^{-E_a/R\,T_k}$$

Equation 2-21

where k_+: reaction rate constant of dissolution (mole/m^{2}s), E_a: activation energy (J/mole) , A: pre-exponential factor (mole/m^{2}s), R: gas constant (J/K.mole), T_K: absolute temperature (K). This equation is based on collision theory. So, term A includes parameters like the frequency of the collisions and orientation of those collisions. The exponential term determines the fraction of collisions with enough energy for a reaction to occur. It depends on the activation energy, gas constant, and absolute temperature.

Many rate constants have been determined through experiments and reported at 25°C, so it is necessary to determine the rate constant at higher temperatures required for in-situ carbon storage scenarios using the second form of the Arrhenius equation. This form uses the already determined K_{25}, and the preexponential term is omitted:

$$k = k_{25} exp\left[\frac{-E_a}{R}\left(\frac{1}{T} - \frac{1}{298.15}\right)\right]$$

Equation 2-22

where E_a: activation energy, K_{25}: rate constant at 25°C, R: gas constant, T: absolute temperature

Also, the pH dependence of mineral dissolution and precipitation rates can be incorporated using separate functions for acidic, neutral and basic mechanisms. These were used in mineral specific reaction rate scripts read by Geochemist's Workbench *React* module.

$$k = k_{25}^{nu} exp\left[\frac{-E_a^{nu}}{R}\left(\frac{1}{T}-\frac{1}{T_0}\right)\right] + k_{25}^{H} exp\left[\frac{-E_a^{H}}{R}\left(\frac{1}{T}-\frac{1}{T_0}\right)\right] a_H^{n_H} + k_{25}^{OH} exp\left[\frac{-E_a^{OH}}{R}\left(\frac{1}{T}-\frac{1}{T_0}\right)\right] a_{OH}^{n_{OH}}$$

Equation 2-23

where E_a: activation energy, R: molar gas constant, T_0=: temperature (298.15 K), nu: neutral mechanism, H: acid mechanism, OH: base mechanism, A: of the catalysing species, n: power term

2.5.2.3 Mineral surface area

The surface area of a sample can be measured by a nitrogen adsorption technique or estimated from geometric considerations (Bethke, 2010). The BET method relies on the assumption of adsorption of monolayers of gas on solid surfaces to estimate surface area. The mineral surface area can be assigned based on average grain size for sedimentary rocks and modified using the methods described in White et al. (1995).

$$A_s = \frac{6}{\rho\, D}\lambda$$

Equation 2-24

where ρ: mineral density (g/cm3), D: mineral grain diameter, λ: roughness factor (measured surface area / geometric surface area). White et al. (1995) suggested a roughness factor of 7 for fresh surfaces and typical of grains less than 100 µm in diameter.

Although a direct dependence of rate upon surface area is assumed in the rate equation, the surface area is less understood parameters and introduce a level of uncertainty to the reaction rate calculation. BET surface area is commonly used in the dissolution kinetics rate law, but the evidence to support this assumption is insignificant. It is known that BET or geometric surface area overestimate the real surface area available to the reaction.

The definition of the reactive surface area based on either geometric or the BET surface area introduces further uncertainty (Aagaard et al., 1982; Gautier et al., 2001). BET surface area is an order of magnitude larger due to the surface roughness. The difference between total surface area and reactive surface area can be between one and three orders of magnitude because of the reactions only occur at selective sites at the surface (White et al., 1990). The

precipitating surface introduces even more uncertainty because precipitation only takes place at specific sites around nuclei initially.

Difficulties in representing the surface area of minerals in natural samples rise from the fact that in the laboratory the minerals are fresh and any surface coatings have been removed, however, in the fields, they may be shielded with oxide, hydroxide, or organic coatings (Bethke, 2010). Other factors considered for limiting the effective reactive surface area are grain to grain contacts, grain edge faces on minerals with a tabular morphology (including clays) and channelling of the reactive fluid flow (Li et al., 2006; Zhu et al., 2006). Kirste (2013) decreased the calculated geometric surface area by a factor of 100 to account for these effects (Table 2-5). So their derived reactive surface areas were consistent with values described by Xu et al. (2006). However, Zhu et al. (2006) reported a reduction of reaction rates on five orders of magnitude compared to laboratory determined rates due to grain coating of natural feldspars.

Table 2-5. The surface area values used in previous studies.

	Reactive Surface Area (cm²/g)					
Mineral	**(Xu et al., 2005)**	**(Xu et al., 2007)**	**(Gherardi et al., 2007)**	**Knauss et al. (2005) (Ketzer et al., 2009) (×edge factor)**	**(Pham et al., 2011)**	**Kirste (2013)**
Quartz	9.8	9.1	10	113.3		10
Chalcedony					225	
Albite	10	9.1	10	114.5	1000	10
K-feldspar	9.8	9.1	10	117.3	1100	10/ 60
Kaolinite	151.6	108.7	23	115.6 (×10)		70
Muscovite			152	106 (×10)	6800	
Chlorite	9.8	9.1	20	111.8 (×10)	16000	70/ 700
Smectite	151.6	108.7	152		500000	150
Illite	151.6	108.7	152	106 (×10)		150
Calcite			10	110.7		10
Dolomite	9.8	9.1	10	105.6	160	10
Magnetite					1020	
Pyrite	12.9	12.9	13	59.9	510	
Hematite	12.9	12.9	13			
Ankerite	9.8	9.1	10		160	
Siderite	9.8	9.1	10		1750	
Magnesite	9.8	9.1	10		1270	
Dawsonite	9.8	9.1	10		98000	

2.5.2.4 Comparing laboratory dissolution rates to the field

The determination of kinetic constants is subject to many complexities, and experimental data should be available over a wide range of pressures and temperatures both far from and close to equilibrium. Furthermore, potential catalysers or inhibitors should be identified; constants should be measured for varying mineral compositions in solid solutions series as

well as for minerals that are not perfectly crystalline. Kinetic data compilations show large variations in kinetic rates as a consequence of different experimental setups, experimental conditions, and selected mineralogies, as shown in Palandri et al. (2004). For slow reacting minerals, these differences can easily span several orders of magnitude. When comparing laboratory-derived kinetic rates with kinetic rates derived in the field, then the results suggest that reactions are taking place much faster in the case of laboratory data. For example, in situ derived silicate reactions rates are far slower than laboratory studies at comparable temperatures and pH values with differences of up to 2–5 orders of magnitude (e.g. Zhu, 2006). Laboratory generated dissolution rates are commonly based on experiments performed at far-from-equilibrium conditions, and in the absence of precipitation of secondary phases. Under natural conditions in the field, fluids can remain in contact with a mineral surface for far longer than in most laboratory experiments, causing the fluid to approach equilibrium with the dissolving minerals. The approach to equilibrium can lower rates by orders of magnitude compared to their laboratory-measured far-from-equilibrium counterparts (Kharaka et al., 2011). Also, the formation of mineral coatings is suggested to play a role in this discrepancy (Cubillas et al., 2005).

The secondary silicate phases that precipitate during weathering are dominated by clay minerals, particularly kaolinite, illite, allophane, smectite, and their amorphous precursors. However, relatively few studies of clay mineral precipitation rates are available. As such, clay mineral precipitation rates remain one of the biggest obstacles to the application of geochemical modelling codes to quantifying chemical weathering in nature. There are several reasons why so few studies of clay mineral precipitation rates exist, including:

- Difficulties in quantifying the precipitating clay mineral phase and its composition;
- Poor understanding of the thermodynamic properties of clay minerals, which depend on both the composition of the precipitating phase and its crystal size; and
- The small particle size of clays, which makes it difficult to keep the clay minerals in an experimental reactor (Kharaka et al., 2011).

2.5.3 Uncertainties

The parametrisation of geochemical models introduces the uncertainties in calculating the fate of CO_2 in the rock-brine system. The parameters include the geochemical model code used, the choice of the thermodynamic database, the ion activity model, the temperature correction of equilibrium constants, the CO_2 fugacity calculation, the selection of primary and

secondary minerals or solid solutions, and the kinetic rates of related reactions. The selection of secondary phases causes significant uncertainty in the modelling results, as the modeller should predict which minerals form in nature as a result of the reactions. This is the reason why any geochemical model should be built upon and then compared with experimental data and observations. The thermodynamic datasets are another major source of uncertainty as they need to be adjusted to the temperature. Activity coefficients of the dissolved species would be determined by equations such as extended Debye-Huckel (B-dot form) or Pitzer algorithm for ionic strength of up to 2 mol/L. The different range of ionic strengths for each equation and different assembly of ions in each database introduces even further uncertainties (Dethlefsen et al., 2012).

Chapter 3. Experimental Results

3.1 XRD Results

The constituents (weight percentage) of 15 samples before exposure to $scCO_2$ from Harvey-3 are depicted in Figure 3-1. Bulk X-ray diffraction analysis was performed on selected samples to characterise their mineral composition after four and nine months. Table 3-1 summarises the results. The collected samples are quartz-rich mudstone with significant Illite/mica and kaolinite and sub-dominant feldspars (Figure 3-3). Average detrital quartz and feldspar grains are 30 and 9 weight per cent respectively. Major clay types are kaolinite, illite-mica with an average of 27 and 31% respectively. Samples H1, H6, H9, H10, H11, and H16 are the clay-rich samples (Figure 3-2) with clay content more than 60%. The most quartz-rich sample is H8 with a maximum of 56.7%, and the highest amount of kaolinite is in samples H1 (43%) and H11 (45). Minor amounts of goethite, pyrite, hematite, and calcite also occur in some of the samples analysed. Sample H1 has the highest amount of goethite (9%) among the samples, a lesser amount of goethite (<2%) are found in most of the samples. Samples are free from carbonates. Only a minor amount of hematite and pyrite is found in some samples. XRD traces are provided in Appendix III. The mineralogy is consistent with data reported in Core Laboratories (2015) petrologic analysis of Harvey-3 samples and is sufficiently representative.

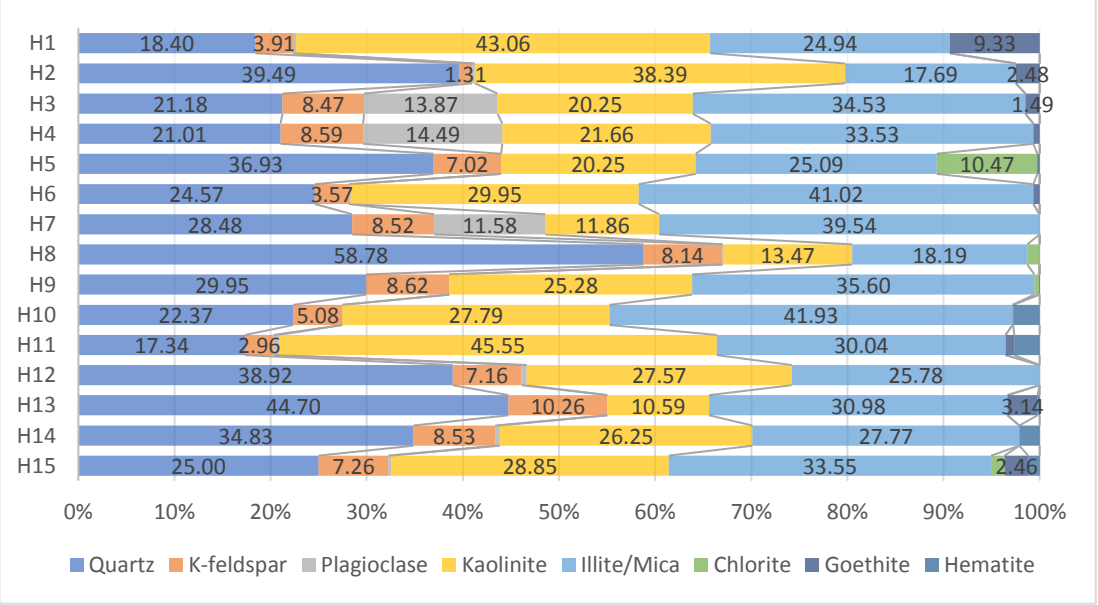

Figure 3-1- Mineralogical composition (weight percentage) of the samples analysed before exposure to $scCO_2$.

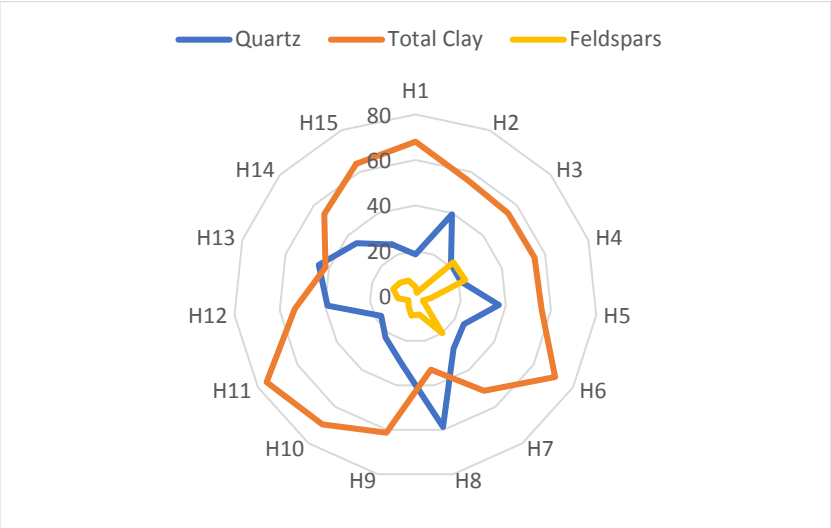

Figure 3-2. Radar chart of the main components of samples in terms of quartz, clay, and feldspars.

Table 3-1 summarises the quantitative amount of minerals in each sample before and after four and nine months of exposure to $scCO_2$. The quartz content is constantly reduced in all the samples, which are a sign of quartz dissolution. However, an increase in the amount of quartz is attributed to the dissolution of feldspar and clay minerals. Microcline is decreased in some samples (H4, H9, H13, H14, and H15) and increased in samples H1 and H2 after exposure. For samples H5, H8, and H10, there is a mixed trend in the amount of microcline. Albite and anorthite rich H4 show a decrease in both minerals post-exposure, but a sharp increase of albite amount in H2. A significant increase in albite and microcline content is observed in sample H2 after nine months.

For clay minerals, kaolinite is decreasing, and muscovite is increasing in most samples (H1, H2, H4, H9, H10, and H14). The clay content in the samples follows an interesting trend. In samples where kaolinite content is continuously decreased, an increase in muscovite content is constantly evident. Meanwhile, the kaolinite content in samples H13 and H14 experienced first a decreased and then an increasing trend, opposite that of muscovite where it was increased and then decreased. However, in samples H5 and H8, both clay minerals are increased and then decreased. Halite is increased in all samples as a result of brine desiccation (Appendix III). Carbonate minerals that are of great significance in mineral trapping of CO_2 through reaction with magnesium and calcium ions provided by silicate minerals are mostly absent in samples analysed.

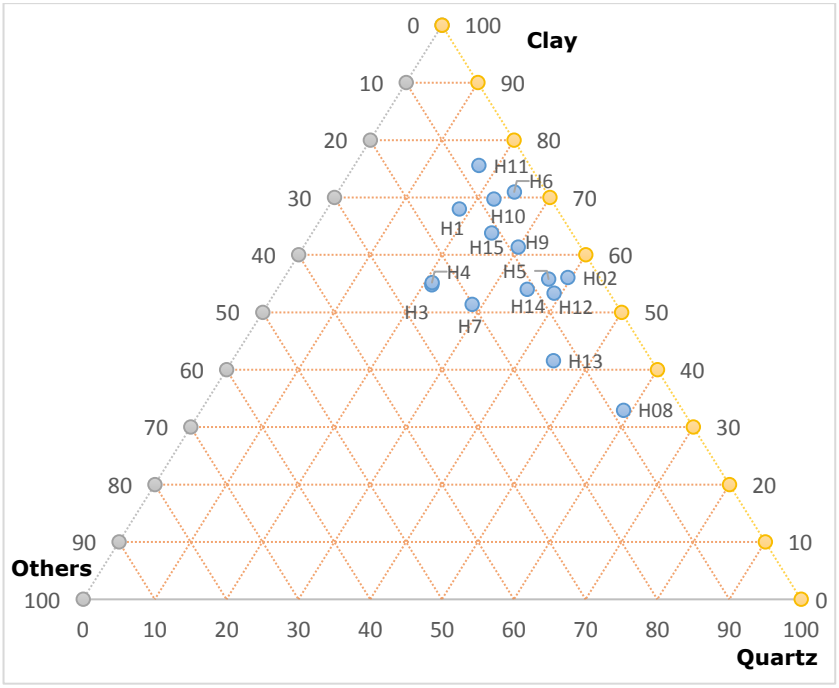

Figure 3-3. Triangular chart of main components of samples in term of quartz, clay, and other minerals.

Table 3-1. XRD Semi-quantitative mineralogy for Harvey-3 seal rocks in weight%, before and after exposure.

Samples	*Quartz*	*Microcline*	*Albite*	*Anorthite*	*Illite/Mica*	*Kaolinite*	*Chlorite*	*Goethite*	*Calcite*	*Pyrite*	*Hematite*	*Halite*
Before exposure												
H1	18.40	3.91	0.35	0.00	24.94	43.06	0.00	9.33	0.00	0.00	0.00	0.00
H2	39.49	1.31	0.31	0.00	17.69	38.39	0.00	2.48	0.00	0.00	0.00	0.33
H4	21.01	8.59	12.24	2.24	33.53	21.66	0.00	0.67	0.00	0.00	0.00	0.20
H5	36.93	7.02	0.00	0.00	25.09	20.25	10.47	0.24	0.00	0.00	0.00	0.06
H8	58.78	8.14	0.10	0.00	18.19	13.47	1.28	0.01	0.00	0.00	0.00	0.00
H9	30.39	8.67	0.00	0.00	34.42	26.43	0.00	0.08	0.00	0.00	0.00	0.05
H10	22.37	5.08	0.01	0.00	41.93	27.79	0.00	0.07	0.00	0.00	2.74	0.00
H13	43.84	9.64	0.00	0.00	31.35	14.91	0.00	0.16	0.00	0.00	0.00	0.02
H14	34.83	8.53	0.47	0.00	27.77	26.25	0.00	0.00	0.00	0.00	2.10	0.00
H15	25.00	7.26	0.30	0.00	33.55	28.85	1.41	2.46	0.00	0.00	1.18	0.01
4 months after exposure												
H1	18.02	4.00	0.47	0.00	27.68	39.70	0.00	9.35	0.00	0.00	0.00	0.78
H2	38.05	1.43	0.13	0.00	21.18	34.92	0.00	2.63	0.00	0.00	0.00	1.66
H4	20.30	8.16	11.50	2.04	34.89	20.86	0.00	0.64	0.00	0.00	0.00	1.61
H5	33.49	6.57	0.00	0.00	27.70	22.08	9.17	0.47	0.00	0.00	0.00	0.50
H8	50.87	7.89	0.17	0.00	22.52	16.32	1.15	0.03	0.00	0.00	0.00	1.05
H9	28.25	8.75	0.03	0.00	36.64	24.62	0.00	0.10	0.00	0.00	0.00	1.62
H10	21.68	5.00	0.15	0.00	41.86	27.34	0.00	0.15	0.00	0.00	2.72	1.09
H13	42.37	10.06	0.00	0.00	32.44	9.43	0.00	4.16	0.00	0.00	0.00	1.54
H14	N/A	N/A	N/A	N/A	N/A	N/A	N/A	N/A	N/A	N/A	N/A	N/A
H15	23.95	7.26	0.29	0.00	39.46	24.89	0.00	2.47	0.00	0.00	0.00	1.70
9 months after exposure												
H1	17.50	4.00	0.48	0.00	28.48	37.86	0.00	9.34	0.00	0.00	0.00	2.34
H2	30.04	3.64	4.22	0.00	27.53	30.73	0.00	1.13	0.00	0.00	0.00	2.70
H4	18.78	7.59	11.71	1.65	36.44	19.82	0.00	0.53	0.00	0.00	0.00	3.48
H5	32.90	7.07	0.00	0.00	28.46	19.94	7.50	0.88	0.00	0.00	0.00	3.26
H8	49.23	8.29	0.28	0.00	19.98	15.72	2.68	0.00	0.00	0.00	0.00	3.82
H9	27.29	8.55	0.00	0.00	36.56	23.27	0.12	0.35	0.00	0.00	0.00	3.87
H10	21.87	5.06	0.38	0.00	40.55	26.83	0.00	0.18	0.00	0.00	2.78	2.34
H13	39.52	9.48	0.00	0.00	30.97	16.40	0.00	1.42	0.00	0.00	0.05	2.17
H14	32.04	8.38	0.54	0.00	32.01	22.72	0.03	0.04	0.00	0.00	1.79	2.45
H15	23.45	6.99	0.13	0.00	33.87	26.42	2.27	1.85	0.00	0.00	1.28	3.75

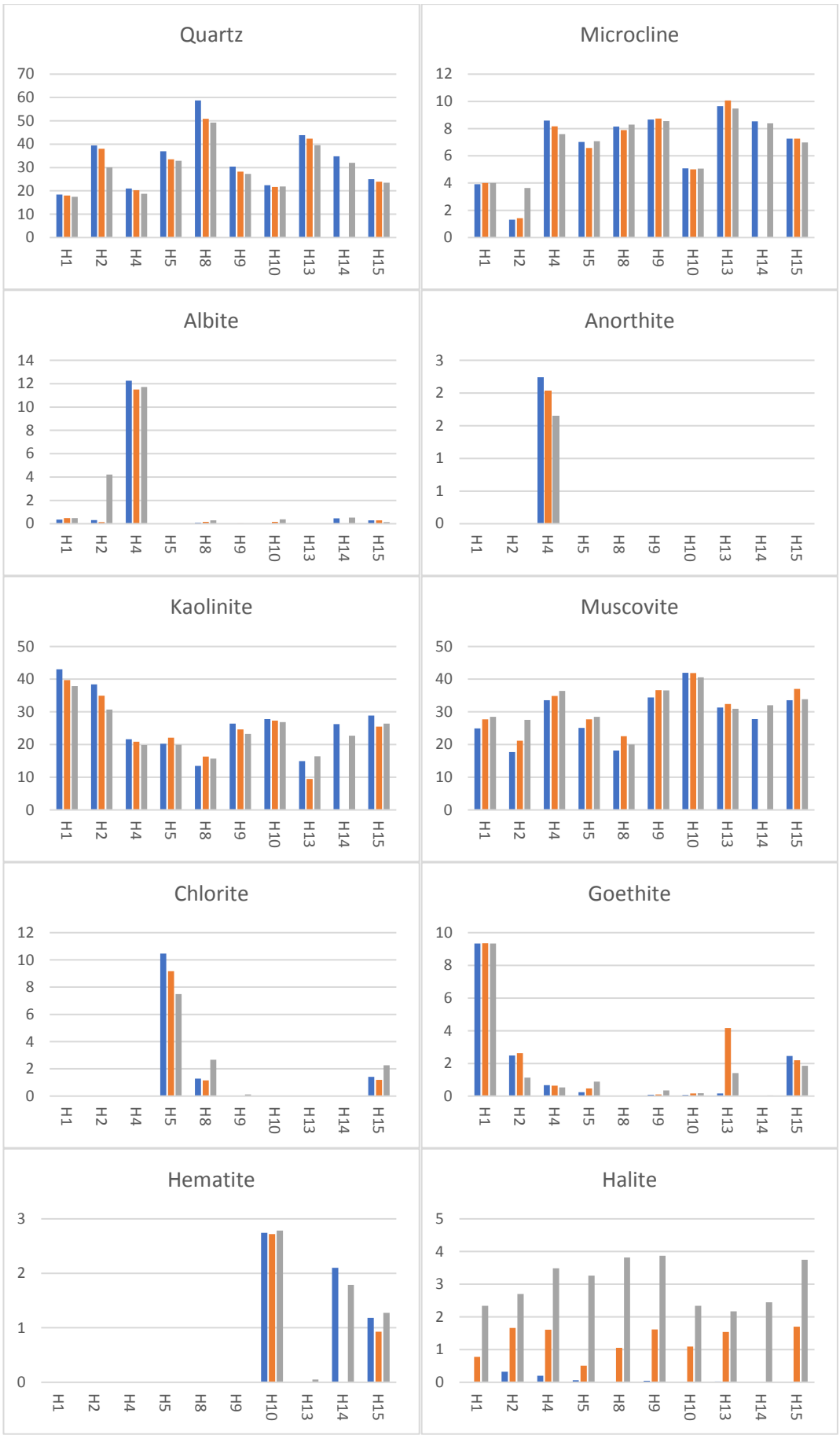

Figure 3-4. Mineral amounts before exposure (blue), and after 4 months (red) and 9 months (grey) exposure.

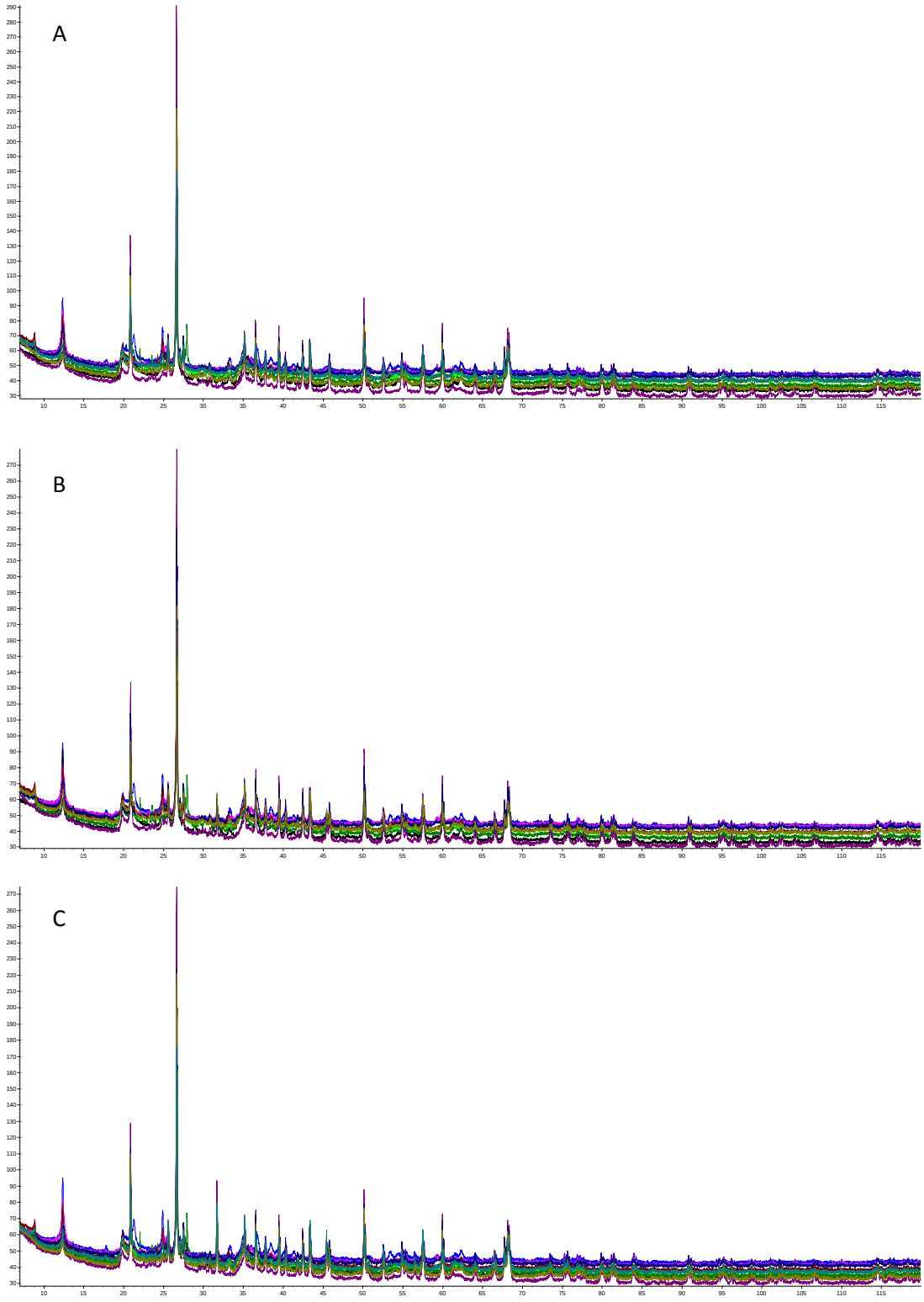

Figure 3-5. A. Diffractogram of all samples before exposure, B. Diffractogram of all samples after four months exposure, C. Diffractogram of all samples after nine months of exposure.

Note that the XRD analysis was carried out on rock post-exposure sample which were not post-experimentally rinsed by water. Samples exposed to CO_2 for a long-term are subject to CO_2 drying-out effect, and therefore crystals of salt (NaCl) participated in the system, further altering the mineralogy.

3.1.1 Control samples

A total of nine samples were selected for observation. Samples OH1, OH2, OH4, OH5, OH8, OH9, OH13, and OH15, were exposed to the same conditions in the absence of $scCO_2$. Observation samples were mixed with the same brine composition and put inside the oven set to 60°C for nine months. Table 3-2 summarises the quantitative amount of minerals in each control sample after exposure to $scCO_2$.

Table 3-2. XRD Semi-quantitative mineralogy for Harvey-3 seal rocks in weight%, observation samples.

	OBS											
Samples	Quartz	Microcline	Albite	Anorthite	Illite/Mica	Kaolinite	Chlorite	Goethite	Calcite	Pyrite	Hematite	Halite
OH1	19.10	3.24	0.40	0.00	28.63	44.76	0.00	3.87	0.00	0.00	0.00	0.00
OH2	37.22	2.22	0.39	0.00	18.30	38.31	0.00	2.28	0.00	0.00	0.00	1.28
OH4	19.65	7.81	10.93	2.57	35.41	17.61	0.00	0.53	0.00	0.00	0.00	5.48
OH5	35.61	6.37	0.00	0.00	26.97	20.21	9.67	0.10	0.00	0.00	0.00	1.07
OH8	44.39	7.79	0.08	0.19	24.97	18.71	0.72	0.00	0.00	0.00	0.00	3.14
OH9	34.05	9.89	0.00	0.12	34.66	20.35	0.28	0.21	0.00	0.00	0.00	0.43
OH10	26.06	7.63	0.24	0.00	38.05	25.63	0.00	1.42	0.00	0.00	0.66	0.31
OH13	46.87	10.87	0.00	0.00	24.96	11.09	1.61	4.40	0.00	0.00	0.21	0.00
OH15	28.06	8.38	0.33	0.04	33.75	24.23	1.58	0.57	0.00	0.00	0.98	2.07

Figure 3-6 compares the mineral amount in samples before exposure and control samples. Quartz is reduced in most of the samples. Clay minerals and feldspar direction of change are different in samples. Chlorite decreased and halite increased. The result of alteration in control samples is different from the results of exposed samples. However, alteration of minerals is observed in all the samples which are just treated with heat and brine.

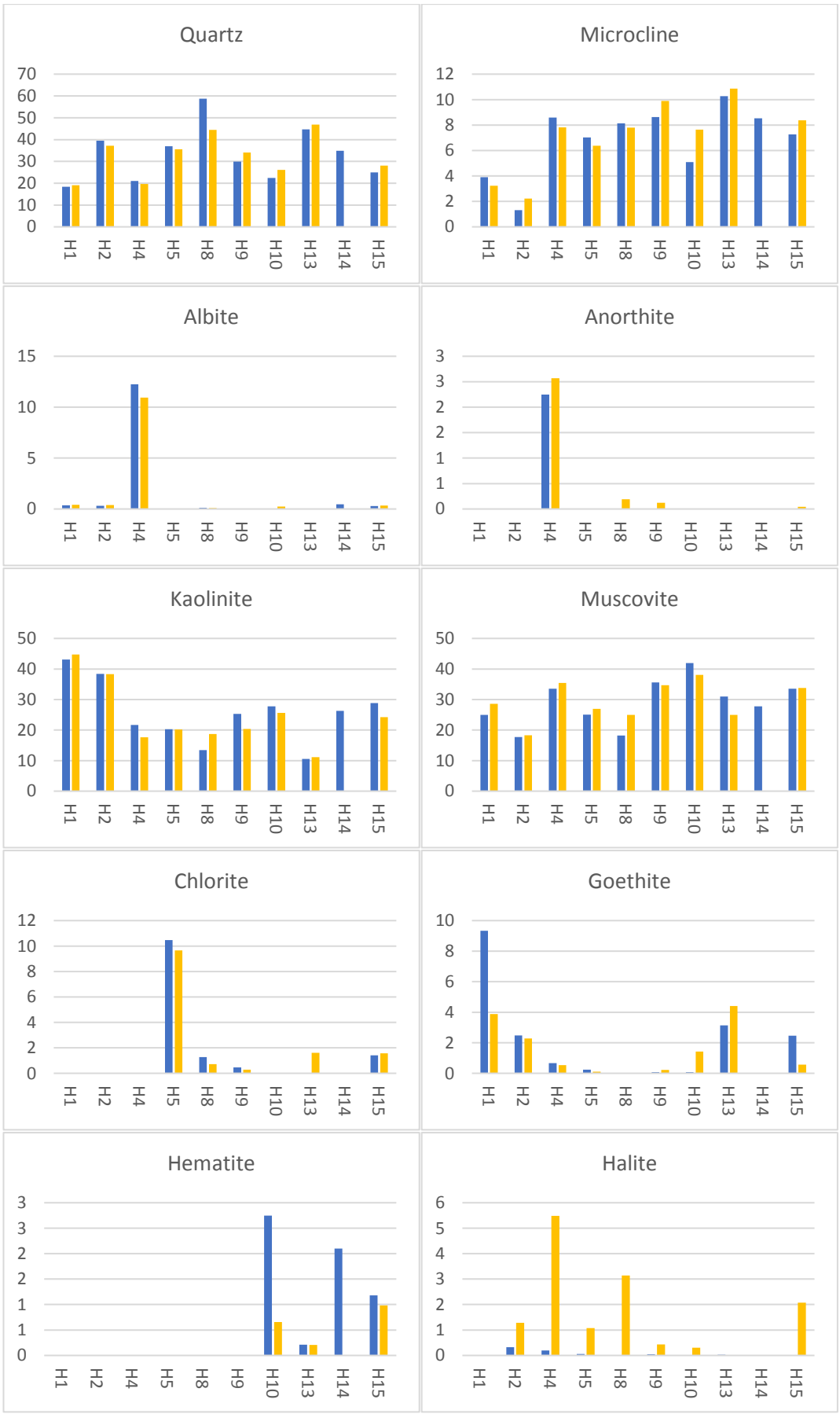

Figure 3-6. Mineral amounts before exposure (blue) and observed (yellow).

3.2 SEM Results

SEM observations reveal several new features after the samples were exposed to $scCO_2$. SEM Images of samples before and after exposure are included in Appendix IV. Images are obtained in SE and BSE mode.

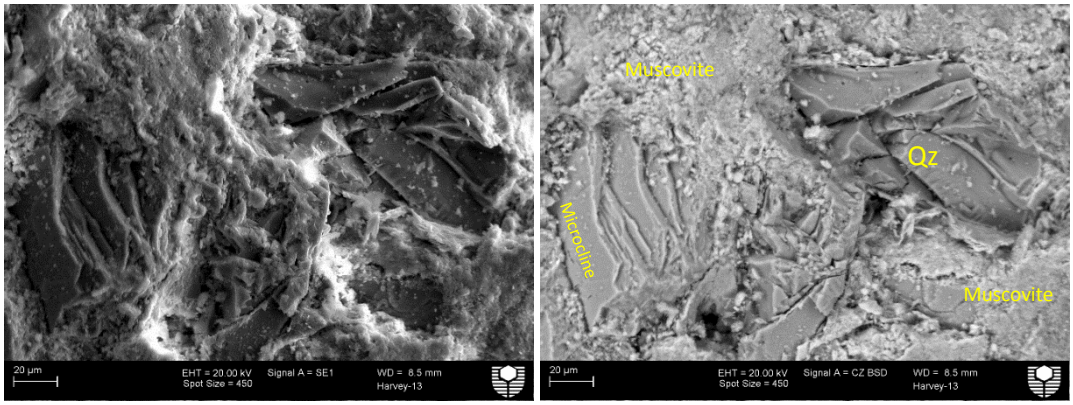

Figure 3-7. SEM image of sample H13 shows K-feldspar and quartz in the abundant clay matrix.

3.3 NMR Results

Nuclear Magnetic Resonance (NMR) experiments were carried out on a low field Magritek bench-top Rock Core Analyser, located in the Department of Petroleum Engineering at Curtin University. A total of 7 core plugs were recovered from the samples received from the core library. The other samples were either too soft or were broken, and plugs could not be taken from them. The study involves six types of T_2 relaxation time measurements: 1) dry state (as received samples from core store) before exposure to $scCO_2$; 2) brine-saturated state before exposure to $scCO_2$; 3) after exposure to $scCO_2$ for four months; 4) brine re-saturated state after exposure to $scCO_2$ for four months; 5) after exposure to $scCO_2$ for nine months, and 6) brine re-saturated state after exposure to $scCO_2$ for nine months. Sample H8 and H10 collapsed during the saturation process and could not be analysed.

Table 3-3- Sample dimensions, volume, and mass.

	H1	***H2***	***H5***	***H8***	***H9***	***H10***	***H13***
Mass (g)	120.06	110.34	113.94	107.20	106.38	104.30	108.23
Height (cm)	4.14	3.76	3.99	3.92	3.82	3.85	3.92
Diameter (cm)	3.82	3.83	3.81	3.81	3.80	3.78	3.80
Volume (cm^3)	47.59	43.24	45.47	44.63	43.45	43.33	44.57

Plots of NMR T_2 relaxation of all the samples are reported in Appendix V. Figure 3-8 lists NMR porosity for the samples analysed. There is a notable increase in porosity for samples that are exposed to $scCO_2$.

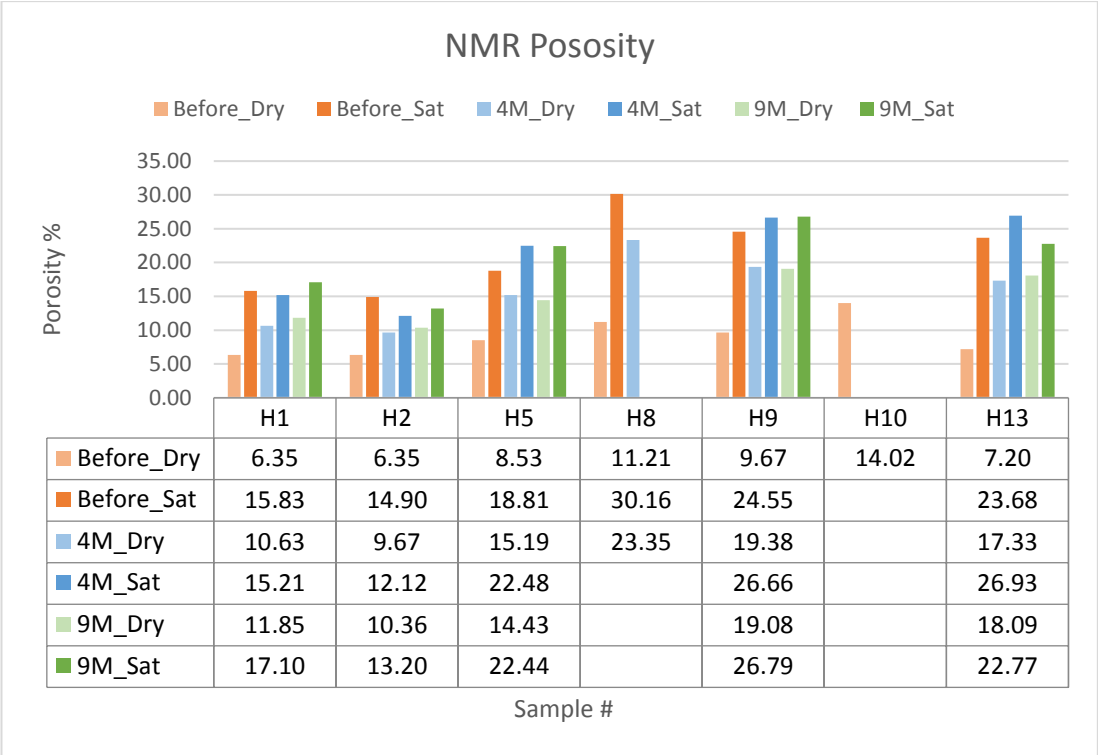

	H1	H2	H5	H8	H9	H10	H13
Before_Dry	6.35	6.35	8.53	11.21	9.67	14.02	7.20
Before_Sat	15.83	14.90	18.81	30.16	24.55		23.68
4M_Dry	10.63	9.67	15.19	23.35	19.38		17.33
4M_Sat	15.21	12.12	22.48		26.66		26.93
9M_Dry	11.85	10.36	14.43		19.08		18.09
9M_Sat	17.10	13.20	22.44		26.79		22.77

Figure 3-8- A comparison of porosities for samples before and after exposure to scCO2.

The average NMR porosities are 7.62%, 19.55%, 14.44%, 20.68%, 14.76%, and 20.46% for Before_Dry, Before_Sat, 4M_Dry, 4M _Sat, 9M_Dry, and 9M_Sat respectively. There is an increase in the average porosity of samples exposed to $scCO_2$.

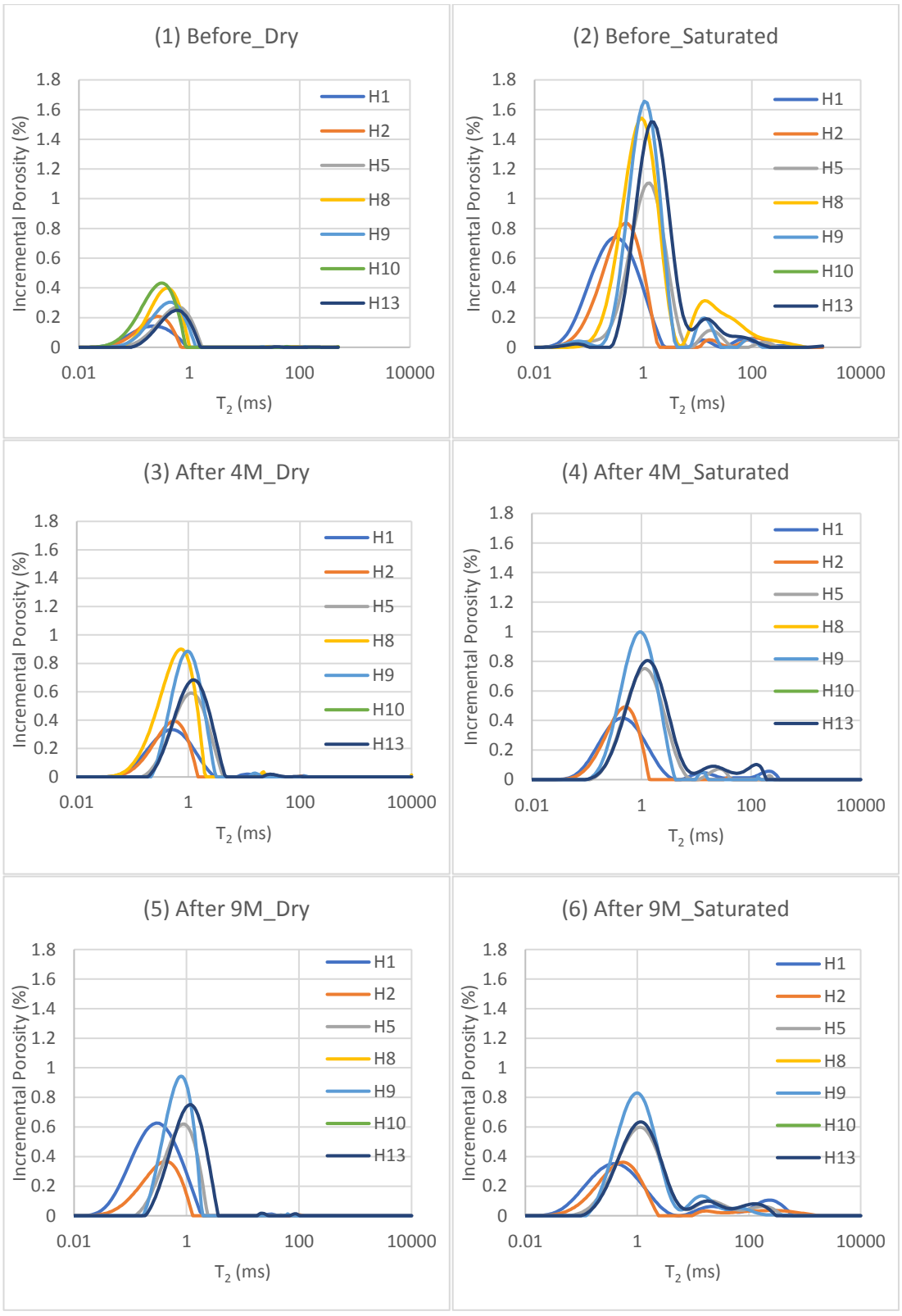

Figure 3-9. T_2 distribution of (1) dry state (as received samples from core store) before exposure to $scCO_2$, (2) brine-saturated state before exposure to $scCO_2$, (3) directly after 4 months exposure to $scCO_2$, (4) brine re-saturated state after exposure to $scCO_2$, (5) directly after 9 months exposure to $scCO_2$, (6) brine re-saturated state after 9 months exposure to $scCO_2$. Sample H10 failed after first saturation and sample H8 failed after second saturation.

Figure 3-9 illustrates combined T_2 distribution for all Before-Dry, Before-sat, 4M-Dry, 4M-Saturated, 9M-Dry, and 9M-Saturated core plugs respectively. The shapes of the T_2

distributions of the Before-dry samples are similar (Figure 3-9). The dominant peak in the case of dry samples is related to clay surface water. In contrast, the T_2 distribution of the saturated samples is bimodal which consists of a dominant peak in lower relaxation times and other peaks in higher T_2 values. A combination of both clay surface water and water in the interstitial pores are observed in such samples. Each exposure stage of saturated samples saw a reduction in NMR signal which is attributed to rock dehydration. Some of the water in the cores are evaporated into the CO_2.

3.4 LPNA Results

A Low-Pressure Nitrogen Adsorption (<18.4 psia, 77K) test was applied on ten samples from Harvey-3 before and after they exposed to $scCO_2$. Values of surface area and pore volume and their distribution along pore width is reported and compared here. Pore size (diameter) is calculated from these values and included in this study. The results indicate some significant changes in the nanopore structure system of the samples after $scCO_2$ and shale interactions. However, the variation trend of the pore structure parameter was quite different after exposure to $scCO_2$, which was related to the discrepancies in the mineralogical and geochemical properties of the samples.

Appendix V illustrates low-pressure nitrogen isotherms for the analysed samples, pore width versus incremental pore volume (IPV), and pore width versus incremental surface area (ISA) for all samples separately before and after exposure to $scCO_2$. For all samples studied the PSD ranges between 1 nm and 120 nm. There are six different types of adsorption isotherms according to IUPAC definition. The isotherm curves can be best represented by Type II isotherms, as physisorption hysteresis is present, as shown in Figure 3-10 (Brunauer et al., 1938). The shape of the isotherms suggests that pore networks are generally dominated by meso- and macropores, with negligible contribution from micropores. The curves also describe a Type H3 hysteresis loop, which is associated with clay particles with slit-shaped pores (Sing et al., 1985).

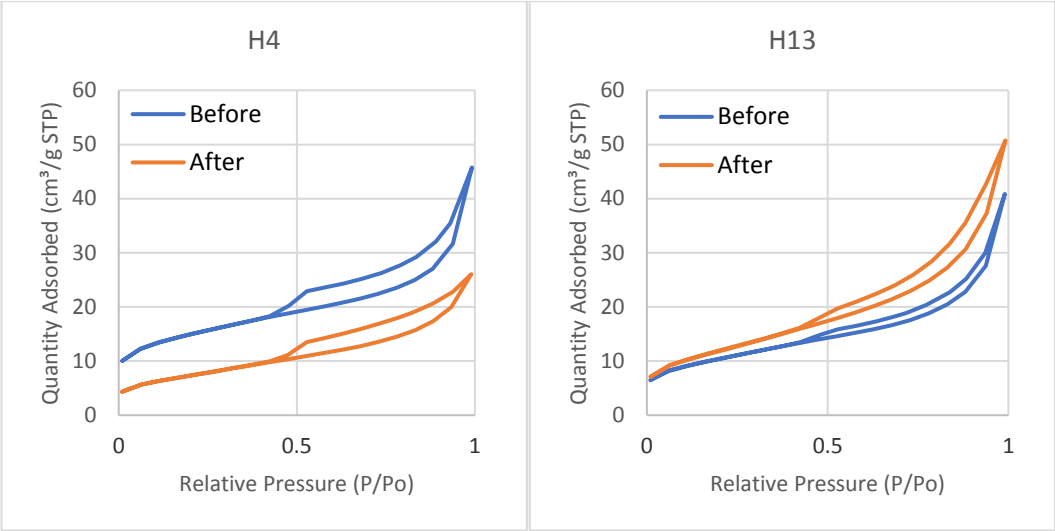

Figure 3-10. The low-pressure nitrogen adsorption isotherms of samples H4 and H13 representing two types of behaviour. In group one represented by H4, the absorbed amount of nitrogen is reduced while in group two represented by H13 the absorbed nitrogen is increased.

Samples H1, H2 H4, H10, H14, and H15 isotherms show that the adsorbed amount of nitrogen in after-exposure samples are lower than the before-exposure samples (Figure 3-10). Samples H5, H8, H9, and H13, however, show an increase in the amount absorbed after exposure when compared with before-exposure isotherms. The low-pressure nitrogen adsorption isotherms of all samples before and after $scCO_2$ exposure are illustrated in Appendix V.

Table 3-4 and Table 3-5 summarise the collected results from low-pressure nitrogen adsorption measurement for samples before and after exposure to $scCO_2$. The average pore width for the Before and After data was found to be 3.90 and 4.5nm respectively. Average pore volume obtained from LPNA tests for Before and After samples is about 4 and 4.4 $cm^3/100g$, which are characterised by a very high contribution of the mesopore size, 76.63% and 83.48% of total porosity respectively. The average BET surface area is found to be 43.42, and 39.42 m^2/g (Before and After). Figure 3-11 and Figure 3-12 compare the total pore volume and variation of micropores, mesopores, and macropores volumes in samples studied. Figure 3-16, and Figure 3-17 compare the BET surface area, and pore size of the analysed samples before and after exposure to $scCO_2$.

Table 3-4- Summary of low-pressure nitrogen adsorption results before exposure to $scCO_2$.

Samples	BET surface area (m^2/g)	Average pore width (nm)	DFT model			
			Micropore Vol. ($cm^3/100\ g$)	Mesopore Vol. ($cm^3/100\ g$)	Macropore Vol. ($cm^3/100\ g$)	Total pore Vol. ($cm^3/100\ g$)
H1	32.96	6.868	0.347	4.859	0.453	5.659
H2	29.71	5.467	0.347	3.500	0.214	4.060
H4	50.29	3.718	1.226	3.186	0.263	4.675
H5	29.29	3.521	0.332	2.186	0.061	2.578
H8	23.88	2.889	0.405	1.299	0.021	1.725
H9	41.34	3.406	0.731	2.720	0.070	3.520
H10	51.96	3.157	0.987	3.067	0.047	4.101
H13	36.54	4.210	0.620	3.033	0.193	3.846
H14	67.61	2.904	1.654	3.205	0.049	4.908
H15	70.63	2.844	1.495	3.504	0.023	5.022

Table 3-5- Summary of low-pressure nitrogen adsorption results after exposure to $scCO_2$.

Samples	BET surface area (m^2/g)	Average pore width (nm)	DFT model			
			Micropore Vol. ($cm^3/100\ g$)	Mesopore Vol. ($cm^3/100\ g$)	Macropore Vol. ($cm^3/100\ g$)	Total pore Vol. ($cm^3/100\ g$)
H1	33.12	4.889	0.315	3.614	0.119	4.048
H2	30.69	4.354	0.344	2.949	0.051	3.344
H4	26.19	4.264	0.409	2.319	0.064	2.792
H5	29.59	5.754	0.324	3.724	0.208	4.256
H8	25.45	3.325	0.332	1.760	0.023	2.115
H9	41.77	4.775	0.573	4.203	0.210	4.986
H10	46.1	4.063	0.775	3.812	0.094	4.682
H13	42.4	5.207	0.548	4.702	0.270	5.520
H14	63.21	3.700	1.363	4.309	0.175	5.847
H15	55.69	4.638	1.088	5.096	0.272	6.457

The low-pressure nitrogen adsorption analysis shows that the pore structure changed after shale samples were exposed to $scCO_2$. For most of the samples studied, there was an increase in the pore volume (H5 – H15). However, there was a decrease in pore volume for samples H1, H2, and H4 (Figure 3-11). Porosity is increased significantly (average 50%) in samples H5, H9, and H13 where after exposure PSD curve sits on top of the preexposed curve along the whole pore width range (Figure 3-13). An increase of average 21% is observed in samples H8, H10, H14, and H15 where after exposure curve is increased only in lower pore width range (<20nm). Figure 3-12 illustrates a decrease in the volume of micropores across the samples. However, the mesopores and macropores follow the same trend as the total pore volume and play the deciding role in the total pore volume changes.

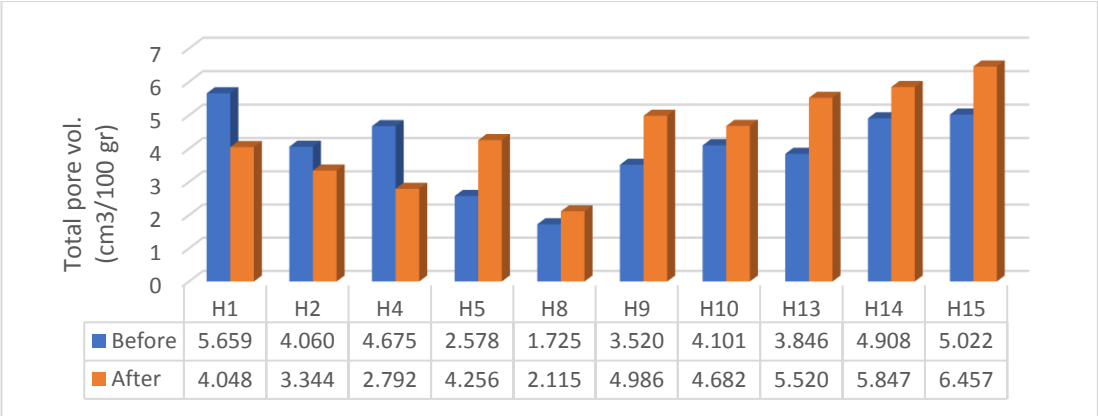

	H1	H2	H4	H5	H8	H9	H10	H13	H14	H15
Before	5.659	4.060	4.675	2.578	1.725	3.520	4.101	3.846	4.908	5.022
After	4.048	3.344	2.792	4.256	2.115	4.986	4.682	5.520	5.847	6.457

Figure 3-11- Histogram showing total pore volume derived from maximum pressure for the analysed samples.

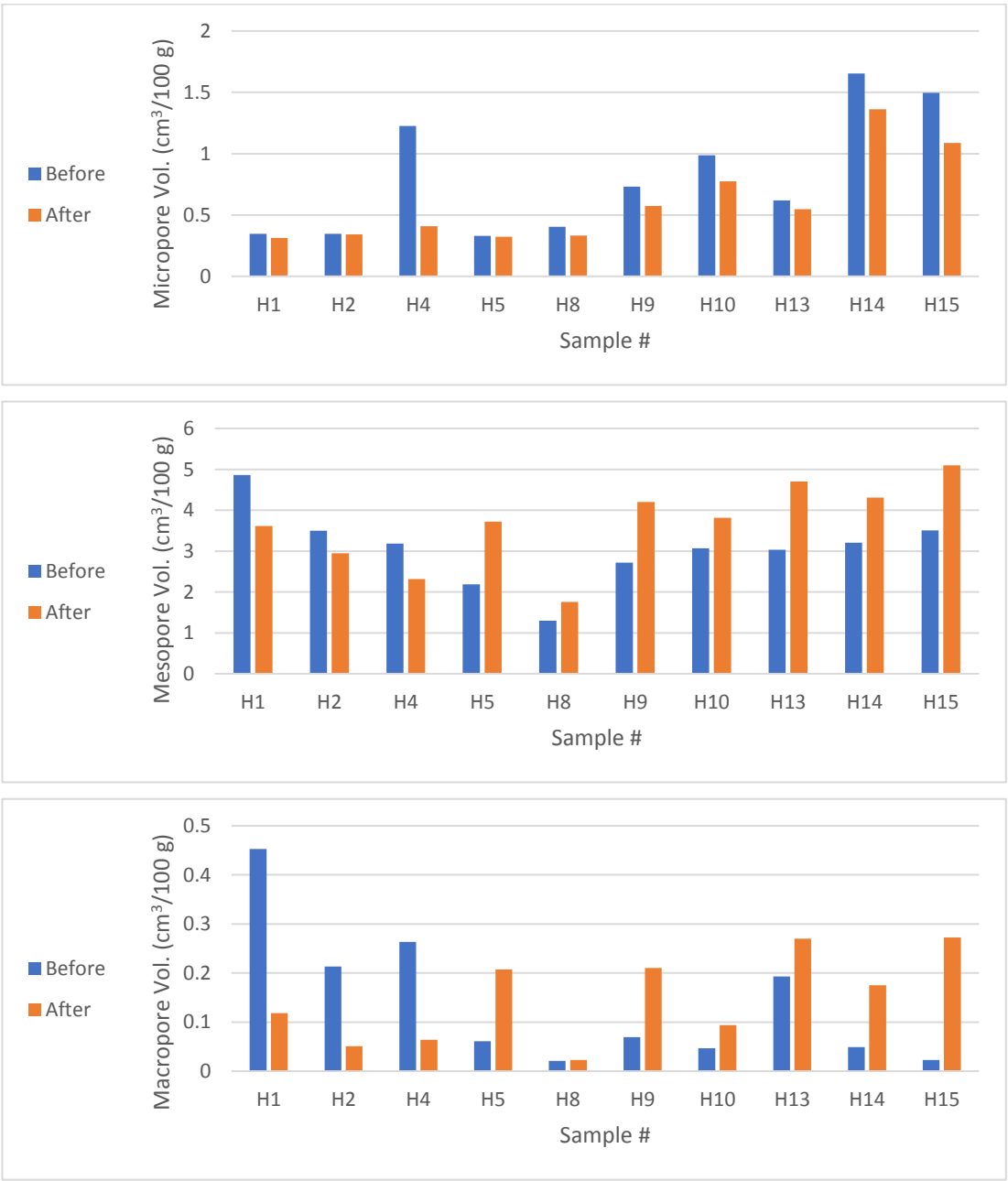

Figure 3-12. Variation of Micropores, Mesopores, and Macropores volumes in samples studied.

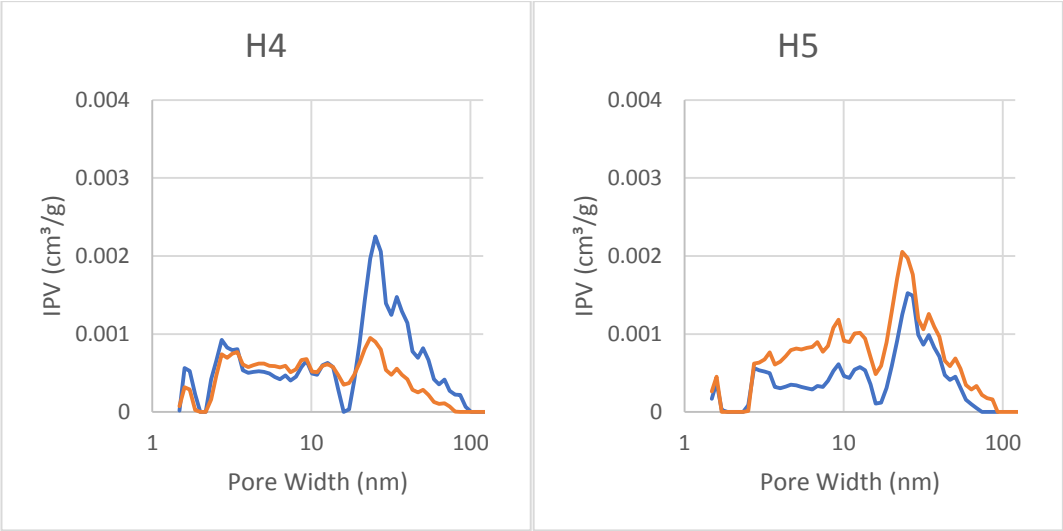

Figure 3-13. The pore size distribution of sample H4 representing the group of samples where the total pore area was reduced, and samples H5 representing the group of samples where the total pore area was enhanced.

Appendix V shows the pore volume and surface area distribution of the micropores, mesopores, and part of macropores. As can be seen for H8, and H10 there are no significant changes in the PSD after exposure to $scCO_2$ for pores larger than 20nm. Pore volume has slightly increased for pores smaller than 20nm of width in these two samples. Whereas for samples H5, H9, and H13 the PSD shows an increase in the pore volume in the whole pore size spectrum, but the general trend follows the PSD of the sample before exposure to CO_2. Samples H14 and H15 show a significant increase of pore volume in pore widths smaller than 20 nm which is followed by a pore volume decrease in pores larger than 20nm. Samples H1, H2, and H4 have a more complex increase/decrease trend. They show a large decrease in the pore volume of the larger pore size range (>18nm) after exposure to CO_2 which results in total pore volume decrease in these three samples (Figure 3-11). In pore sizes smaller than 18 nm, a mixed pattern is observed. Samples H1 and H2 show increase then decrease but sample H4 shows decrease then increase in pore volume in lower mesopore range.

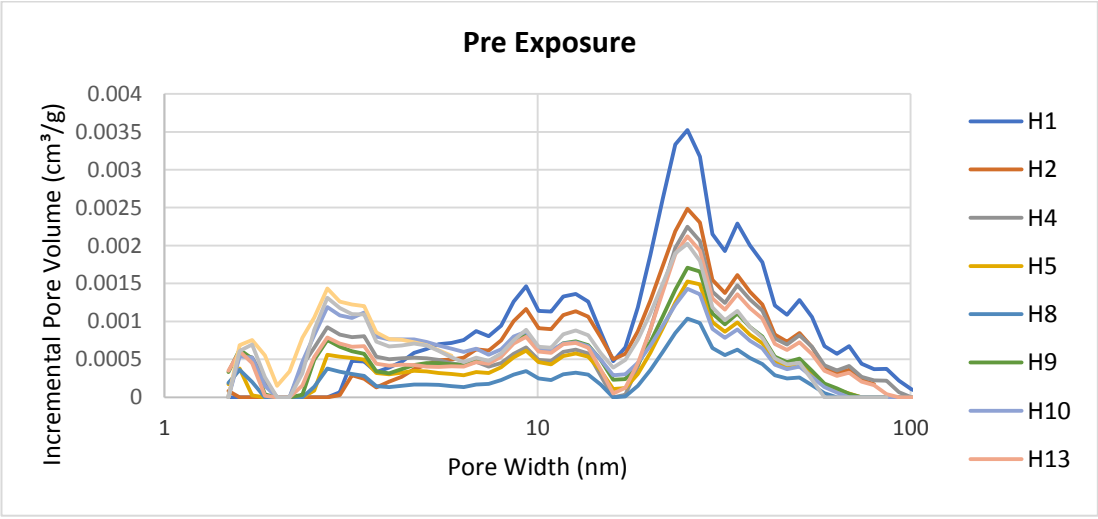

Figure 3-14- Pore size distribution for the sample analysed before exposure to $scCO_2$.

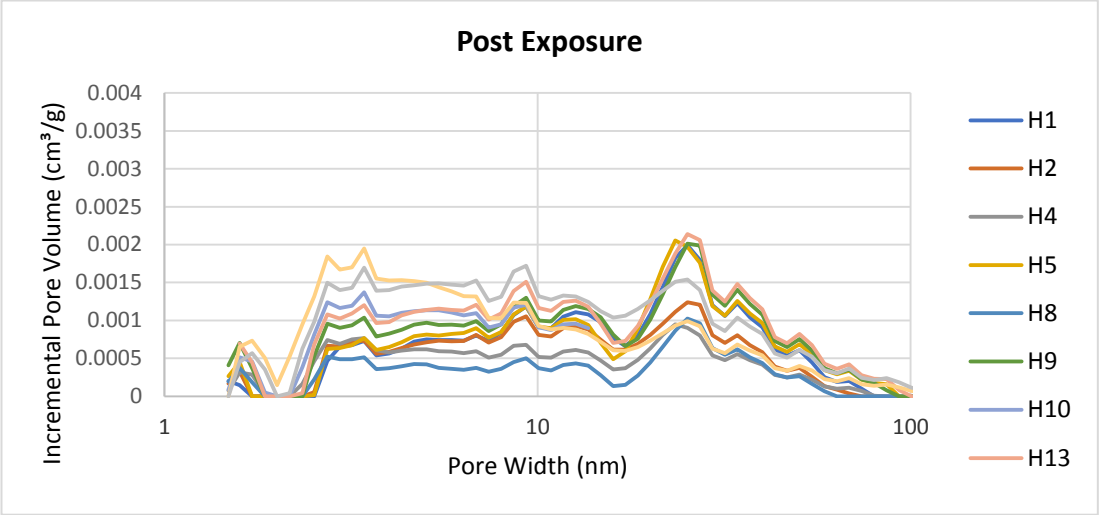

Figure 3-15- Pore size distribution for the sample analysed after exposure to $scCO_2$.

In summary, pore with 18-20 nm is the turning point for most of the samples. In the first three samples, the substantial decrease of pore volume above this turning point results in an overall pore volume reduction of samples. For the remaining samples (H5 to H15) total pore volume is increased, but the contribution of pore sizes above or below the turning point is different. Pore size below the turning point play the deciding role in samples H8, H10, H14, and H15, as the pore volume increase is this range is so large that either cover the reduction in larger pore sizes, or there is no PV reduction in the larger pore size range. On the other hand, in samples H5, H9, and H13 pore volume is increased in the whole 2-100nm range and no turning point is observed.

In general, the surface area is increased in most of the samples after exposure, especially in mesopore size ranges. As can be seen in Figure 3-16, BET surface area in samples H2, H5, H8, H9, H13 is slightly increased, and in samples H1, H4, H10, H14, and H15 is decreased after exposure. Among the samples, H8 has the lowest surface area, which is the most quartz-rich sample (57%). Samples H4, H10, H14, and H15 have a surface area in the range of 50-70 m^2/g and samples H1, H2, H5, H9, and H13 are in the range of 30-40 m^2/g range. The pore diameter was calculated using the volume to surface area ratio and shows the same trend as pore volume changes. The calculated average pore diameter follows the same decreasing/increasing trend of pore volume except for sample H4 after exposure to CO_2 (Figure 3-17).

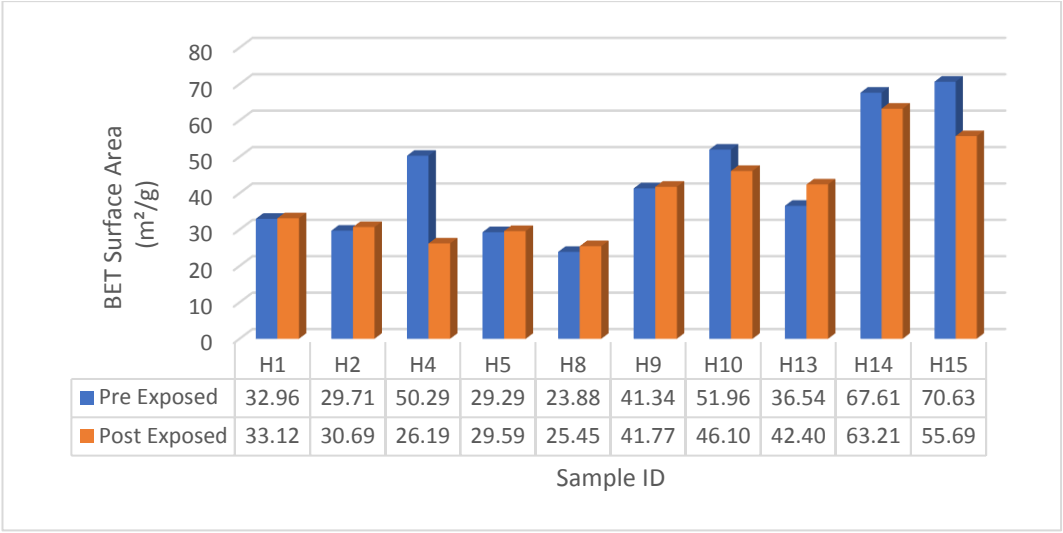

Figure 3-16- Histogram showing the measured BET surface area for the analysed samples.

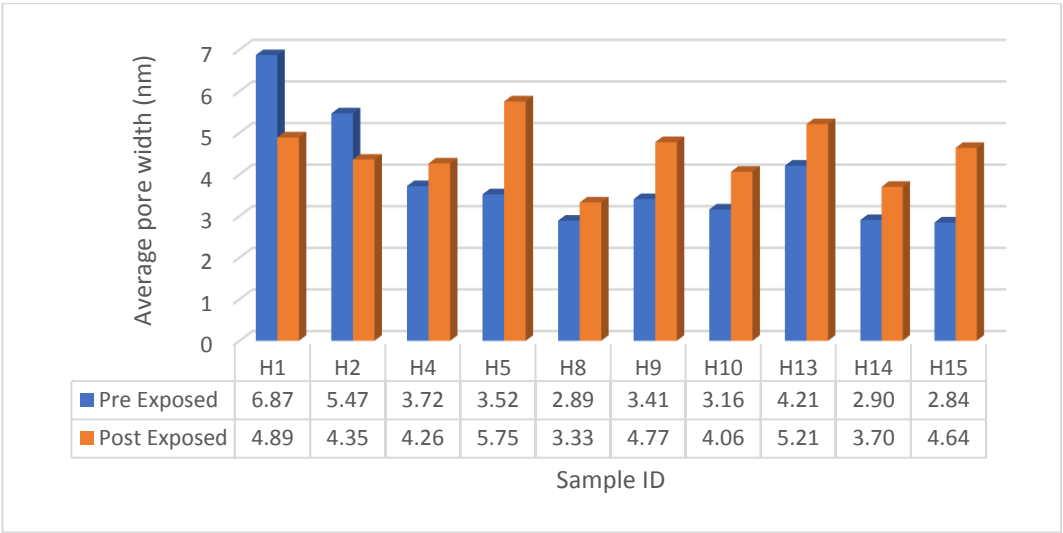

Figure 3-17- Histogram showing the average pore size of the analysed samples.

3.4.1 Control Samples

A total of eight control samples were selected for observation. Samples OH1, OH2, OH4, OH5, OH8, OH9, OH13, and OH15, were exposed to the same conditions in the absence of $scCO_2$. Control samples were in different from of powders, rock chips and small disks and mixed with the same brine composition were put inside the oven set to 60°C for nine months. Changes caused uniquely by CO_2 was recognised by comparison with observation samples. The summary of results for control samples is shown in Table 3-6. Figure 3-18, Figure 3-19, and Figure 3-20 compare changes in total pore volume, BET surface area, and average pore width between the exposed sample and control samples with pre-exposed samples. Different changes in petrophysical parameters of the samples are observed which are not in agreement with either original samples or exposed samples and some cases are even more dramatic. Figure 3-21 shows PSD for the observation samples.

Table 3-6- Summary of low-pressure nitrogen adsorption results for observation samples

Samples	BET surface area (m^2/g)	Average pore width (nm)	DFT model			
			Micropore Vol. ($cm^3/100\ g$)	Mesopore Vol. ($cm^3/100\ g$)	Macropore Vol. ($cm^3/100\ g$)	Total pore Vol. ($cm^3/100\ g$)
H1	16.36	6.620	0.137	2.426	0.145	2.707
H2	28.98	6.619	0.331	4.056	0.408	4.796
H4	42.30	2.960	0.583	2.538	0.009	3.130
H5	31.98	4.051	0.319	2.828	0.091	3.238
H8	17.10	3.971	0.225	1.430	0.043	1.698
H9	23.96	3.806	0.289	1.961	0.029	2.279
H13	40.13	4.668	0.405	4.205	0.073	4.683
H15	33.64	3.434	0.683	2.166	0.039	2.888

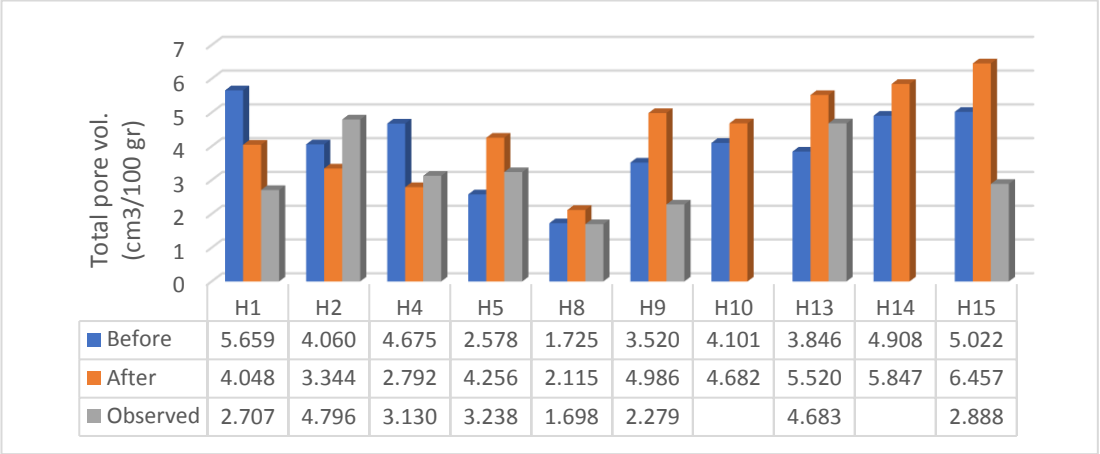

Figure 3-18- Histogram showing total pore volume derived from maximum pressure for the analysed samples.

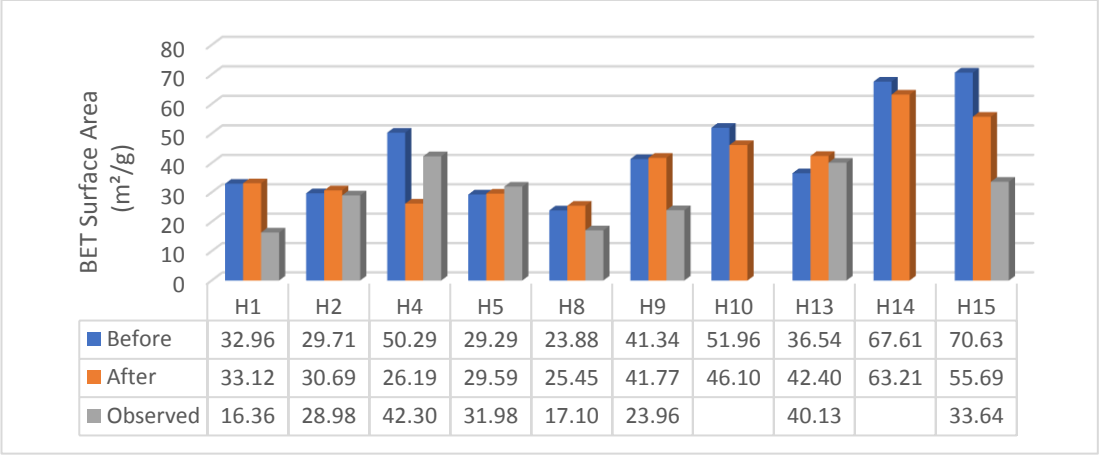

Figure 3-19- Histogram showing the measured BET surface area for the analysed samples.

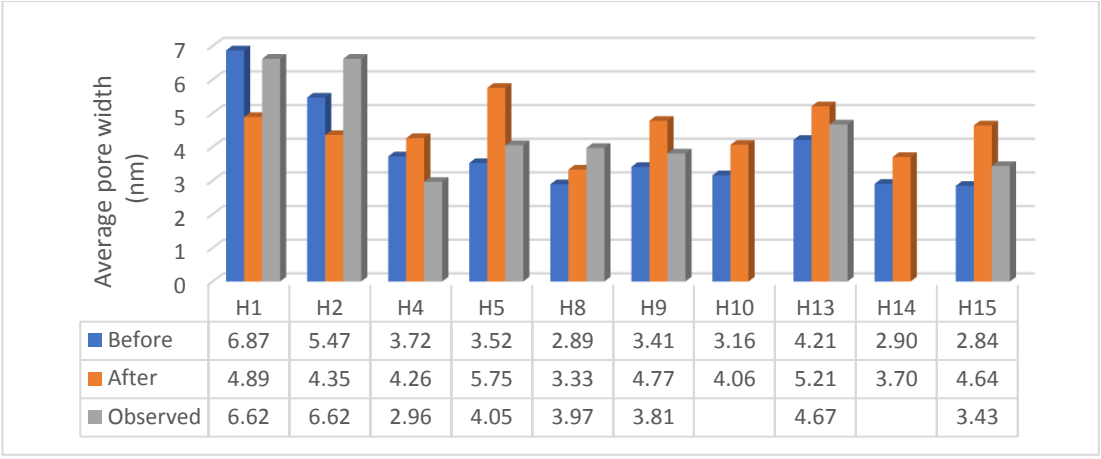

	H1	H2	H4	H5	H8	H9	H10	H13	H14	H15
Before	6.87	5.47	3.72	3.52	2.89	3.41	3.16	4.21	2.90	2.84
After	4.89	4.35	4.26	5.75	3.33	4.77	4.06	5.21	3.70	4.64
Observed	6.62	6.62	2.96	4.05	3.97	3.81		4.67		3.43

Figure 3-20- Histogram showing the average pore size of the analysed samples.

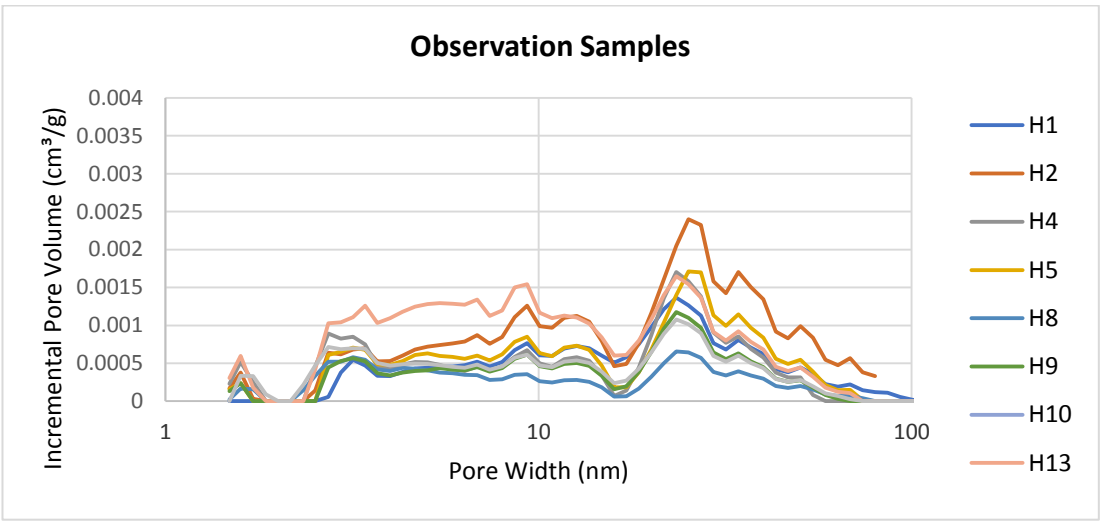

Figure 3-21- Pore size distribution for the control sample

3.5 MICP Results

Table 3-7 presents the results obtained from MICP measurements on five samples before and after exposure to $scCO_2$. Variation can be observed, comparing the petrophysical parameters in the tested samples. Porosity is increased in post-exposed samples H5, H9, and H13, and decreased in H1 and significantly decreased in H2. Pore areas in samples H1, H2 and H5 are decreased after exposure and increased in samples H9 and H13. Pore diameter in all the samples is enhanced after the exposure.

Table 3-7. Summary of results from the MICP test for samples before and after exposure to $scCO_2$.

Sample		Porosity (%)	Total pore area (m^2/g)	Peak diameter (nm)	Median pore diameter (volume) (nm)	Median pore diameter (area) (nm)	Average pore diameter (4V/A) (nm)	Threshold pressure (psi)
H1	Before	9.59	14.61	8.74	11.3	9.6	11.3	8349
	After	9.21	12.28	12.5	14.8	11.4	14.2	6708
H2	Before	10.65	18.53	12.5	13.4	9.6	12.7	6310
	After	4.59	4.17	15.1	21.4	11.9	20.4	1736
H5	Before	10.12	10.26	21.1	23.6	9.1	16.2	1897
	After	10.80	6.35	21.1	64.1	12.1	28.1	316
H9	Before	13.93	10.89	21.1	43.6	8.9	22	412
	After	16.32	17.2	18.1	63.5	9.4	24.1	392
H13	Before	14.09	13.6	21.1	30	9	17.9	1179
	After	19.14	18.32	18.1	31.4	9.2	19.6	1090

A porosity range of 9.59-14.09% for Before samples and 4.17-18.53% for After samples were recorded. Porosity was reduced for samples H1 and H2 from average 10.12% to 6.90% but was enhanced from average 12.72% to 15.42% in case of samples H5, H9, and H13. The general peak pore throat diameter of samples H1 and H2 show Before at 10.62nm and After at 13.80nm, smaller than samples H5, H9, and H13 which have values of 21.10nm and 19.10nm for before and after exposure samples respectively (Figure 3-23). The average peak diameter of 10.62nm was increased to 13.80nm after exposure for samples H1 and H2. However, the higher average peak diameter of 21.10nm for before exposure samples H5, H9, and H13 was decreased to 19.10nm after the exposure.

Capillary pressure curves (Figure 3-22) summarise the relationship between the pressure applied to the sample at different stages and the volume of intruded mercury, for each tested sample. Capillary pressure curves and pore size distribution of each sample, before and after exposure are presented in Appendix VII. Samples H1 and H2 have sigmoidal capillary pressure curves. Samples H5, H9, and H13 show distinctly bimodal pore-size distributions

All the samples exhibited 100% mercury saturation close to 60,000psi. The highest entry pressures are observed for samples H1 and H2, whereas H9 display the lowest ones. Samples H1 and H2 are likely to have the most uniform pore size distributions, due to the more abrupt increment at low normalised mercury saturation, without further visible changes to the rate of intrusion (Figure 3-22). Since most of the intrusion occurs at higher pressure, H1 and H2 are also presumed to have the largest proportion of narrow pore sizes. This is verified by pore size distribution curves in Figure 3-23. In contrast, the more stepwise intrusion observed in the H5, H9, and H13 curves (Figure 3-22) is indicative of significant compression beyond the

initial entry point, which is related to the presence of a wider and continuous range of pore sizes (also confirmed by MICP PSD in Appendix VII).

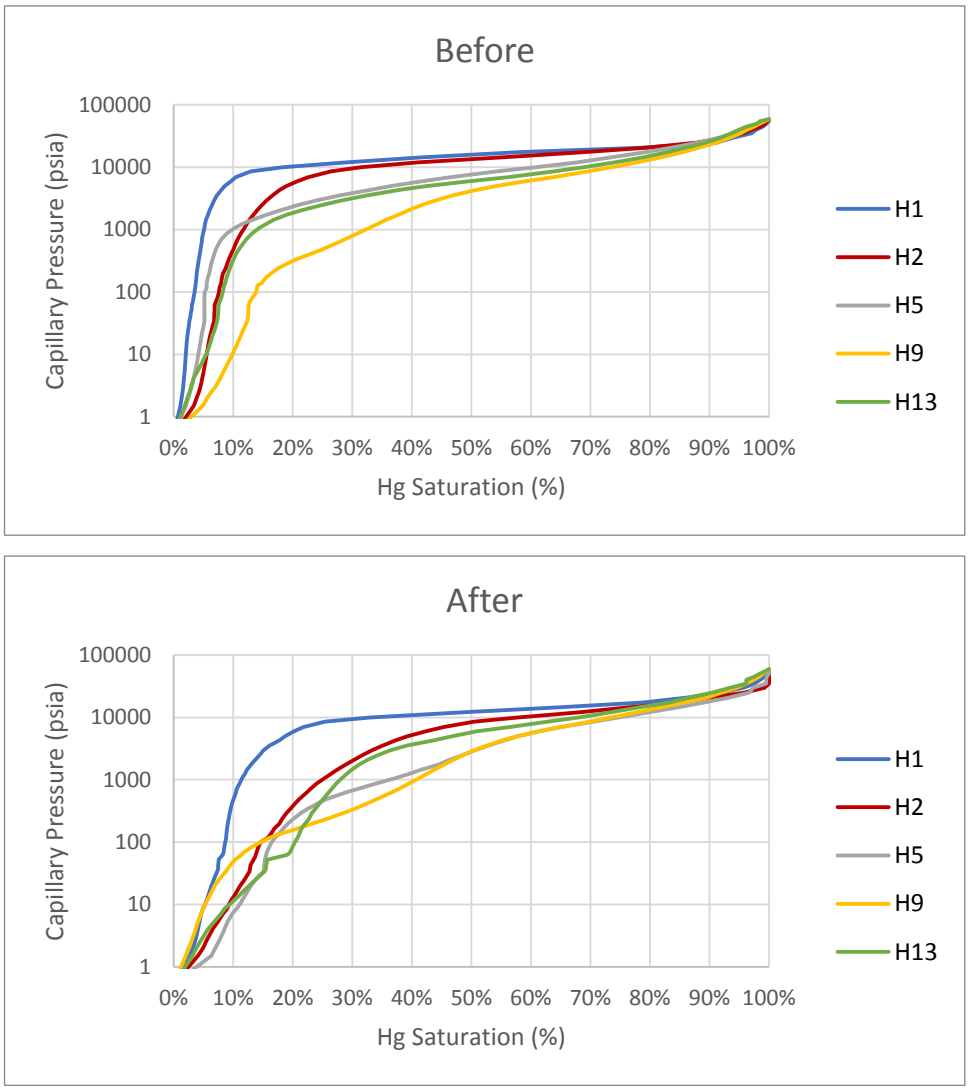

Figure 3-22. Capillary pressure vs. Hg saturation before and after exposure.

The pore size distribution of samples (Figure 3-23) demonstrate a dual trend. The first two samples exhibit narrow-distributed models with higher peak values. A major throat size in the range of 6-18nm is observed for samples H1 and H2; larger mesopores are very limited in term of volume. The other three samples (H5, H9, and H13) demonstrate lower peaks and a wider range of pore throats spreading in the mesopore and macropore range.

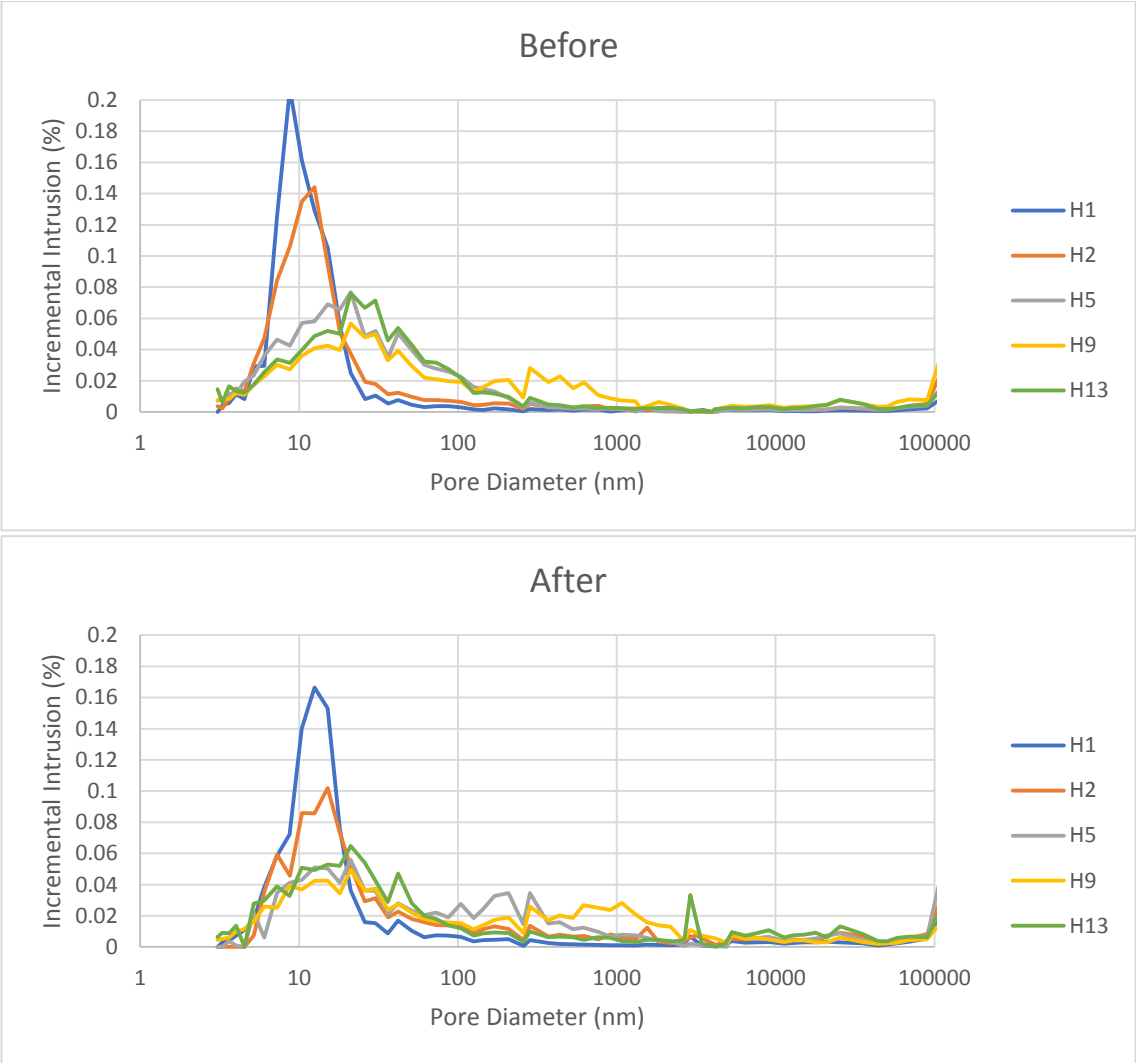

Figure 3-23. Incremental Intrusion vs Pore Size

In this work, the MICP threshold pressures for shale samples have been determined graphically, at the point of inflection in the cumulative curves upon which the first rapid increase is observed. The same trend as capillary pressure curves and pore size distribution is also observed in threshold pressure, where the two first samples have the highest and the other three samples have the lowest threshold pressure. However, after exposure to $scCO_2$, samples H2 and H5 show the greatest decrease in their $P_{Threshold}$ of 72% and 83%, where all the samples' threshold pressure is decreased. The height of the CO_2 column is calculated assuming a contact angle of 140° for air-mercury system and Hg surface tension of 485 dynes/cm (Dewhurst et al., 2002).

Table 3-8. Parameters used for the calculation of maximum CO_2 column heights retained by different shale intervals before and after exposure to $scCO_2$.

Sample	*Depth (m)*	*P pore (psi)*	*T (°C)*	*ρ_{CO_2} (g/cm³)*	*ρ_{brine} (g/cm³)*	*γ_b, CO_2 (mN/m)*	*$P_{Threshold}$ (psi) Before*	*$P_{Threshold}$ (psi) After*	*CO_2 column height (m), Before*	*CO_2 column height (m), After*
H1	1417.5	2055	64.6	0.494	0.990	28.06	8349	6708	1067.3	857.5
H2	1412.0	2047	64.5	0.493	0.990	28.07	6310	1736	805.4	221.6
H5	1187.6	1722	56.9	0.443	0.993	28.68	1897	316	223.3	37.2
H9	916.3	1329	47.7	0.326	0.996	30.94	412	392	43.0	40.9
H13	766.1	1111	42.6	0.229	0.998	34.01	1179	1090	117.7	108.8

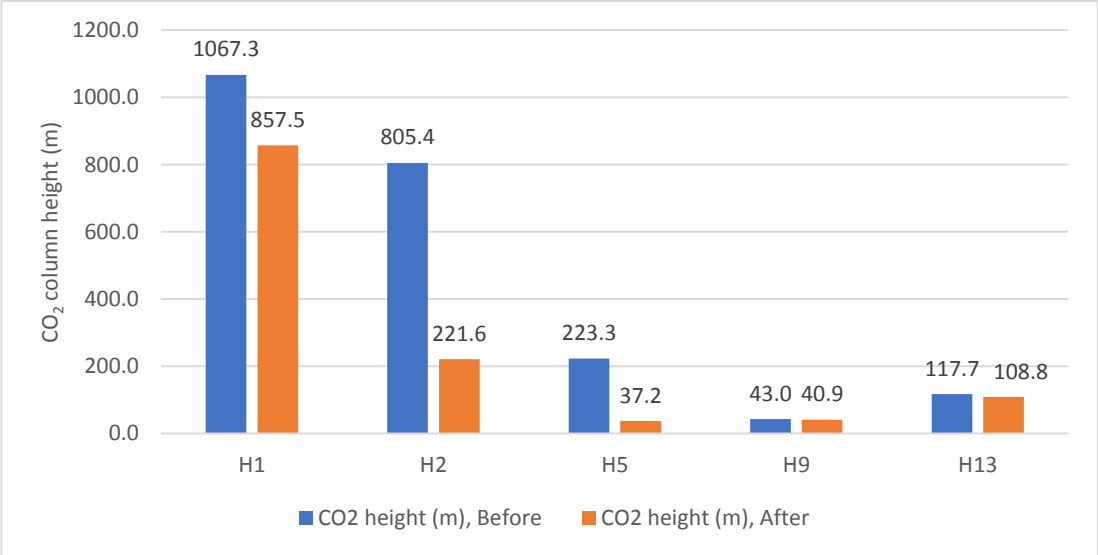

Figure 3-24. Bar chart showing CO_2 column height (m) for shale samples before and after exposure to $scCO_2$.

Chapter 4. Geochemical Modelling Results

The mineralogical analysis provides a record of the reaction results between $scCO_2$ and caprock minerals in laboratory timescale. Reaction path modelling was carried out for all fifteen samples from Harvey-3 well to provide a set of geochemical processes that can explain the observed changes in mineralogy as well to infer longer time reactions. The input parameters for geochemical reaction path modelling are XRD quantitative mineralogy, surface areas, porosity data, pressure, temperature, and formation water chemistry data. Two sets of simulations were performed: one using the water chemistry of the brine used in the experiments (NaCl brine) and another one using the formation water chemistry data from Harvey 3 Lesueur formation fluid sampling report (Rockwater, 2015) summarised in Table 2-3. Mineral modal amounts were taken from XRD diffraction analysis of samples (Figure 3-1 and Table 3-1). The reactive surface areas used for the modelling are reported in Table 4-1. Simulations were run at a specified temperature and pressure related to the depth of each sample using the Geochemist's Workbench React module. Brine/rock ratio of 1:1 was considered for modelling experimental conditions, whereas, for reservoir conditions, brine/rock ratio is calculated based on the porosity of the samples at around 1:12. Simulations were at fixed CO_2 partial pressure to simulate the CO_2 plume and caprock interaction.

In addition to the initial minerals identified by XRD as initial phases, several possible secondary minerals such as calcite, ankerite, magnesite, siderite, hematite, and dawsonite were added to the product list with their corresponding rates and surface area (Table 4-1). The precipitation of possible secondary minerals is represented using the same kinetic expression as that for dissolution. However, several aspects regarding precipitation are different from dissolution, including nucleation, crystal growth and Ostwald ripening processes, as well as the calculation of the reactive surface area (Xu et al., 2005). These processes for mineral precipitation are not considered in the current model.

4.1 Selecting the appropriate data

The thermodynamic data and kinetic rate of mineral phases data are required for the geochemical reaction path modelling, which are only available for well-defined *stoichiometric* minerals. The numerical codes developed for modelling the static systems such as GWB come with their thermodynamic database, which can be modified or extended to new phases, as long as required thermodynamic data are available, but kinetics data

should be supplied by the user. The calculation of reaction path is based on the kinetic rates determined by laboratory experiments under acidic and neutral conditions. These rates are usually reported at 25°C of temperature. The rate constants at the desired temperature are calculated from the Arrhenius equation based on activation energy and pre-exponential factor data reported in several sources. In this study, the temperature-dependent kinetic rate constants are calculated from the second form of the Arrhenius equation, using parameters E_A and K_{25} and surface are based on Pham et al. (2011), reported in Table 4-1. Different surface area values have been reported for minerals. The surface area of 50,000-700,000 cm^2/g is common for clays and soils (White et al., 1995).

Table 4-1- List of kinetic rate parameters used in the simulations.

Minerals	***Log(k), mole/m²s, 25°C, Acidic & Neutral***	***Log(k), mole/m²s, 60°C, Acidic & Neutral***	***Ea (KJ/mol)***	***A, mole/m²s***	***Surface area (cm²/g)***	***Reference***
Quartz	- -13.99	- -12.37	- 87.7	- 24	500	(Tester et al., 1994)
Chalcedony	- -12.31	- -11.11	- 65	- 1.20E-01	225	(Rimstidt et al., 1980) α-Cristobalite
K-feldspar	-10.06 -12.41	-9.11 -11.71	51.7 38	0.1 1.78E-06	1100	(Palandri et al., 2004)
Albite	-10.16 -12.56	-8.96 -11.27	65 69.8	1.52 0.19	1000	(Palandri et al., 2004)
Anorthite	-3.50 -9.12	-3.19 -8.79	16.6 17.8	2.57E-01 1.00E-06	1000	(Palandri et al., 2004)
Kaolinite	-11.31 -13.18	-10.10 -12.77	65.9 22.2	1.74E+00 5.13E-10	100,000	(Palandri et al., 2004
Muscovite	-11.85 -13.55	-11.45 -13.15	22 22	1.00E-08 2.00E-10	130,000	(Palandri et al., 2004)
Chlorite	-9.79 -13.00	-8.17 -11.38	88 88	4.27E+05 2.63E+02	16000	Lowson (2005)
Goethite	- -7.94	- -6.35	- 86.5	- 1.62E+07	500	(Palandri et al., 2004)
Calcite	-0.30 -5.81	-0.03 -5.38	14.5 23.5	1.66E+02 2.04E-02	500	(Palandri et al., 2004)
Magnesite	-6.38 -9.34	-6.38 -9.34	14.40 23.50	1.38E-04 6.03E-06	1270	(Palandri et al., 2004)
Siderite	-3.01 -8.90	-3.35 -7.74	20.92 62.76		1750	Steefel (2001) Gautelier et al. (1999)
Dawsonite	- -7.00	- -5.84	- 62.76	- 1.00E+04	98,000	(Palandri et al., 2004)
Ankerite						Set to siderite
Pyrite	-7.52 -4.55	-6.47 -3.50	56.9 56.9	2.82E+02 2.63E+05	510	(Palandri et al., 2004)
Hematite						Set to pyrite
Halite	- -0.21	- -0.07	- 7.4	- 12.30		(Palandri et al., 2004)

4.2 Equilibrium Modelling

As discussed in the Modelling Methodology section, it is reasonable to hypothesise that the formation brine is in chemical equilibrium with a certain number of minerals before CO_2 injection into the aquifer, at in-situ conditions of pressures and temperature. Upon CO_2 injection, this equilibrium is altered to an extent which depends on f_{CO2}. Because of this induced disequilibrium, the CO_2-containing aqueous solution will start to react with the primary minerals of the host rock (Luigi, 2007e). In this section, an equilibrated brine is calculated based on the measured brine/synthetic solution and minerals in equilibrium with the fluid. Then, a kinetic model is applied with the equilibrated solution, CO_2, and caprock minerals to investigate the composition of the fluid after one hundred years. Also, another set of simulations is applied using the initial pure NaCl brine without the equilibrium step.

Equilibrium modelling is performed in the first stage, as it provides the correct values or estimates the missing data in the analytical report. At a given temperature, formation minerals are equilibrated with species in the brine, and in-situ composition of formation water is estimated to be used in the next stage of the modelling. *Spec8* module of Geochemist's Workbench software package was used here to undertake the equilibrium modelling.

The calculated equilibrium brine composition of reservoir fluid at each sample temperature and pressure (Table 2-1) is shown in Figure 4-1. The reservoir fluid is close to the initial measured brine composition (Table 2-3). The relatively high concentration of Na+, K+, and Cl- is observed in reservoir fluid.

	H1	H2	H3	H4	H5	H6	H7	H8	H9	H10	H11	H12	H13	H14	H15
SiO2	17.9	17.9	17.9	17.9	17.8	17.8	17.8	17.7	17.7	17.7	17.7	17.7	17.7	17.6	17.6
Zn2+	1.75	1.75	1.75	1.75	1.74	1.74	1.74	1.73	1.73	1.73	1.73	1.73	1.73	1.73	1.73
Mn2+	9.84	9.84	9.86	9.86	9.79	9.79	9.76	9.74	9.73	9.73	9.72	9.72	9.7	9.7	9.7
Al3+	5.04	5.04	5.05	5.05	5.01	5.01	5	4.99	4.98	4.98	4.98	4.97	4.97	4.94	4.94
Fe2+	16.2	16.2	16.3	16.3	16.2	16.2	16.1	16.1	16.1	16.1	16	16	16	16	16
HCO3-	313	313	313	313	311	311	311	310	310	310	310	310	310	310	310
SO42-	1630	1630	1640	1640	1620	1620	1620	1620	1620	1610	1610	1610	1610	1610	1610
Cl-	29600	29600	29700	29700	29500	29500	29400	29300	29300	29300	29300	29200	29200	29200	29200
Mg2+	606	606	607	607	603	603	601	600	600	599	599	598	598	597	597
Ca2+	2230	2230	2240	2240	2220	2220	2210	2210	2210	2210	2210	2210	2200	2200	2200
K+	13400	13400	13400	13400	13300	13300	13300	13200	13200	13200	13200	13200	13200	13200	13200
Na+	11200	11200	11200	11200	11200	11200	11100	11100	11100	11100	11100	11100	11100	11100	11100

Figure 4-1. Equilibrated water composition in mg/kg relative to the depth of samples for reservoir conditions (SpecE8 results)

4.3 Kinetics Modelling

The second stage is the kinetics-based reaction path modelling. Mineral phases with their kinetics constrain and gas phases such as CO_2 are introduced to the aqueous system, at the temperature and pressure of interest. The potential reactions have then proceeded as a function of time under thermodynamic and kinetic conditions. *React* module of the Geochemist's Workbench software package was used here to undertake reaction path modelling.

There are two main components in a *React* model. The first component is the initial system, which was set to the equilibrated water chemistry (see section 4.2). The second component is the process that alters it, which is the reaction with minerals in the system and the CO_2.

After calculating the initial equilibrium state, *React* calculates each step of the reaction path by adding or removing reactants or varying the fugacity of gases in an external buffer.

It has been established in previous studies that carbonate dissolution buffers pH, and due to the dependence of most reaction rates to pH, a decrease in reaction rates is expected after the initial pH is buffered. The absence of carbonates in the initial mineralogy of studied samples eliminated this pH buffering step, so it is assumed that the reactions are progressed at their potentially fastest rates. The detection of carbonates as initial phases in the system is crucial for the study of systems targeted for CO_2 storage, as their quantitative analysis method might have limits of detection higher than their present value.

4.3.1 NaCl brine condition

Simulations using the known mass of minerals (Table 3-1) and 30,000 ppm NaCl brine was carried out at 60°C and 14.1 MPa of pressure. Models were run to simulate the experiment for up to 100 years. The models were run as static with CO_2 content buffered as the experiment was dynamic with CO_2 injected at a very low fixed rate. The reaction was traced using React module of GWB in which kinetic rate laws control the time rates at which reactions proceed. Note that we used muscovite as a proxy for the clay mineral illite.

The model setup is not reflecting the exact conditions of the experiment as the model can only assume water as the single fluid phase with dissolved CO_2 content set by equilibrium with the $scCO_2$ phase. The dissolution of $scCO_2$ into brine affects its chemical character and its interaction with the rock minerals. This modelling can not simulate the reactions between pure $scCO_2$ phase or important process of evaporation of water into the dry CO_2 phase. The results of the kinetic geochemical modelling performed for experimental conditions are given in Table 4-2, and Appendix VIII.A. Table 4-2 shows the total dissolution/ precipitation amounts after 100 years of simulation. Appendix VIII.A shows the reaction path traces for simulations. In all of the traces, the first reactions taking place at the highest rate is quartz precipitation and either kaolinite or muscovite dissolutions.

The dissolution of $scCO_2$ in the brine resulted in a decrease of the pH. Carbonates dissolution that follows the pH decrease is not observed here as the rock mineral assemblage lacked any carbonates (calcite or dolomite). Quartz is increased in all the samples modelled, and other minerals decreased. Both kaolinite and muscovite (clay minerals) showed a significant decrease across the samples. Feldspars (microcline, albite, and anorthite) are dissolved too in lesser amounts. In samples containing chlorite, goethite, or hematite, the dissolution rates are higher or almost immediate. The simulated net changes generally show an increase in

pore space as dissolution exceeds precipitation. The results of modelling the laboratory experiments did not predict any halite precipitation. Without the evaporation process being modelled, no halite, gypsum, or sylvite would form in the model. So the results of experiment and modelling are different when precipitation of minerals is because of desiccation.

Table 4-2. Summary of indicated mineral composition changes (cm^3 reacted) in the modelling under experimental conditions after 100 years. The change could be an increase (+), decrease (-), or uncertain/not significant change (o).

Sample/ mineral	***Quartz***	***Microcline***	***Albite***	***Anorthite***	***Kaolinite***	***Muscovite***	***Chlorite***	***Goethite***	***Hematite***	***Halite***
H1	87.5	-2.6	-0.47	0	-124	-60.7	0	-21.9	0	0
H2	71.9	-0.9	-0.43	0	-110.5	-43.1	0	-5.81	0	-18.51
H3	84.7	-5.7	-16	-7.5	-58.3	-84.1	0	-3.5	0	-0.9
H4	86.1	-5.8	-16.6	-8.1	-62.4	-81.6	0	-1.6	0	-0.3
H5	71.7	-4.7	0	0	-58.3	-61.1	-39.8	-0.5	0	0
H6	89.1	-2.4	-0.2	0	-86.3	-99.9	0	-1.6	0	-0.2
H7	77.8	-5.7	-12.5	-8.6	-34.1	-96.2	0	0	0	0
H8	44.1	-5.5	-0.1	0	-38.8	-47.3	-4.9	-0.1	0	-0.4
H9	79	-5.8	0	0	-72.8	-86.7	-1.7	-0.2	0	0
H10	87.7	-3.4	0	0	-80	-102.1	0	-0.2	0	-0.1
H11	96.6	-2	-0.8	0	-131.2	-73.1	0	-2.1	-5	-0.1
H12	70	-4.8	-0.7	0	-79.8	-62.7	0	0	0	-0.1
H13	54.5	-6.9	0	0	-30.5	-75.4	0	-7.4	0	-0.5
H14	71	-5.7	-0.6	0	-75.6	-67.6	0	0	-4	-0.2
H15	82.2	-4.9	-0.4	0	-83.7	-81.7	5.6	-5.8	0	0

The 1:1 brine/rock ratio contributed to more brine being available and facilitated the dissolution of minerals in acidic condition. The modelling results are consistent as modelling parameters such as the temperature (60°C), and brine composition is fixed for all the samples.

4.3.2 Reservoir condition

Geochemical reaction path modelling was conducted for each of the fifteen core samples. The simulations were run with the addition of CO_2. The models were set static with the initial CO_2 content at a fugacity of 90 bar, approximately equivalent to 130 bar pressure (Kirste, 2013). Simulations were run for 100 years total time. Simulations are to represent parts of the seal that are in contact with the $scCO_2$-saturated brine phase. The simulation gave an indication of how reactive the rocks are and their capacity to buffer the pH for the given conditions. The results of the kinetic geochemical modelling performed for reservoir conditions are given in Table 4-3 and Appendix VIII.B.

Table 4-3. Summary of indicated mineral composition changes (cm^3 reacted) in the modelling under reservoir condition after 100 years. The change could be an increase (+), decrease (-), or uncertain/not significant change (o).

	Quartz	***Microcline***	***Albite***	***Anorthite***	***Kaolinite***	***Muscovite***	***Chlorite***	***Calcite***	***Dolomite***	***Goethite***	***Hematite***	***Halite***	***Alunite***	***Gibbsite***	***Nontronit-K***	***Nontronite-Na***	***Nontronite-Mg***	***Magnesite***	***Dawsonite***	***Chalcedony***
H1	-0.9	-27.2	-5.65	0	-46	53.4	0	0	0	-332.3	235.4	0	2.5	0	34.53	0	0	0	0	-0.9
H2	-1.8	-9.1	-5	0	-20.3	16	0	0	0	-88.6	59.8	-13.1	2.8	0	25.6	0	0	0	0	-1.8
H3	-1.8	-55	-140.7	-83	-4.2	125.7	0	31.6	1.8	-53.2	0	-8	0	11.8	0	217.2	0	0	0	-1.8
H4	0.5	-47	-134.6	-89.85	45.3	115.4	0	34.13	1.8	-23.7	0	-2.3	0	0	0	96.7	0	0	0	0.5
H5	2.5	-27	0	0	136	78.2	-469.3	0	5.4	-8.4	0	0	0	0	0	0	34.4	300	13	2.5
H6	-0.6	-14.4	-1.7	0	-27.2	24.4	0	0	0	-23.7	12.1	-1.9	2.8	45.7	28.4	0	0	0	7.6	-0.6
H7	1.3	-26.5	-67	-95.1	13.7	74.7	0	24.7	0.07	-0.8	0	0	0	0	0	0	0	0	54.9	1.3
H8	1.8	-18.9	-0.6	0	-40	70	-54.2	0	5.6	-0.5	0	-0.8	0	0	0	0	1.9	27.4	0	1.8
H9	0.5	-24.2	0	0	-63	77.4	-19.3	0	5.9	-3	0	0	0	0	0	0	12.3	4	0	0.5
H10	-0.2	-17.4	0	0	-41.2	43.4		0	0	-2.4	-1.5	-0.5	2.8	0	18.34	0	0	0	0	0
H11	-0.2	-9.7	-2.4	0	37.2	37.8	0	0	0	-31.6	20.6	-0.5	2.8	0	13.4	0	0	0	0	0
H12	0.8	-15	-2.1	0	-33.3	31.1	0	0	0	0	0	-1	2.7	0	0	0	0	0	8.2	0.8
H13	-0.3	-29.3	0	0	-50.2	56	0	0	0	-112	76.1	-4.3	2.4	0	29.7	0	0	0	0	-0.3
H14	-0.2	-23.4	-1.4	0	-48	52.4	0	0	0	0	-4.5	-2	2.8	0	25.4	0	0	0	0	-0.2
H15	-0.1	-10.3	-0.5	0	-80.3	64	-31.9	0	0	-87.6	55.3	0	0	0	0	0	0	0.1	33.3	0

The path that reactions follow, needs to be assessed on a case by case basis as it depends on the thermodynamic properties and mineral and brine compositions. Numerical models are composed here to compare with observations from the experimental methods. The best practice is to select the same conditions as of the experiments as much as possible and is

within the software capabilities to achieve similar results and extend the reaction paths to the longer intervals

Differences in the initial formation water chemistry and temperature contribute to some of the variability in dissolution/ precipitation amounts. Reaction rates are temperature dependent; thus, the higher rate is expected at higher temperatures. The reaction traces can be grouped according to the minerals precipitating and dissolving into different classifications.

Nontronite is the iron (III) rich member of the smectite group of clay minerals. Different types are nontronite-Na [$Na_{0.3}Fe^{3+}_2(Si,Al)_4O_{10}(OH)_2 \cdot nH_2O$], nontronite-K [$K_{0.3}Fe^{3+}_2(Si, Al)_4O_{10}(OH)_2 \cdot nH_2O$], nontronite-Ca [$Ca_{0.165}Fe^{3+}_2(Si,Al)_4O_{10}(OH)_2 \cdot nH_2O$], and nontronite-Mg [$Mg_{0.165}Fe^{3+}_2(Si, Al)_4O_{10}(OH)_2 \cdot nH_2O$].

In samples bearing clinochlore (i.e. chlorite), chlorite is dissolved, and the released magnesium combined with dissolved CO_2 to form magnesite. In some cases (H9) when the reaction path did not include secondary magnesite, Mg-nontronite was formed. The rapid release of Si from dissolving chlorite, feldspars, and kaolinite also results in that solution becomes supersaturated with smectite (nontronite-k or nontronite-k). Albite in the absence of dawsonite, broke down to form Na-nontronite in Na-rich minerals. In simulations of samples H5, H6, H7, H13, and H14 dawsonite was introduced as a secondary mineral. Equation 1-13 shows the possible reaction of albite to produce dawsonite. In samples H13 and H14, reaction paths with and without dawsonite as a secondary mineral was tested. In reaction path where dawsonite was produced, muscovite and kaolinite reactions were reversed from precipitation and dissolution respectively to dissolution and precipitation.

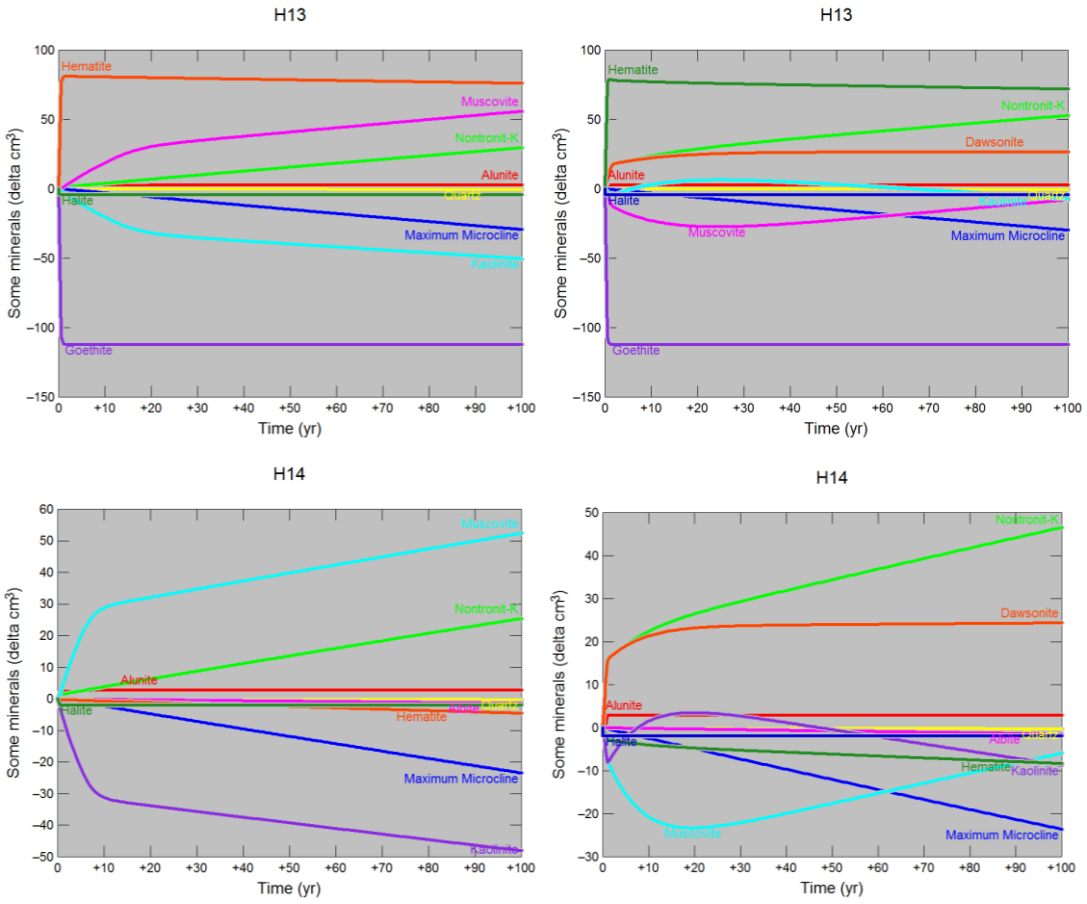

Figure 4-2. Comparing reaction path in the absence of dawsonite (left) to a reaction path in the presence of dawsonite as a secondary mineral in samples H13 and H14.

As described in geochemical modelling of Gunter et al. (1993), dissolution of anorthite was followed by the precipitation of calcite and kaolinite in H3, H4, and H7 (Figure 4-3). Equation 1-12 shows the release of Ca^{2+} by anorthite dissolution for the formation of calcite. Due to the fact that samples studied here were rich in K-feldspar and most of them lacked Ca-feldspar, a potential source for Ca was not available to form the calcite and kaolinite assemblage.

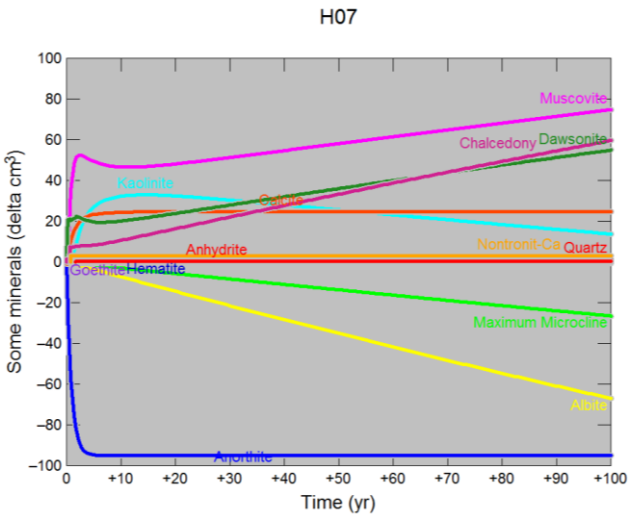

Figure 4-3. Reaction path of sample H7 rich in anorthite which resulted in calcite and kaolinite precipitation.

Chapter 5. Discussions and conclusions

As discussed in previous chapters, ten samples out of fifteen original samples were chosen to be used in this research. These ten samples were analysed with XRD and LPNA methods in powder form. Only five plugs were recovered for NMR measurement. The same samples were also analysed with MICP and SEM methods. The overall experimental procedure started with testing the samples in their original state, then expose them to $scCO_2$, and finally test them again after the exposure phase. Some samples were also tested midway through the exposure phase. In this study, several methodologies for assessing CO_2-rock interactions are discussed and applied.

The primary goal of this chapter is to present a detailed discussion and interpretation of the experimental and modelling results presented in Chapter 1 and Chapter 4. The contents of this chapter are categorised into mineralogical changes and petrophysical changes. Since the obtained results depend on the specific properties of the samples and measurements' methodology and limitations, the discussions are further divided and presented into the sample group and method. Depending on the response of the sample to the exposure, the results are discussed and compared with equivalent simulation results as well.

As discussed in Chapter 1, mitigation of climate change by $scCO_2$ storage into the subsurface initiates the CO_2-water-rock interactions in geologic storage strata that in time reduces the pH, which in turn, is expected to be buffered by reactions with silicate/oxide/carbonate phases. Increasing the pH with time due to this buffering effect may result in carbonate or other phases re-precipitating in the pore system (Busch et al., 2008; Wollenweber et al., 2010). Alumino-silicate minerals such as feldspars and clays are still attacked by acids under this elevated pH (Gaus, 2010). The petrophysical properties of the rock are expected to be altered as a result of such reactions. Changes of mineralogical composition and caprock's sealing properties have been reported in several experimental studies on mineral transformations in CO_2 geosequestration (Bertier et al., 2006; Kaszuba et al., 2003, 2005; Kharaka et al., 2006; Liu et al., 2012; Lu et al., 2012; Pearce et al., 2016; Rosenbauer et al., 2005; Wigand et al., 2008). Credoz et al. (2009) suggested that potential pathways for CO_2 leakage through the caprock could be induced as the result of geochemical alteration occurring along with the reservoir-caprock interface with CO_2-brine mixture. However, Busch et al. (2008) suggested that the depth of influence of such reactions is only limited to the lower part of the caprock in the vicinity of CO_2 plume.

A pre-existing weakness in the seal coupled with interaction associated with the flow regime is of crucial importance. Both buoyant supercritical CO_2 and dissolved CO_2 depending on geology and heterogeneity of seal and the defined dissolution rate can alter the caprock in long-term (thousands of years after injection (Gaus, 2010). Although these conditions are important in predicting the long-term caprock behaviour, the long-term leakage risk is in its most simplified way is associated with three leakage pathways in wells, faults, and through the caprock when the pressure exceeds the capillary entry pressure for scCO_2 (Kreft et al., 2007). Gaus (2010) suggested that it is extremely unlikely for chemical reactions to trigger leakage pathways in the absence of a flow regime to generate significant dissolution reactions.

Assessing CO_2-rock interaction is an important part of seal integrity studies, as these potentially affect physical properties through highly coupled processes. The driving process of CO_2-rock interaction includes dissolution of CO_2 in brines, acid-induced reactions, reactions due to brine concentration, clay desiccation, pure CO_2-rock interactions and reactions induced by other gasses than CO_2 (Gaus, 2010). Observed changes in the petrophysical properties of the after-exposure samples are generally attributed to the three mechanisms of mineral dissolution, mineral precipitation and physical compaction (Izgec et al., 2008). Fines migration of susceptible minerals such as kaolinite is another important mechanism which can alter the properties of rock samples. Migration of clay fines generated and released by mineral dissolution was believed to have occurred in the exposure experiment conducted in this work. The occurrence and the extent of the effects of these mechanisms on a sample depend on the exact mineral composition, presence of core-scale heterogeneities and the original textural features of the sample and therefore, may vary from one sample to the other. Much of the discussions presented in the upcoming sections of this chapter are to determine how CO_2 induced dissolution and precipitation reactions affect the pore space evolution and thus the physical properties of after-exposure samples as revealed by the complementary measurements conduced.

Laboratory experiments of rock samples with CO_2 and brine are frequently applied as a strategy for studying the potential geochemical reactions. Most of the published experiments have been conducted for less than three months and at very high temperatures to increase the chemical reaction rates (De Silva et al., 2015). Some drawbacks of such batch experiments cannot be fully resolved, including short laboratory time scales and the increase of reactive surface area and reaction temperature, variation in brine/rock ration and the potential formation of experimental artefacts during reactor depressurisation and cooling (Szabó et

al., 2016). However, mineral trapping is a long-term process, and short time-scale experiments are less accurate in predicting field conditions. Therefore, there is a necessity for experiments conducted over long-term time-scales at low temperatures to represent actual reservoir conditions (De Silva et al., 2015). The performance of reference experiments in CO_2-free brine is essential for the interpretation of results. The experiments need to be further supported with coupled geochemical modelling. Several experimental- modelling caprock studies are available (Alemu et al., 2011; Liu et al., 2012) and their conditions and results are summarised in Appendix I.

The main aim of this work was to estimate the directions of geochemical reaction and petrophysical alteration as a result of dissolution/ precipitation mechanisms in potential shaly caprock in Southwest hub, Western Australia under in-situ conditions. Short laboratory time scales of batch experiments are one drawback, which is why we tried to expand the reaction time to the maximum possible of nine months as opposed to several weeks to several months in previously published studies (Appendix I.A). Elevated temperature is one other drawback which we avoided by selecting the in-situ temperature of 60°C. Samples were in different form according to the requirement of each method. Core plugs, disks, rock fragments, and powdered samples were used in the reactor to avoid unnecessary changes to the surface area.

5.1 The effect on mineralogy

The XRD analysis of the original caprock samples showed that samples H8 and H13 are quartz-rich, samples H1, H9, H10, and H15 are clay-rich (total clay>60%), and samples H2, H4, H5, H13, and H14 have more clay content than quartz. The siliceous samples investigated in the current study are marked by a strong component of clay minerals, with up to 75% kaolinite and illite. Samples are rich in both kaolinite (average: 26% and maximum 43%) and illite (average: 29% and maximum 42%). Quartz content is 33% on average, with a maximum of 59%. The dominant feldspar in samples is microcline (average 7% and maximum 10%). Samples H14 and H15 originated from the Eneabba Formation, and samples H1- H13 originated from the same formation (Yalgroup Member of Lesueur Formation), but different localities. The different mineralogical composition of the samples leads to different reaction responses to the CO_2-brine and brine systems. The results of experiments and kinetic modelling only partially confirm each other, and reason for the different responses are discussed below.

SEM images of samples have been produced to be compared with after exposure images to examine precipitation of any mineral phases. XRD analysis of samples has been carried out to measure the exact weight percentage of each mineral phase. The results were compared to after exposure results to monitor any changes in the amount of mineral phases. X-ray diffraction (XRD) and scanning electron microscopy (SEM) results showed several changes in mineralogy because of rock-brine-CO_2 reactions. Quartz, kaolinite, and goethite were dissolved in most samples and muscovite and halite were precipitated in general. Feldspars showed mixed behaviour across the samples.

Previous experimental work (Kaszuba et al., 2003) showed some reactions occurring on a measurable time scale only at high temperatures of 200°C. Other works (Rosenbauer et al., 2005) noted only a limited reaction of CO_2 with pure mineral phases (anorthite and glauconite) at 50°C and 150°C and low pressure. Changes in caprock fluid transport properties may happen regardless of the extent and scale of the mineralogical composition alteration. Wollenweber et al. (2010) reported carbonate dissolution and re-precipitation, leading to alteration of shaly caprock transport parameters. In this case, no detectable mineral alterations were observed. The loss of quartz (Rathnaweera, Ranjith, & Perera, 2016), feldspars (Liu et al., 2012), kaolinite (Credoz et al., 2009), and chlorite (Armitage et al., 2013) has been reported in other studies resulting in an increase in porosity and opening up pore throats, leading to an increase in permeability.

The primary mineral composition is a major factor in determining the results of reactions. Geochemical simulations by Kaszuba et al. (2005) reported the formation of dawsonite and ankerite as the major CO_2 trapping minerals. However, dawsonite rarely occurs in experimental results or natural cases as argued in Kaszuba et al. (2011). Precipitation of siderite and ankerite requires Fe^{2+} released by dissolution of chlorite and hematite. Precipitation of dawsonite requires Na^{+} supplied by the dissolution of oligoclase. In this study, samples H3, H4, and H7 were oligoclase rich (average 11% albite and 2% anorthite). Based on simulation under the reservoir condition, in H3 and H4, Na from the dissolution of albite has formed nontronite-Na (Table 4-3). In this two samples simulation including the secondary dawsonite did not converge. However, in the case of sample H7 with the inclusion of dawsonite as a secondary phase, Na from albite is gathered in dawsonite. In the case of samples H5, H6, H12, H13, and H14, dawsonite is also formed from a small amount of Na in the samples or brine. The simulation results also indicate that Mg from chlorite dissolution in samples H5, H8, and H9 has formed magnesite.

The experimental data provide constraints on the geochemical behaviour of reservoir and cap rocks and provide a basis for refining geochemical modelling efforts. The experiment has shown that the rock-forming minerals reacted in response to $scCO_2$ injected into the system (Wigand et al., 2008). However, the observations and modelling revealed several unexpected features of the reaction process which are explained in the following sections. Geochemical changes in experimental method and simulations under the reservoir and experimental conditions are compared with the initial state and to each other. The changes in XRD mineral content of samples are summarised in Figure 3-4 and Figure 5-2. The indicated directions of change for modelling the reservoir and experiment conditions are summarised in Table 4-2 and Table 4-3.

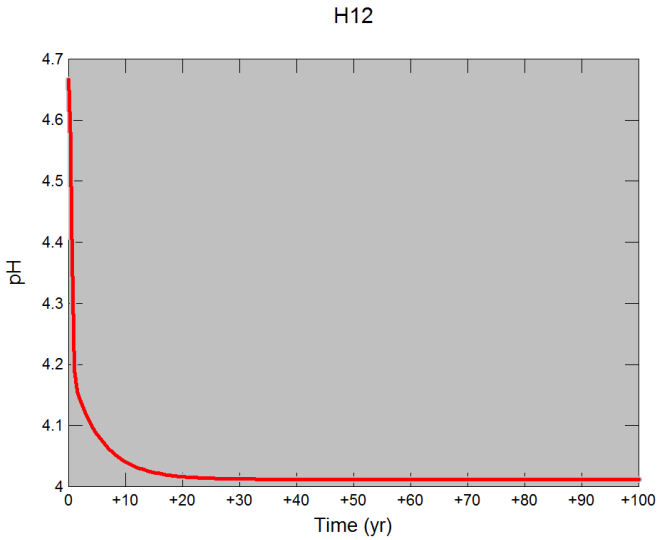

Figure 5-1. Changes in the pH of samples H12

Several studies have recognised the generation of carbonic acid and higher pH values as the main reason for the dissolution of minerals which leads to the release of chemical species forming secondary minerals (Bertier et al., 2006; Busch et al., 2008; Ketzer et al., 2009; Lahann et al., 2013; Wigand et al., 2008; Wollenweber et al., 2010). Here a pH drop from seven to around four is reported, which is due to acidification caused by CO_2 dissolution in the water phase (Figure 5-1). In the absence of calcite, reactive minerals such as feldspars, kaolinite and chlorite start to dissolve. Dissolution of these minerals releases Si, Al, Na, K, Fe, and Ca, which can form new compounds. The dissolution of feldspars and kaolinite results in the formation of muscovite/illite. The simulation of reaction under reservoir condition indicated dissolution of feldspars (microcline, albite, and anorthite), kaolinite, chlorite, and goethite. In general. Si, Al, K, Na, Ca, Mg, and Fe released from these minerals accumulated in different phases. Goethite dissolution which released Fe is associated with hematite precipitation. Magnesium released from chlorite dissolution with dissolved CO_2 contributed

to magnesite or Mg-nontronite formation. Albite dissolution is associated with dawsonite or Na-nontronite precipitation. Anorthite dissolution is associated with calcite precipitation and microcline dissolution is associated with muscovite and K-nontronite formation.

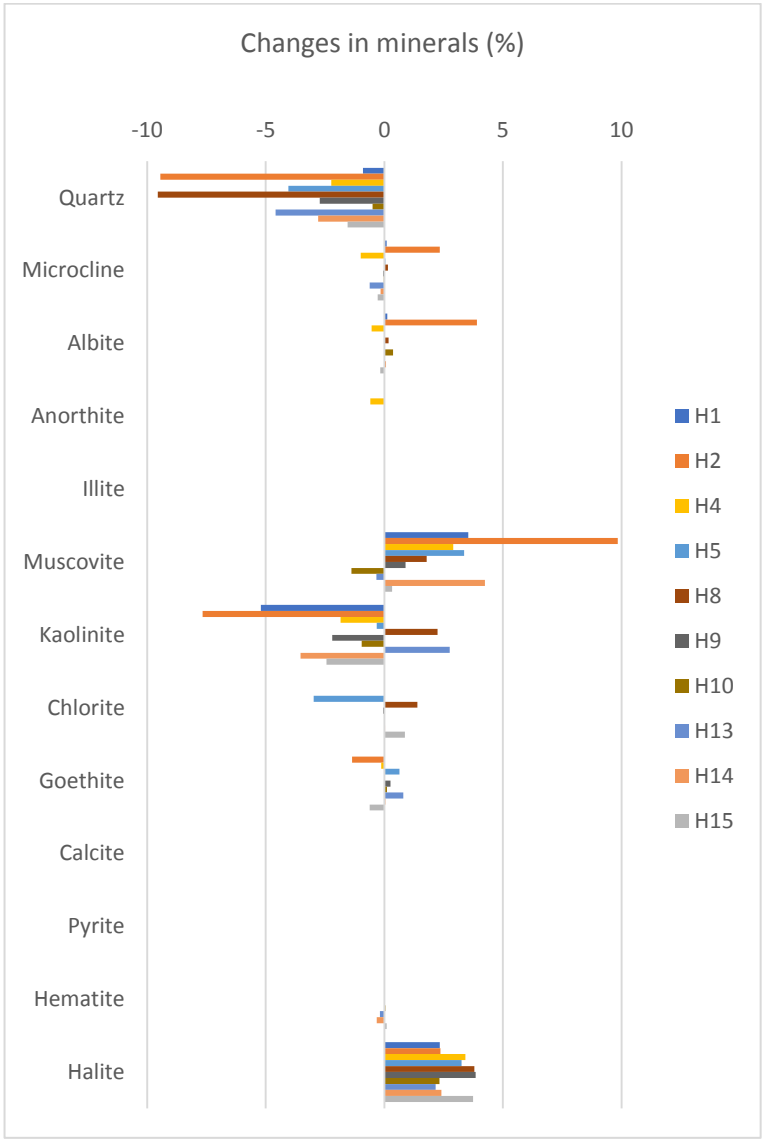

Figure 5-2 Changes in mineral content after exposure in percentage.

The decrease in the quartz content of the samples, observed in experiments, is attributed to the dissolution of quartz itself. Rathnaweera, Ranjith, and Perera (2016) reported a significant quartz dissolution under 40°C after 1.5-year interaction with $scCO_2$ and suggested that over a short period and under low temperature, quartz dissolution is too minor to be observed. Szabó et al. (2016) also reported a moderate dissolution of quartz, however in durations ranging 28-57 days. Kaszuba et al. (2003) also observed dissolution of quartz along with oligoclase and biotite dissolution during their batch experiment at elevated temperature and pressure (2000°C and 200 bars) (Appendix I.A). On other hand, an increase

in quartz content has also been reported (Yin et al., 2016). In such a case, the additional quartz is the product of other minerals dissolution such as feldspars and clay minerals. In an experiment with two types of shale caprocks, Alemu et al. (2011) reported no major mineralogical alteration in case of clay-rich shale, wherein the case of carbonate-rich shale, plagioclase and clay minerals where dissolved, carbonates dissolved and re-precipitated, and smectite was formed (Appendix I.A). Credoz et al. (2009) used purified clay minerals to evaluate clay minerals reactivity and find kaolinite to be the most reactive clay minerals in the long-term experiments.

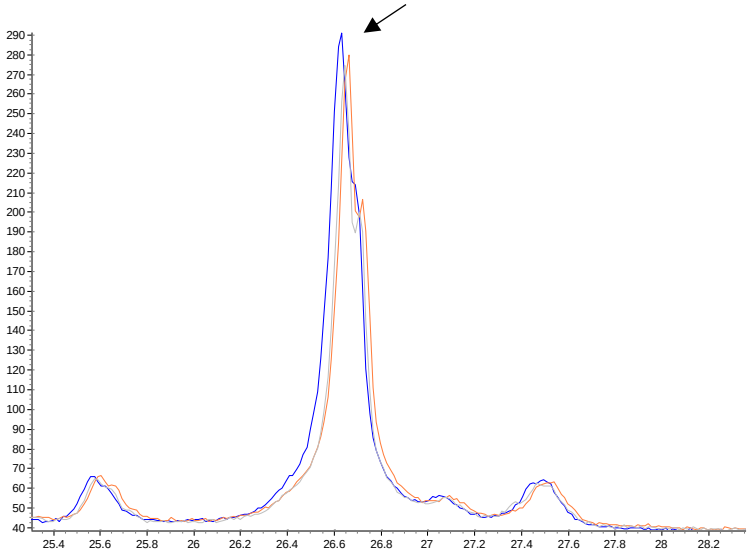

Figure 5-3. Quartz peak in XRD diffractogram, showing a reduction after exposure. The blue curve is before, orange is after four months, and grey is after nine months exposure to CO_2.

The formation of kaolinite from K-feldspar or albite was not observed in contrast to the models of Gunter et al. (2000), Gaus et al. (2005) and Lagneau et al. (2005), as well as the present geochemical modelling. In this study, both k-feldspar and kaolinite were reduced, and muscovite is increased in most samples. The kaolinite and muscovite trend are almost opposite in each sample.

Carbonates precipitation, such as precipitation of dawsonite, siderite, calcite, dolomite, and magnesite, has been reported in several studies (Gunter et al., 2000; Moore et al., 2005). However, carbonate formation was not observed during this study. Since the shale sample used in this experimental study did not contain any carbonates and a very limited amount (2%) of Ca-feldspar in just one of the samples, a potential source for Ca was not available to form calcite and kaolinite assemblage. Also, low cation concentrations with acidic pH were observed, which showed that dissolution prevailed over carbonate precipitation (Wigand et al., 2008).

The formation of halite was interpreted as an experimental artefact. NaCl precipitated from Na and Cl coming from the solution since the solid was not rinsed with deionised water before analysis (Credoz et al., 2009).

5.2 The effect on petrophysical properties

Low-pressure nitrogen adsorption method shows a slight increase in porosity observed in seven out of ten samples (Figure 3-11), except for samples H1, H2, and H4. Samples recorded a pore volume range of 1.7-5.7 cm^3/g before exposure, which is changed to 2.1-6.4 cm^3/g after exposure to CO_2. There is an average 1.17 cm^3/g increase in the pore volume of ten samples and an average 1.4 cm^3/g decrease in the pore volume of three other samples tested.

Porosities are also estimated with MICP and NMR method for five samples. Samples H1 and H2 recorded a reduction in their porosity in both these methods and samples H5, H9, and H13 show an enhancement in their porosities. MICP porosities range is 9.6-16.3% for pre-exposure samples and 4.6-19.1% for after-exposure samples (Table 3-7). There is an average 2.7% increase in MICP porosity of three samples and an average 3.2% decrease in MICP porosity of two other samples tested.

NMR porosities are measured in both dry and saturated states. Dry samples before exposure (as received) had porosities in range of 6.35-9.67% and range of 9.67-19.38% after four months of treatment and 10.36-19.08% after nine months of CO_2 treatment. NMR porosities in saturated states are generally higher than dry states, and their ranges for before, after four months, and after nine months CO_2 exposure is 14.90-24.55%, 12.12-26.93%, and 13.20-26.79% respectively (Figure 3-8). While NMR porosity of samples in the dry state increased across the sample about 7.7%, NMR porosity of saturated samples increased an average 3% in three samples and decreased an average 1.7% in two other samples tested.

The received samples have systematic monomodal distribution, with a relaxation time (T_2) centred around 0.3-0.7 ms (Appendix V.A). After saturation, the previous population showed a shift toward longer T_2, centred between 9-1.6 ms, with the exception of samples H1 and H2 which stayed between 0.33-0.46 ms. This first population is defined as the short relation time. A second population defined as long relaxation time was also recorded for the samples at around 13.5 ms. This second population is more likely the effect of the macropores filled by brine during the saturation process. Saturated samples show porosity values significantly higher than partially saturated samples.

The average pore width results of LPNA method show an increase in most samples (H5, H8, H9, H10, H13, H14, and H15 and a decrease in three samples of H1, H2, and H4 (Figure 3-17). The average pore width range according to this method is 2.9-6.9 nm for pre-exposure samples, which is changed to 3.3-5.8 nm after exposure. However, the MICP average pore width is increased across all samples. Average pore diameter range of before-exposure samples is 11.3-22nm, and after-exposure samples range is 12.7-28.1nm (Table 3-7).

The leaching of mineral constituents of the shale is the main reason for porosity increase. Mineral dissolution and precipitation can induce changes in porosity and permeability. This relationship is essential and is considered in our model. Changes in porosity during the simulation are calculated from changes in mineral volume fractions. The results of modelling indicate an increase in porosity in the samples (Figure 5-4). The significant increase of porosity observed in most experimental samples would potentially deteriorate the sealing capacity of the caprock.

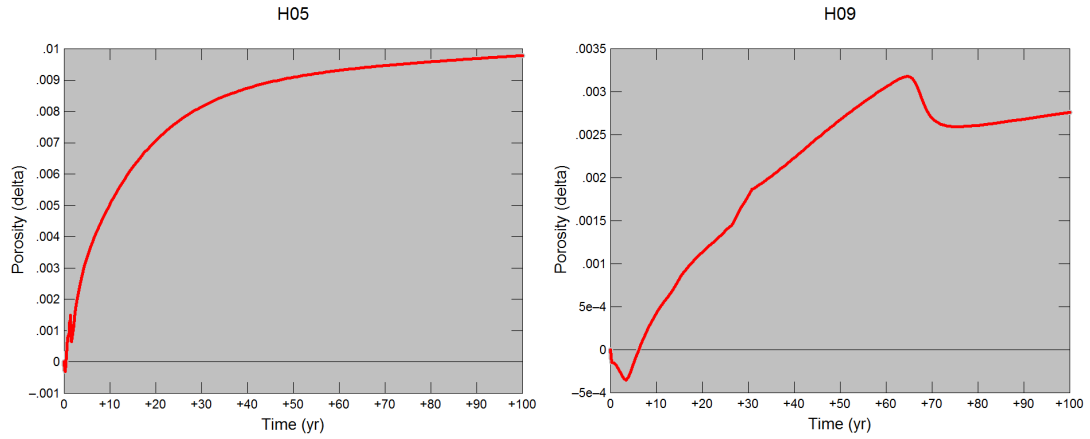

Figure 5-4. Changes in porosity of samples H5 and H9 according to the modelling under reservoir conditions.

The bulk porosities from LPNA, MICP, and NMR presents some differences (Figure 5-5). The porosities from NMR, averaging about 20% for saturated samples, are much higher than LPNA and MICP porosities which are about 12% and 4cm^3/g respectively. This scale of differences has also been investigated by Hildenbrand et al. (2003) for mudstone samples. Possible explanations include: the ability of NMR to measure both connected and isolated pores (pores located within the grains and clay-bound water spaces) in contrast with MICP that only measures the connected pores; NMR samples are saturated with brine which make them prone to clay swelling and crack, while MICP samples were dried which induce potential clay shrinkage (Hinai et al., 2015).

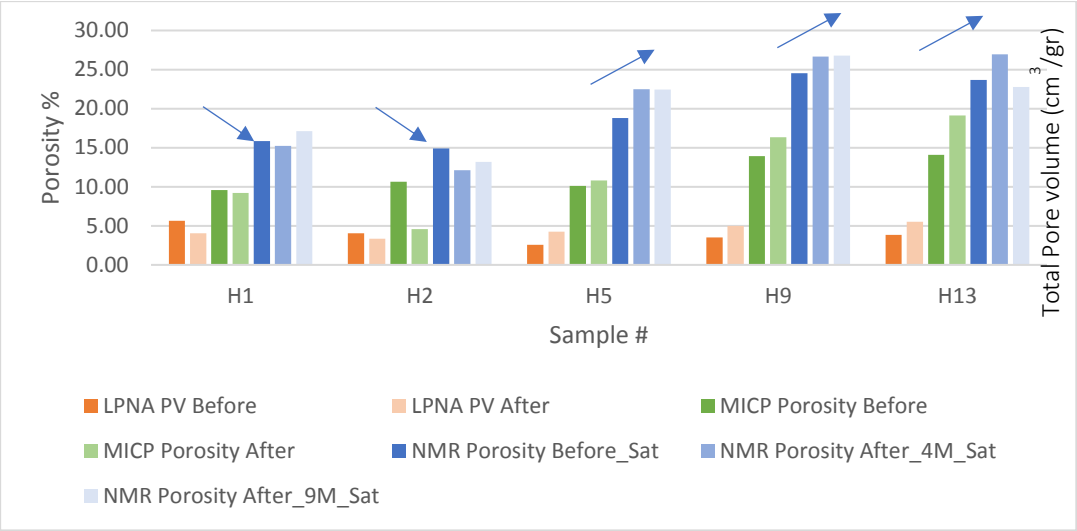

Figure 5-5. Porosity results from LP-NA, MICP, and NMR-Sat methods. LP-NA pore volume values are in cm^3/gr, and MICP and NMR values are porosity in percentage.

Two groups of samples were identified from capillary pressure profiles in Appendix VII. Capillary pressure curves in samples H1 and H2 (Appendix VII.A) start to plateau earlier than the other three samples and remain mostly flat for a considerably larger portion of the curves. This suggests a unimodal type of pores in the first two samples compared with more complex pore sizes in the last three samples covering a large range of pore sizes. The general peak pore throat radius shows H1 and H2 samples at 12.5nm smaller than H5, H9, and H13 samples which have values around 21.1nm (Table 3-8 and Figure 3-23). More specifically, pore throat distribution reveals a second minor population in the second group of samples that have a pore throat size larger than 250nm that is easily invaded by mercury injection at low pressure. Samples H1 and H2 (group one) have the smallest average pore diameter at 11.3-12.7nm.

Similarly, threshold pressure shows distinctive values in these two groups. Group one threshold pressures are in the range of 6700-8350psi and group two threshold pressures range is 412-1900psi, which is significantly lower than group one (Table 3-7). Threshold pressure for all five samples is reduced in all five samples. However, the decrease is significant in the case of samples H2, where it is decreased from 6310 psi to 1736 psi.

When the buoyancy pressure due to accumulated CO_2 plume dominates the capillary pressure of caprock, the plume intrudes into the pore throats, and the occurrence of capillary leakage is inevitable in the caprock. The capillary pressure of the CO_2-brine can be equated to the buoyancy pressure of the injected CO_2 column (Rezaee et al., 2017). Here, the experimental investigation of capillary pressure was conducted, and the result was used to

calculate the height of the CO_2 column. Mercury injection capillary pressure (MICP) indicated a reduction in the capillary pressure and the calculated maximum column heights of CO_2.

There is some positive relationship between MICP porosity and the average pore diameter. However, a strong relationship exists between MICP porosity and peak pore throat diameter and threshold pressure (Figure 5-6). The general trend exerts the expected relationship between these three parameters. Smaller porosities and peak pore diameter (group one) correspond to higher threshold pressure and vice versa (group two).

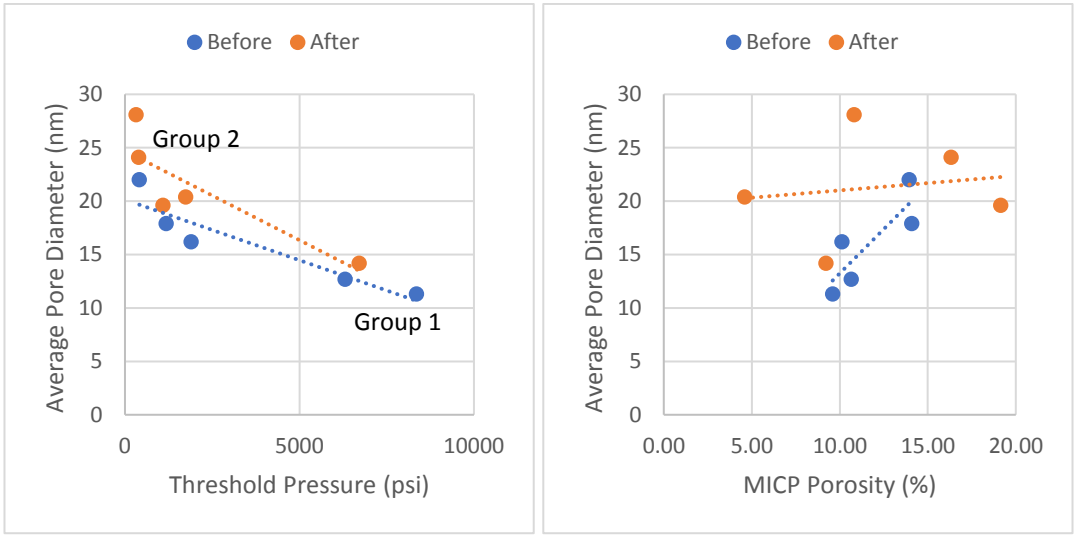

Figure 5-6. Pore throat diameter versus threshold pressure and MICP porosity.

These two groups are distinctive in their content of kaolinite clays. Group one, including samples H1 and H2, with high kaolinite content, records high threshold pressure due to low pore throat diameter. The second group of samples, H5, H9, and H13, with lower kaolinite content, has lower entry pressure and a more diverse range of pore throat diameter.

Total area in pores is estimated from both LPNA and MICP methods. Ten samples were tested with LPNA before and after exposure. However, only five of them were measured with MICP method (H1, H2, H5, H9, and H13). LPNA surface area shows slight changes in most samples. A slight positive change is observed in samples H1, H2, H5, H8, H9 and a slight negative change in sample H10. However, in samples, H5 and H15 total pore area are decreased significantly and in the case of sample H13, it is increased significantly. MICP total pore area shows more dramatic changes. Total pore area is decreased in samples H1, H2, and H5 and is increased in samples H9 and H13. In the case of samples H2, the reduction is very significant (-77%). MICP confirms LPNA total pore area results in terms of the direction of change in samples H9 and H13 where both methods show an enhancement in total surface area.

However, the slight LPNA pore area increase in samples H1, H2, and H5 does not agree with MICP pore area, which shows a significant decrease after exposure to $scCO_2$.

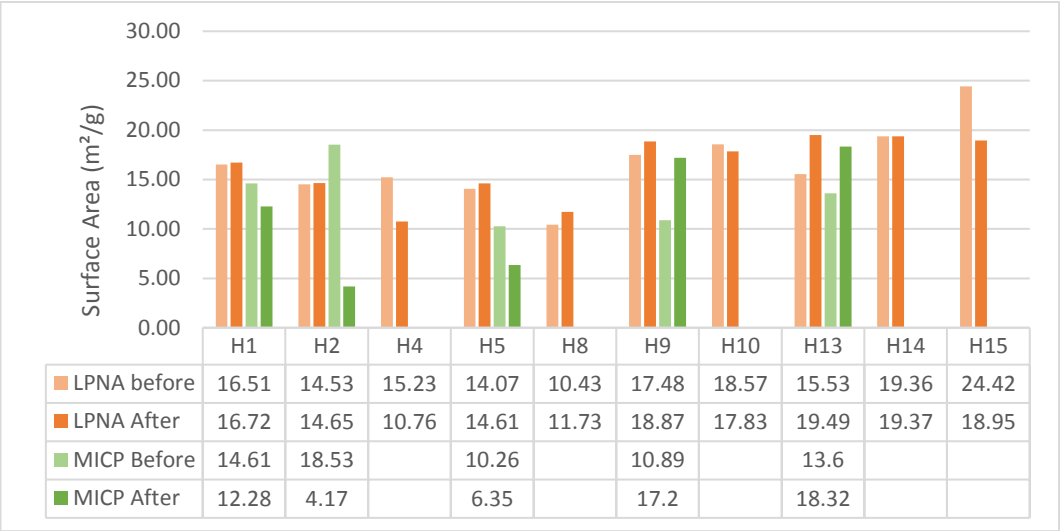

	H1	H2	H4	H5	H8	H9	H10	H13	H14	H15
LPNA before	16.51	14.53	15.23	14.07	10.43	17.48	18.57	15.53	19.36	24.42
LPNA After	16.72	14.65	10.76	14.61	11.73	18.87	17.83	19.49	19.37	18.95
MICP Before	14.61	18.53		10.26		10.89		13.6		
MICP After	12.28	4.17		6.35		17.2		18.32		

Figure 5-7. Surface area estimates before and after exposure to $scCO_2$ form LPNA (orange) and MICP (green)

The BET surface areas were found to be 23.9-70.6 m^2/g (Table 3-4). There was a direct relationship found between the BET surface area and the occurrence of Illite/mica (Figure 5-8). Group one of samples has a lower percentage of Illite/mica clays but higher kaolinite percentages compared with group two of samples. The second group of samples with higher kaolinite content has higher threshold pressure due to low pore throat diameter and lower porosities (Figure 5-6 and Figure 5-8). Furthermore, the presence of kaolinite influences the NMR response (Figure 5-8). As the kaolinite content increases, the T_2 relaxation time peak tends to decrease, with corresponding smaller pore sizes or a restricted environment.

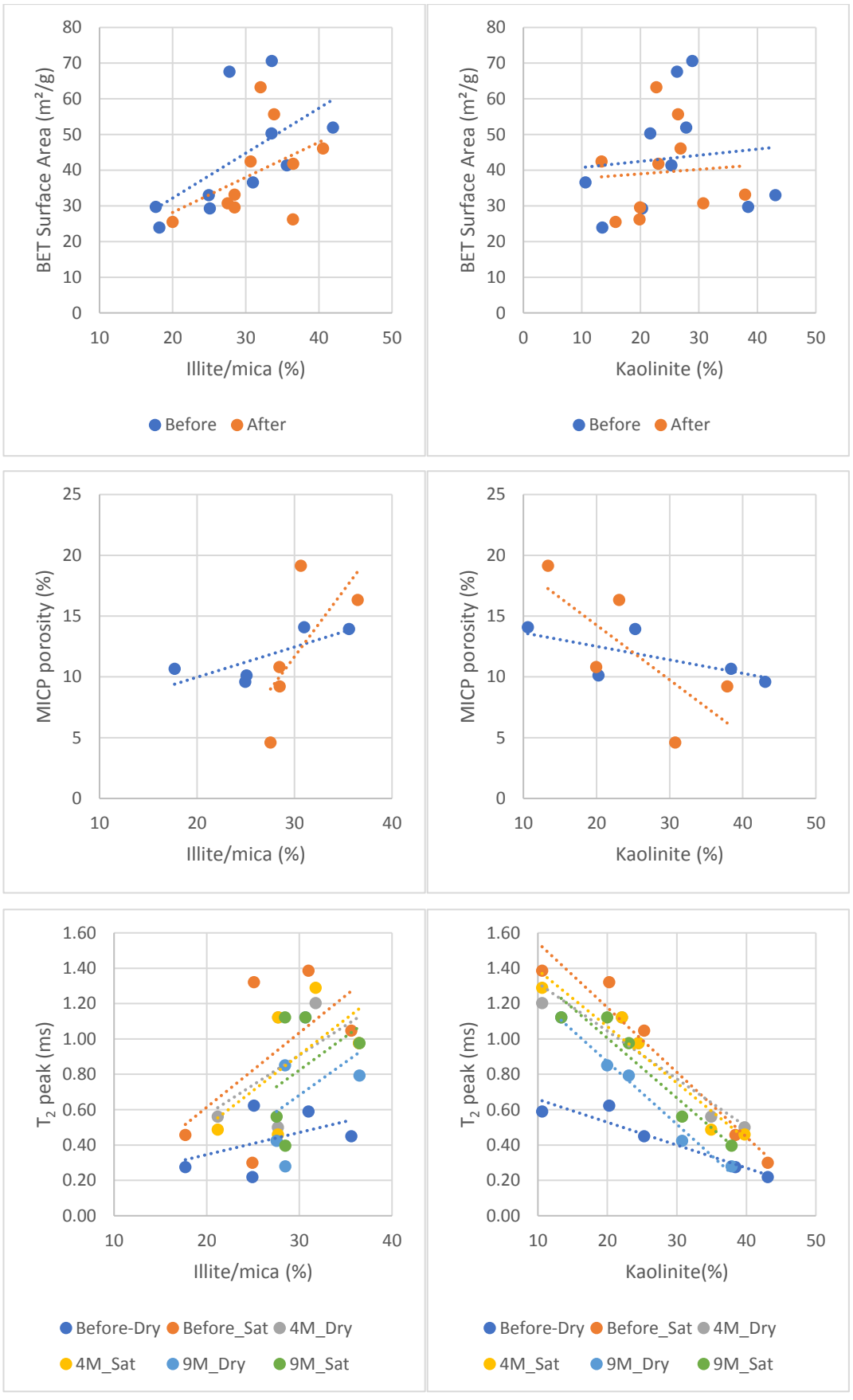

Figure 5-8. Influence of Illite/mica and kaolinite on various parameters.

The high presence of total clay (mostly kaolinite) could cause blocking of the pore throats and giving access to the neighbouring larger pores during the saturation process, leading to lower T_2 amplitude values. The long T_2 in group two of samples is an indication of macropores, and potentially new crack induces by artificial saturation under pressure and brine reactivity with shales, during the sample recovery and preparation steps.

There is no strong relationship between LPNA average pore width and either total pore area or total pore volume (Figure 5-9). Average pore width shows a strong relationship with fractions of micro-, meso-, and macropores. Before and after exposure samples show a decrease in micropore percentage and an increase in mesopore and macropore percentage with an increasing pore diameter (Figure 5-10 and Figure 5-11). Based on IUPAC pore classification, LPNA pore volume showed a pore range from 65.3% to 86.2% mesopores, 6.1 to 33.7% micropores, and a small portion of 0.5 to 8% macropores.

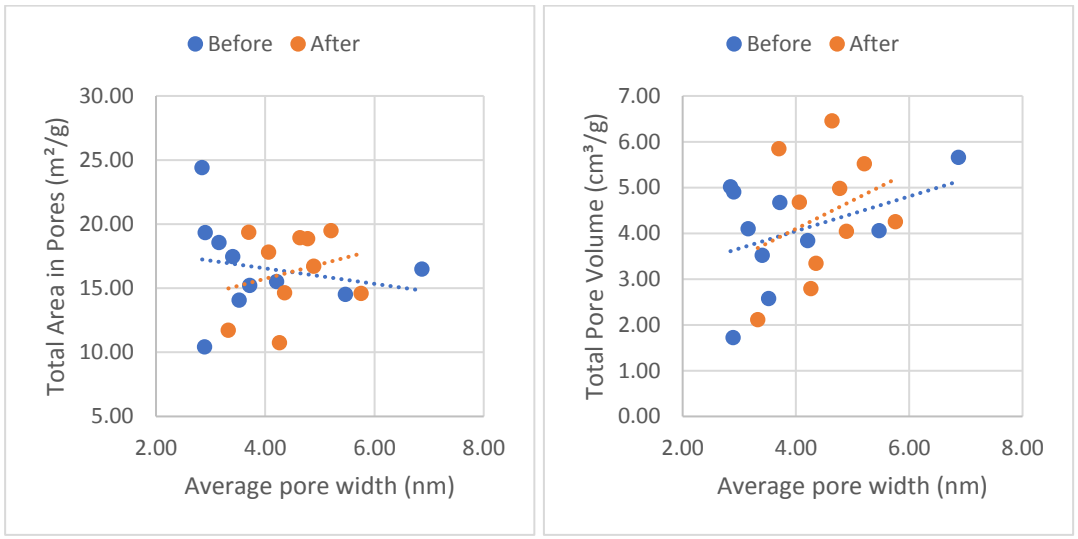

Figure 5-9. Relationship between average pore width versus total pore area (left), and total pore volume (right) from LPNA measurements.

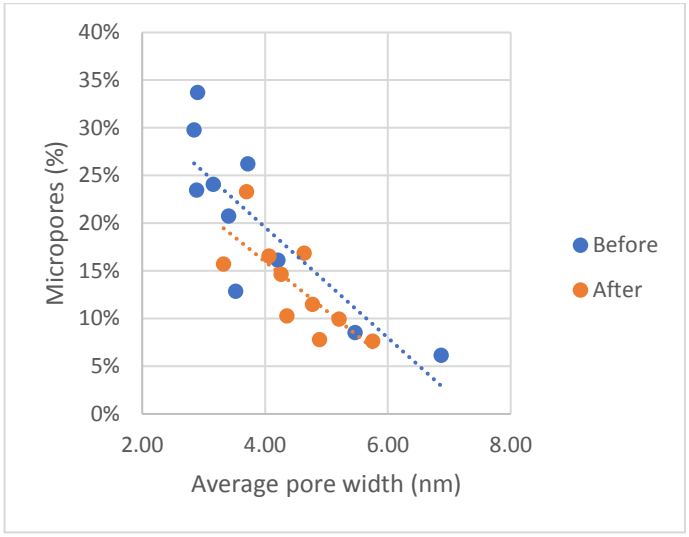

Figure 5-10. Relationship between average pore width versus the percentage of micropores.

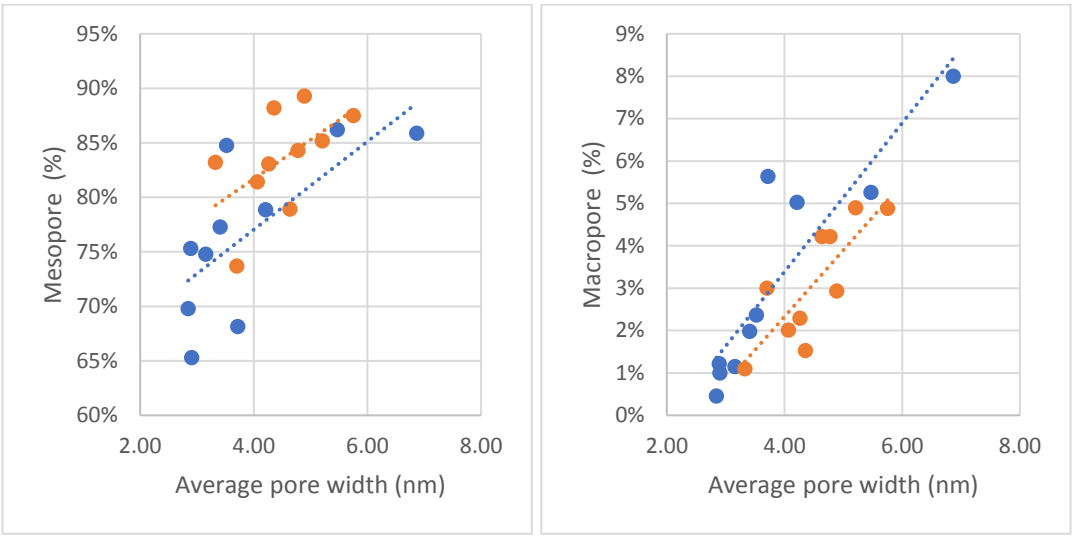

Figure 5-11. Relationship between average pore width versus mesopore percentage (left), and macropores percentage (right).

5.2.1 PSD Comparisons

LPNA results show different changes in samples PSD. After nine months of exposure, an increase was observed in the pore volume of micropores and mesopores smaller than about 8nm in samples H1, H2, and H4. Sample H4 is different in this matter to the other two samples in than the pore volume of micropore range was decreased (Appendix V-B). However, the pore volume of pores larger than about 8 nm was decreased in samples H1, H2, and H4. The isotherm curves of after exposure in these three samples (Appendix V-A) sits lower than the before exposure isotherm curves. In samples H5, H9, and H13, the pore volume is increased across all pore size range. The corresponding isotherm curves of after samples sit above the before samples in case of mentioned four samples. Samples H10, H14, and H15 follow a deferent pattern. Their pore volumes are increased in pore sizes smaller than about 20nm

and are decreased above this turning point. Their after-exposure isotherms are lower than the before exposure isotherms.

MICP results are two-folded too. MICP shows a decrease in porosity of samples H1 and H2 and an increase in samples H5, H9, and H13. Although H5 porosity is slightly increased, which puts it in the second group, its total pore volume is decreased from 10.26 m^2/g to 6.35m^2/g (Table 3-7). The MICP PSD does not include the micropore range as the LPNA does. MICP advocates substantial pore volume in the meso- and macropores range. Samples H1 and H2 obtained from MICP analysis have the largest mesopore volume and the least macropore volume. The slight inconsistency between MICP and LPNA is because MICP only quantifies pore throat sizes and not the pore bodies, whereas LPNA quantifies both of them (Hinai et al., 2015).

The grouping mentioned above is also obvious in the MICP pore size distribution curves. Samples H1 and H2 with the most uniform pore size distributions have the largest proportion of their pores in narrow pore sizes (peak at about 10nm) which is reduced after exposure. A dual behaviour is observed in pore volume distribution of samples H5, H9, and H13. Pore sizes are reduced below around 200nm and enhanced above this point. PSD analysis using NMR and MICP methods gives similar results, with pore distribution covering meso- and macropores. The pressure injection of mercury in MCIP method is not enough to override the strong capillary pressure of pores<2nm and some of the nanopore signal associated with micro-porosity is not detectable by low-field NMR (Hinai et al., 2015). The same trend is also observed in NMR results. NMR Pore size distribution of samples H1 and H2 are in the lower pore size range and, showing a lower total porosity than other samples (H5, H9, and H13).

As can be seen in this section, combining MICP and LPNA techniques yields a full pore size spectrum of the shale samples from micro- to macropore. By comparing the PSD in the overlapped area (mesopore), the position of the peaks does not match precisely. For all analysed samples, mercury porosimetry suggests a lower mode pore diameter compared to that obtained from nitrogen adsorption. The underestimation in MICP method would be induced by several reasons. Tight pores are not completely intruded by mercury. The increased injection pressure applied to access the smaller pores would compress the sample, decreases the measured pore throat size. MICP measures the pore throats and not the actual pore size, and therefore the measured pore size using mercury would be lower than that obtained from the nitrogen adsorption (Giesche, 2006; Kuila et al., 2014; Kuila et al., 2013).

The combination of MICP and LPNA pore size distribution with NMR results is an ideal approach to overcome each method's limitations. The external factor such as dehydration/hydration state or sample preparation, as well as their innate pore size resolution limits, affect their application. To convert T_2 relaxation time from the NMR method into PSD, a scaling factor is required. Surface relaxivity is introduced in Hinai et al. (2015) to determine the T_2 equivalent pore diameter using the following formula:

$$D = T_2 . \rho_2$$

Equation 5-1

where D is MICP pore throat diameter (nm), ρ_2 is the surface relaxivity, commonly denoted as the scaling factor, and T_2 is the transverse NMR relaxation time (ms). In this method, the scaling factor was determined graphically by finding the difference between dominant pore diameter (MICP) and the dominant T_2 relaxation time (NMR) and then apply the scaling factor to the NMR data for each sample. The scaling factors used here are summarised in Table 5-1.

Table 5-1. Scaling factors used to convert NMR T_2 to MICP PSD

Samples	***Scaling factor (nm/ms)***
H1 Before	27.693
H1 After	31.540
H2 Before	27.423
H2 After	26.984
H5 Before	13.685
H5 After	13.478
H9 Before	20.190
H9 After	15.487
H13 Before	11.538
H13 After	16.115

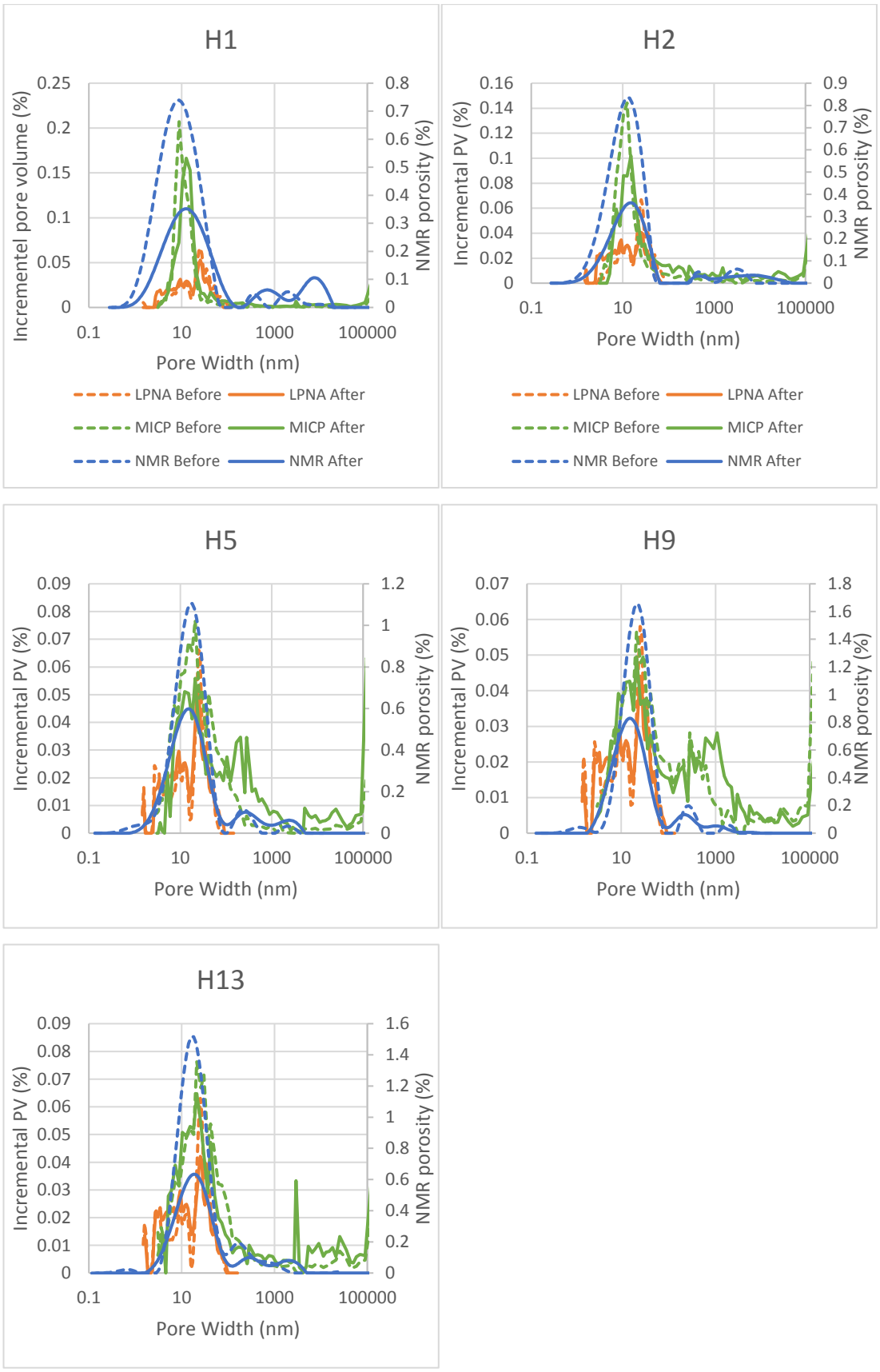

Figure 5-12. Pore size distribution from three methods compared.

5.3 Conclusions and Recommendations

Five laboratory techniques (MICP, LPNA, low-field NMR, SEM, and XRD) accompanied with a simulation approach have been utilised to assess the alteration of petrophysical and chemical properties of shale caprocks under the influence of supercritical CO_2. The following conclusions can be reached about the effect of supercritical CO_2 on the shale samples in this study.

The experimental study of shaly caprock samples under in situ reservoir conditions (T =60°C, P = 14.1 MPa) has shown that injection of $scCO_2$ into saline formation water of deep saline aquifers influences their chemical character and their sealing efficiency. Reactions of the mixture of $scCO_2$ and brine are documented by changes in mineral composition of exposed samples relative to the initial samples confirmed by XRD and SEM examinations. The injection of $scCO_2$ into the brine resulted in a decrease of the pH and dissolution of quartz, aluminosilicates such as K-feldspar and clay minerals such as kaolinite and precipitation of muscovite (illite).

Comparing the results of this study with other experimental studies leads to the conclusion that each carbon sequestration system may behave differently due to differences in brine compositions and rock types. For this reason, it may be advisable to perform a specific case study for each type of reservoir before sequestering $scCO_2$ into geological formations.

Geochemical reaction path modelling associated the dissolution of K-feldspar, albite, and anorthite to precipitation of muscovite and Na-nontronite (or dawsonite), and calcite respectively. Chlorite dissolution resulted in the formation of magnesite or Mg-nontronite, and Fe from goethite dissolution formed hematite. The use of geochemical modelling without constraints from such experiments is not reliable because the results are not consistent in all cases with the results of experimental studies (Wigand et al., 2008).

Changes in pore structure properties are likely to occur as a result of dissolution and re-precipitation of minerals and compounds within the sample. NMR, MICP, and LPNA tests indicate that these mineralogical alterations have led to an increase in pore space of most samples. NMR analysis shows a noticeable increase in T_2 relaxation time and porosity when samples are exposed to $scCO_2$. MICP results also show a distinct shift toward smaller capillary pressure values for samples exposed to $scCO_2$. This agrees with a general shift in the MICP curves toward larger pore and pore throat sizes for most of the samples analysed. The reduction of the threshold pressure has led to a reduction of the calculated maximum column

height of CO_2 retention for samples exposed to $scCO_2$ similar to a previous study (Rezaee et al., 2017). The changes are observed in the core plugs and fragment samples of different depths in the studied well, and determination of the radius of influence on the seal was not possible in this study.

Samples are grouped based on the clay content and pore sizes. The higher kaolinite content of samples H1 (43.06%) and H2 (38.39%) along with their smaller pore sizes would contribute to their anomalous behaviour in terms of petrophysical alterations. Shale samples with higher kaolinite and lower quartz demonstrated uniform but poorly connected pores with the majority of pore sizes in the smaller pore size range. Their porosity reduced after exposure to CO_2 when the smaller pores decreased. By contrast, for shale samples of lower kaolinite and higher quartz contents (H5, H9, and H13) with unevenly distributed but well-connected pores, the porosity has enhanced. The overall larger pore size allowed CO_2 to penetrate more easily and to interact with pore minerals. The dissolution in connected larger pores could play a major role in porosity enhancement in these samples.

A shale composition such as group one studied here is considered geochemically suitable caprock for CO_2 geological storage, as it contains clay minerals and matrix permeability is in nano Darcy range. Matrix solution transport would not be significant, and dissolution could not lead to increased porosity and permeability. In another word, seal integrity is maintained in such a case.

The results of this study also indicate that chemical/mineralogical alterations of the shale samples, after exposure to $scCO_2$, have measurable effects on the porosity, permeability, and sealing properties of shales, with a tendency to enhance the transport properties. Although the mineralogical changes in the shale samples are not volumetrically substantial, they have a significant effect on the rock's petrophysical characteristics (Rezaee et al., 2017). But even these enhanced transport properties are not likely to create substantial leakage problems through the undisturbed matrix of massive shale sequences (Busch et al., 2008).

Appendix I.

A. Laboratory experiments work on CO_2 sequestration

#	BASIN/ FORMATION	MAJOR MINERALS	WATER TYPE/ IONIC STRENGTH	T (°C)	P (MPA)	METHODS/ ANALYSES USED	KEY OBSERVATIONS	REFERENCES
1	Sherwood Sandstone and late Triassic Mercia Mudstone.	Plagioclase and K-feldspar, hematite, illite, quartz, dolomite, calcite, kaolinite, zeolites	synthetic seawater and deionized water which were equilibrated with supercritical CO_2	105 , 80	9, 20	simple batch experiments, 3 and 8 months	Significant alteration of pre-existing calcite and dolomite, dissolution of anhydrite accompanied by precipitation of calcite and possible corrosion of detrital feldspars with precipitation of Na-smectite	(Pearce et al., 1996; Rochelle et al., 1996)
2	Glauconitic sandstone, Alberta Basin (1500m depth)	Quartz (87%), K-feldspar (2%), plagioclase (1%), glauconite (5%), kaolinite (2%), calcite (1%), dolomite (1%), siderite (1%)	High salinity water	105	9	1 month experimental 4:1 water–rock ratio (SEM, XRD, grain size analysis)	Very little reaction observed in fast-reacting carbonate minerals due to high salinity.	(Gunter et al., 1997)
3	Sandstone from Tensleep formation, Wyoming, USA (981–1208m depth)	Quartz, anhydrite, dolomite, K-feldspar	Saline water with 9.69 g/L salinity	80	16.6	7 days – experimental (core flooding)	The permeability of downstream decreased while porosity increased due to the blockage of pore spaces by kaolinite	(Shiraki et al., 2000)
4		Anorthite and glauconite	Na-Ca-Cl synthetic brine	50, 150	4.1, 13.8	vessels placed on a shaker table for 1 month	Precipitation of carbonate minerals did not occur.	(Sass et al., 2001)

#	BASIN/ FORMATION	MAJOR MINERALS	WATER TYPE/ IONIC STRENGTH	T (°C)	P (MPA)	METHODS/ ANALYSES USED	KEY OBSERVATIONS	REFERENCES
5	Reconstituted arkose and Silurian Maplewood shale, USA	Artificial arkose (1:1:1:0.3 quartz: plagioclase: microcline: biotite). Silurian shale as aquitard (illite and mica 65 vol.%, quartz 27%, feldspar 5%, chlorite 2%)	5.5 mol/kg synthetic brine containing Na^+ Mg^{2+} K^+ and Cl^-	200	20	59 days steady state, 80 days after CO_2 injection. Brine samples analysis (ICP-ES, ICP-MS, and ion chromatography). Solid analysis (optical microscopy, SEM+EDS, XRD)	Precipitation of clay minerals, magnesite, and analcime. Decreased pH and enrichment in Cl^- in brine due to CO_2 desiccation of the brine.	(Kaszuba et al., 2003)
6	Oriskany Formation in Indiana County, Pennsylvania						Pressure and temperature play only a small role in the process.	(Soong et al., 2004)
7	Reconstituted arkose and Silurian Maplewood shale, USA	Same as above.	5.5 mol/kg NaCl	200	20	32 days steady state, 45 days after CO_2 injection. 77 days of separate experiment in the absence of CO_2. Brine sample analysis, experimental (XRD, SEM+EDS) and modelling.	Magnesite precipitation followed by dissolution, precipitation of siderite, clay minerals, and analcime. Decreased pH, increased SiO2, K^+ and Ca^{2+} and decreased Na^+ and Cl^- concentrations	(Kaszuba et al., 2005)
8	Leadville Limestone Formation, Colorado. Sandstones from Mount Tom, Massachusetts	Limestone (38% calcite). Arkosic sandstone (quartz, plagioclase, K-feldspar, kaolinite). Banded sandstone (quartz, K-feldspar, kaolinite, minor plagioclase)	Groundwater brine ($NaCl/CaSo_4$) and a synthetic mix of deep aquifer brine (Na, Ca)Cl	25, 120	10 to 60	Aqueous samples analysis (ICP-AES, ICP-MS, ion chromatography)	Limestone: the dissolution of calcite and porosity increase (low-sulphate brine). Precipitation of anhydrite, dolomitisation of the limestone, and decrease in porosity (high-sulphate brine). The solubility of CO_2 in brine increased in the presence of	(Rosenbauer et al., 2005)

#	BASIN/ FORMATION	MAJOR MINERALS	WATER TYPE/ IONIC STRENGTH	T (°C)	P (MPA)	METHODS/ ANALYSES USED	KEY OBSERVATIONS	REFERENCES
	and Coconino, Arizona.						limestone and arkosic sandstone.	
9	Springerville–St. Johns CO_2 field, Arizona and New Mexico, USA	Albite, orthoclase, and anorthite in the presence of dolomite and quartz	Natural aquifer water saturated with dolomite, quartz and other carbonates				At 0.03 mol/kg CO_2 concentration (pH = 6) kaolinite is saturated and produced from orthoclase. At 0.07 mol/kg CO_2 concentration, dawsonite becomes fully saturated and produced.	(Moore et al., 2005)
10	Westphalian and Buntsandstein sandstones from Belgium	Quartz, K-feldspar, illite, smectite, chlorite, carbonates (ankerite, dolomite, siderite)	Saline water	80	15	8 months – experimental (SEM/ EDS/ EMPA element mappings)	Large dissolution of carbonates and some dissolution of feldspar could enhance rock porosity and permeability. significant precipitation of kaolinite, siderite, and calcite could increase the storage capacity of CO_2	(Bertier et al., 2006)
11						batch experiments and plug flow experiments	Reactions of CO_2 impregnated brine with microfracture surfaces in the samples	(Aplin et al., 2006)
12	Cretaceous Muderong Shale, Carnarvon Basin, Australia	Quartz 27%, kaolinite 26%, illite-smectite 27%, mica 8%, chlorite 5%, siderite 2%, orthoclase 3%, pyrite 2%		45-50	<20	Diffusion experiments, high-pressure sorption experiments, low-pressure nitrogen sorption experiments	Significant CO_2 storage capacity reported in shale, related to aqueous solubility, geochemical reactions and physical sorption mainly on clay minerals.	(Busch et al., 2008)
13	Cretaceous Muderong	Quartz 20%, Illite 39%, smectite 19%, chlorite 3%,		50	15	Gas sorption, Batch reactors (2-32 days), XRD, BET	Smectite and K-feldspar content increased, illite and siderite decreased.	(Busch et al., 2009)

#	BASIN/ FORMATION	MAJOR MINERALS	WATER TYPE/ IONIC STRENGTH	T (°C)	P (MPA)	METHODS/ ANALYSES USED	KEY OBSERVATIONS	REFERENCES
	Shale, Australia. Paleozoic shale, Saar area, Germany	K-feldspar 4%, pyrite 2%, siderite 4%, kaolinite 10%					CO_2 sorption capacity decreased with moisture reduction.	
14	Bunter sandstone	Quartz (65.7%), K-feldspar (17.4%), albite (7.9%), illite (4.9%), dolomite (1.6%), hematite, halite and kaolinite < 1% Porosity 14.5%	1M NaCl Solution	60	15	XRD, SEM+EDS analysis ICP-MS, ICP-OES, electron microprobe (EMP) 62.3 days experimental	Dissolution of carbonates started just after the injection of $scCO_2$ and feldspar and albite in the later stage of the experiment. Precipitation of montmorillonite.	(Wigand et al., 2008)
15	Nagaoka Sandstone, Japan	Quartz, feldspar, chlorite, mica, calcite, smectite, pyrite	Formation water from Nagaoka site	50	10	Field-scale study	50,000 ppm of CO_2 could be dissolved, dissolution of chlorite and feldspar at an early stage of the test	(Mito et al., 2008)
16	Upper Jurassic Draupne Formation, North Sea	Powdered Draupne claystone		35	3.5	CO^2 capillary breakthrough experiments	An apparent breakthrough of the supercritical CO was obtained at a pressure of ~35 bars,	(Soldal, 2008)
17	Upper Jurassic Draupne Formation, North Sea			35	7.5	Supercritical CO_2 breakthrough experiments (58 days)	CO_2 percolation potential is higher where there is a higher pore pressure build-up	(Angeli et al., 2009)
18	Saint Martin de Bossenay (SMB, Paris basin, France) caprock			150	10	Batch experiments 30–60 days XRD, microprobe, and TEM	Illitization of smectite, precipitation of kaolinite, and dissolution of anhydrite before reprecipitation	(Kohler et al., 2009)

#	BASIN/ FORMATION	MAJOR MINERALS	WATER TYPE/ IONIC STRENGTH	T (°C)	P (MPA)	METHODS/ ANALYSES USED	KEY OBSERVATIONS	REFERENCES
19	Chinle Shale, Utah, USA. Comblanchien Formation, Paris basin, France	1) I/S 40%, quartz 40%, calcite 10%, hematite 7%, and dolomite 3% 2) Calcite 45%, I/S 15%, kaolinite 10%, quartz 10%, gypsum 5%, pyrite 5%, others 5%. 3) Purified I/S 4) Smectite and I/S 5) Illite	Synthesized NaCl brine 0.25M	80–150	0.1–15	Batch reactor experiments 30-360 days, 1) bine+scCO_2 2) brine+ dissolved CO_2 ICP –AES, STA, XRD and SEM+EDS	Carbonate dissolution and at 150°C. Precipitation of a more complex mixed carbonate (Fe, Ca, Mg), and partial dissolution of kaolinite, and precipitation of smectite in the long-term (365 days).	(Credoz et al., 2009)
20	Sandstone from Parana Basin, Argentina	Quartz (67%), kaolinite (6–7%), calcite (4–13%), K-feldspar (4–5%), albite and plagioclase	Carbonated distilled water	200	15	100 h experimental SEM analysis	Dissolution of calcite, feldspar, and pyrite. Kaolin precipitation for the first time from the batch-soak study.	(Ketzer et al., 2009)
21			Water			Reactivity, CO_2 permeability and diffusion experiments on shale plug	Effective gas permeability increased by a factor 3–8 the decrease of capillary entry pressure by 33–46% increase in the effective CO_2 diffusion coefficient of about 50%.	(Wollenweber et al., 2010; Wollenweber et al., 2009)
22	Adamswiller sandstone, Paris Basin, France	Quartz (71%), feldspar (9%), clay (11%), mica (5%), iron and titanium oxides	CO_2-saturated distilled water and wet scCO_2	90	28	1-month experimental (SEM, XRD)	No changes occurred with CO_2-saturated water. Porosity and permeability increased by 4% and by 6–7 times respectively with wet scCO_2.	(Rimmelé et al., 2010)

#	BASIN/ FORMATION	MAJOR MINERALS	WATER TYPE/ IONIC STRENGTH	T (°C)	P (MPA)	METHODS/ ANALYSES USED	KEY OBSERVATIONS	REFERENCES
23		Three argillite type caprocks				Through-diffusion experiments (400 days)	Degradation of the containment properties of the samples	(Berthe et al., 2011)
24				160	150	50 days SEM images, 3D pore reconstructions, and SANS	increase in pores at length scales ranging from 10 s of nm to over 1 µm. New precipitates grew into the pore space observed in some cases. Dissolution features (e.g., pitting and etching) were observed.	(Navarre-Sitchler et al., 2011)
25	Navajo sandstone, Colorado Basin, USA	Quartz (90%), feldspar (2%), smectite, kaolinite	0.2 mol/kg KCl	200	30	23 days experimental (XRD, SEM, ion chromatography)	No dawsonite precipitation due to the non-availability of Na^+ ions in the aqueous medium. Dissolution of feldspar Conversion of smectite into illite (illitisation) occurred. Chemical reactions induced by CO_2 injection cause pore throat clogging by moving the smectite.	(Lu et al., 2011)
26	Mt. Simon Sandstone, USA. At 2 km depth	Quartz (74%), K-feldspar (25%), plagioclase (0.5%), dolomite (1%)	Salinities same as formation water	75	20	0–10,000 years simulation time 1D hydrogeological model	Stepwise pH distribution with the distance due to the buffering of pH at different levels observed.	(Liu et al., 2011)
27	Sandstone from Rio-Bonito formation, Brazil	Quartz, albite, anorthite, calcite, dolomite, illite, kaolinite/chlorite, and illite-smectite mixed layer	0.1M NaCl solution	80	0-12	3–6 months of experiments(SEM/TEM/XRD)	No reaction after 3 months. Part of illite-smectite mixed layer turned into illite.	(Lima et al., 2011)

#	BASIN/ FORMATION	MAJOR MINERALS	WATER TYPE/ IONIC STRENGTH	T (°C)	P (MPA)	METHODS/ ANALYSES USED	KEY OBSERVATIONS	REFERENCES
28	Adventalen Shale, Svalbard, Norway	A carbonate-rich shale: calcite 29%, ankerite 7%, plagioclase 6%, illite 26%, Chlorite 19%, and quartz 13%; and a clay-rich shale: illite 22%, chlorite 38%, quartz 26%, plagioclase 8% , pyrite 1%, siderite 5%.	1 M NaCl	80-250	11	1-5 weeks batch experiments (expose to supercritical CO_2 and brine mixture) water/rock ratio 20:1 XRD and SEM	Clay-rich shale didn't show major alteration. In carbonate-rich shale at 250°C plagioclase, chlorite and illite dissolved formed swelling clay (smectite), calcite dissolved and re-precipitated, with no traces of the formation of other carbonates than calcite.	(Alemu et al., 2011)
29	Eau Claire shale, Wisconsin, US	Quartz, orthoclase, illite, and a small amount of chlorite	synthetic brine	200	30	Batch experiments (SEM and XRD) 60 days	Secondary minerals: illite and smectite, clinochlore, anhydrate, and siderite in the vicinity of pyrite.	(Liu et al., 2012)
30								(Yu et al., 2012)
31	Several sandstone types from North German Basin	Quartz, feldspar, calcite, illite, barite, chlorite kaolinite	Formation brine	100	10	12–35 days experimental – in an autoclave system (SEM)	Development of micro-fractures in detrital minerals. Initial dissolution of calcite.	(Marbler et al., 2013)
32	Mudstone, caprock of the Krechba gas field, In Salah in Algeria	Dominant silicate minerals, quartz, illite and potassium feldspar, with subordinate quantities of chlorite and kaolinite, and small quantities of siderite and pyrite		95	25	72 hours of measurements with a flow rate of 0.015 cm^3/h XRD, SEM	Increase in the permeability of the caprock by a factor of 8. Increase in porosity from 7 to 10%. A decrease in internal surface area. Significant loss of siderite and chlorite.	(Armitage et al., 2013)

#	BASIN/ FORMATION	MAJOR MINERALS	WATER TYPE/ IONIC STRENGTH	T (°C)	P (MPA)	METHODS/ ANALYSES USED	KEY OBSERVATIONS	REFERENCES
33	Tournemire underground tunnel, Mesozoic marine basin, French Massif Central	Calcite (43%), quartz (15.5%), micas, kaolinite, and chlorite, minor quantities of feldspar and pyrite	synthetic water	53	8.4	2 months, Solid (LP-NA) and liquid phase analysis by atomic adsorption spectroscopy, ionic chromatography, and ICP-MS	A minor increase in micro- and mesopores (<10nm) due to calcite dissolution. Increase in concentration of Ca, Mg, Na, K, Si ions in water attributed to aluminosilicates dissolution. A decrease in SO_4 ion indicated gypsum precipitation.	(Garrido et al., 2013)
34	Early Triassic Hawkesbury sandstone, Sydney Basin, Australia	Quartz 60%, calcite 26%, Kaolinite 6%, barite 5%, siderite 1%, Muscovite 1%, other clay minerals 1%	20% NaCl	40	10	1.5 years Sandstone-brine- sc-CO_2 exposure compared with sandstone-brine only.	Significant pH drop in the saline pore fluid. Dissolution of minerals: calcite, siderite, barite, and quartz. Permeability increased. CO_2 drying-out effect and salt (NaCl) precipitation.	(Rathnaweera, Ranjith, & Perera, 2016)
35	Triassic Hawkesbury sandstone, Sydney Basin, Australia	Quartz 90%, calcite 6%, kaolinite 2%, muscovite 1%, and other clay minerals <1%	15% NaCl	35	4-10 (injection), 20-35 (confining)	Triaxial permeability test with CO_2-brine co-injections and CO_2 only injections	CO_2- brine co-injection eliminates enhances the carbonation efficiency and mineral trapping, and the solubility trapping. It also creates reduced CO_2 relative permeability and improves hydrodynamic trapping.	(Rathnaweera, Ranjith, Perera, et al., 2016)
36	Longmaxi formation, Sichuan Basin of China	Quartz 40.2-46.8% Clay minerals 24.8-30.8% Carbonates 10.9-15.8% Others 7.4-17.5%	No brine	40	16	30 days exposure, SEM, XRD, LP-NA, FTIR	Limited influence of reactions on the pore morphology and mesopores, but significant influence on the micropores. Specific surface area and the number of micropores	(Yin et al., 2016)

#	BASIN/ FORMATION	MAJOR MINERALS	WATER TYPE/ IONIC STRENGTH	T (°C)	P (MPA)	METHODS/ ANALYSES USED	KEY OBSERVATIONS	REFERENCES
							decreased. Average pore size increased. The surface roughness of shale samples decreased.	
37	Pannonian Basin, Hungary	MS1, S1, S2 samples: Quartz 49, 34, 15%, K-feldspar 2, 1, 2%, Plagioclase 3, 3, 0%, Illite/muscovite 32, 26, 25%, kaolinite 5, 5, 4%, Chlorite 9, 0, 0%, Calcite 0, 12, 1%, Dolomite 0, 14, 0%, Ankerite 0 ,0, 49%, Siderite 0, 2, 2 %	250 mmol/L NaCl	180	13	1-2 months batch experiments. UV-Colorimetry, IC, and ICP-OES XRD	Dissolution of the carbonate minerals. Feldspar dissolution leads to secondary carbonate and clay mineral formation. Boehmite and smectite formation also expected.	(Szabó et al., 2016)
38	Shale units in the Latrobe Group in the Gippsland Basin, Australia			66	15.17	3 months of exposure. XRD, SEM, NMR, MICP	Dissolution and precipitation kaolinite, natrojarosite, silica, and gypsum. reduction in the capillary threshold pressures and an increase in pore volume	(Rezaee et al., 2017)
39	Berea sandstone	Quartz 86%, kaolinite 2.51%, oligoclase 1.52%, clinochlore 1.08%, illite 4.58%, sanidine 4.20%	2 wt.% NaCl brine	60	13.8	Batch experiment QEMSCAN, Micro-CT, XRD, Surface Area Analysis (BET), ICP-MS	Quartz increased, illite decreased, porosity increased. The surface area increase is related to changes in pore volume and pore size.	(Kweon et al., 2017)
40	Longmaxi formation, Chang-7 member of	Quartz (62%, 23%), clay minerals (20%, 47.5%), feldspar (5.4%, 20.7%), calcite (3%, 3%),		80	15	10, 20, and 30 days experiments. Optical microscope, XRD, element analysis, LPGA, FTIR	A significant change in the nanopore structure of the system due to hydrocarbon extraction, mineral reactions,	(Pan et al., 2018)

#	BASIN/ FORMATION	MAJOR MINERALS	WATER TYPE/ IONIC STRENGTH	T (°C)	P (MPA)	METHODS/ ANALYSES USED	KEY OBSERVATIONS	REFERENCES
	the Yanchang Formation, China	Dolomite (4.8%, 3%), and pyrite (4.3%, 2.5%).					and clay and organic matter swelling. A decrease in pore surface area and volume in Longmaxi sample opposite to Chang-7 samples.	
41	Deep coal seams, Qinshui Basin in China	Sandstone and mudstone samples: quartz (48%, 19%), plagioclase (13%, 2%), k-feldspar (0%, 2%), calcite (0%, 2%), illite/smectite (25%, 54%), kaolinite (10%, 20%), chlorite (2%, 0%) biotite (2%, 1%).	1 M NaCl	160	15	3, 6, 9, and 12 days. Rock-CO_2- brine and CO_2-free tests. XRF, XRD, EMP, SEM+EDS.	Lithic sandstone: quartz, plagioclase, illite and chlorite increased considerably, whereas illite/smectite, biotite and kaolinite decreased. Calcareous mudstone: major mineralogical alteration.	(Wang et al., 2016)
42	Middle Bakken formation, Sanish field, North Dakota, USA	Two samples: quartz (29.21%, 47.85%), analbite (40.4%, 13.6%), calcite (24.2%, 6.5%), dolomite (4.9%, 21%), muscovite (-, 6.5%), clay (1.29%, 4.55%)		40	10.3	10-20-30-40days. Rock mechanical change, mineral alteration (XRD) and the pore structure properties' variation (LPNA)	Mesopore volume increased in sample 1 and decreased in samples 2. Surface area decreased. Quartz and muscovite increased, analbite, calcite, dolomite, and clay decreased.	(Wang et al., 2019)
43	Evergreen Formation, Surat Basin, Queensland, Australia	Quartz 27.3%, Orthoclase 6%, Na(Ca)plagioclase 14.7%, Illite/Muscovite M1 19%, Kaolinite 2%, Chlorite 1, Calcite 16.3%, Dolomite	Formation water	60	12	Reaction with CO_2 containing SO_2 SEM-EDS	Extensive calcite cement dissolution with the growth of gypsum in the formed pore space, barite precipitation on mineral surfaces.	(J. Pearce et al., 2018)

#	BASIN/ FORMATION	MAJOR MINERALS	WATER TYPE/ IONIC STRENGTH	T (°C)	P (MPA)	METHODS/ ANALYSES USED	KEY OBSERVATIONS	REFERENCES
		0.5%, Ca(Na)plagioclase 13%					Silica and aluminium rich precipitate was also observed coating grains	
44	Gothic Shale and Marine Tuscaloosa Formation	The Gothic Shale: silt-sized quartz, calcite, dolomite, and mica in a clay matrix of illite and smectite with authigenic pyrite. Marine Tuscaloosa: quartz 60%, feldspar 14%, chlorite 9%, kaolinite 5%, and illite 5%, with trace calcite 5%.	formation specific brine	160	15	45 days exposure to CO_2	Concentrations of iron, aqueous silica, and sulphate changed, Initial pH decreased. Carbonate and silicate dissolution enhanced. Marine Tuscaloosa Formation was more reactive than the Gothic Shale	(Miller et al., 2016)
45	Gothic Shale and Marine Tuscaloosa Formation	Gothic Shale, a carbonate mudstone is more carbonate-rich than Marine Tuscaloosa, a silica-rich mudstone.	Determined through geochemical modelling with sampling data as the starting point.	160	15	Autoclave reactor with brine and shale samples for 45 days with CO_2 and argon.	Pore connectivity and total porosity increased in the Gothic Shale. porosity increased but pore connectivity decreased in the Marine Tuscaloosa. increased porosity at length scales <200 nm led to increased pore connectivity.	(Mouzakis et al., 2016)

B. Modelling work on CO_2 sequestration

#	SANDSTONE TYPE/ BASIN	MAJOR MINERALS	WATER TYPE/ IONIC STRENGTH	T (°C)	P (MPA)	METHODS/ANALYSIS USED	KEY OBSERVATIONS	REFERENCE
1	Edmonton, Alberta, Canada	Two aquifer mineralogies: Carbonate aquifers (dolomite-calcite-quartz), siliciclastic aquifers (anorthite, chlorite, albite and K-feldspar)	two waters: brackish 4,000 ppm and a brine 100,000 ppm	25	15	SOLMINEQ.88 PATH.ubc GeoCalc	Brackish formation water took up more CO_2. In carbonate aquifers, significant amounts of clays increased CO_2 uptake a little. in siliciclastic aquifers, the maximum amount of CO_2 is trapped depending on type and amount of feldspars and clays	(Gunter et al., 1993)
2	Alberta Sedimentary Basin, Western Canada	Quartz (87%), K-feldspar (2%), plagioclase (1%), glauconite (5%), kaolinite (2%), calcite (1%), dolomite (1%), siderite (1%). average porosity of 12%	formation water (Na 28,800, K 690, Ca 2,970, Mg 578, HCO3 198, Cl 51,600 and SO4 366 mg/L, with a pH of 7.2)	54	26	Geochemical model PATHARC.94	It takes 6–40 years for chemical reactions to equilibrate	(Gunter et al., 1997)
3	Glauconitic Sandstone aquifer and Nisku carbonate aquifer of the Alberta Sedimentary Basin	Glauconitic Sandstone: 87% quartz, 2% K-feldspar, 1% albite, 5% annite, 2% kaolinite, 1% calcite, 1% dolomite and 1% siderite. Carbonate aquifer: dolomite and/or calcite (both containing traces of Fe), possibly accompanied by small amounts (< 1% in	Na: 28,800 mg/l K: 690 Ca: 2970 Mg: 578 HCO3: 198 Cl: 51,600 SO4: 366 pH: 7.2	54	26	PATHARC.94 100,000 and 1000 years	Aluminosilicate aquifers are better traps for CO_2 than carbonate aquifers. Nisku (carbonate) aquifer: The pH increased from 3 to 5; 0.00001 moles of siderite and 0.06 moles of calcite dissolved, and 0.02 moles of dolomite precipitated. Glauconitic Sandstone (silicate): The pH raised to 8;	(Gunter et al., 2000)

#	SANDSTONE TYPE/ BASIN	MAJOR MINERALS	WATER TYPE/ IONIC STRENGTH	T (°C)	P (MPA)	METHODS/ANALYSIS USED	KEY OBSERVATIONS	REFERENCE
		general) of anhydrite, illite, pyrite, and quartz.					Albite, K-feldspar and kaolinite also broke down and muscovite was synthesised; Precipitation of 1 mol of siderite, 0.05 mol of calcite and 0.02 mol of dolomite.	
4	Glauconitic sandstone aquifer of the Alberta Sedimentary Basin	Three different rock types (a glauconitic sandstone, a common sedimentary rock, and dunite)	1M NaCl	54	26	Batch reaction modelling by TOUGHREACT up to 15,000 years	Precipitation of illite, K-feldspar, siderite, ankerite, dawsonite, and dolomite. The precipitation of ankerite and siderite is sensitive to goethite or glauconite. The accumulation of carbonates leads to a considerable decrease in porosity.	(Xu et al., 2000b, 2004)
5	Sandstone from Gulf Coast, USA	Quartz (58%), kaolinite (2%), calcite (2%), illite (1%), oligoclase (20%), K-feldspar (8%), chlorite (5%), average porosity of 10%	1M NaCl	75	20	Simulation with TOUGHREACT up to 100,000 years	Product solid phases: illite, dawsonite, and ankerite, whereas calcite and siderite initially precipitated and then re-dissolved.	(Xu et al., 2003, 2005)
6	Permian White Rims Sandstone with a thickness of 61-244 m, high porosity and permeability and lying at over 1 km depth	Quartz (77% by volume), kaolinite (2.25%), Na-smectite (2.25%), calcite (1.8%), anorthite (0.66%), albite (0.60%), K-feldspar (0.60%), porosity 15%.	3M NaCl equilibrated with the reservoir minerals	54	26	Reactive transport modelling by ChemTOUGH (30 years injection simulation, 1,000 years reaction time)	21% of the injected CO_2 was trapped in carbonate minerals (calcite and dawsonite), 52% was present underground as a separate gas phase or dissolved in ground-waters, and 17% had leaked to the ground surface	(White et al., 2005)

#	SANDSTONE TYPE/ BASIN	MAJOR MINERALS	WATER TYPE/ IONIC STRENGTH	T (°C)	P (MPA)	METHODS/ANALYSIS USED	KEY OBSERVATIONS	REFERENCE
7	Sleipner site, Norwegian part of the North Sea	Illite (24.7 wt. %), chalcedony (21.5%), kaolinite (18.0%), plagioclase (12.4%), a high-FeMg smectite (8.8%), 14 Å-clinochlore (4.1%), pyrite (2.8%), K-feldspar (2.1%), siderite (1.6%) and calcite (1.0%). Initial porosity was set to 5%	Equilibrating an aqueous solution containing 0.479M chloride with caprock minerals at 37°C	37	10.1	PHREEQC v2.6 reaction path modelling (both in stoichiometric mode and in the time frame) and reactive transport modelling	Main secondary carbonate mineral is calcite accompanied by a limited amount of dawsonite in all the three runs with different plagioclase composition.	Gaus et al. (2005)
8	Bunter sandstones, Bunter Aquifer, North Sea	Quartz (49.5%), annite (24%), feldspar (12.5%), calcite (3%), hematite (3%), dolomite (3%), pyrite (1%)	Saline water with 303 g/L NaCl salinity	66	15.7	Chemical modelling	Dissolution of annite and feldspar. No other mineral precipitation during the first 10,000 years of injection	Lagneau, 2005
9	Frio Formation, Texas, USA	Sandstone reservoir: 88.5% quartz, 9% K-feldspar, 1% calcite, 0.5% siderite, 0.5% pyrite and 0.5% muscovite. Carbonate reservoir: 49.25% calcite, 49.25% dolomite, 0.75% siderite and 0.75% pyrite.	0.7 m NaCl and reservoir fluid	64	10	Reaction progress models and reactive transport simulators (CRUNCH) 84.3 b CO_2 fugacity	Formation of calcite, magnesite, and dawsonite. Addition of H_2S and SO_2 to CO_2 injection does not alter the total carbon intake after 100 years.	(Knauss et al., 2005)
10		Reservoir: calcite 12%, dolomite 4%, quartz 35%, illite 2%, K-				Batch, 1D and 2D reactive transport simulations	Porosity reduction when caprock was homogeneous. In the case of	(Gherardi et al., 2007)

#	SANDSTONE TYPE/ BASIN	MAJOR MINERALS	WATER TYPE/ IONIC STRENGTH	T (°C)	P (MPA)	METHODS/ANALYSIS USED	KEY OBSERVATIONS	REFERENCE
		feldspar 5%, chlorite 9%, albite 14%, kaolinite 3%, Na-smectite 1%, Muscovite 16% Caprock: calcite 29%, dolomite 4%, quartz 20%, illite 2%, chlorite 6%, kaolinite 5%, Na-smectite 15%, muscovite 19%				TOUGH-REACT	fractured caprock, porosity was enhanced	
11	sandstone take from U.S. Gulf coast sediment					Modified TOUGH-REACT study of coupled behaviour of geochemical reactions and convective mixing	Coupled behaviour of geochemical reactions and convective mixing causes CO_2 dissolution in the aquifer to be largely enhanced, reducing the risk of CO_2 back-migration to the atmosphere.	(Ennis-King et al., 2007)
12	Bunter sandstone	Quartz (65.7%), K-feldspar (17.4%), albite (7.9%), illite (4.9%), dolomite (1.6%), hematite, halite and kaolinite < 1% porosity 14.5%	1M NaCl Solution	60	15	PHREEQC (version 2.12.1 equilibrium calculation and kinetic model	High concentrations of Ca and Mg due to rapid solution dolomite. Very low Al due to precipitation of montmorillonite, dawsonite, albite, and kaolinite. Only quartz, kaolinite, dawsonite, and Al-hydroxides reach values near saturation	(Wigand et al., 2008)
13	Chinle Shale, Utah, USA, Comblanchien Formation, Paris basin, France	a) I/S 40%, quartz 40%, calcite 10%, hematite 7%, and dolomite 3% b) Calcite 45%, I/S 15%, kaolinite 10%, quartz	NaCl brine 0.25M	80		Reaction path modelling 10,000 years 1) rock-brine 2) rock- $CO_{2\ (aq)}$	1) a) rock- brine: no kaolinite precipitation and pH increase. 1) b) pH increased, dolomite dissolved, calcite dissolved and re-precipitated.	(Credoz et al., 2009)

#	SANDSTONE TYPE/ BASIN	MAJOR MINERALS	WATER TYPE/ IONIC STRENGTH	T (°C)	P (MPA)	METHODS/ANALYSIS USED	KEY OBSERVATIONS	REFERENCE
		10%, gypsum 5%, pyrite 5%, others 5%.				3) rock- $CO_{2\ (sc)}$	2) a+b) pH increased, calcite dissolution buffered CO_2 dissolution, Ca-montmorillonite to montmorillonite-Na. 3) a+b) pH increased, calcite and dolomite dissolution.	
14	Rio Bonito Formation (Permian), southern Brazil	3 samples: quartz (67%), kaolinite (6.7, 0, 6.7%), calcite (4.7, 13.7, 0%), dolomite (0, 0, 5.3), K-feldspar (4, 5, 4.7%), albite (1.4, 0, 1.4), pyrite (0, 1.4, 0.4),	Pure deionized water	200	8.05	CO_2 fugacity of 80.5 bar. PHREEQC V.2.8	pH is lowered to 5.36 Complete dissolution of feldspars and partial dissolution of carbonates (calcite, dolomite). Kaolinite precipitated.	(Ketzer et al., 2009)
15	Rotliegend sandstone, Nederland (At 3 km depth)	Quartz (58%), K-feldspar (8%), dolomite (16%), kaolinite (3.5%), illite (0.7%)	Rotliegend Formation water of 100,000 ppm salinity	50	28	0–10,000-year simulation time	Small amounts of kaolinite and dolomite precipitated. The contribution of mineral trapping is insignificant. Mobility trapping and solubility trapping are the main trapping mechanisms for CO2 storage	(Ranganathan et al., 2011)
16	Mt. Simon sandstone aquifer					10m thick sandstone layer located at a 2km depth 10,000 years simulation	Hydrodynamic and solubility trapping processes were complete by 10,000 years feldspar dissolution precipitation of alunite and anhydrite	Liu et al. (2011)
17						PHREEQC		(Pham et al., 2011)
18	Gippsland Basin	12 samples with average quartz 52.6%,	Equilibrated water with Na	53-84	11.5-19.1	100 years GWB	Dissolution of siderite, chlorite, and K-feldspar and precipitation	(Kirste, 2013)

#	SANDSTONE TYPE/ BASIN	MAJOR MINERALS	WATER TYPE/ IONIC STRENGTH	T (°C)	P (MPA)	METHODS/ANALYSIS USED	KEY OBSERVATIONS	REFERENCE
		K-feldspar 4.7%, siderite 2.3%, pyrite 0.3%, natrojarosite 1.9%, illite 12.7%, kaolinite 21.3%, chlorite 2.4%, and porosity 10%	573, K 12 Ca 25, Cl 504, SO_4 123, HCO_3 678, Al 0.002, Fe 0.106. SiO_2 29.7 mg/L				of kaolinite, siderite, magnesite, and SiO2	
19	Pannonian Basin, Hungary	MS1, S1, S2 samples: Quartz 49, 34, 15%, K-feldspar 2, 1, 2%, Plagioclase 3, 3, 0%, Illite/muscovite 32, 26, 25%, kaolinite 5, 5, 4%, Chlorite 9, 0, 0%, Calcite 0, 12, 1%, Dolomite 0, 14, 0%, Ankerite 0 ,0, 49%, Siderite 0, 2, 2 %	250 mmol/L NaCl	180	13	Kinetic geochemical modelling with PHREEQC	Feldspar dissolution which led to secondary carbonate and clay mineral formation. Boehmite and smectite formation also expected.	(Szabó et al., 2016)
20	Evergreen Formation, Surat Basin, Queensland, Australia	Quartz 27.3%, Orthoclase 6%, Na(Ca)plagioclase 14.7%, Illite/Muscovite M1 19%, Kaolinite 2%, Chlorite 1, Calcite 16.3%, Dolomite 0.5%, Ca(Na)plagioclase 13%	Formation water	60	12	30 or 100 years	Kinetic geochemical modelling of the experimental data: calcite and chlorite dissolution, with gypsum, kaolinite, goethite, smectite and barite precipitation. A decrease in porosity. Increased reactive surface areas: Calcite, siderite, chlorite and plagioclase were the main minerals dissolving. Smectite, siderite, ankerite, hematite and kaolinite were predicted to precipitate, with SO_2 sequestered	(J. Pearce et al., 2018)

#	SANDSTONE TYPE/ BASIN	MAJOR MINERALS	WATER TYPE/ IONIC STRENGTH	T (°C)	P (MPA)	METHODS/ANALYSIS USED	KEY OBSERVATIONS	REFERENCE
							as anhydrite, alunite, and pyrite. Minimal porosity change.	
21	Jianghan Basin, China	Mudstone: Illite 67.2%, chlorite 7.6%, chlorite/smectite mixed 0.4%, illite/smectite mixed 23.2%, kaolinite 1.4%		47	10.1	one-dimensional model vertical model TOUGHREACT	Dissolution of K-feldspar and albite plays a key role in the variation of caprock permeability. Permeability increased by 60% at the bottom of caprock after 5000 years. A positive correlation of temperature with dissolution. A negative correlation of common-ion effect resulted from increased salinity, with mineral dissolution.	(Li et al., 2019)
22	Baltic Sea region	Shale sample: chlorite 12.4%, quartz 37%, albite 8%, orthoclase 3.5%, calcite 5.4%, dolomite 7%, muscovite 24%, pyrite 2.4% and organic matter.	synthetic brine 105 g/l concentration of NaCl saturated with carbon dioxide (0.8 mol CO_2/kg of solution)	50	10	Batch experiments and 2D computer modelling with ToughReact	Very fast calcite dissolution, then reverse process of calcite precipitation. Dissolution of dolomite	(Labus et al., 2017)
23	Newcastle formation, County of Crook, State of Wyoming, USA	pure SWy2 Na-montmorillonite clay	pure, deionized water with less than 6.7×10^{-2} µS⁄cm electric conductance	80	10	Kinetic geochemical modelling with PHREEQC	Fast reaction of Na-montmorillonite. Cation Exchange Capacity was the deciding factor. A minor proportion of other ions, as well as the main interlayer cations, took part in cation exchange.	(Falus et al., 2019)

#	SANDSTONE TYPE/ BASIN	MAJOR MINERALS	WATER TYPE/ IONIC STRENGTH	T (°C)	P (MPA)	METHODS/ANALYSIS USED	KEY OBSERVATIONS	REFERENCE
24	Little Grand Wash Fault, Green River, Utah	illite, quartz, dolomite, K-feldspar, gypsum and hematite, with a significant clay fraction	mixtures of Na-Cl-SO4 brine and meteoric groundwater			10^5 years	Dissolution of hematite, dolomite and K-feldspar and precipitation of Fe-bearing dolomite, gypsum, pyrite and illite over centimetre length-scales	(Kampman et al., 2017)

Appendix II.

A. Photos of core samples as received from the core library.

Core samples from Harvey-3 well. Depths are in meters.

Drilled date: 07/03/2015 to 24/06/2016

Well location easting (MGA zone 50): 387,392.24, Northing: 6,343,895.95

Ground elevation (AHD): 20.20m

Total depth: 1550.2m, Cored section: 584- 1550m.


Sample #5
Depth: 1187.60
Well: Harvey 3A
0.0 cm
10.0 cm


Sample #6
Depth: 1169.30
Well: Harvey 3A
0.0 cm
10.0 cm


Sample #7
Depth: 1046.60
Well: Harvey 3A
0.0 cm
10.0 cm


Sample #8
Depth: 940.65
Well: Harvey 3A
0.0 cm
10.0 cm


Sample #9
Depth: 916.30
Well: Harvey 3A
0.0 cm
10.0 cm


Sample #10
Depth: 887.15
Well: Harvey 3A
0.0 cm
10.0 cm

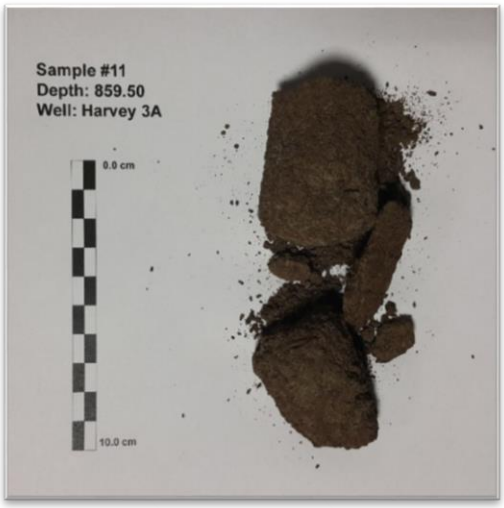
Sample #11
Depth: 859.50
Well: Harvey 3A
0.0 cm
10.0 cm


Sample #12
Depth: 823.10
Well: Harvey 3A
0.0 cm
10.0 cm


Sample #13
Depth: 766.10
Well: Harvey 3A
0.0 cm
10.0 cm


Sample #14
Depth: 738.20
Well: Harvey 3A
0.0 cm
10.0 cm


Sample #15
Depth: 725.20
Well: Harvey 3A
0.0 cm
10.0 cm

Appendix III. XRD

A. Changes in mineral contents

Before (Blue) and after four- (Red) and nine- (Grey) months exposure to $scCO_2$.

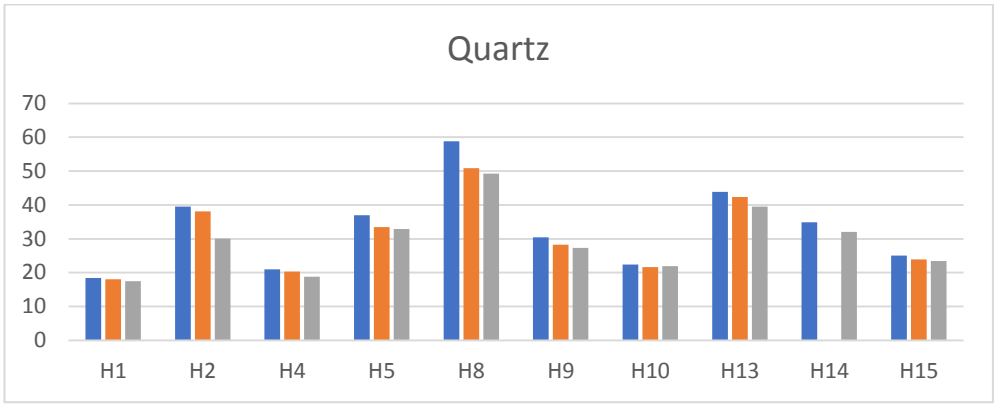

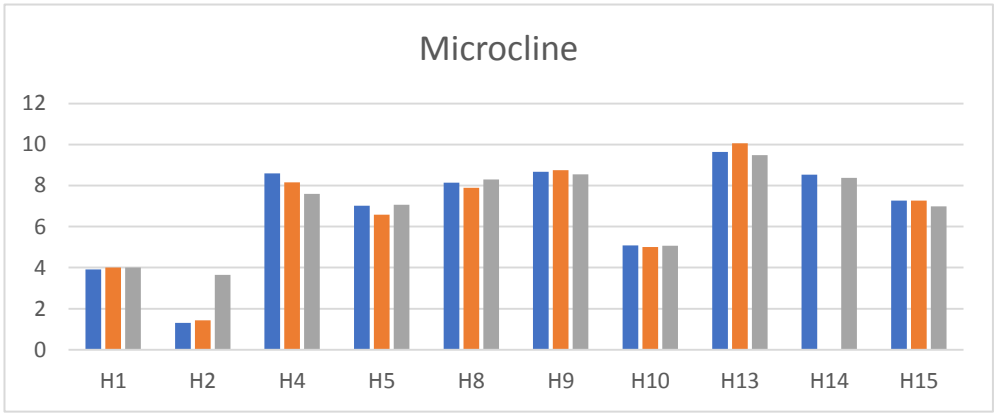

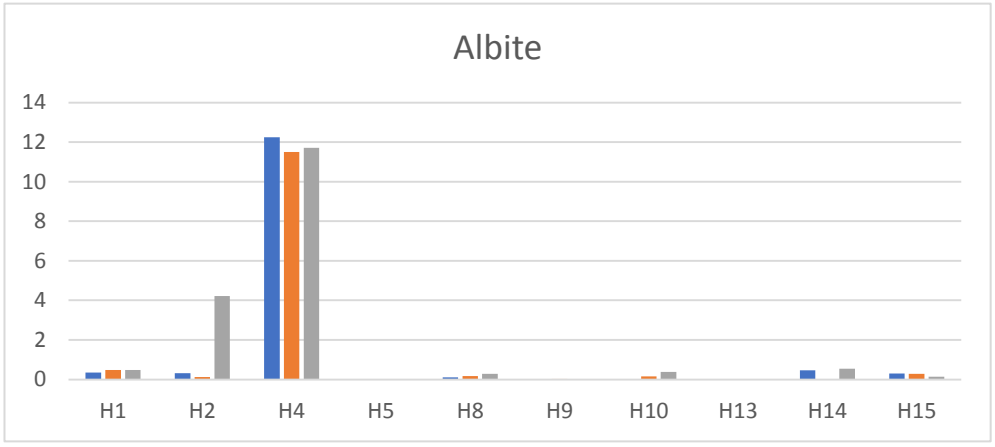

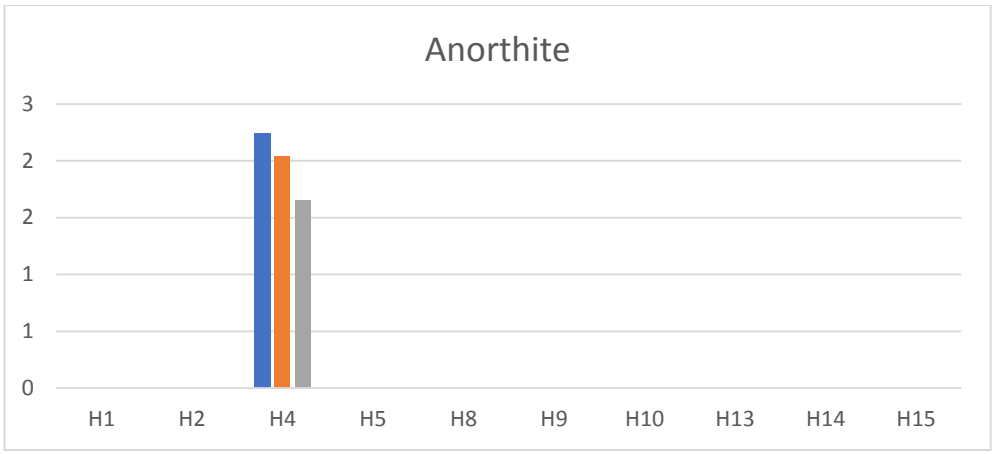
Anorthite
3
2
2
1
1
0
H1
H2
H4
H5
H8
H9
H10
H13
H14
H15

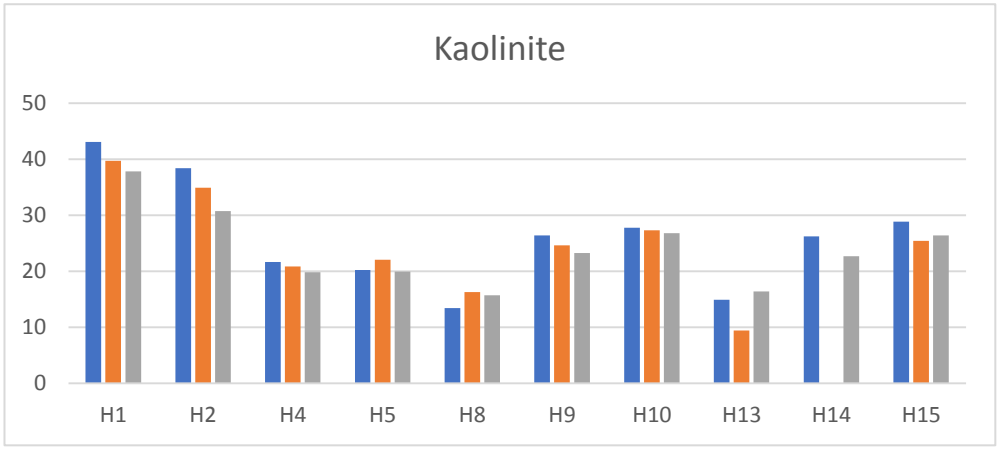
Kaolinite
50
40
30
20
10
0
H1
H2
H4
H5
H8
H9
H10
H13
H14
H15

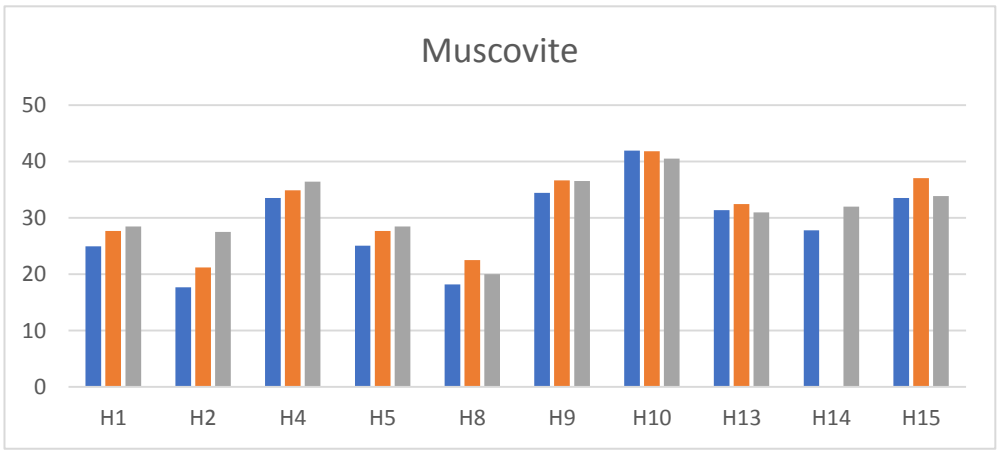
Muscovite
50
40
30
20
10
0
H1
H2
H4
H5
H8
H9
H10
H13
H14
H15

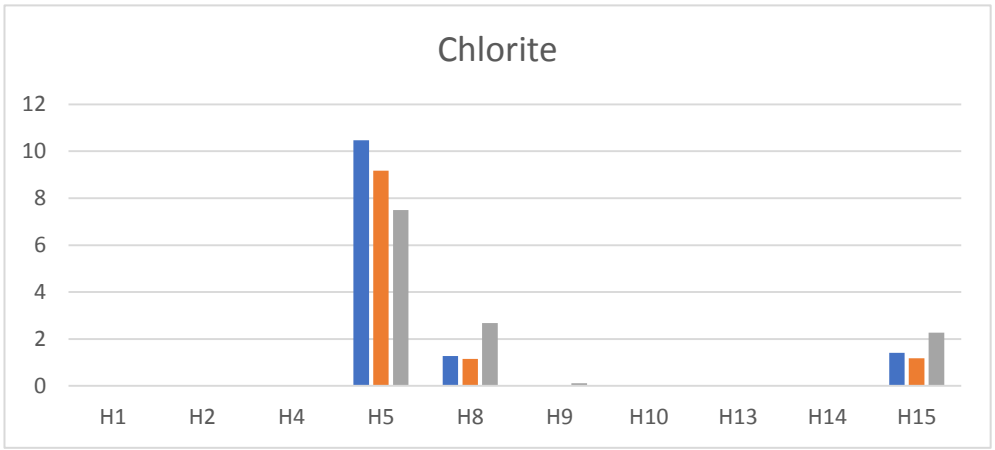
Chlorite
12
10
8
6
4
2
0
H1
H2
H4
H5
H8
H9
H10
H13
H14
H15

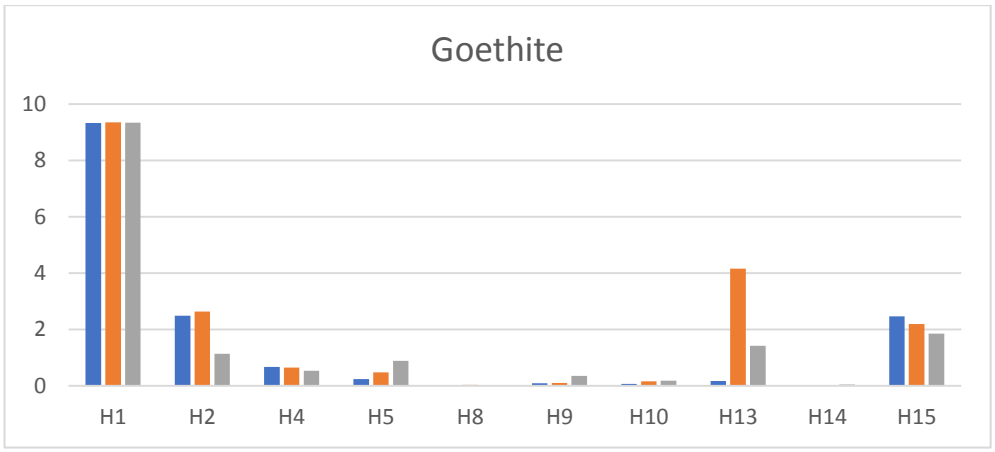
Goethite
10
8
6
4
2
0
H1
H2
H4
H5
H8
H9
H10
H13
H14
H15

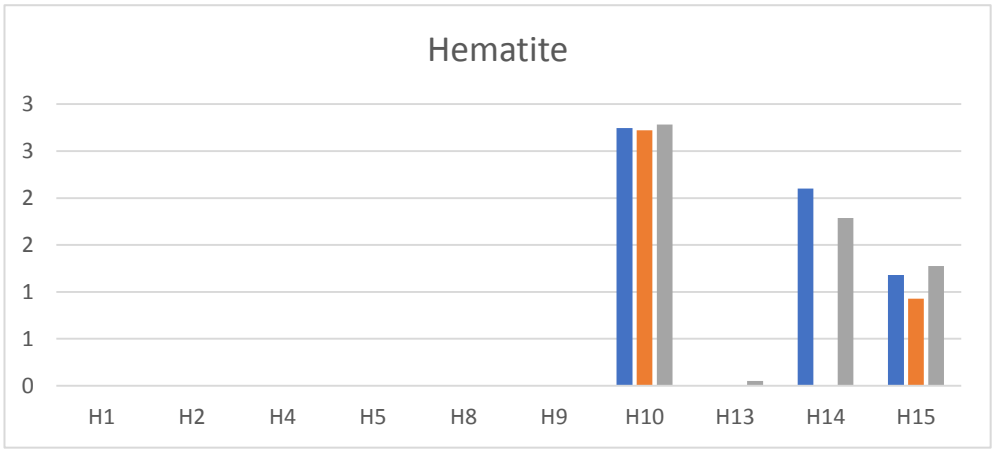
Hematite
3
3
2
2
1
1
0
H1
H2
H4
H5
H8
H9
H10
H13
H14
H15

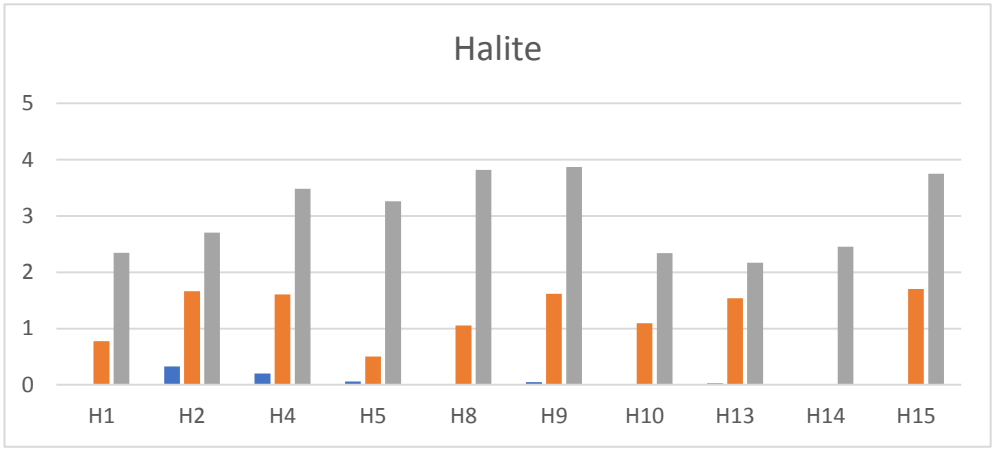
Halite
5
4
3
2
1
0
H1
H2
H4
H5
H8
H9
H10
H13
H14
H15

B. XRD diffractogram and phase ID of before reaction samples

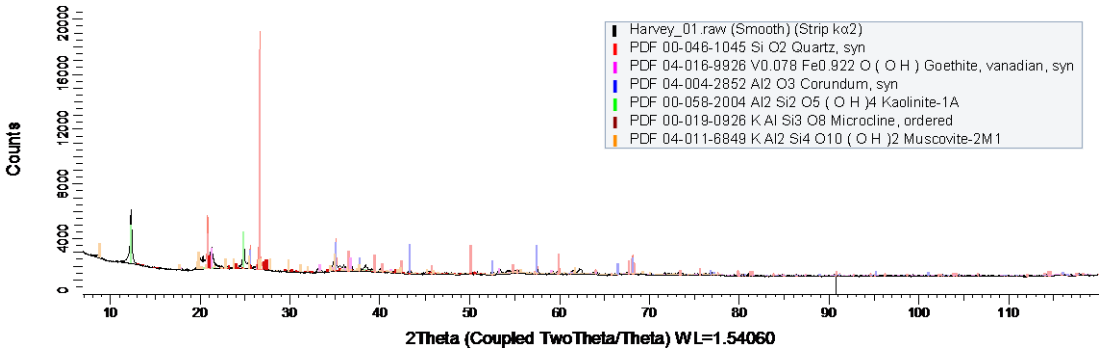

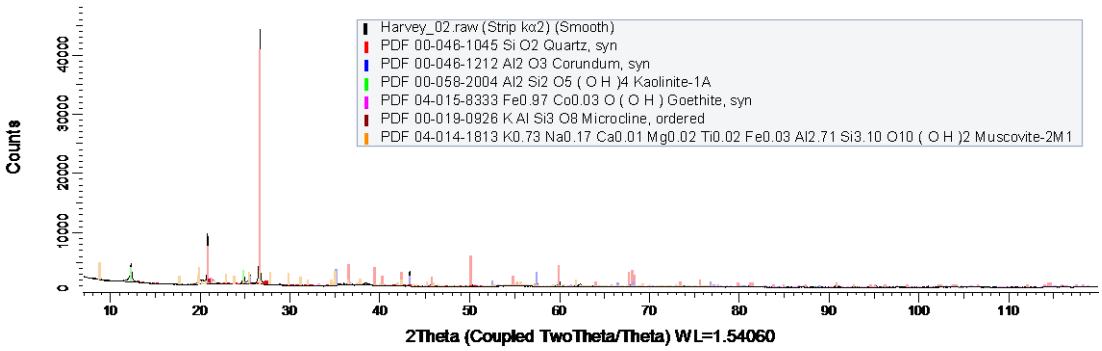

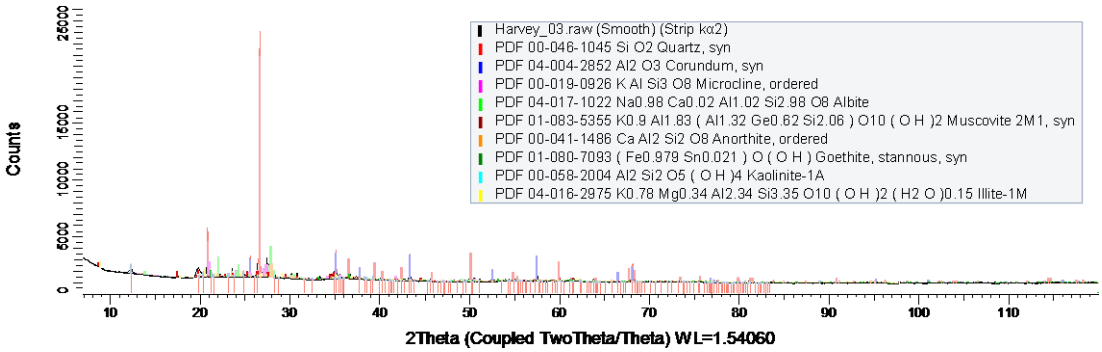

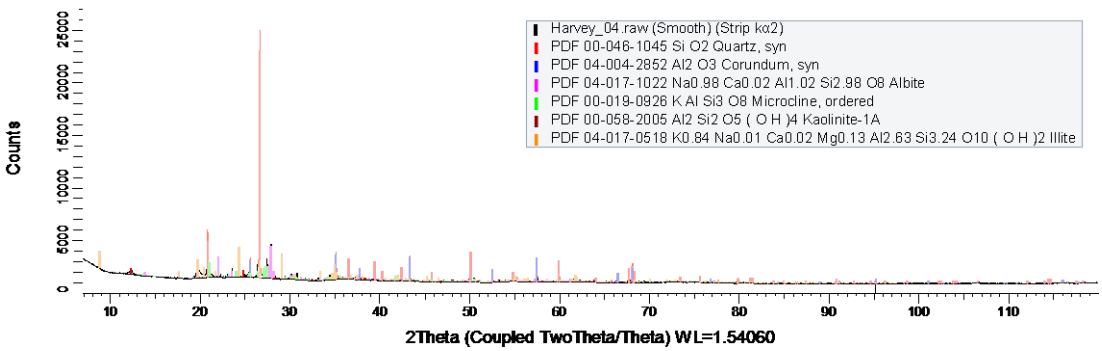

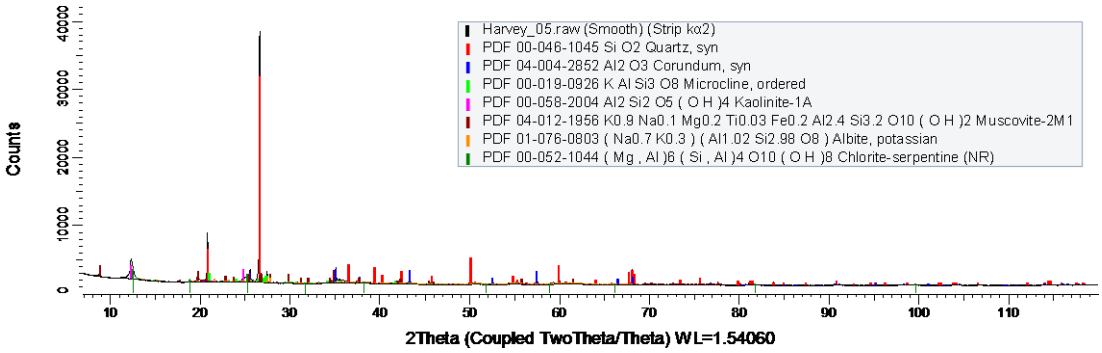
Harvey_05.raw (Smooth) (Strip kα2)
PDF 00-046-1045 Si O2 Quartz, syn
PDF 04-004-2852 Al2 O3 Corundum, syn
PDF 00-019-0926 K Al Si3 O8 Microcline, ordered
PDF 00-058-2004 Al2 Si2 O5 (O H)4 Kaolinite-1A
PDF 04-012-1956 K0.9 Na0.1 Mg0.2 Ti0.03 Fe0.2 Al2.4 Si3.2 O10 (O H)2 Muscovite-2M1
PDF 01-076-0803 (Na0.7 K0.3) (Al1.02 Si2.98 O8) Albite, potassian
PDF 00-052-1044 (Mg , Al)6 (Si , Al)4 O10 (O H)8 Chlorite-serpentine (NR)
Counts
2Theta (Coupled TwoTheta/Theta) WL=1.54060

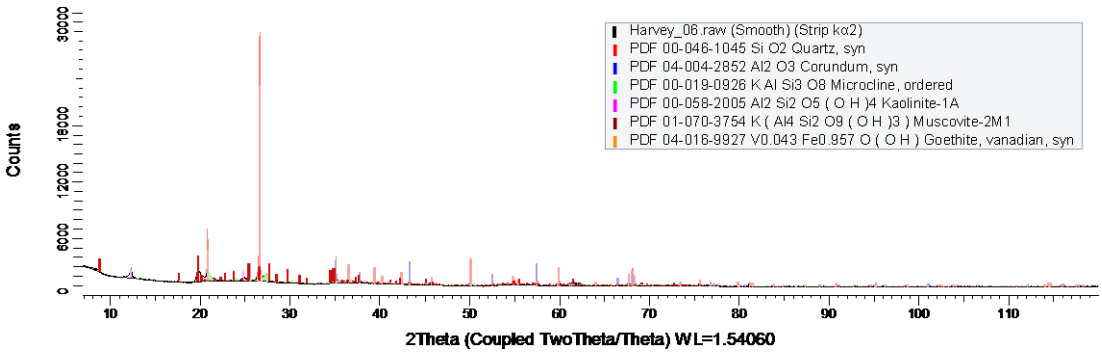
Harvey_06.raw (Smooth) (Strip kα2)
PDF 00-046-1045 Si O2 Quartz, syn
PDF 04-004-2852 Al2 O3 Corundum, syn
PDF 00-019-0926 K Al Si3 O8 Microcline, ordered
PDF 00-058-2005 Al2 Si2 O5 (O H)4 Kaolinite-1A
PDF 01-070-3754 K (Al4 Si2 O9 (O H)3) Muscovite-2M1
PDF 04-016-9927 V0.043 Fe0.957 O (O H) Goethite, vanadian, syn
Counts
2Theta (Coupled TwoTheta/Theta) WL=1.54060

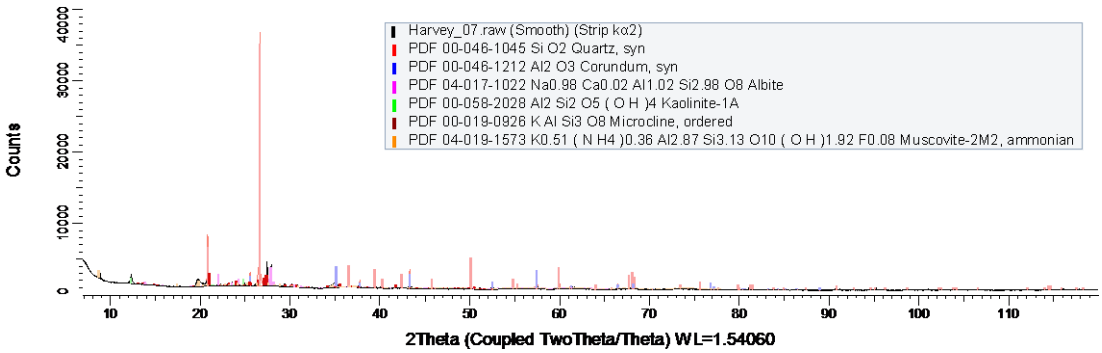
Harvey_07.raw (Smooth) (Strip kα2)
PDF 00-046-1045 Si O2 Quartz, syn
PDF 00-046-1212 Al2 O3 Corundum, syn
PDF 04-017-1022 Na0.98 Ca0.02 Al1.02 Si2.98 O8 Albite
PDF 00-058-2028 Al2 Si2 O5 (O H)4 Kaolinite-1A
PDF 00-019-0926 K Al Si3 O8 Microcline, ordered
PDF 04-019-1573 K0.51 (N H4)0.36 Al2.87 Si3.13 O10 (O H)1.92 F0.08 Muscovite-2M2, ammonian
Counts
2Theta (Coupled TwoTheta/Theta) WL=1.54060

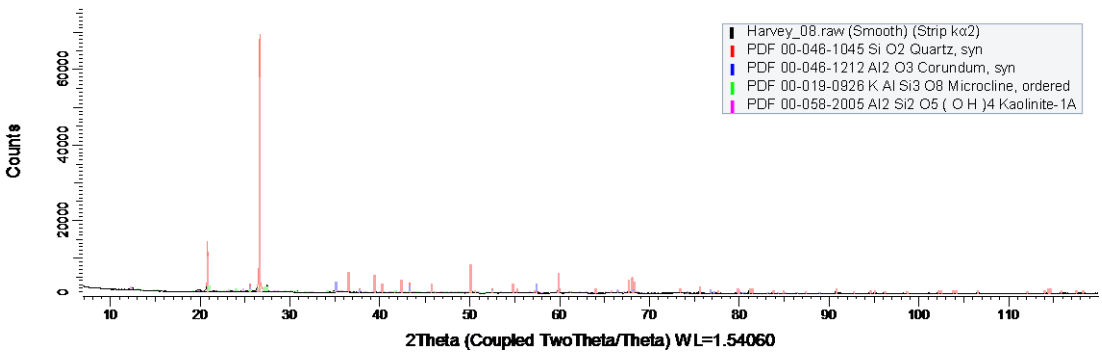
Harvey_08.raw (Smooth) (Strip kα2)
PDF 00-046-1045 Si O2 Quartz, syn
PDF 00-046-1212 Al2 O3 Corundum, syn
PDF 00-019-0926 K Al Si3 O8 Microcline, ordered
PDF 00-058-2005 Al2 Si2 O5 (O H)4 Kaolinite-1A
Counts
2Theta (Coupled TwoTheta/Theta) WL=1.54060

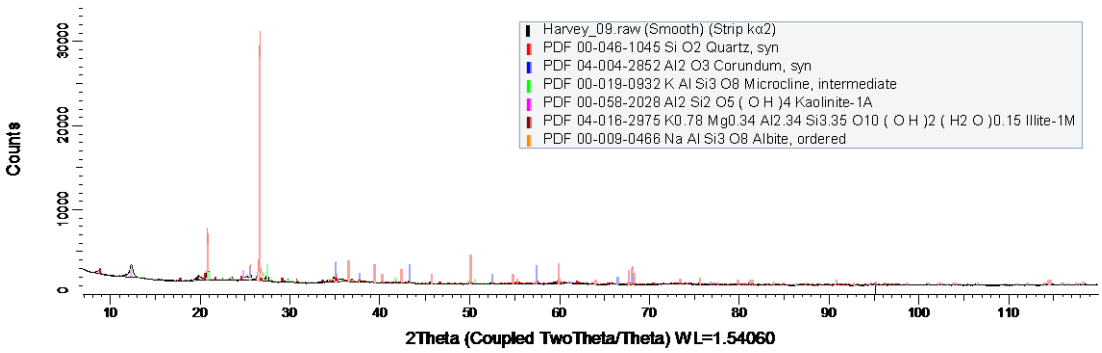
Harvey_09.raw (Smooth) (Strip kα2)
PDF 00-046-1045 Si O2 Quartz, syn
PDF 04-004-2852 Al2 O3 Corundum, syn
PDF 00-019-0932 K Al Si3 O8 Microcline, intermediate
PDF 00-058-2028 Al2 Si2 O5 (O H)4 Kaolinite-1A
PDF 04-016-2975 K0.78 Mg0.34 Al2.34 Si3.35 O10 (O H)2 (H2 O)0.15 Illite-1M
PDF 00-009-0466 Na Al Si3 O8 Albite, ordered
Counts
2Theta (Coupled TwoTheta/Theta) WL=1.54060

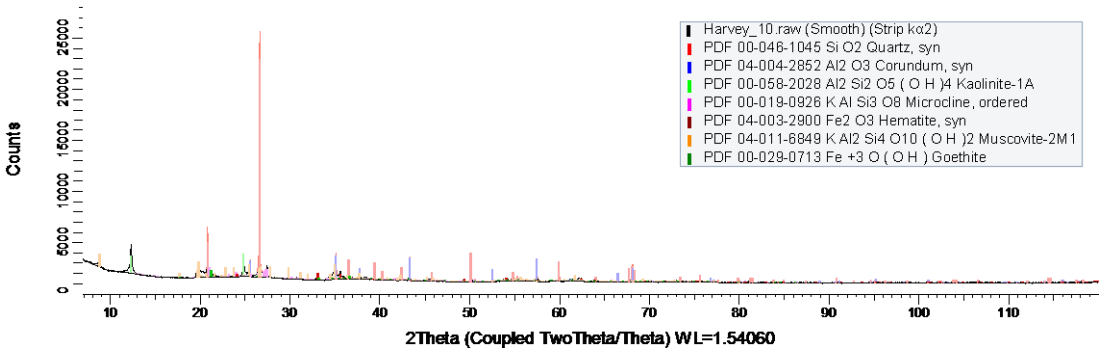
Harvey_10.raw (Smooth) (Strip kα2)
PDF 00-046-1045 Si O2 Quartz, syn
PDF 04-004-2852 Al2 O3 Corundum, syn
PDF 00-058-2028 Al2 Si2 O5 (O H)4 Kaolinite-1A
PDF 00-019-0926 K Al Si3 O8 Microcline, ordered
PDF 04-003-2900 Fe2 O3 Hematite, syn
PDF 04-011-6849 K Al2 Si4 O10 (O H)2 Muscovite-2M1
PDF 00-029-0713 Fe +3 O (O H) Goethite
Counts
2Theta (Coupled TwoTheta/Theta) WL=1.54060

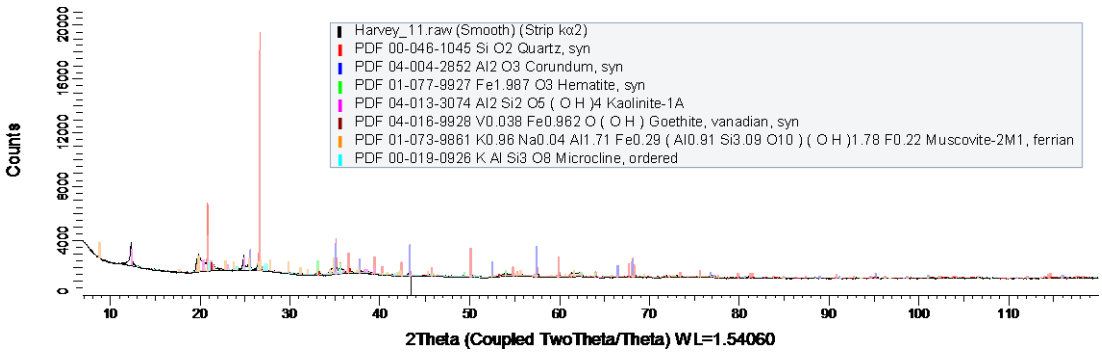
Harvey_11.raw (Smooth) (Strip kα2)
PDF 00-046-1045 Si O2 Quartz, syn
PDF 04-004-2852 Al2 O3 Corundum, syn
PDF 01-077-9927 Fe1.987 O3 Hematite, syn
PDF 04-013-3074 Al2 Si2 O5 (O H)4 Kaolinite-1A
PDF 04-016-9928 V0.038 Fe0.962 O (O H) Goethite, vanadian, syn
PDF 01-073-9861 K0.96 Na0.04 Al1.71 Fe0.29 (Al0.91 Si3.09 O10) (O H)1.78 F0.22 Muscovite-2M1, ferrian
PDF 00-019-0926 K Al Si3 O8 Microcline, ordered
Counts
2Theta (Coupled TwoTheta/Theta) WL=1.54060

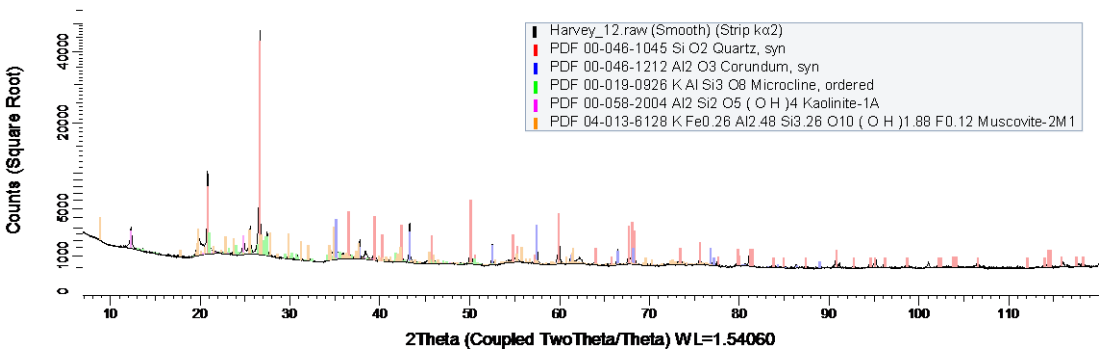
Harvey_12.raw (Smooth) (Strip kα2)
PDF 00-046-1045 Si O2 Quartz, syn
PDF 00-046-1212 Al2 O3 Corundum, syn
PDF 00-019-0926 K Al Si3 O8 Microcline, ordered
PDF 00-058-2004 Al2 Si2 O5 (O H)4 Kaolinite-1A
PDF 04-013-6128 K Fe0.26 Al2.48 Si3.26 O10 (O H)1.88 F0.12 Muscovite-2M1
Counts (Square Root)
2Theta (Coupled TwoTheta/Theta) WL=1.54060

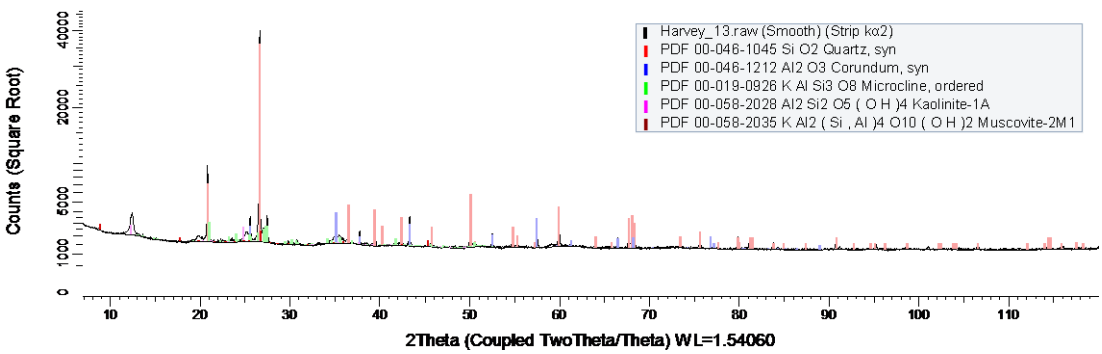
Harvey_13.raw (Smooth) (Strip kα2)
PDF 00-046-1045 Si O2 Quartz, syn
PDF 00-046-1212 Al2 O3 Corundum, syn
PDF 00-019-0926 K Al Si3 O8 Microcline, ordered
PDF 00-058-2028 Al2 Si2 O5 (O H)4 Kaolinite-1A
PDF 00-058-2035 K Al2 (Si , Al)4 O10 (O H)2 Muscovite-2M1
Counts (Square Root)
2Theta (Coupled TwoTheta/Theta) WL=1.54060

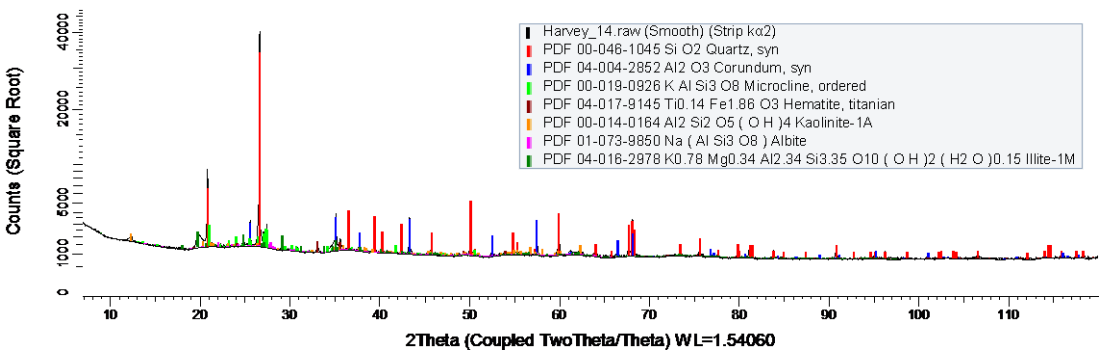
Harvey_14.raw (Smooth) (Strip kα2)
PDF 00-046-1045 Si O2 Quartz, syn
PDF 04-004-2852 Al2 O3 Corundum, syn
PDF 00-019-0926 K Al Si3 O8 Microcline, ordered
PDF 04-017-9145 Ti0.14 Fe1.86 O3 Hematite, titanian
PDF 00-014-0164 Al2 Si2 O5 (O H)4 Kaolinite-1A
PDF 01-073-9850 Na (Al Si3 O8) Albite
PDF 04-016-2978 K0.78 Mg0.34 Al2.34 Si3.35 O10 (O H)2 (H2 O)0.15 Illite-1M
Counts (Square Root)
2Theta (Coupled TwoTheta/Theta) WL=1.54060

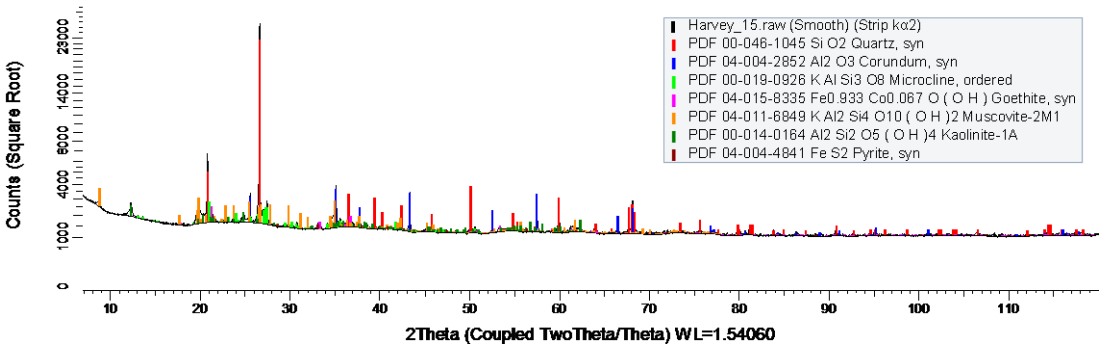
Harvey_15.raw (Smooth) (Strip kα2)
PDF 00-046-1045 Si O2 Quartz, syn
PDF 04-004-2852 Al2 O3 Corundum, syn
PDF 00-019-0926 K Al Si3 O8 Microcline, ordered
PDF 04-015-8335 Fe0.933 Co0.067 O (O H) Goethite, syn
PDF 04-011-6849 K Al2 Si4 O10 (O H)2 Muscovite-2M1
PDF 00-014-0164 Al2 Si2 O5 (O H)4 Kaolinite-1A
PDF 04-004-4841 Fe S2 Pyrite, syn
Counts (Square Root)
0
1000
4000
8000
14000
23000
10
20
30
40
50
60
70
80
90
100
110
2Theta (Coupled TwoTheta/Theta) WL=1.54060

C. XRD diffractogram and phase ID of after 9 months reaction samples

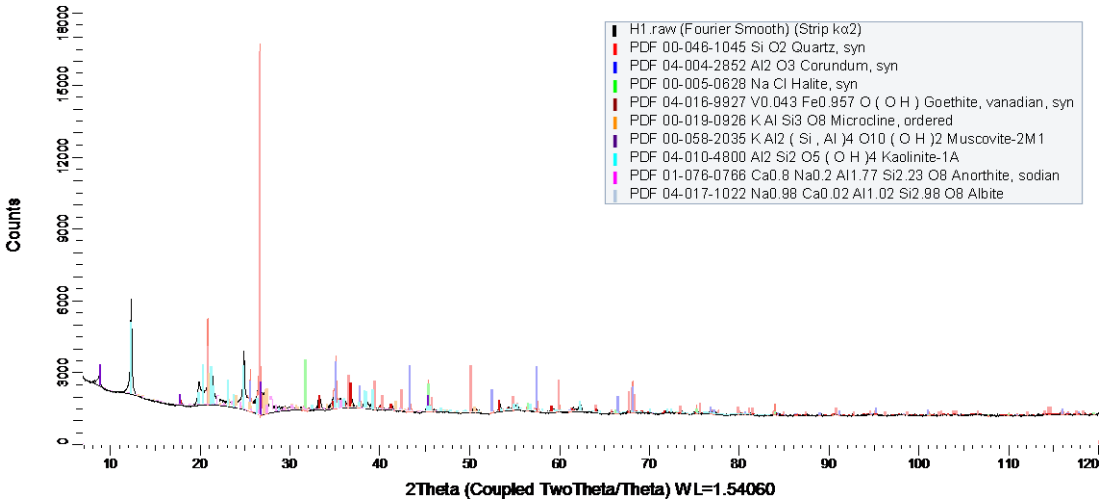

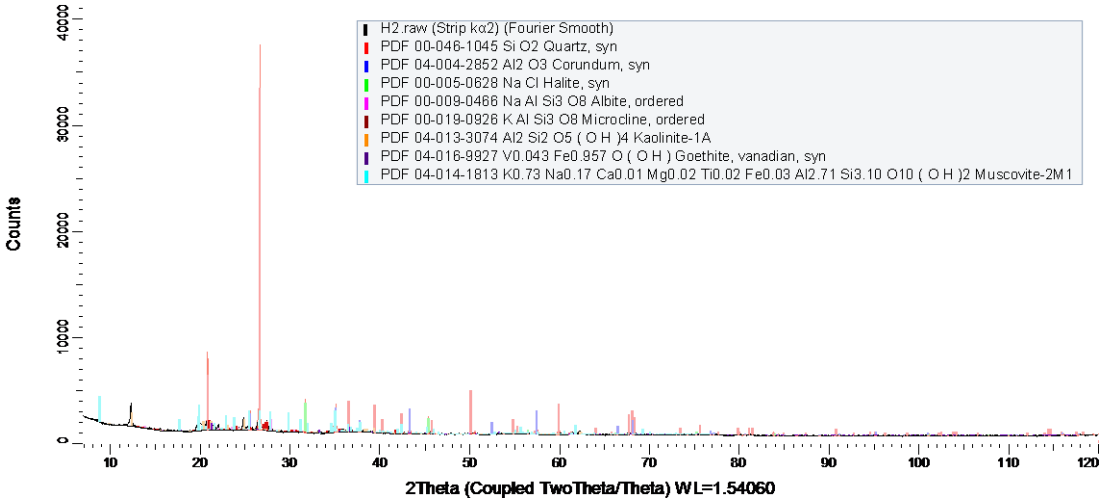

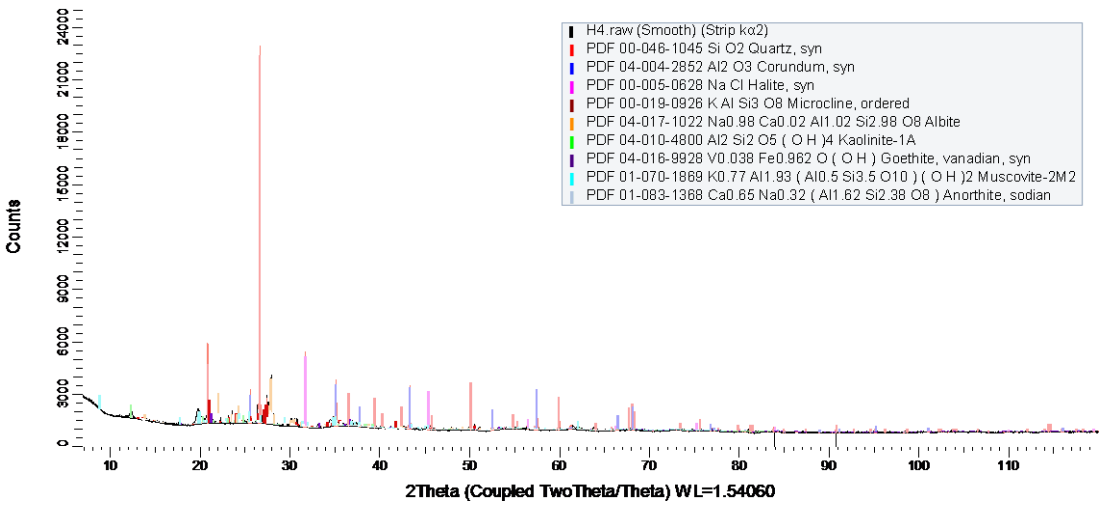

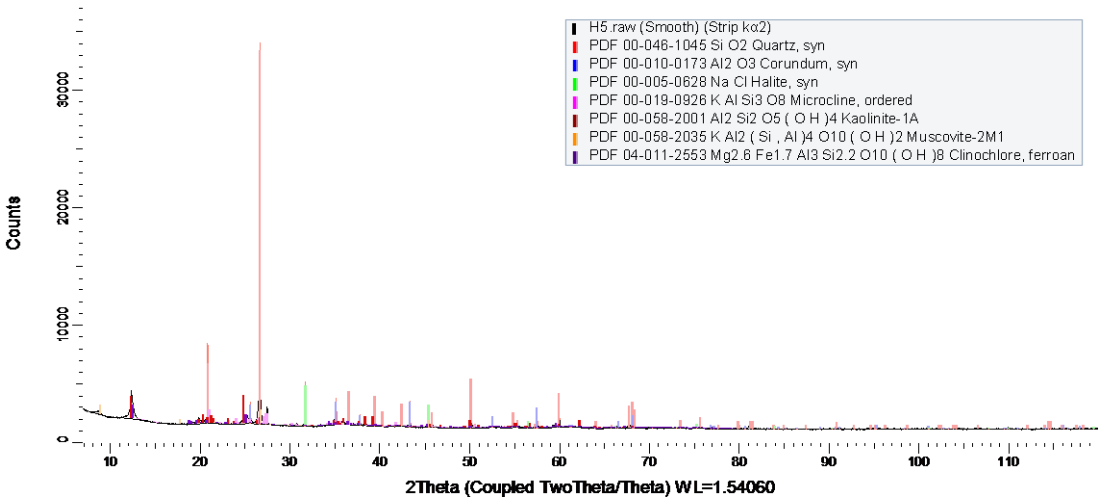
H5.raw (Smooth) (Strip kα2)
PDF 00-046-1045 Si O2 Quartz, syn
PDF 00-010-0173 Al2 O3 Corundum, syn
PDF 00-005-0628 Na Cl Halite, syn
PDF 00-019-0926 K Al Si3 O8 Microcline, ordered
PDF 00-058-2001 Al2 Si2 O5 (O H)4 Kaolinite-1A
PDF 00-058-2035 K Al2 (Si , Al)4 O10 (O H)2 Muscovite-2M1
PDF 04-011-2553 Mg2.6 Fe1.7 Al3 Si2.2 O10 (O H)8 Clinochlore, ferroan
Counts
2Theta (Coupled TwoTheta/Theta) WL=1.54060

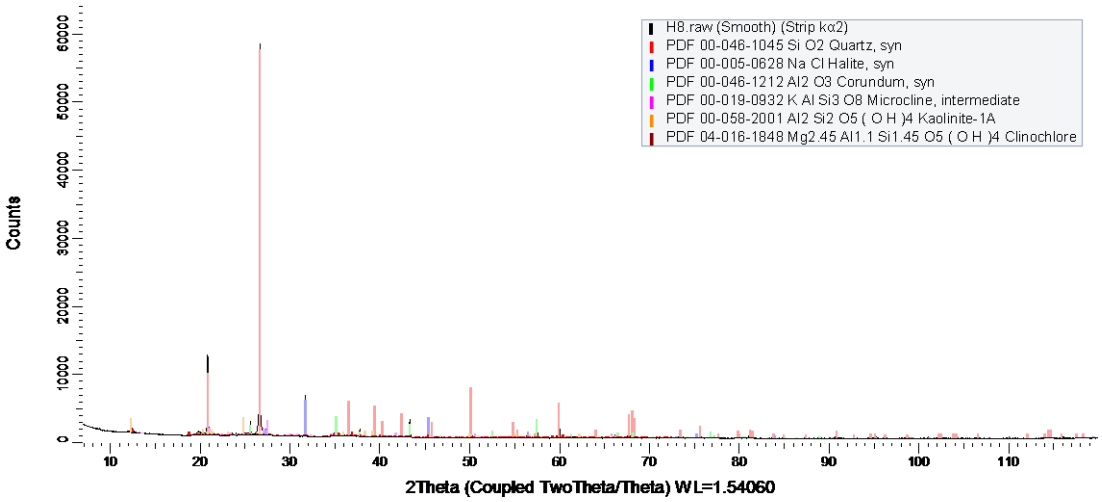
H8.raw (Smooth) (Strip kα2)
PDF 00-046-1045 Si O2 Quartz, syn
PDF 00-005-0628 Na Cl Halite, syn
PDF 00-046-1212 Al2 O3 Corundum, syn
PDF 00-019-0932 K Al Si3 O8 Microcline, intermediate
PDF 00-058-2001 Al2 Si2 O5 (O H)4 Kaolinite-1A
PDF 04-016-1848 Mg2.45 Al1.1 Si1.45 O5 (O H)4 Clinochlore
Counts
2Theta (Coupled TwoTheta/Theta) WL=1.54060

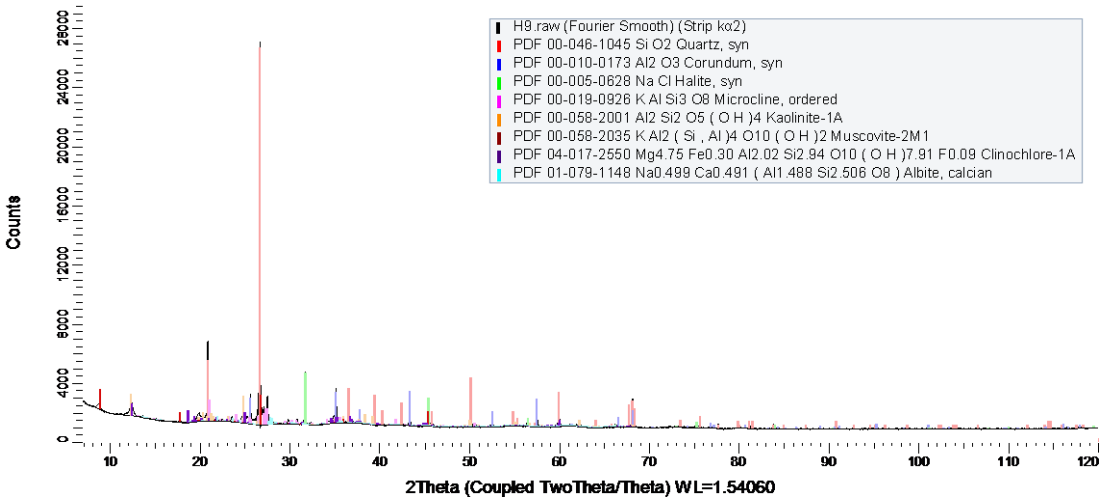
H9.raw (Fourier Smooth) (Strip kα2)
PDF 00-046-1045 Si O2 Quartz, syn
PDF 00-010-0173 Al2 O3 Corundum, syn
PDF 00-005-0628 Na Cl Halite, syn
PDF 00-019-0926 K Al Si3 O8 Microcline, ordered
PDF 00-058-2001 Al2 Si2 O5 (O H)4 Kaolinite-1A
PDF 00-058-2035 K Al2 (Si , Al)4 O10 (O H)2 Muscovite-2M1
PDF 04-017-2550 Mg4.75 Fe0.30 Al2.02 Si2.94 O10 (O H)7.91 F0.09 Clinochlore-1A
PDF 01-079-1148 Na0.499 Ca0.491 (Al1.488 Si2.506 O8) Albite, calcian
Counts
2Theta (Coupled TwoTheta/Theta) WL=1.54060

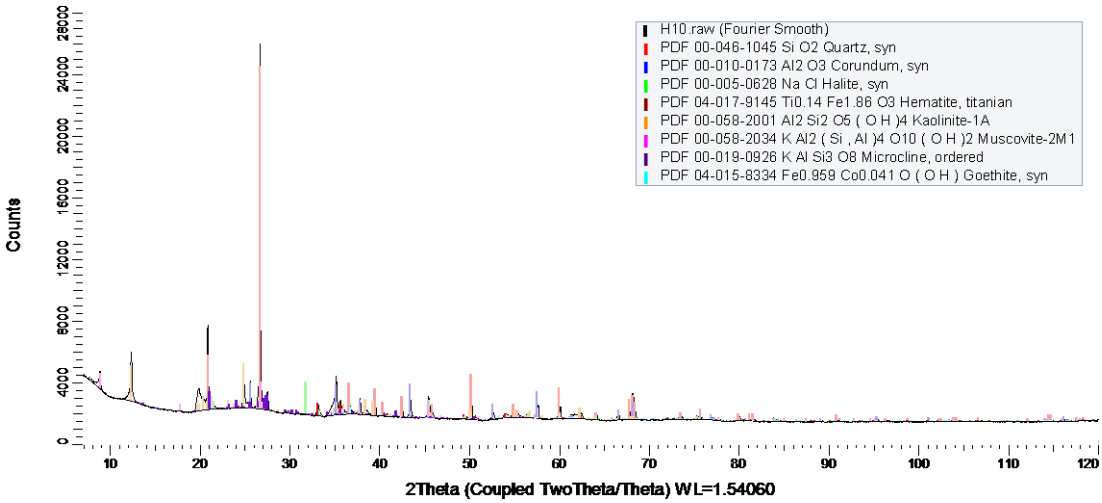
H10.raw (Fourier Smooth)
PDF 00-046-1045 Si O2 Quartz, syn
PDF 00-010-0173 Al2 O3 Corundum, syn
PDF 00-005-0628 Na Cl Halite, syn
PDF 04-017-9145 Ti0.14 Fe1.86 O3 Hematite, titanian
PDF 00-058-2001 Al2 Si2 O5 (O H)4 Kaolinite-1A
PDF 00-058-2034 K Al2 (Si , Al)4 O10 (O H)2 Muscovite-2M1
PDF 00-019-0926 K Al Si3 O8 Microcline, ordered
PDF 04-015-8334 Fe0.959 Co0.041 O (O H) Goethite, syn
Counts
2Theta (Coupled TwoTheta/Theta) WL=1.54060

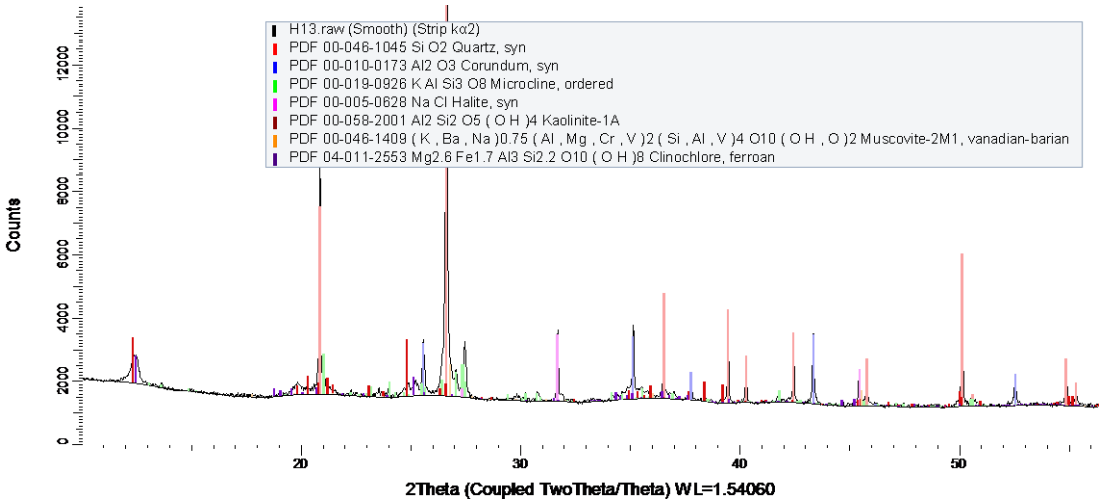
H13.raw (Smooth) (Strip kα2)
PDF 00-046-1045 Si O2 Quartz, syn
PDF 00-010-0173 Al2 O3 Corundum, syn
PDF 00-019-0926 K Al Si3 O8 Microcline, ordered
PDF 00-005-0628 Na Cl Halite, syn
PDF 00-058-2001 Al2 Si2 O5 (O H)4 Kaolinite-1A
PDF 00-046-1409 (K , Ba , Na)0.75 (Al , Mg , Cr , V)2 (Si , Al , V)4 O10 (O H , O)2 Muscovite-2M1, vanadian-barian
PDF 04-011-2553 Mg2.6 Fe1.7 Al3 Si2.2 O10 (O H)8 Clinochlore, ferroan
Counts
2Theta (Coupled TwoTheta/Theta) WL=1.54060

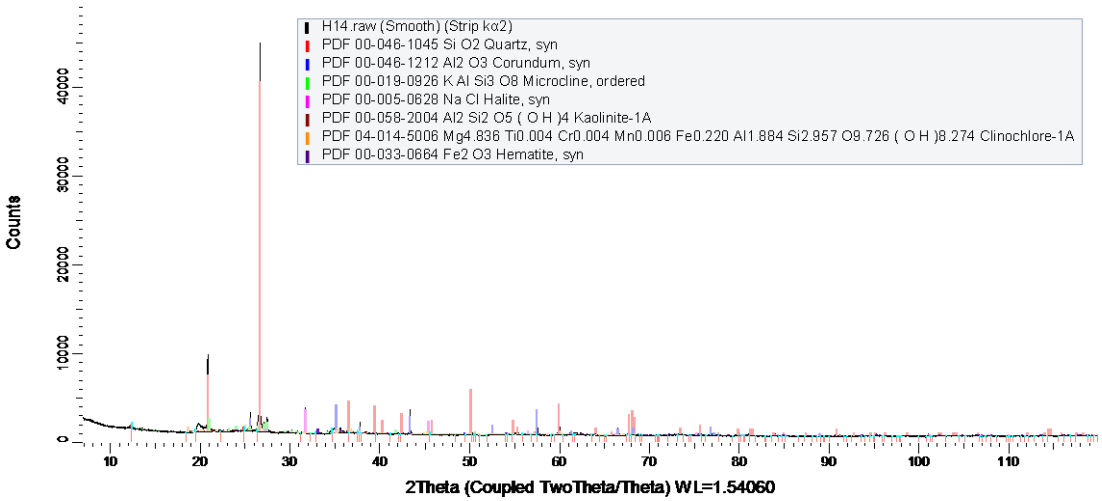
H14.raw (Smooth) (Strip kα2)
PDF 00-046-1045 Si O2 Quartz, syn
PDF 00-046-1212 Al2 O3 Corundum, syn
PDF 00-019-0926 K Al Si3 O8 Microcline, ordered
PDF 00-005-0628 Na Cl Halite, syn
PDF 00-058-2004 Al2 Si2 O5 (O H)4 Kaolinite-1A
PDF 04-014-5006 Mg4.836 Ti0.004 Cr0.004 Mn0.006 Fe0.220 Al1.884 Si2.957 O9.726 (O H)8.274 Clinochlore-1A
PDF 00-033-0664 Fe2 O3 Hematite, syn
Counts
2Theta (Coupled TwoTheta/Theta) WL=1.54060

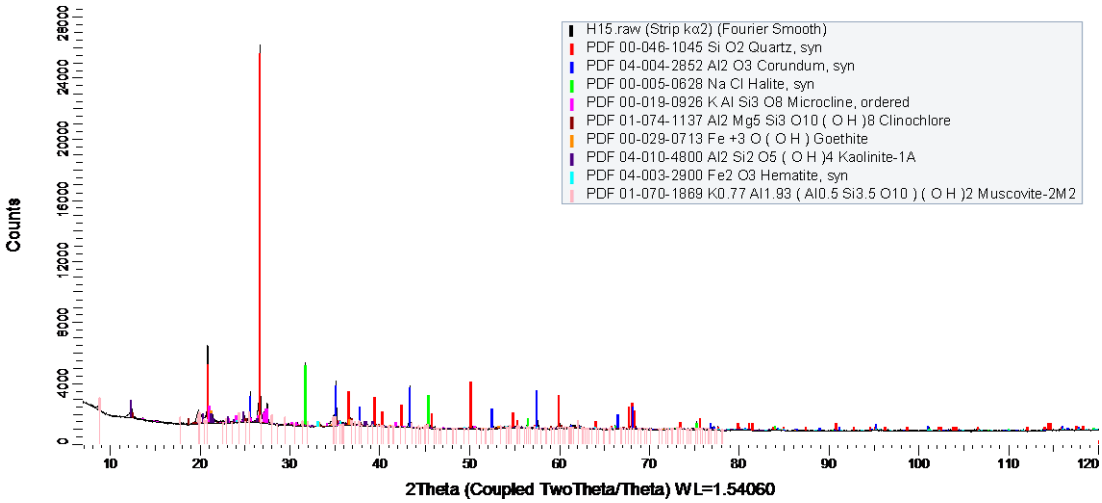
H15.raw (Strip kα2) (Fourier Smooth)
PDF 00-046-1045 Si O2 Quartz, syn
PDF 04-004-2852 Al2 O3 Corundum, syn
PDF 00-005-0628 Na Cl Halite, syn
PDF 00-019-0926 K Al Si3 O8 Microcline, ordered
PDF 01-074-1137 Al2 Mg5 Si3 O10 (O H)8 Clinochlore
PDF 00-029-0713 Fe +3 O (O H) Goethite
PDF 04-010-4800 Al2 Si2 O5 (O H)4 Kaolinite-1A
PDF 04-003-2900 Fe2 O3 Hematite, syn
PDF 01-070-1869 K0.77 Al1.93 (Al0.5 Si3.5 O10) (O H)2 Muscovite-2M2
Counts
0
4000
8000
12000
16000
20000
24000
28000
10
20
30
40
50
60
70
80
90
100
110
120
2Theta (Coupled TwoTheta/Theta) WL=1.54060

D. Before and after reaction XRD diffractograms comparison

Blue: Before, Red: after 4 months, Green: after 9 months

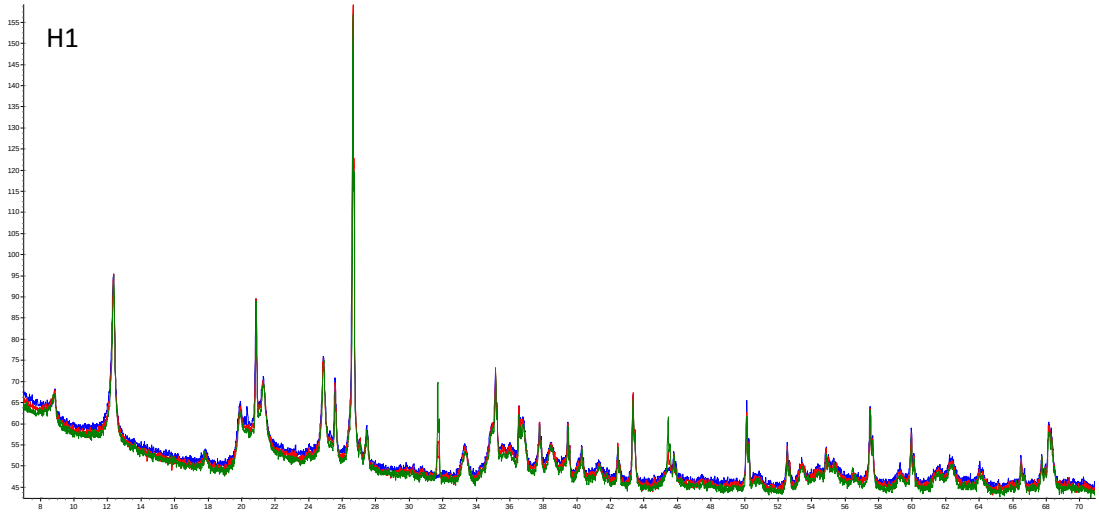

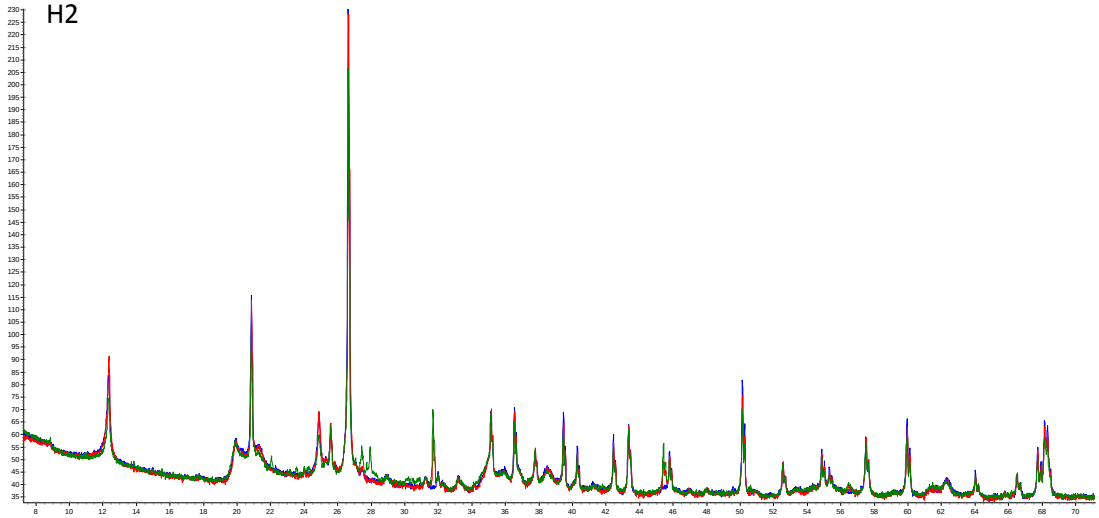

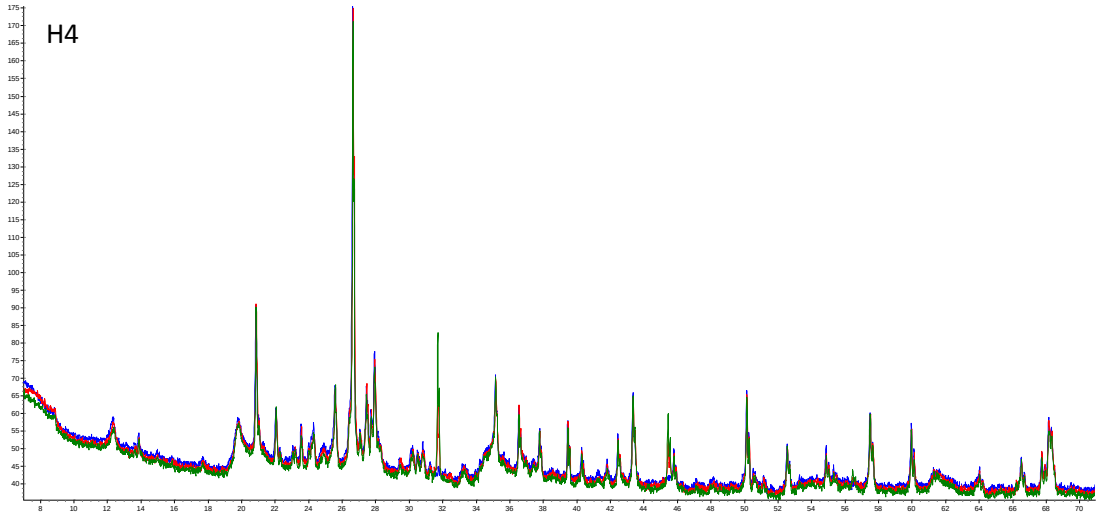

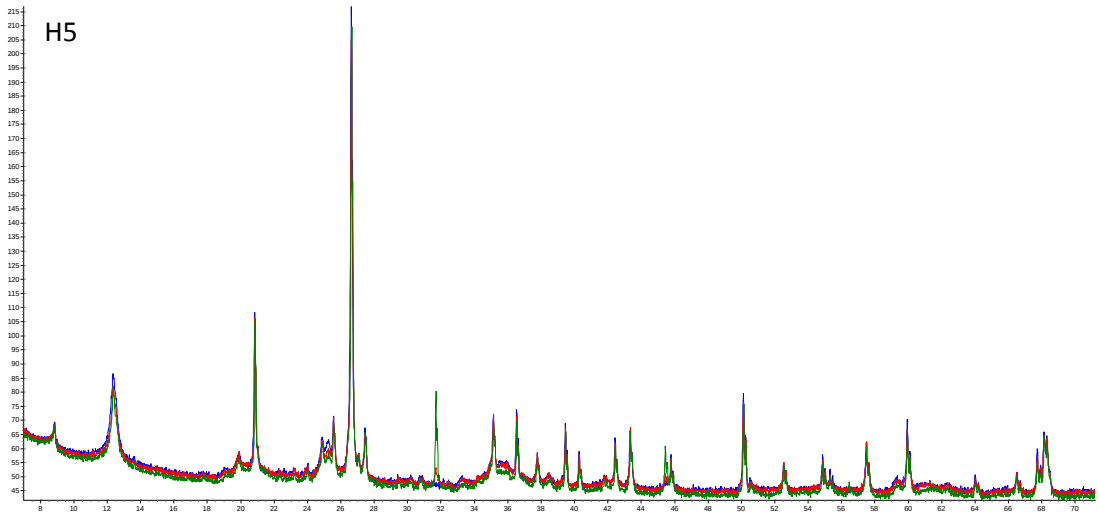
H5

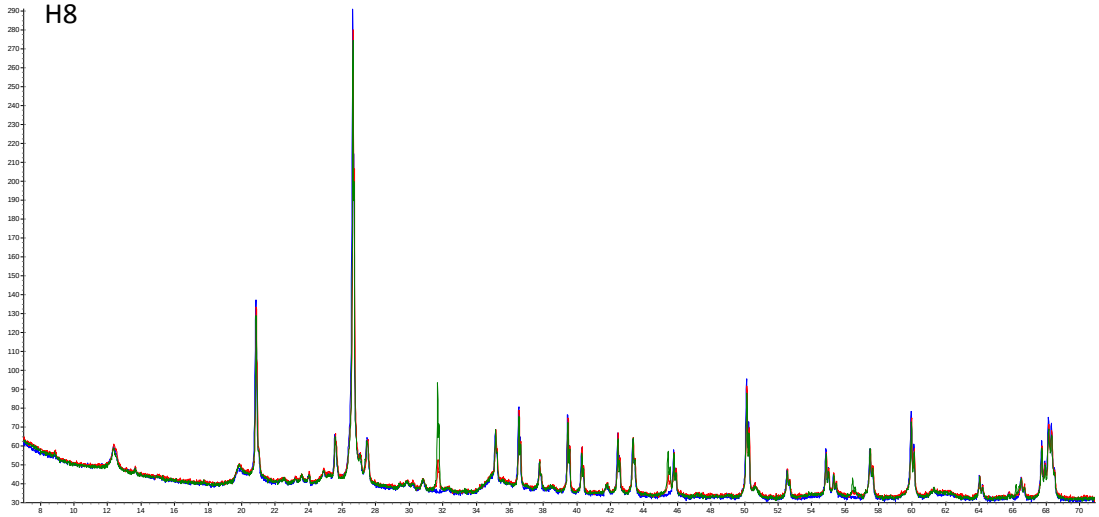
H8

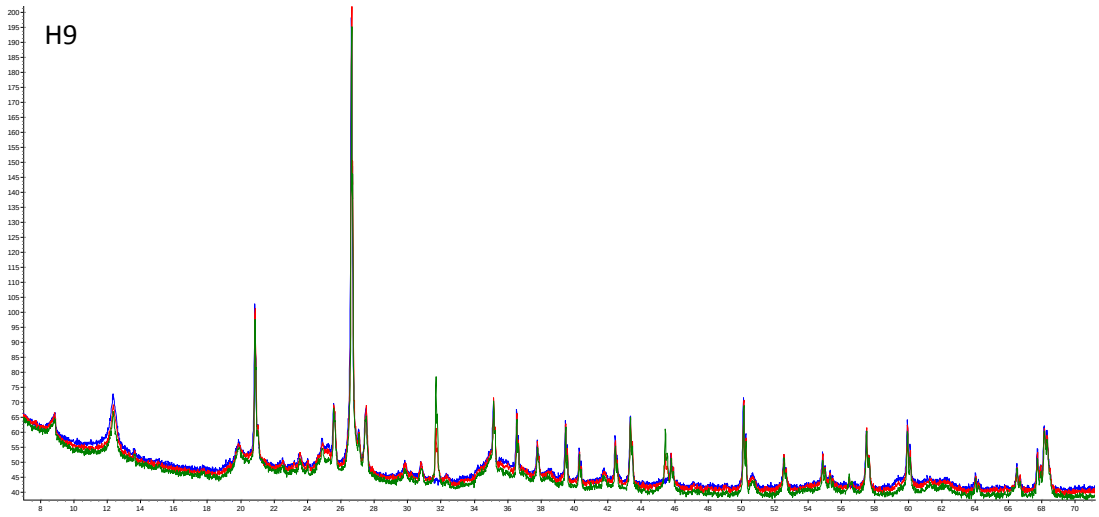
H9

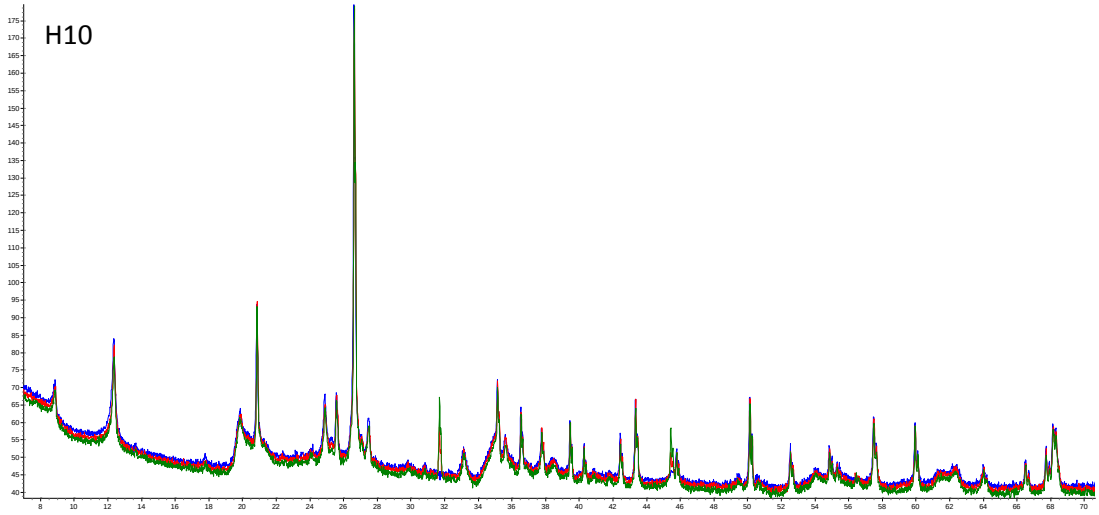
H10

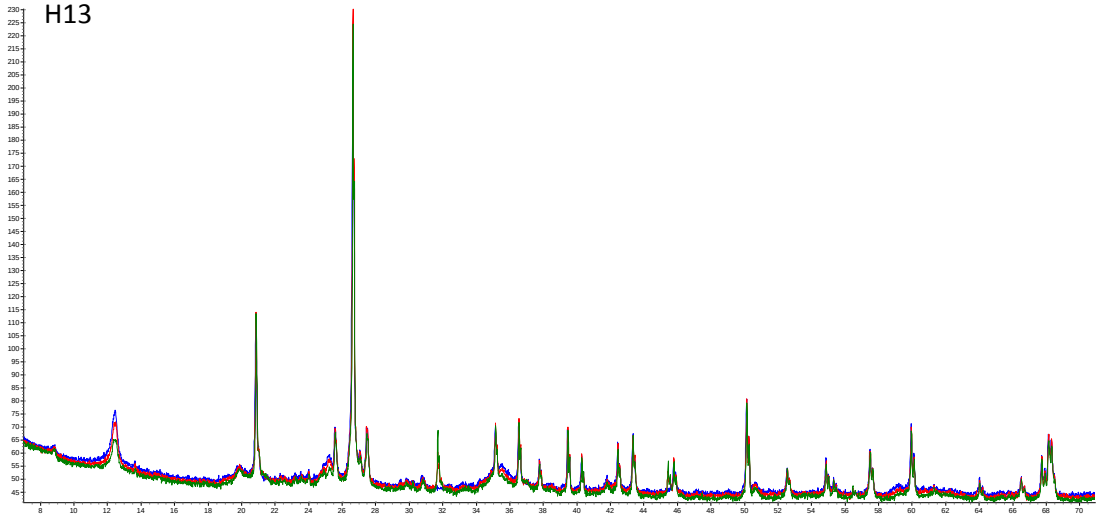
H13

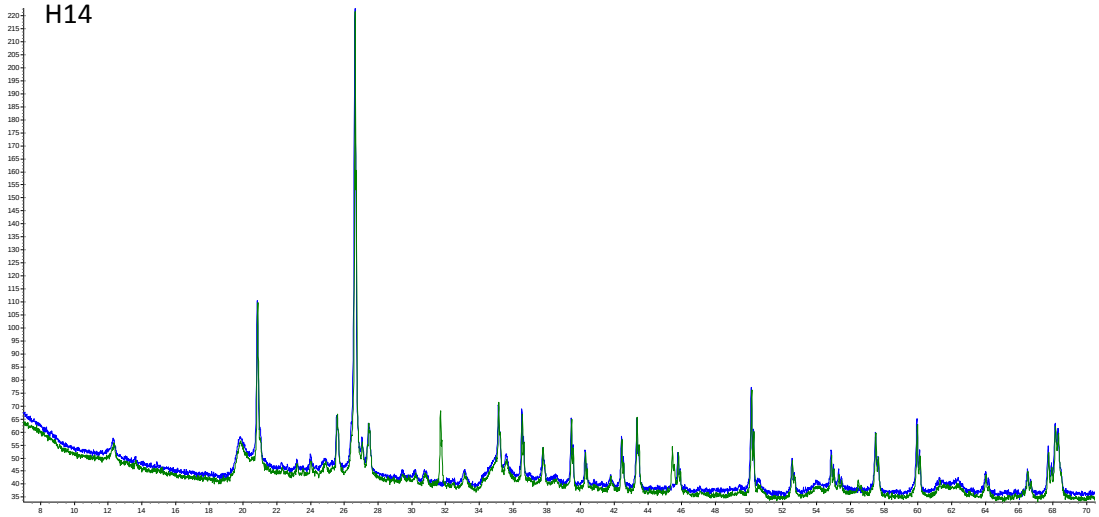
H14

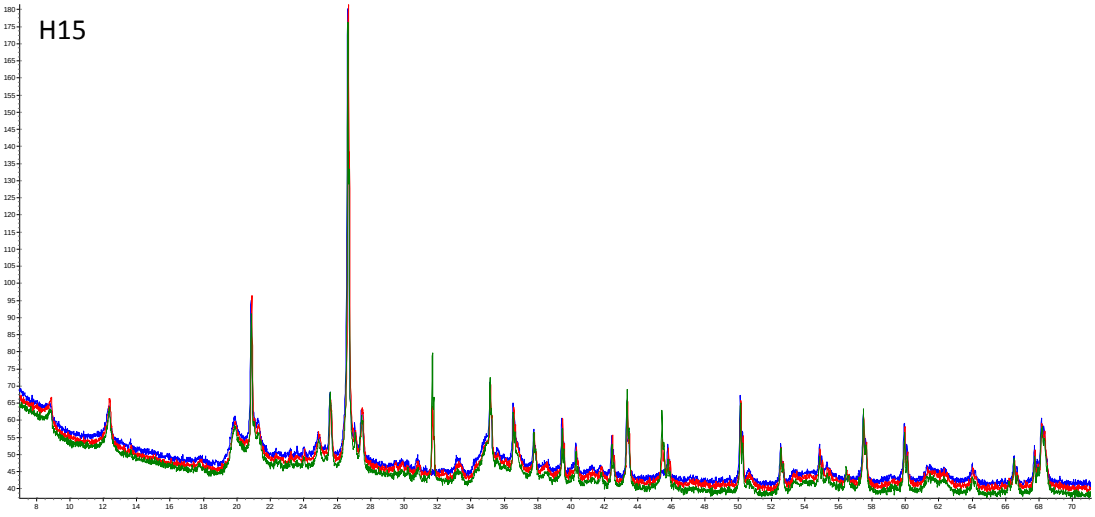
H15

Appendix IV. SEM

A. Before exposure

SE (Left) and BSE (right) images of sample H1.

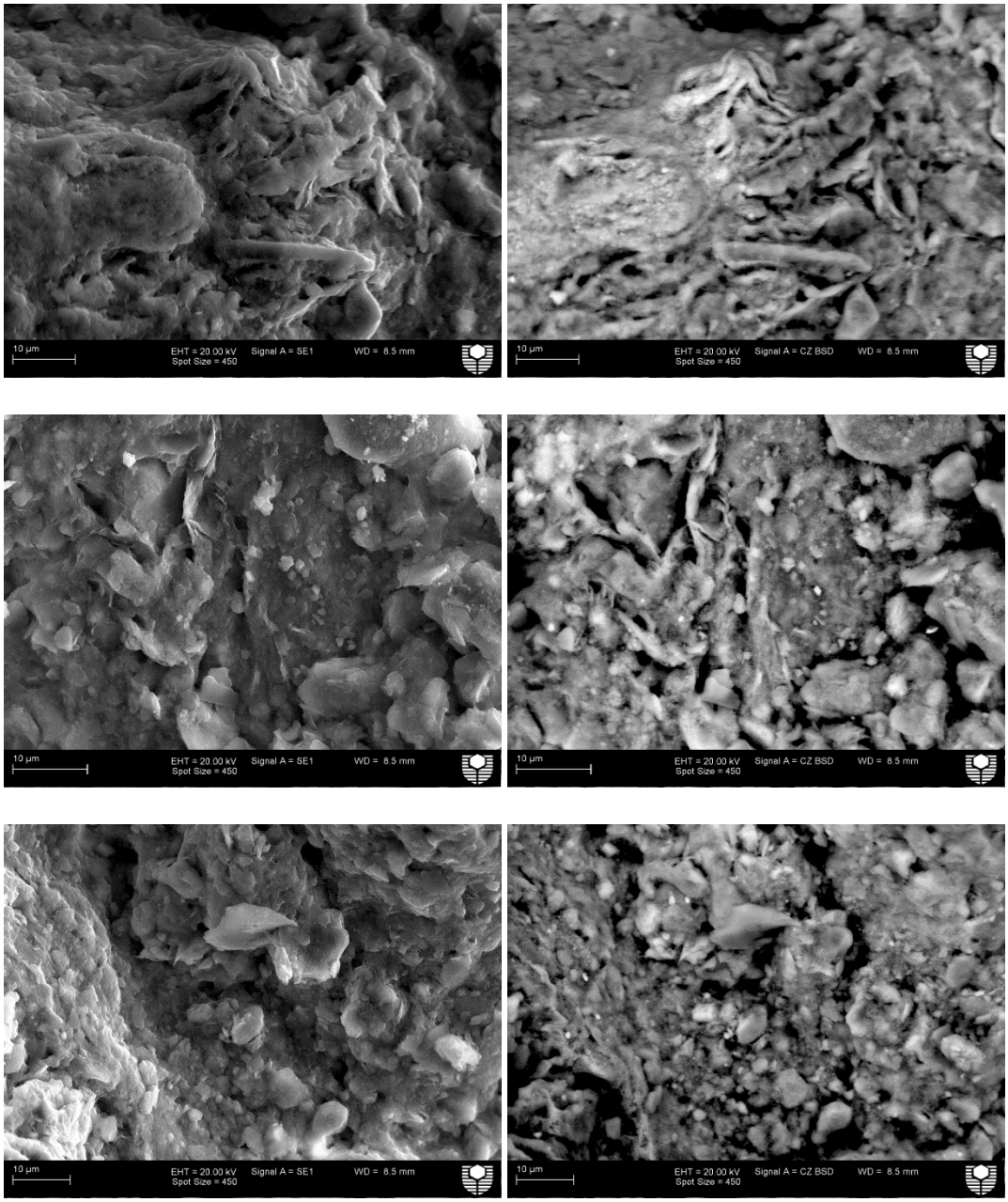

SE (Left) and BSE (right) images of sample H2.

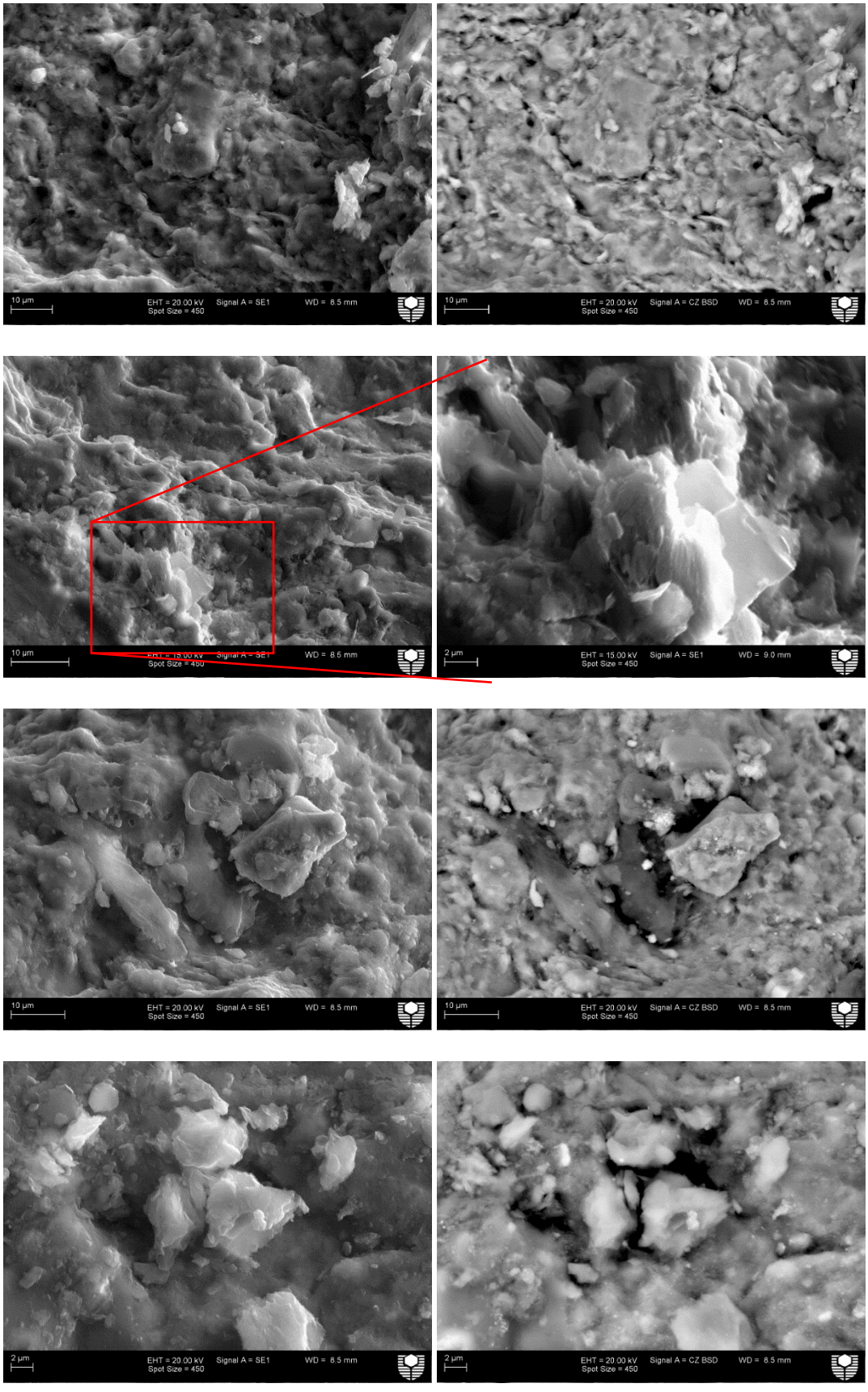

SE (Left) and BSE (right) images of sample H5 show grains including quartz in the abundant clay matrix.

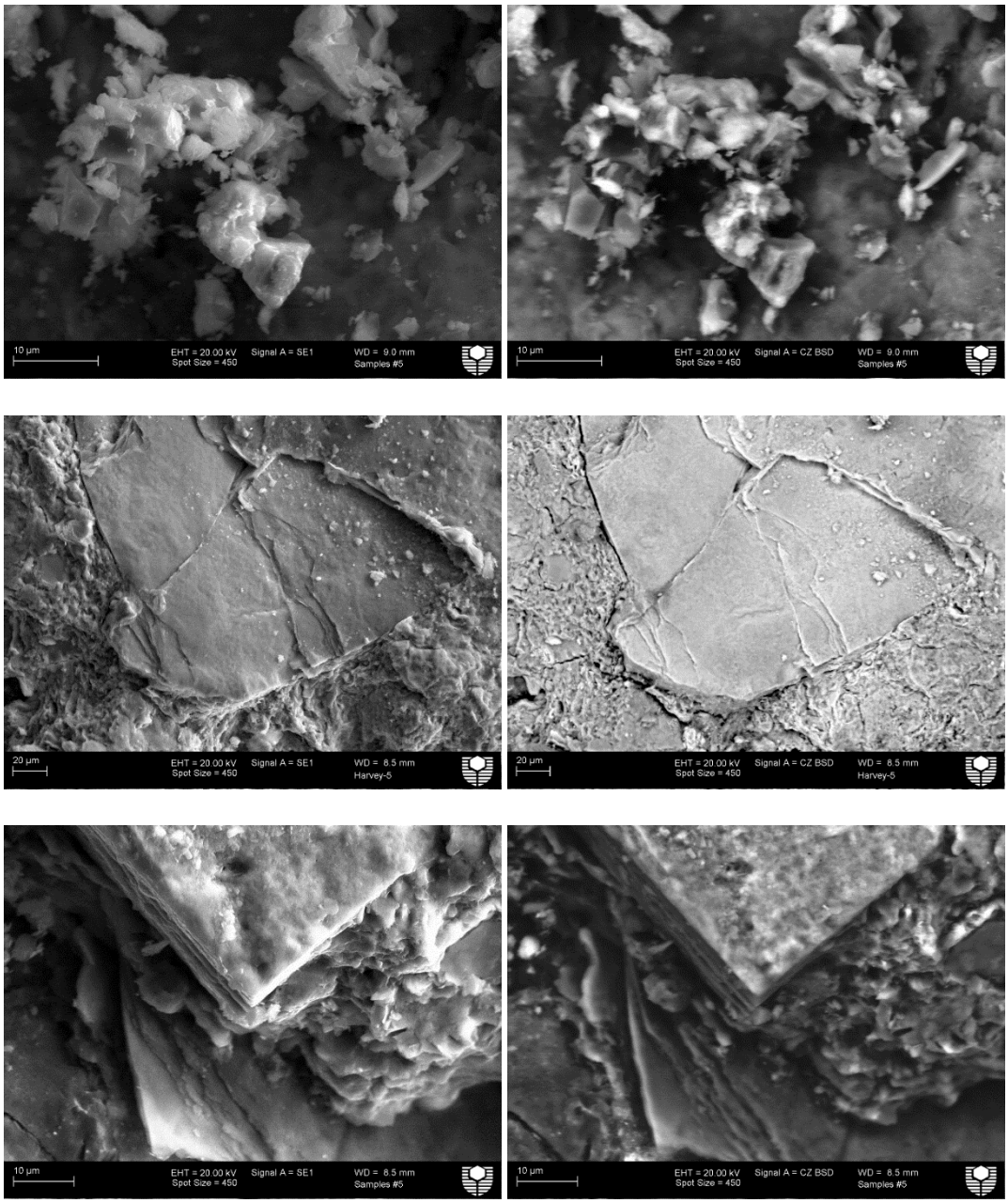

SE (Left) and BSE (right) images of sample H8 shows mostly quartz and feldspars.

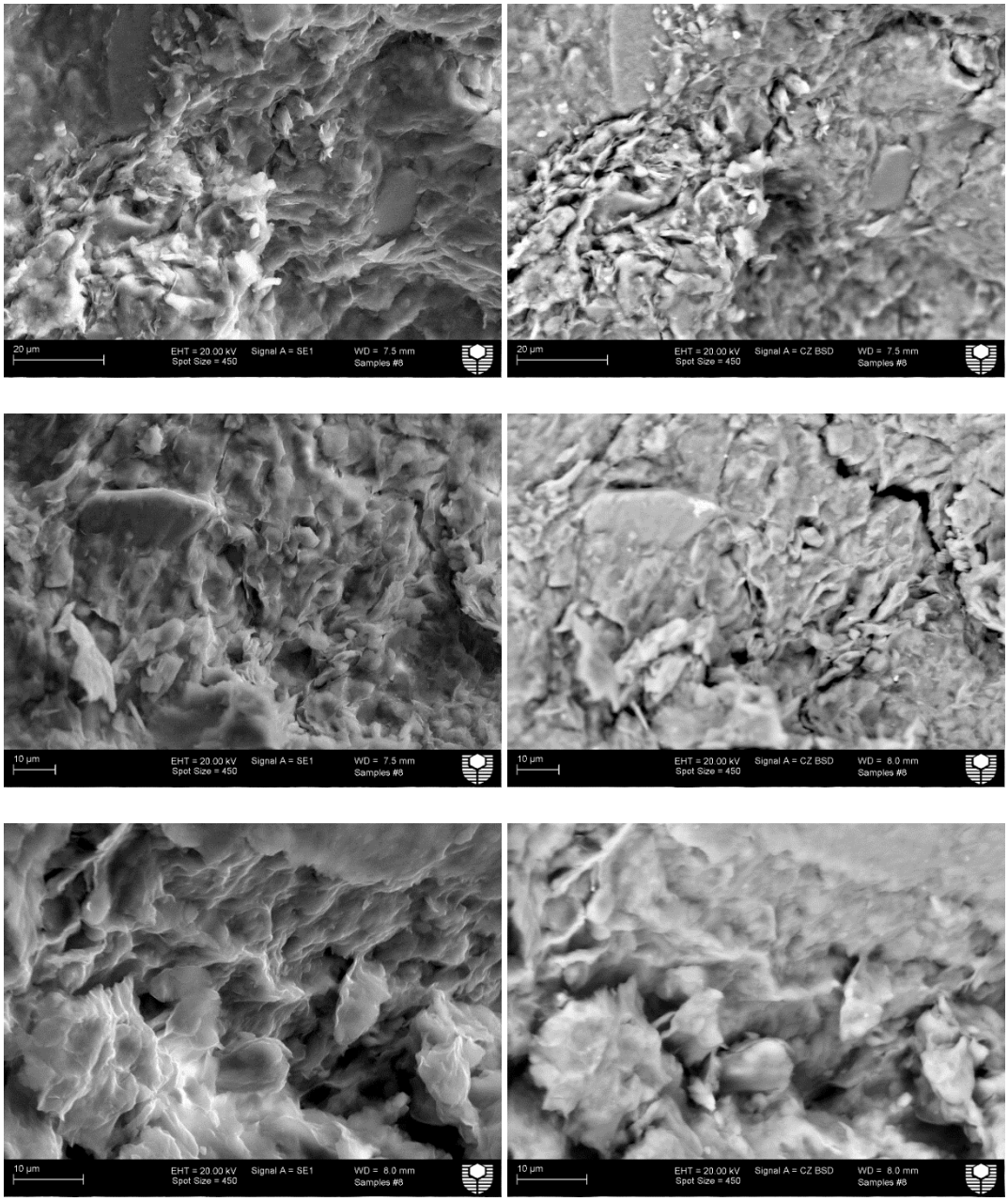

SE (Left) and BSE (right) images of sample H9 shows quartz grains in abundant kaolinite and illite matrix.

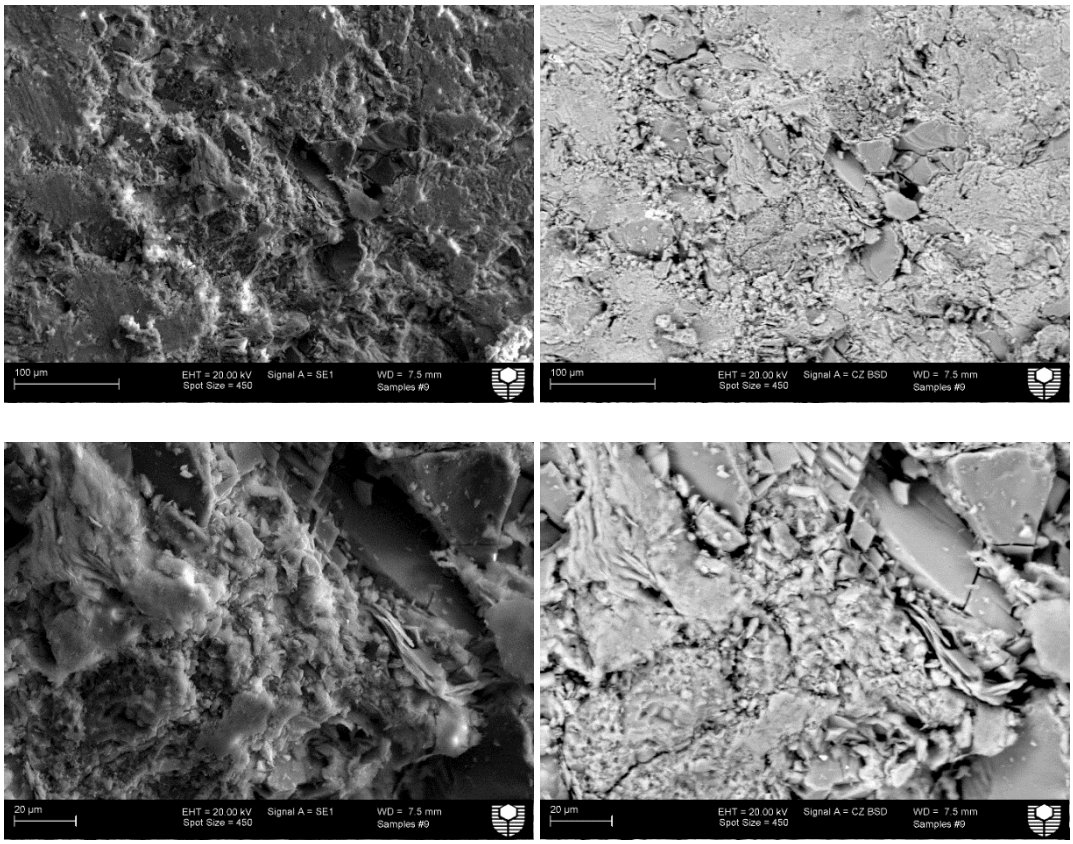

SE (Left) and BSE (right) images of sample H9 shows the abundant authigenic kaolinite.

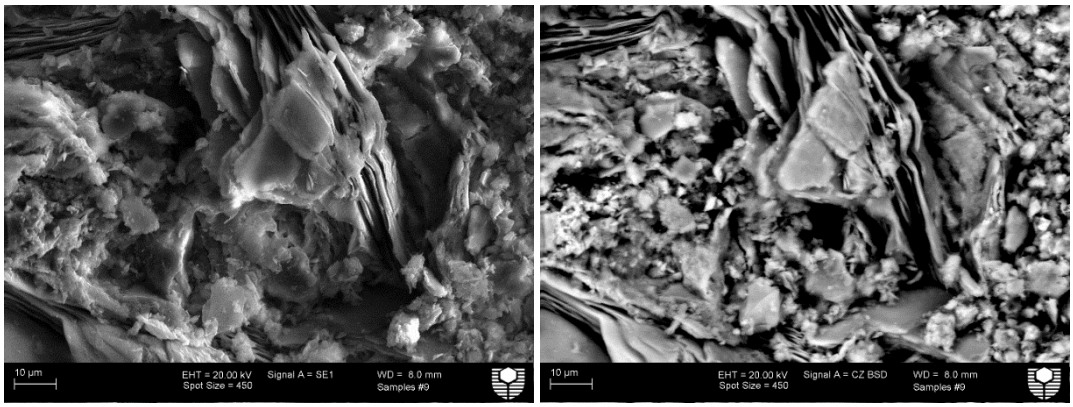

BSE images of sample H13 shows grains, including K-feldspar and quartz in the abundant clay matrix. XRD analysis indicates that kaolinite and Illite are the most abundant matrix clay type.

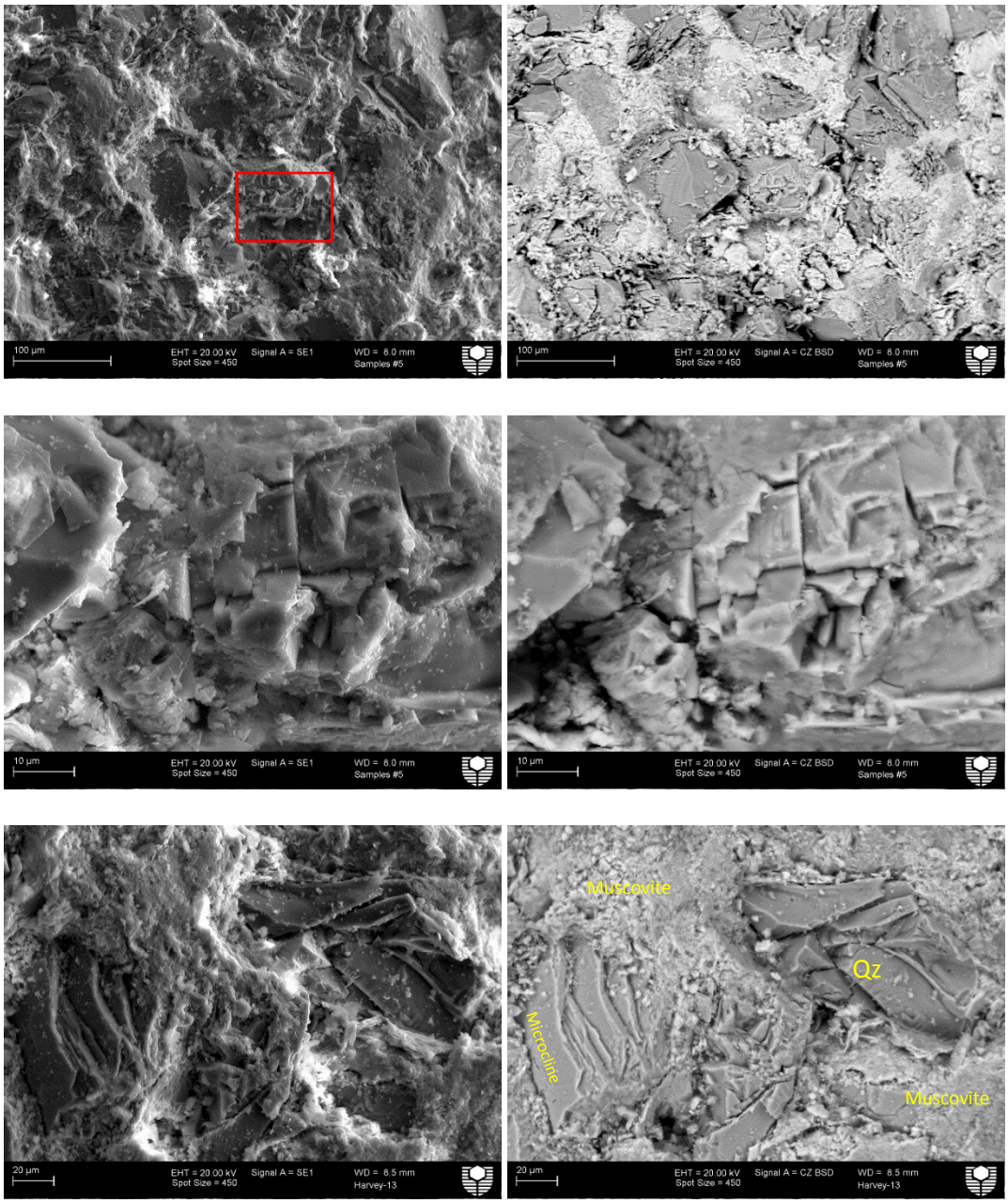

B. After exposure

SE (Left) and BSE (right) images of sample H1.

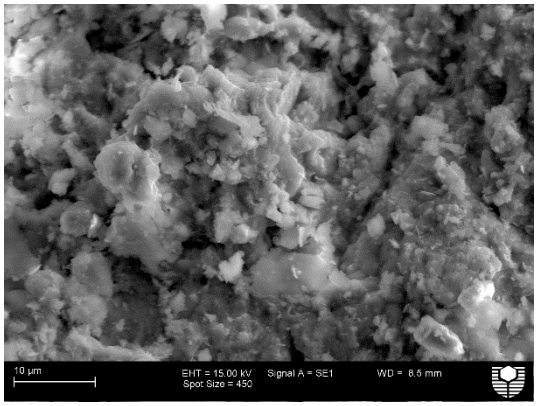

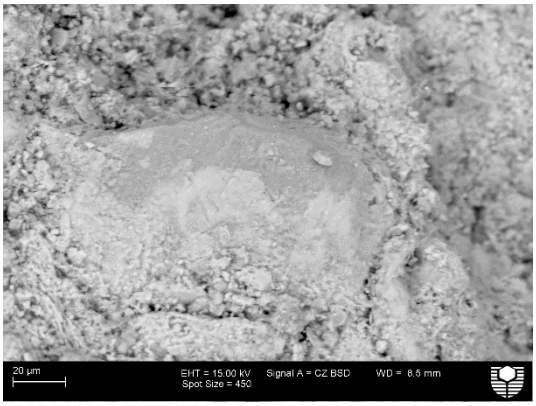

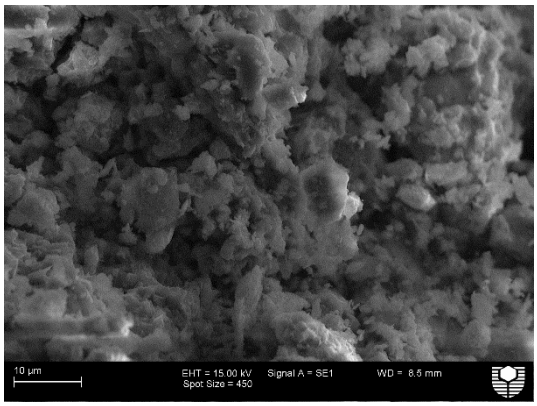

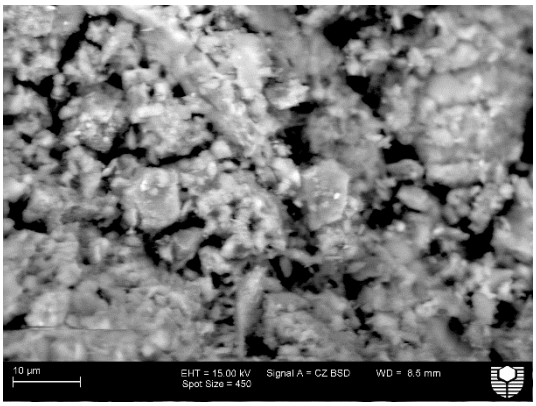

SE (Left) and BSE (right) images of sample H2. Magnification of boxes D and E are presented in the following images.

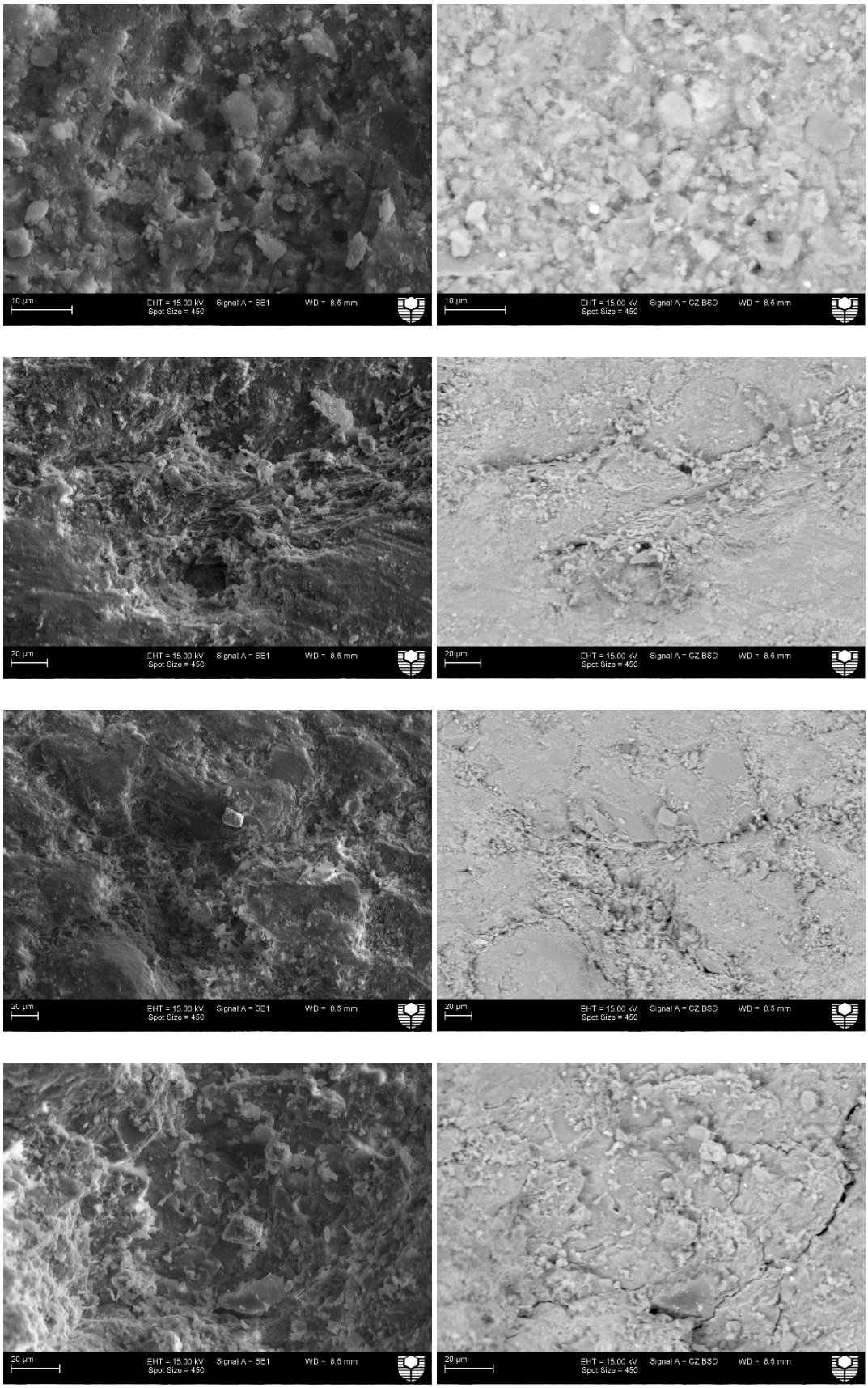

SE (Left) and BSE (right) images of sample H5.

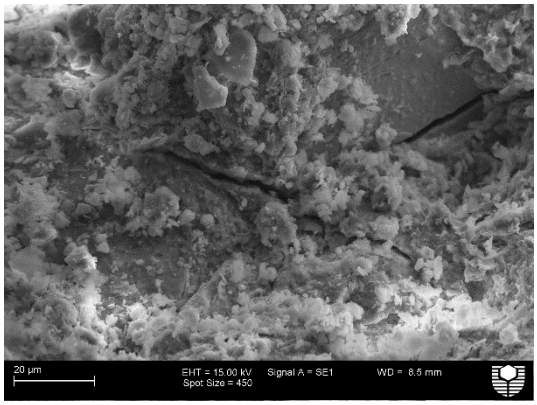

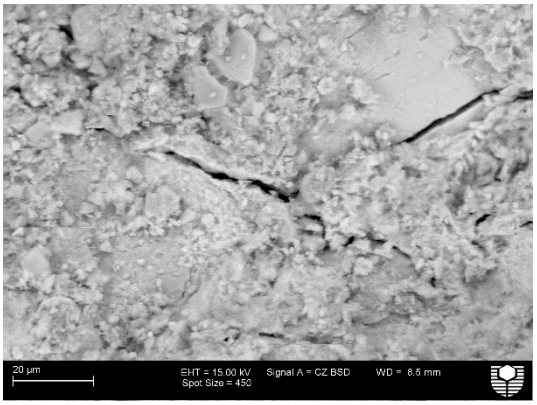

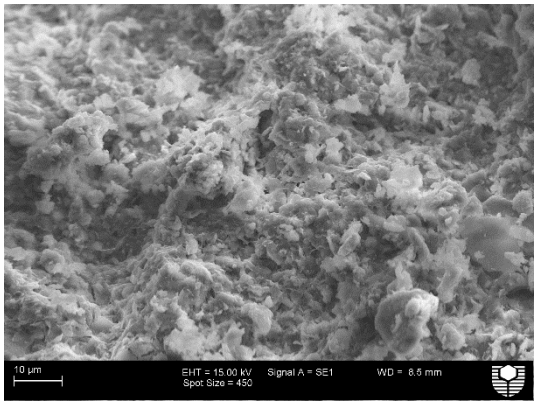

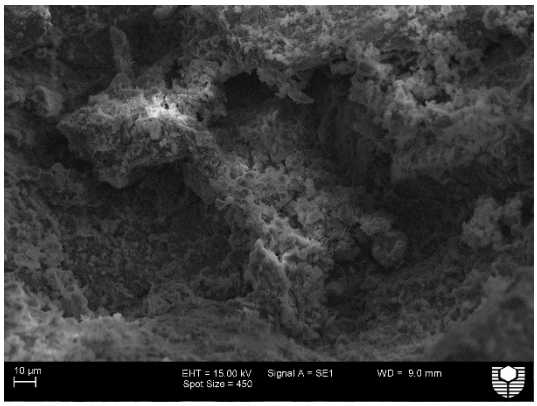

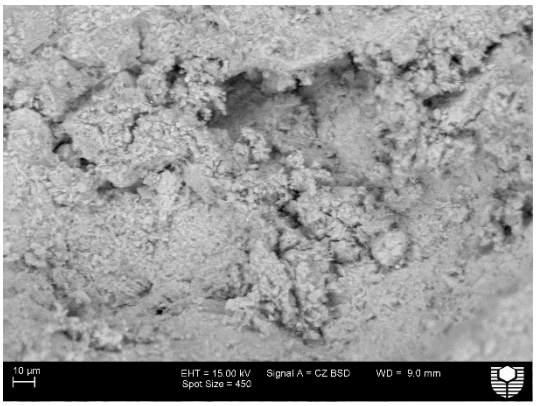

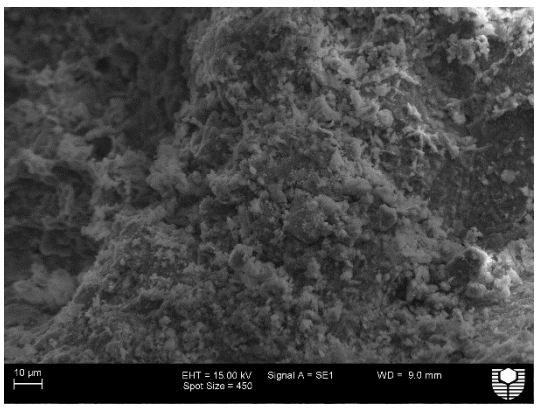

SE (Left) and BSE (right) images of sample H9.

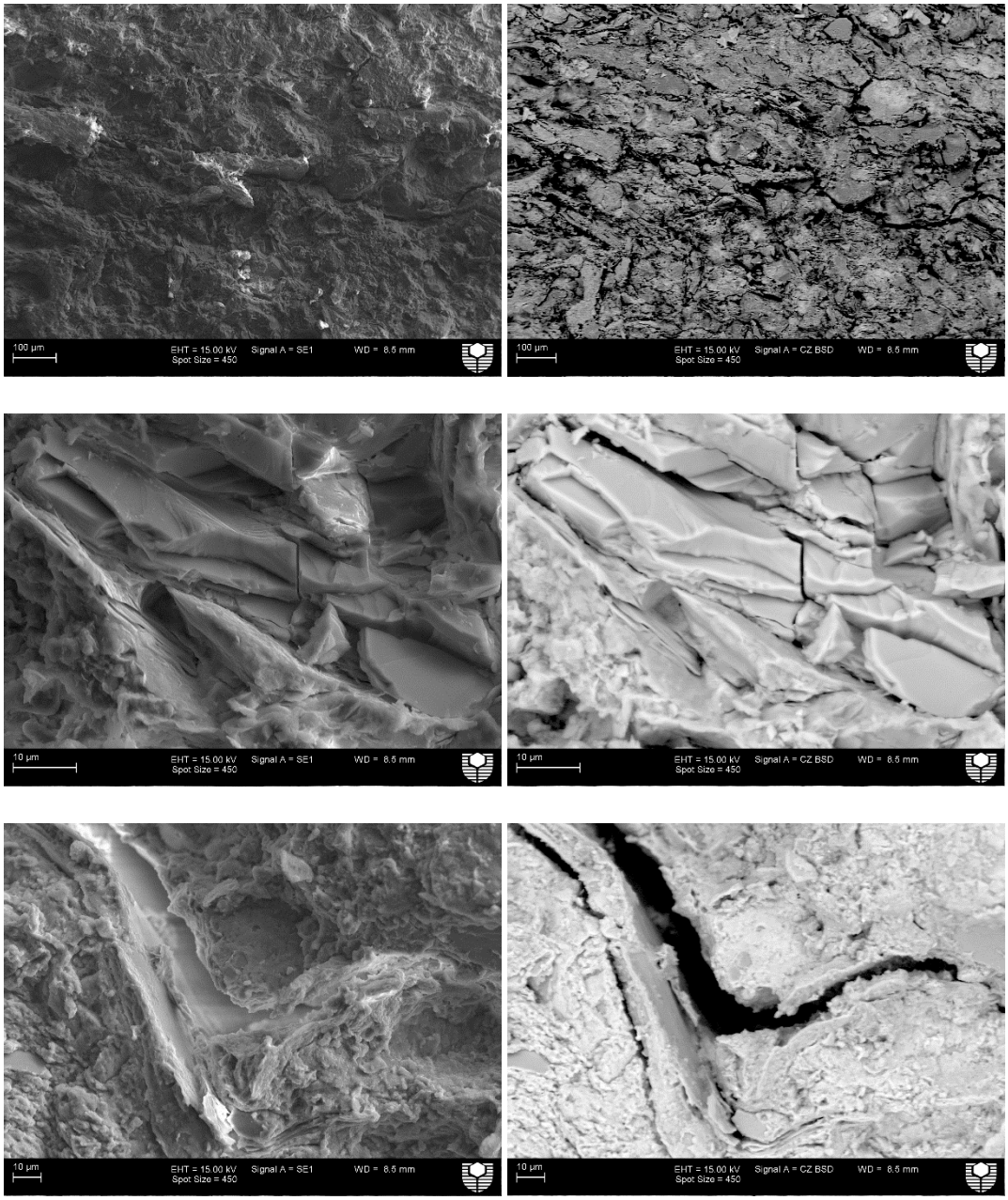

SE (Left) and BSE (right) images of sample H13.

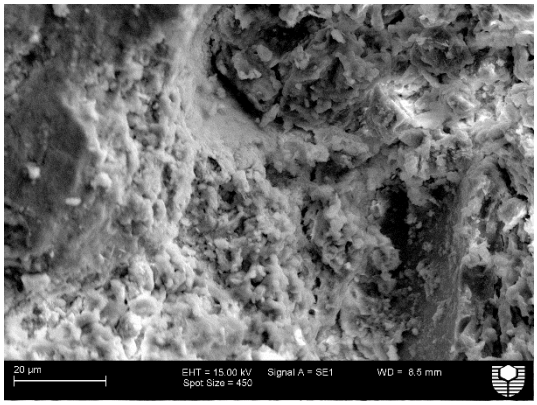

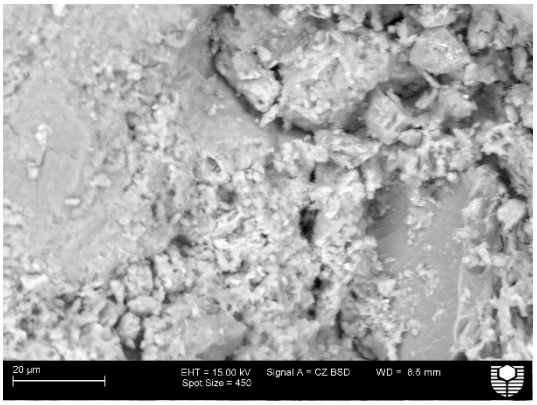

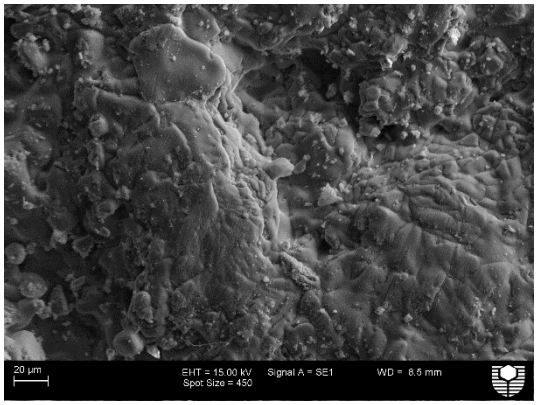

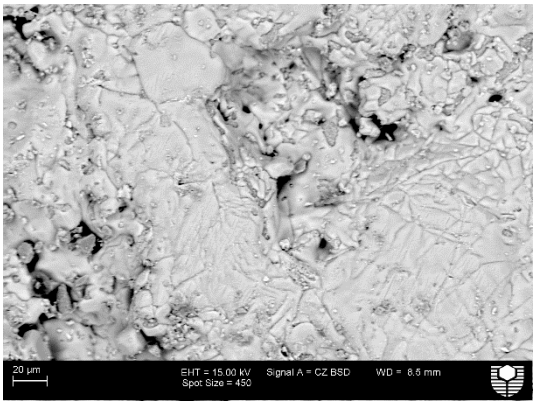

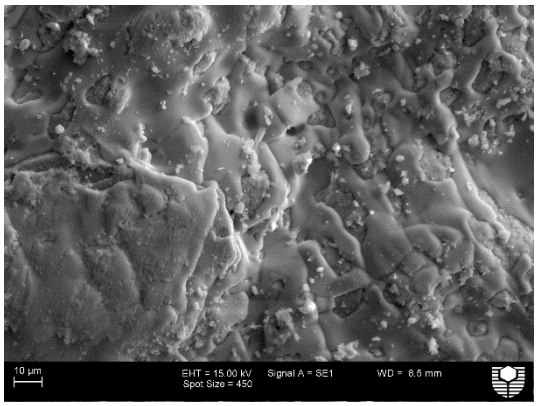

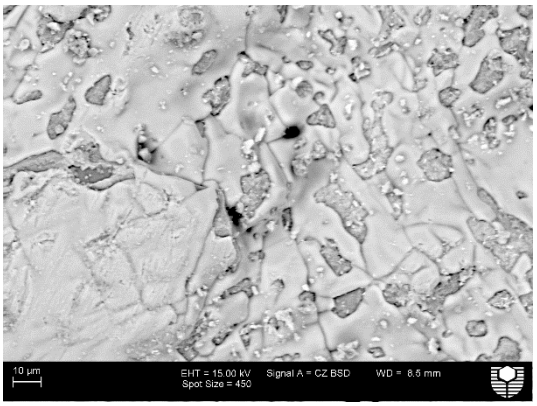

SE (Left) and BSE (right) images of sample H15.

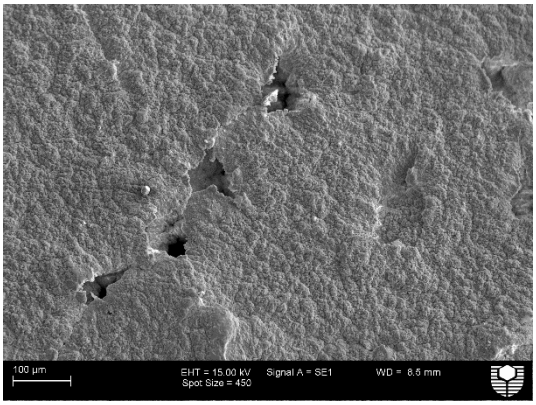

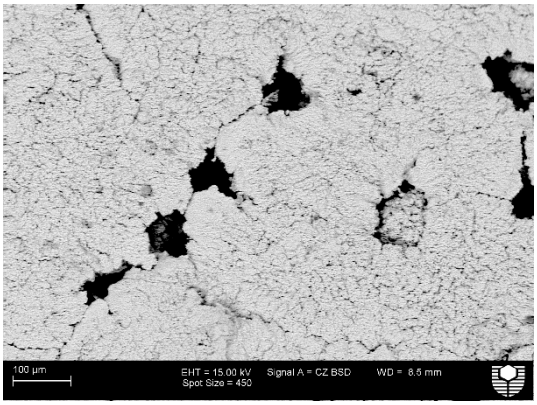

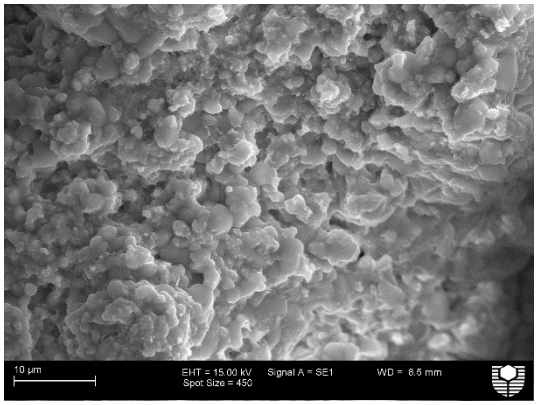

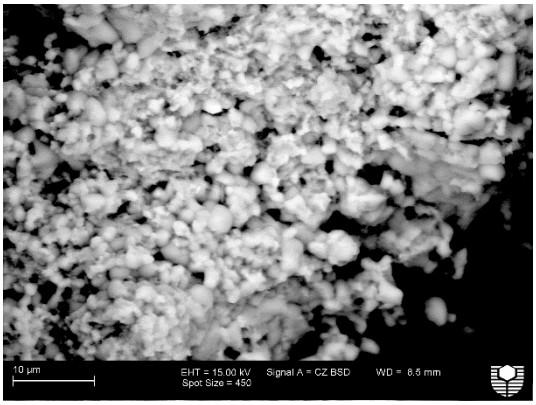

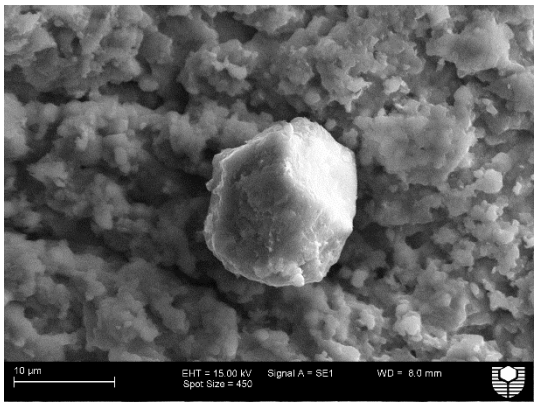

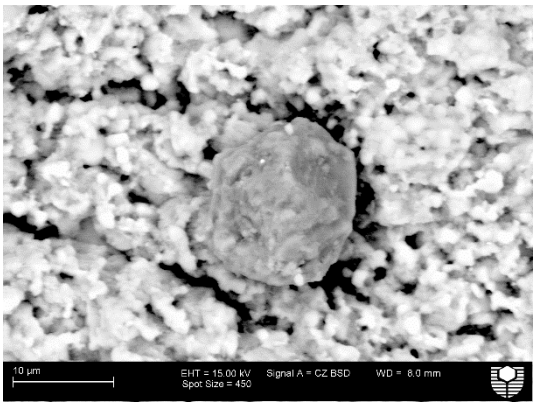

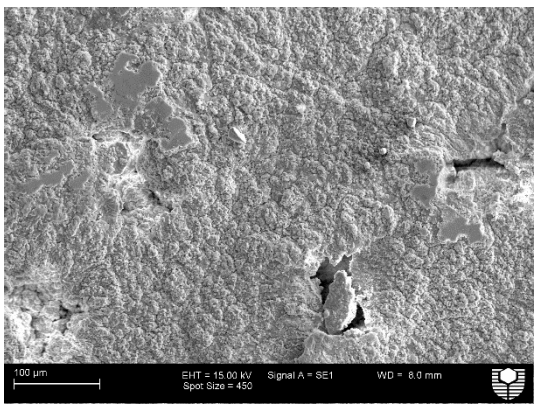

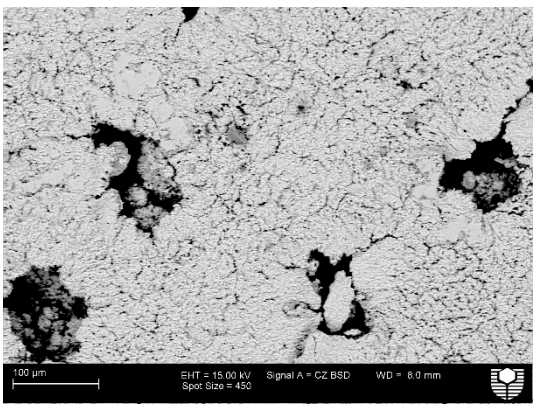

Appendix V. NMR

A. T_2 distribution of all samples versus incremental porosity

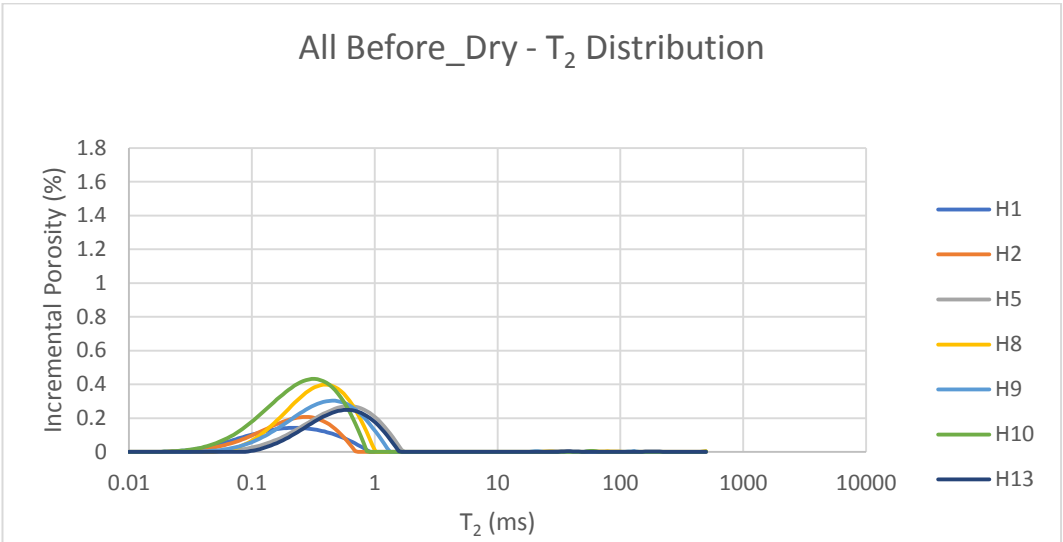

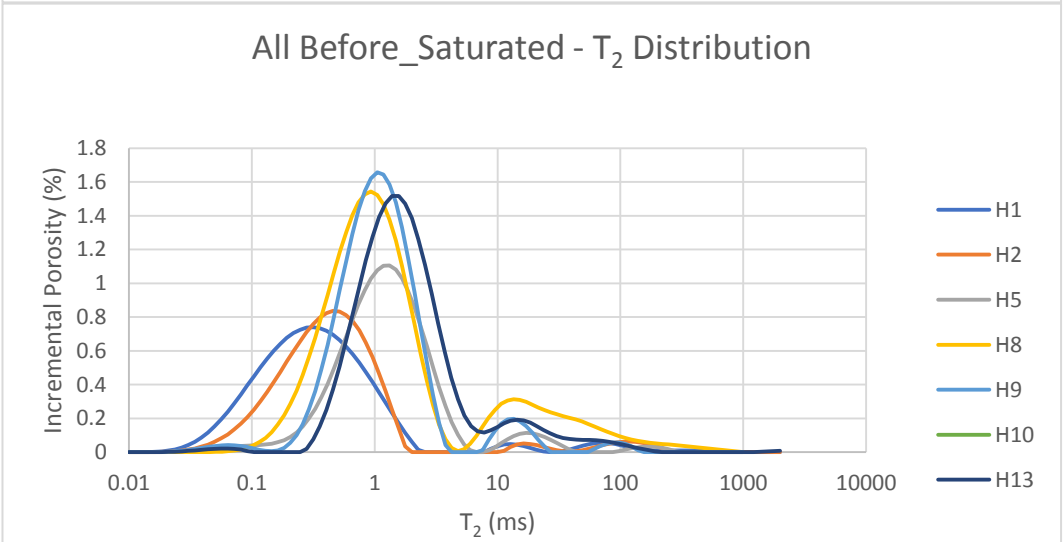

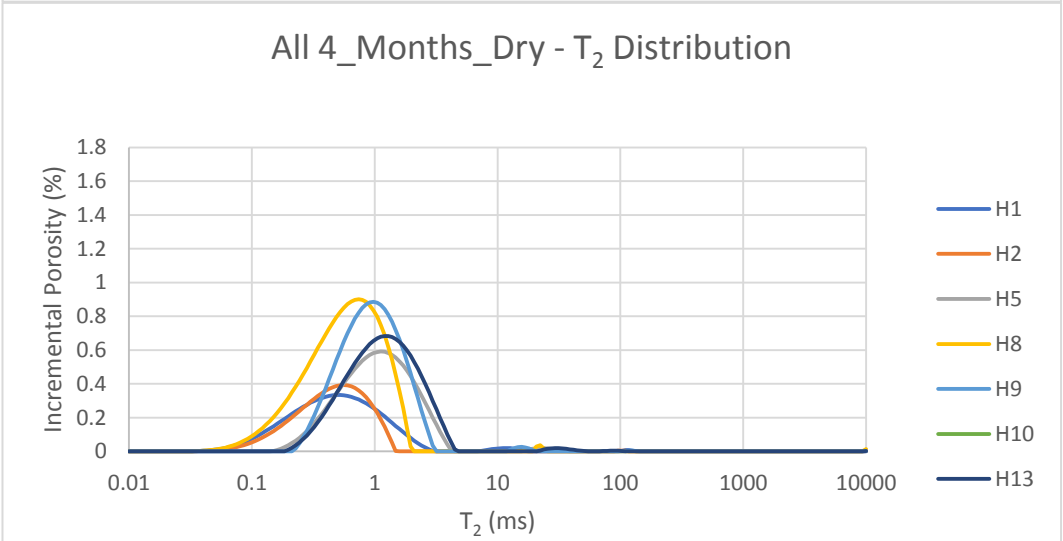

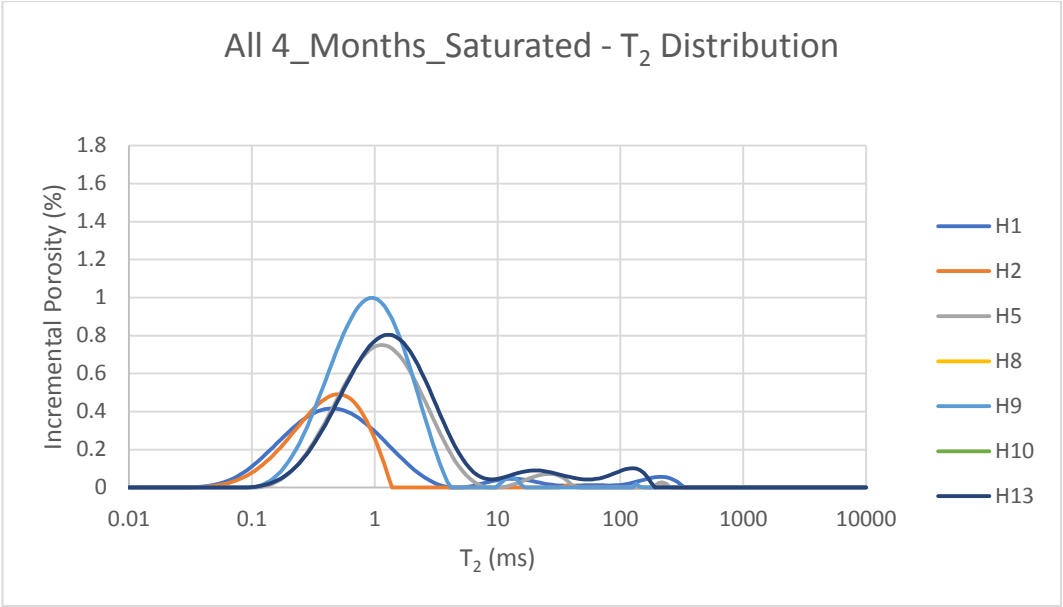

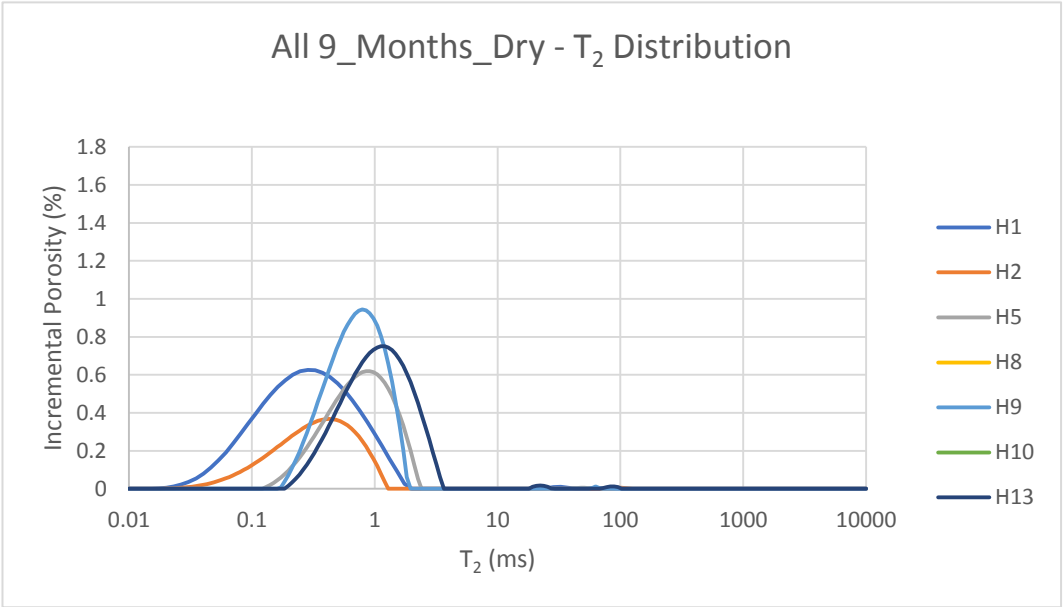

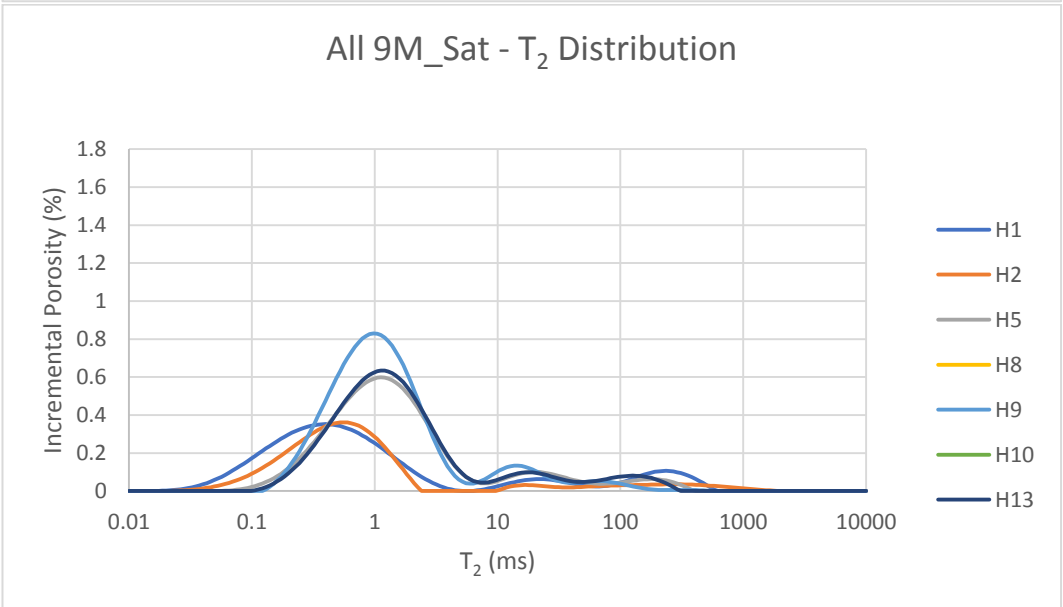

Sample H10 failed after first saturation and sample H8 failed after second saturation.

B. T_2 distribution of all samples versus cumulative porosity

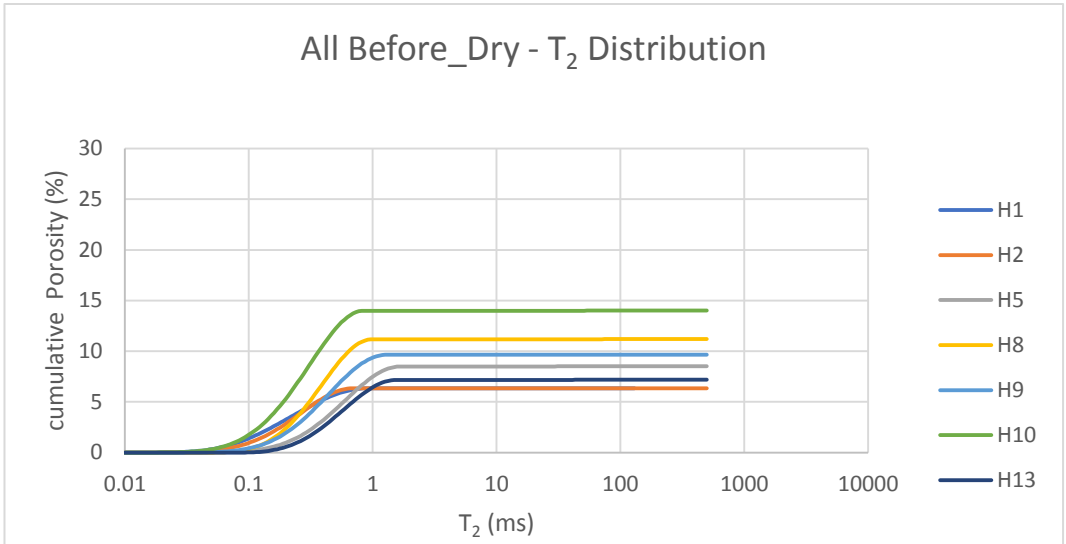

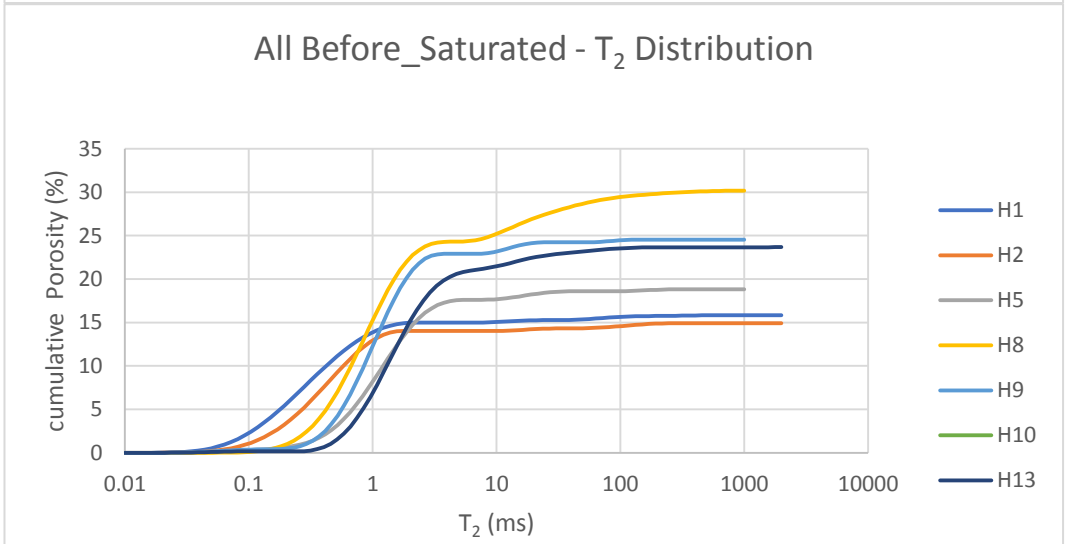

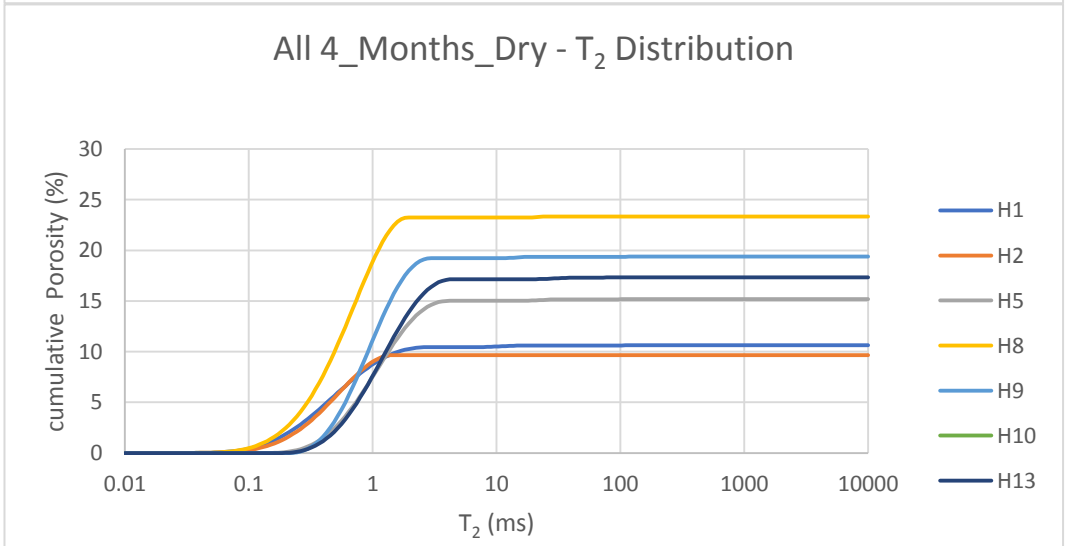

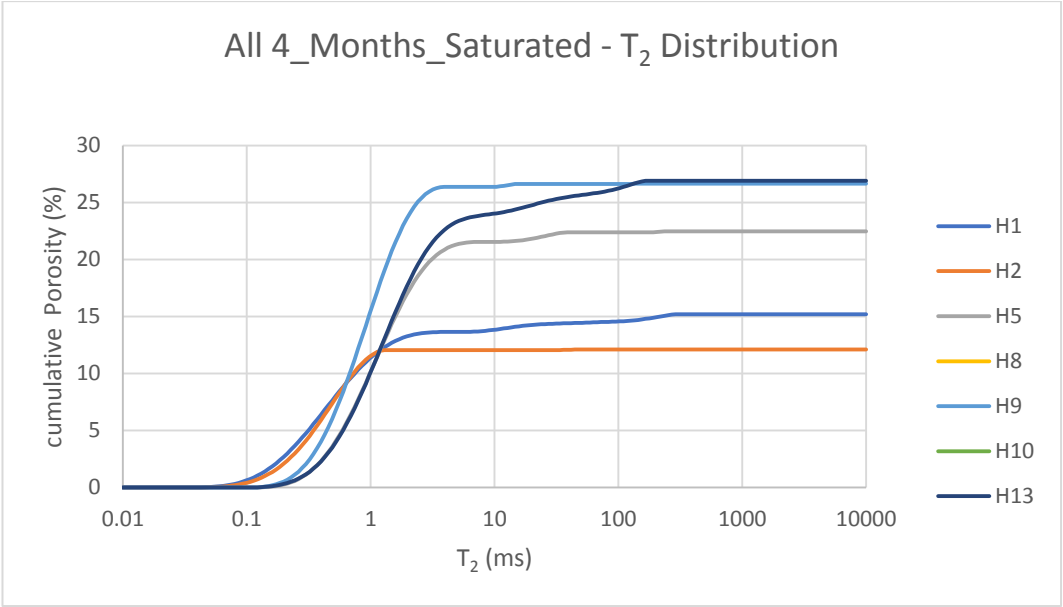
All 4_Months_Saturated - T2 Distribution
cumulative Porosity (%)
30
25
20
15
10
5
0
0.01
0.1
1
10
100
1000
10000
T2 (ms)
H1
H2
H5
H8
H9
H10
H13

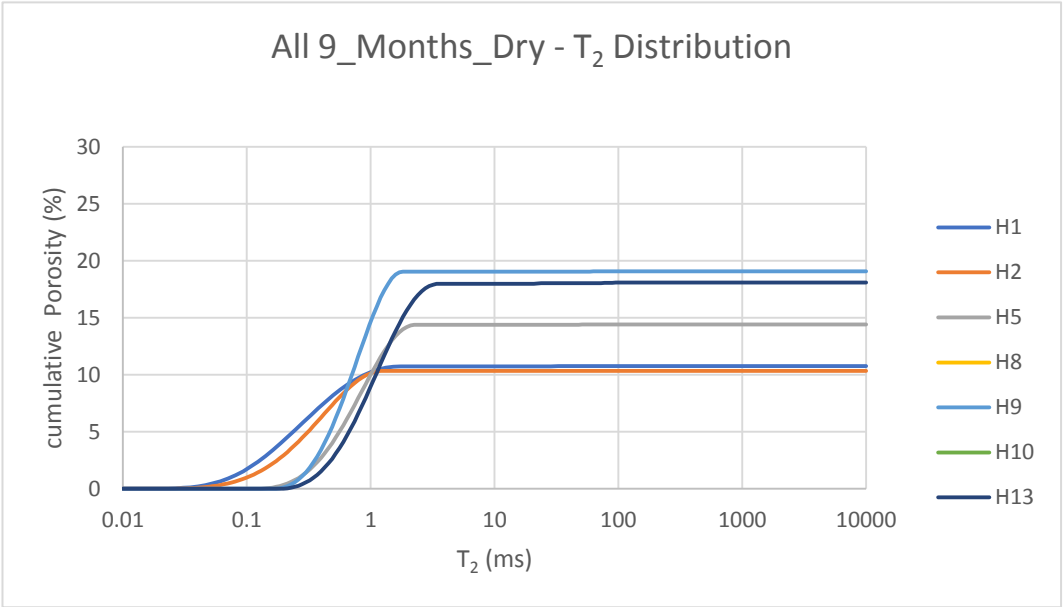
All 9_Months_Dry - T2 Distribution
cumulative Porosity (%)
30
25
20
15
10
5
0
0.01
0.1
1
10
100
1000
10000
T2 (ms)
H1
H2
H5
H8
H9
H10
H13

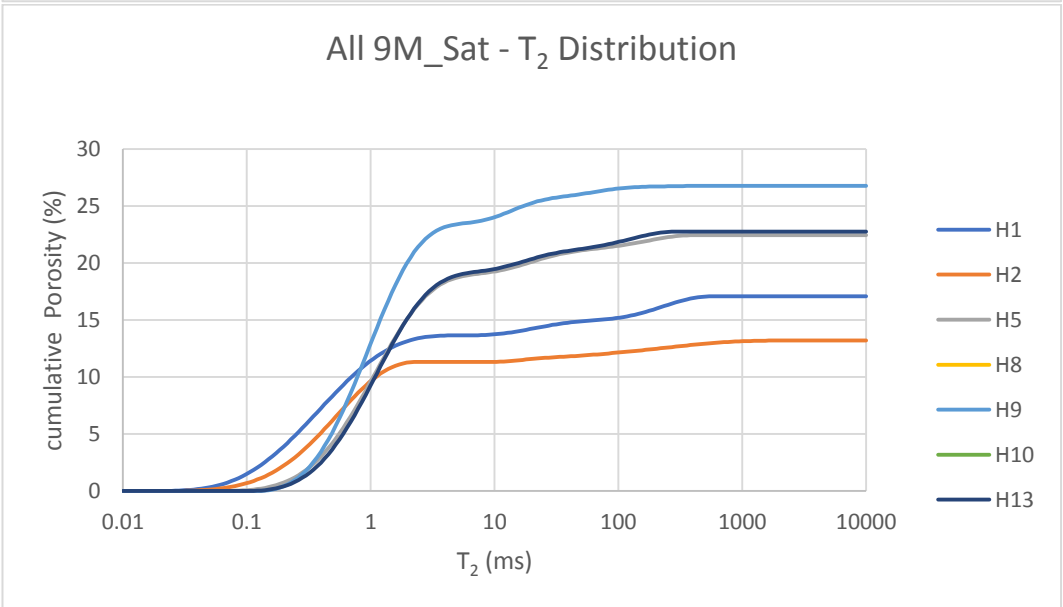
All 9M_Sat - T2 Distribution
cumulative Porosity (%)
30
25
20
15
10
5
0
0.01
0.1
1
10
100
1000
10000
T2 (ms)
H1
H2
H5
H8
H9
H10
H13

C. Plots of NMR T_2 relaxation of all the samples

(Before_Dry, Before_Sat, 4M_Dry, 4M_Sat, 9M_Dry, and 9M_Sat)

T_2 versus incremental porosity (left) and cumulative porosity (right)

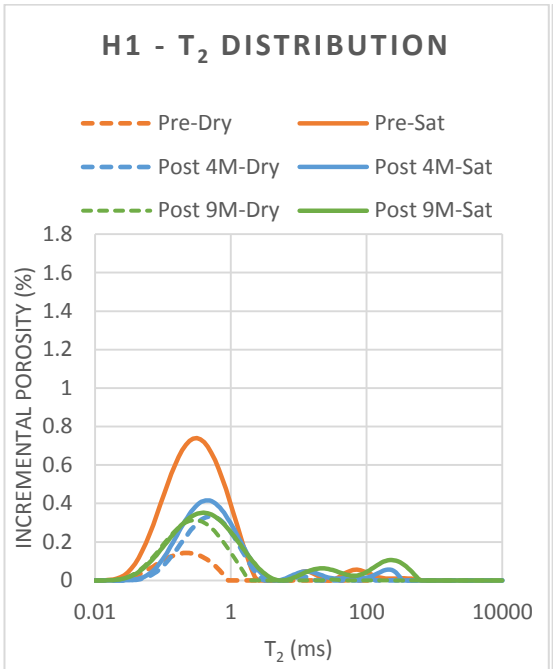

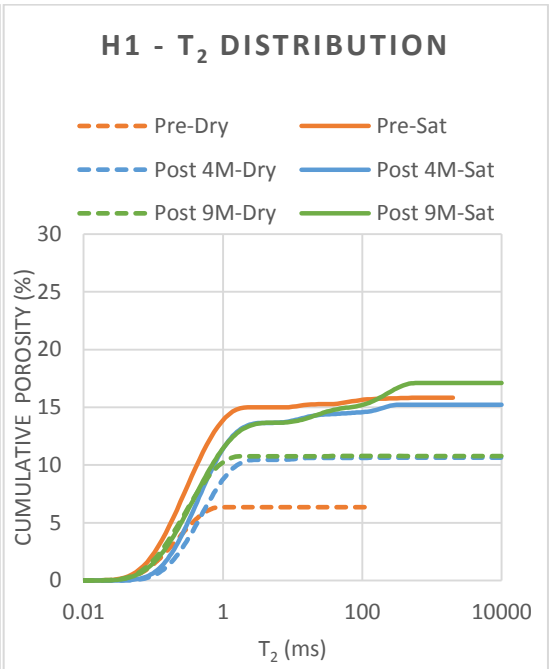

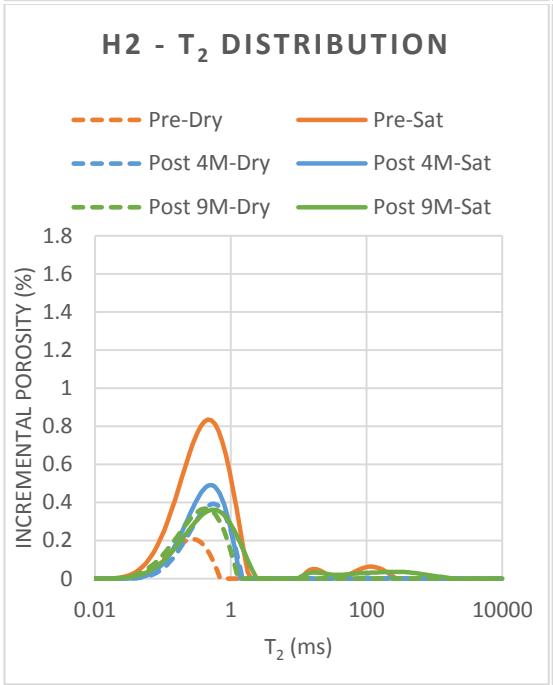

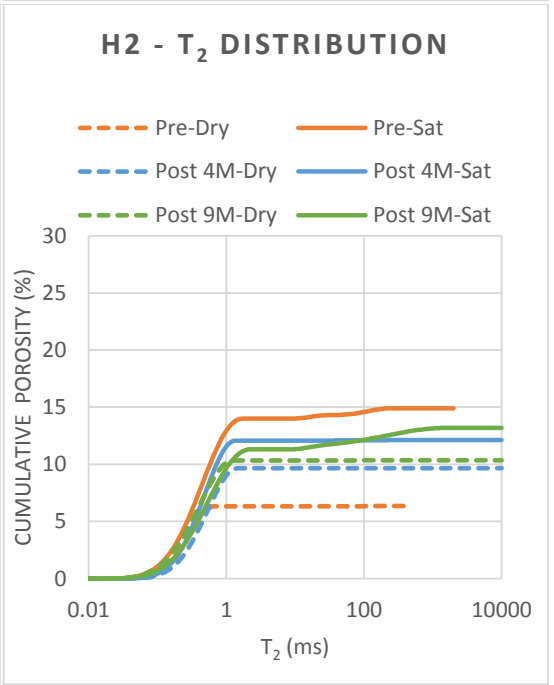

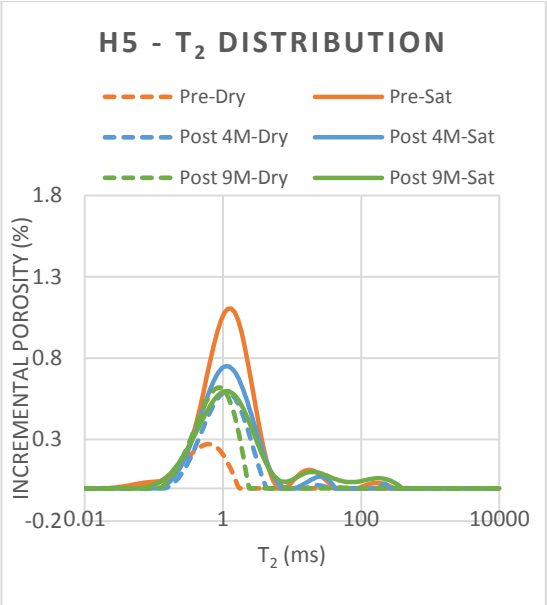
H5 - T2 DISTRIBUTION
Pre-Dry
Pre-Sat
Post 4M-Dry
Post 4M-Sat
Post 9M-Dry
Post 9M-Sat
INCREMENTAL POROSITY (%)
1.8
1.3
0.8
0.3
-0.2
0.01
1
100
10000
T2 (ms)

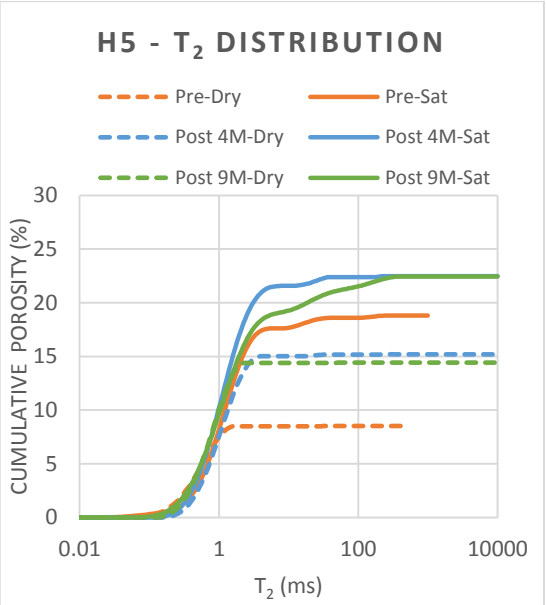
H5 - T2 DISTRIBUTION
Pre-Dry
Pre-Sat
Post 4M-Dry
Post 4M-Sat
Post 9M-Dry
Post 9M-Sat
CUMULATIVE POROSITY (%)
30
25
20
15
10
5
0
0.01
1
100
10000
T2 (ms)

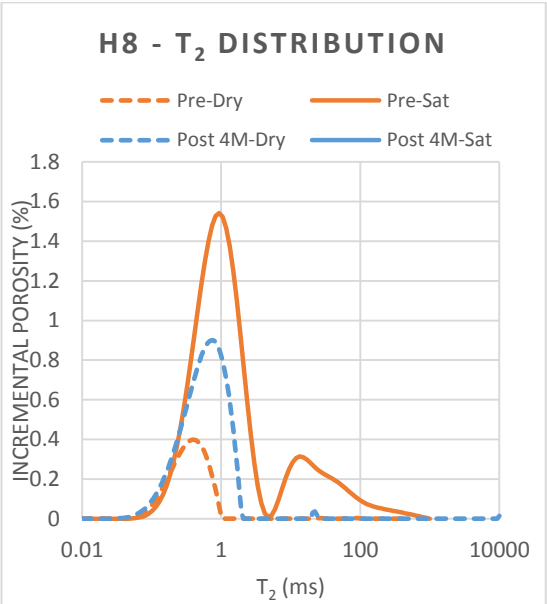
H8 - T2 DISTRIBUTION
Pre-Dry
Pre-Sat
Post 4M-Dry
Post 4M-Sat
INCREMENTAL POROSITY (%)
1.8
1.6
1.4
1.2
1
0.8
0.6
0.4
0.2
0
0.01
1
100
10000
T2 (ms)

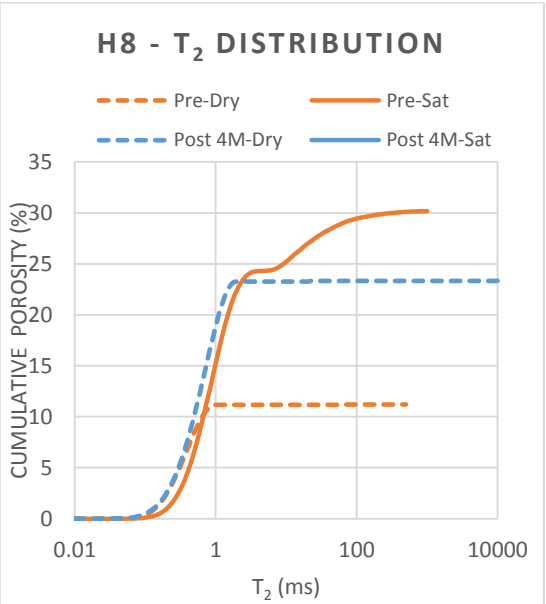
H8 - T2 DISTRIBUTION
Pre-Dry
Pre-Sat
Post 4M-Dry
Post 4M-Sat
CUMULATIVE POROSITY (%)
35
30
25
20
15
10
5
0
0.01
1
100
10000
T2 (ms)

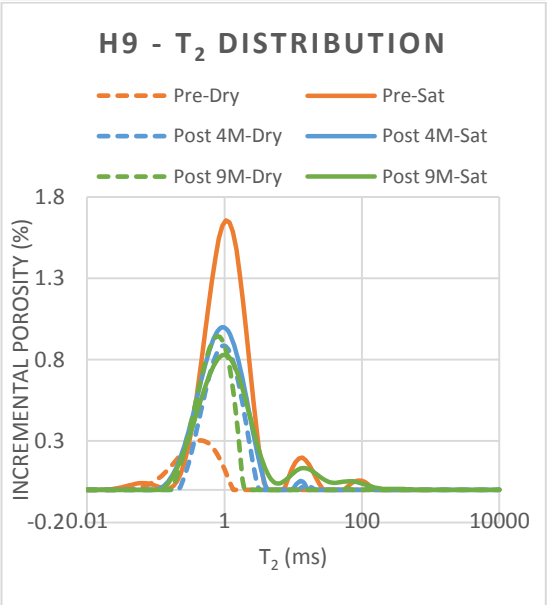
H9 - T2 DISTRIBUTION
Pre-Dry
Pre-Sat
Post 4M-Dry
Post 4M-Sat
Post 9M-Dry
Post 9M-Sat
INCREMENTAL POROSITY (%)
1.8
1.3
0.8
0.3
-0.2
0.01
1
100
10000
T2 (ms)

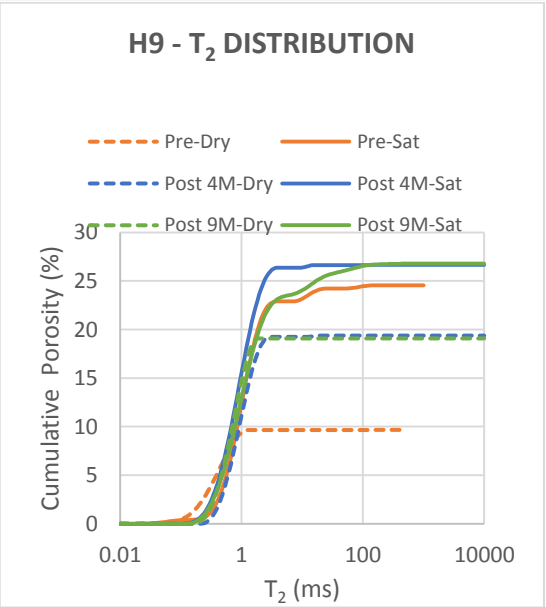
H9 - T2 DISTRIBUTION
Pre-Dry
Pre-Sat
Post 4M-Dry
Post 4M-Sat
Post 9M-Dry
Post 9M-Sat
Cumulative Porosity (%)
30
25
20
15
10
5
0
0.01
1
100
10000
T2 (ms)

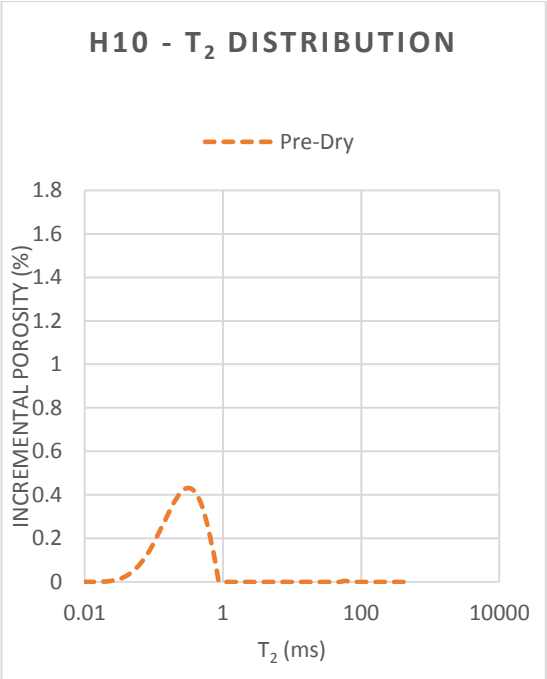
H10 - T2 DISTRIBUTION
Pre-Dry
INCREMENTAL POROSITY (%)
1.8
1.6
1.4
1.2
1
0.8
0.6
0.4
0.2
0
0.01
1
100
10000
T2 (ms)

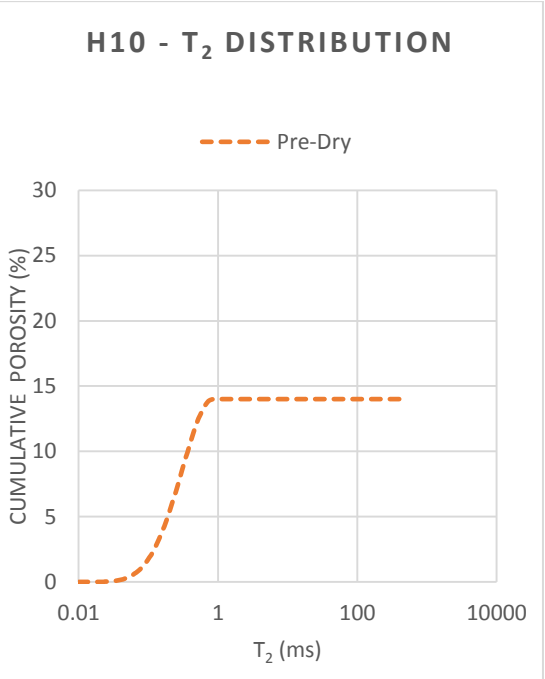
H10 - T2 DISTRIBUTION
Pre-Dry
CUMULATIVE POROSITY (%)
30
25
20
15
10
5
0
0.01
1
100
10000
T2 (ms)

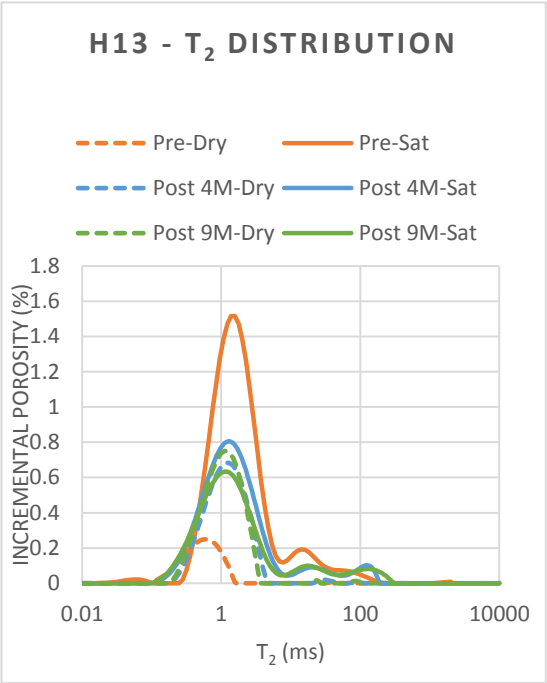
H13 - T2 DISTRIBUTION
Pre-Dry
Pre-Sat
Post 4M-Dry
Post 4M-Sat
Post 9M-Dry
Post 9M-Sat
INCREMENTAL POROSITY (%)
1.8
1.6
1.4
1.2
1
0.8
0.6
0.4
0.2
0
0.01
1
100
10000
T2 (ms)

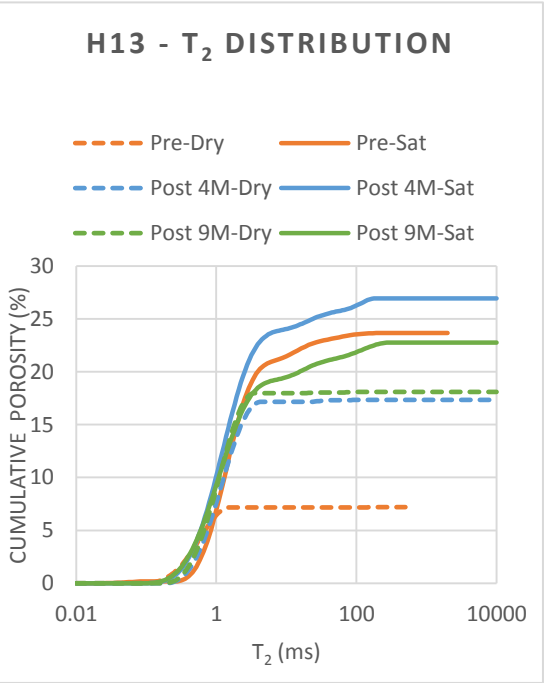
H13 - T2 DISTRIBUTION
Pre-Dry
Pre-Sat
Post 4M-Dry
Post 4M-Sat
Post 9M-Dry
Post 9M-Sat
CUMULATIVE POROSITY (%)
30
25
20
15
10
5
0
0.01
1
100
10000
T2 (ms)

D. NMR signal attenuation for the CPMG experiments

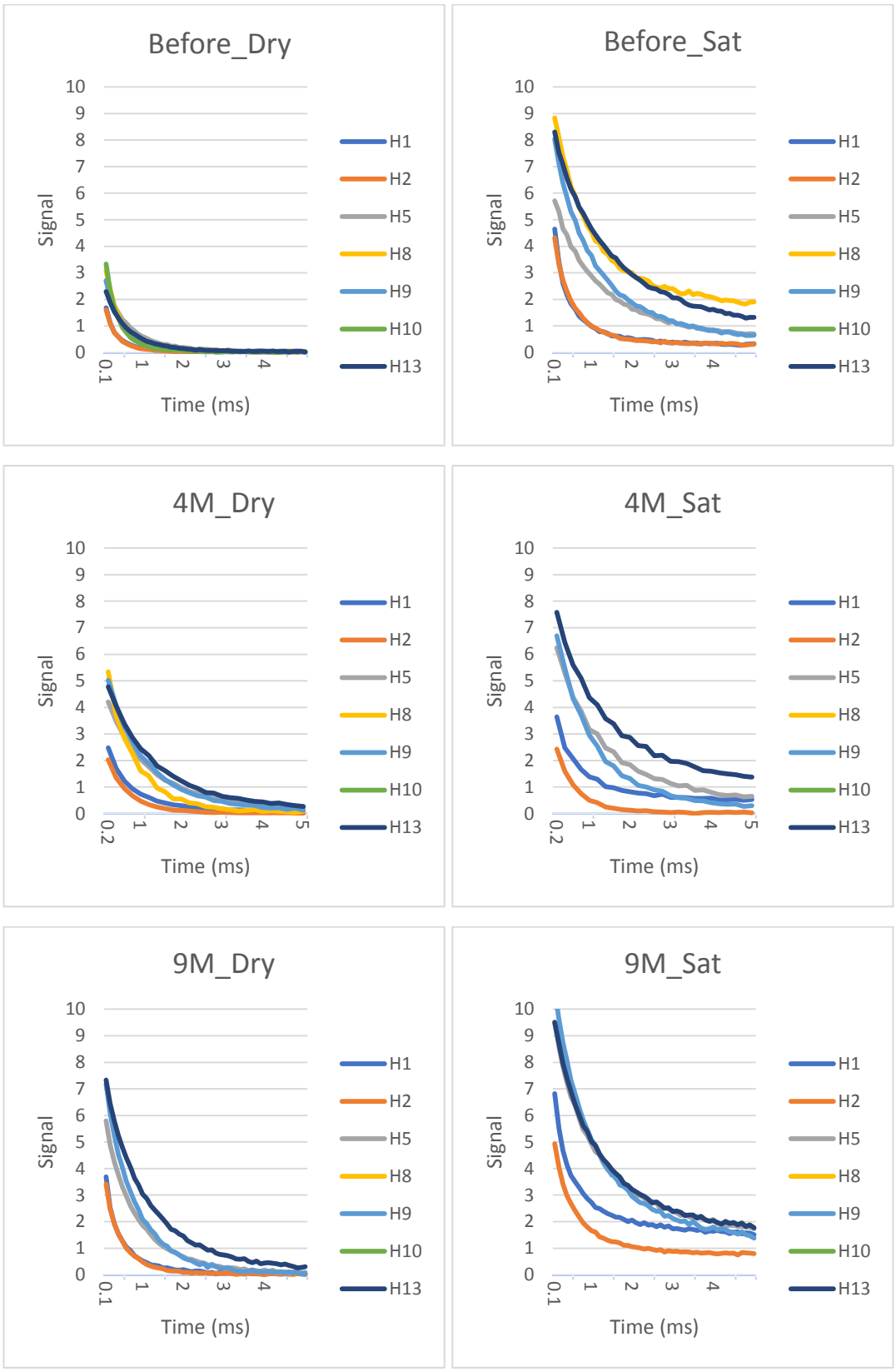

Appendix VI. LPNA

A. Low-pressure nitrogen isotherms

Low-pressure nitrogen isotherms for the analysed samples before (Blue) and after (Orange) exposure to $scCO_2$

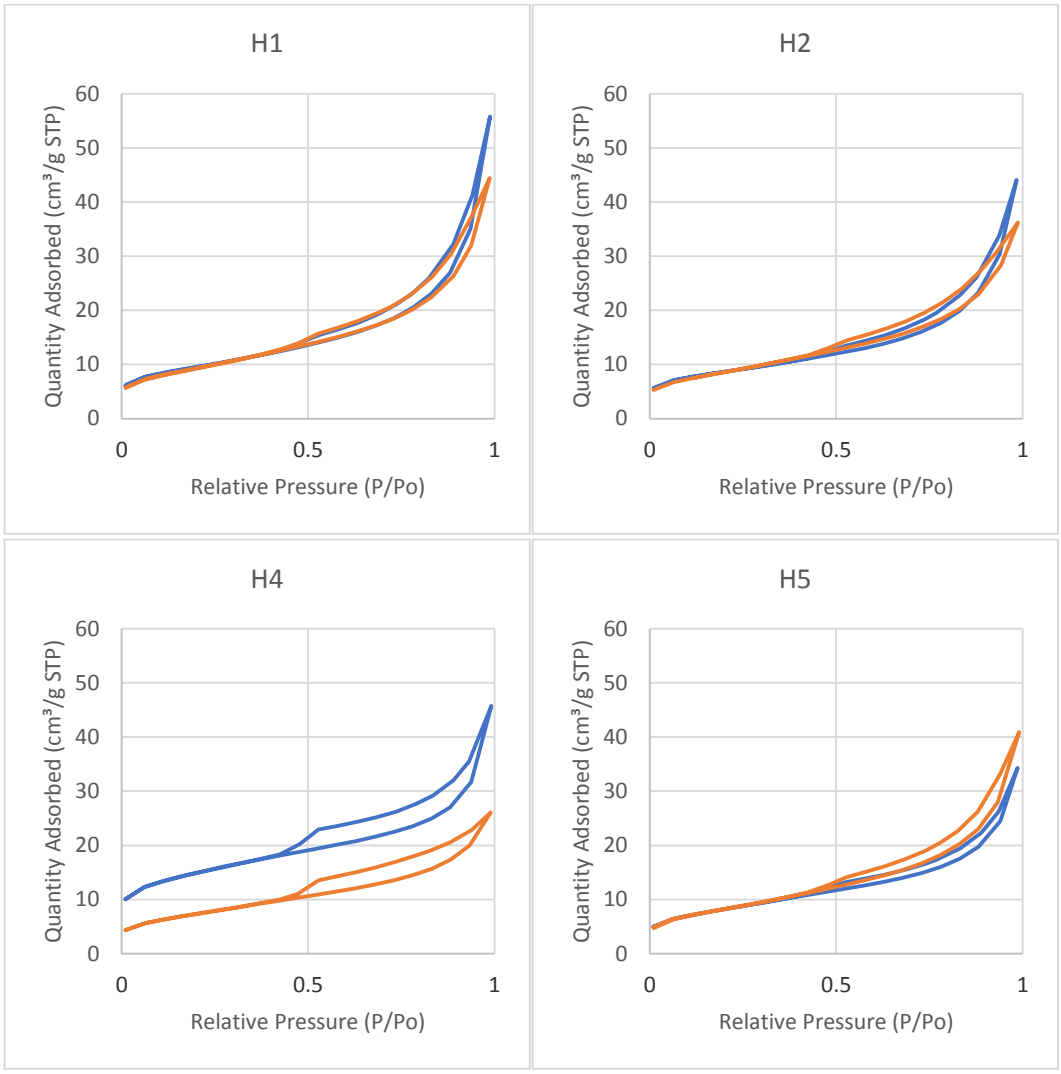

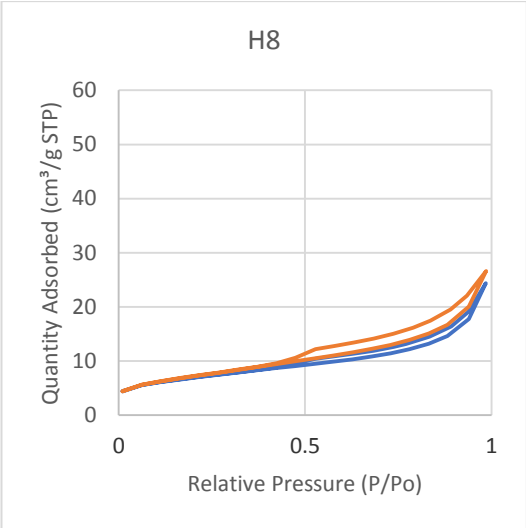
H8
Quantity Adsorbed (cm³/g STP)
60
50
40
30
20
10
0
0
0.5
1
Relative Pressure (P/Po)

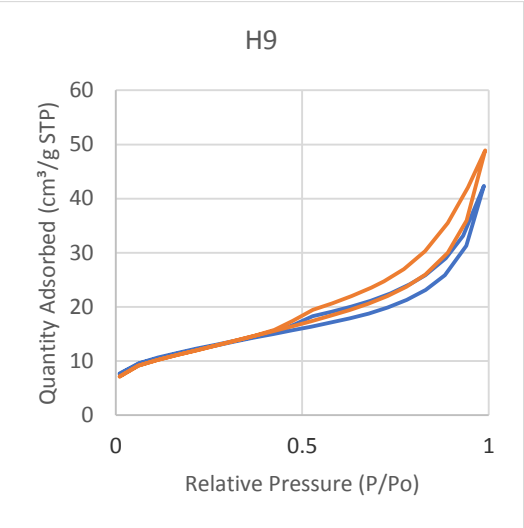
H9
Quantity Adsorbed (cm³/g STP)
60
50
40
30
20
10
0
0
0.5
1
Relative Pressure (P/Po)

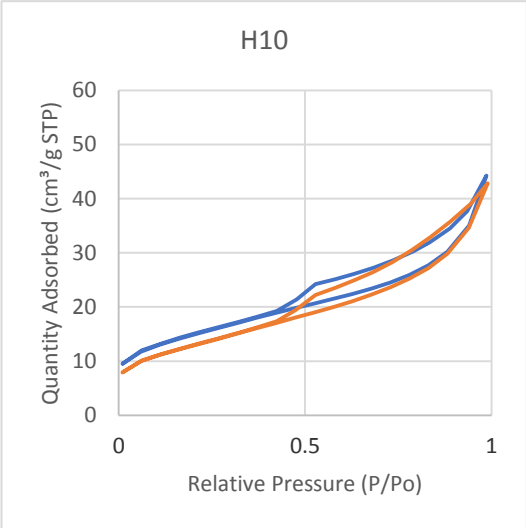
H10
Quantity Adsorbed (cm³/g STP)
60
50
40
30
20
10
0
0
0.5
1
Relative Pressure (P/Po)

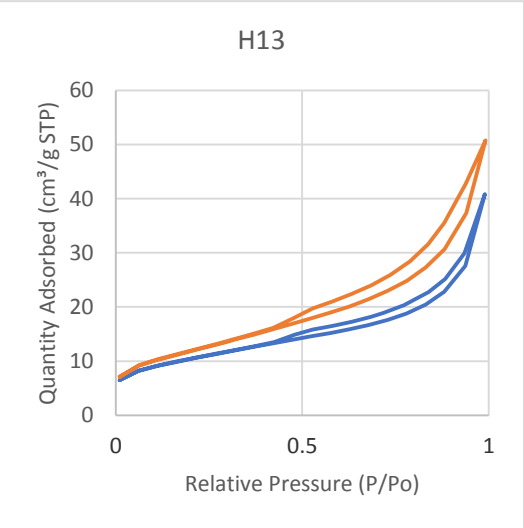
H13
Quantity Adsorbed (cm³/g STP)
60
50
40
30
20
10
0
0
0.5
1
Relative Pressure (P/Po)

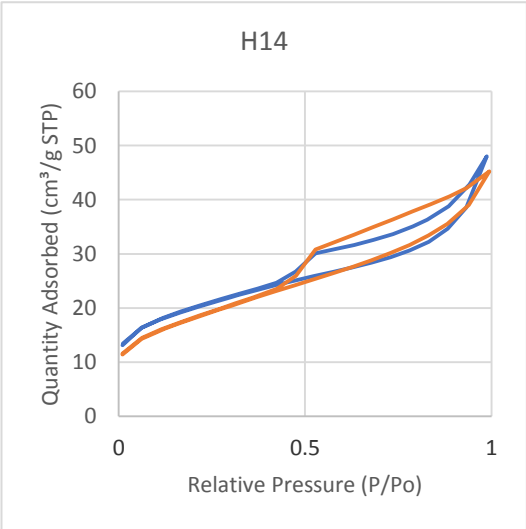
H14
Quantity Adsorbed (cm³/g STP)
60
50
40
30
20
10
0
0
0.5
1
Relative Pressure (P/Po)

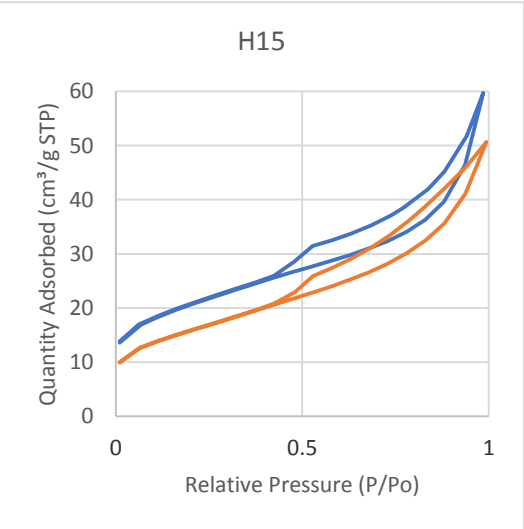
H15
Quantity Adsorbed (cm³/g STP)
60
50
40
30
20
10
0
0
0.5
1
Relative Pressure (P/Po)

B. Incremental pore volume (IPV) versus pore width

Blue and the red curves are for before and after exposure to $scCO_2$

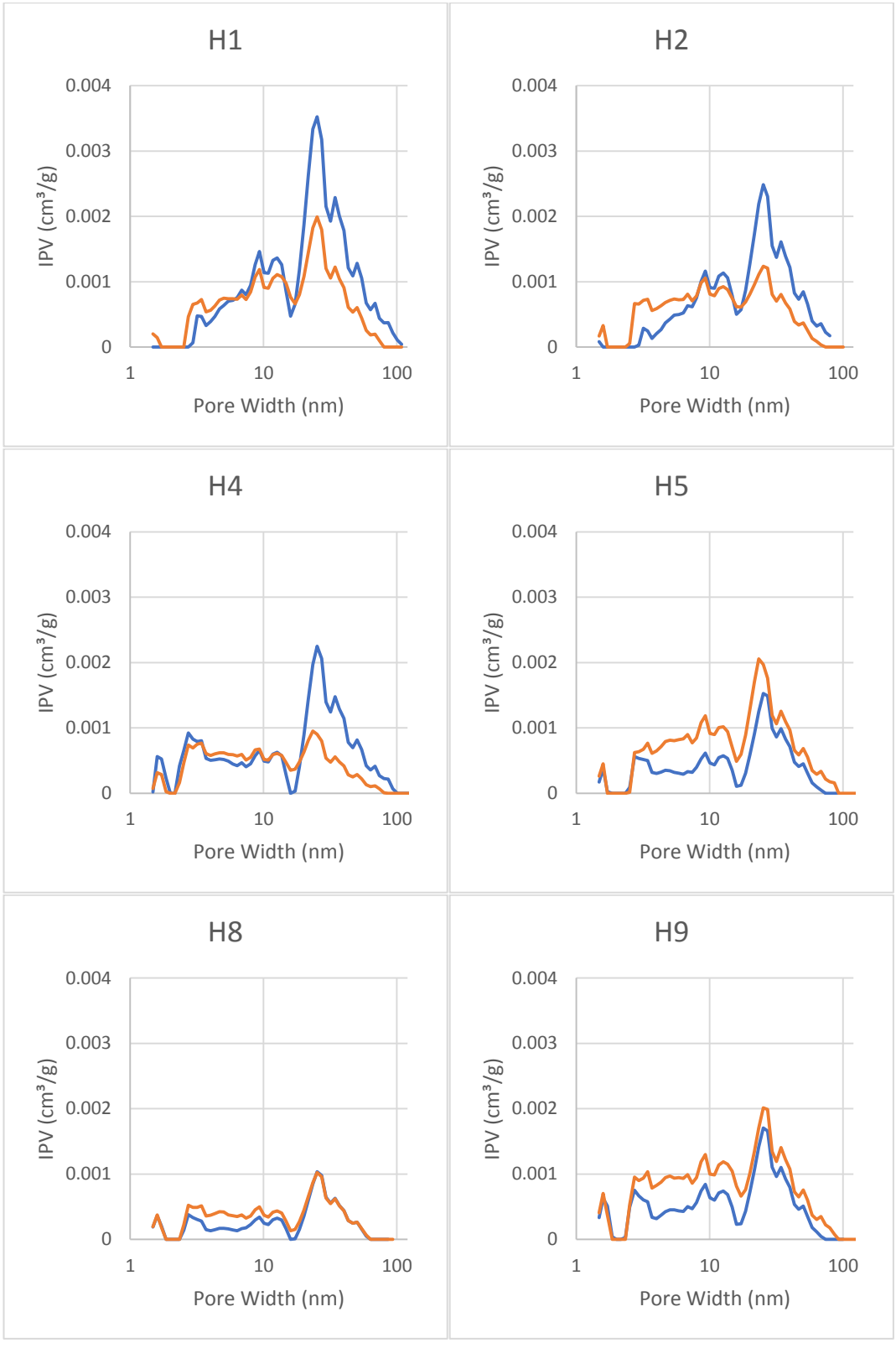

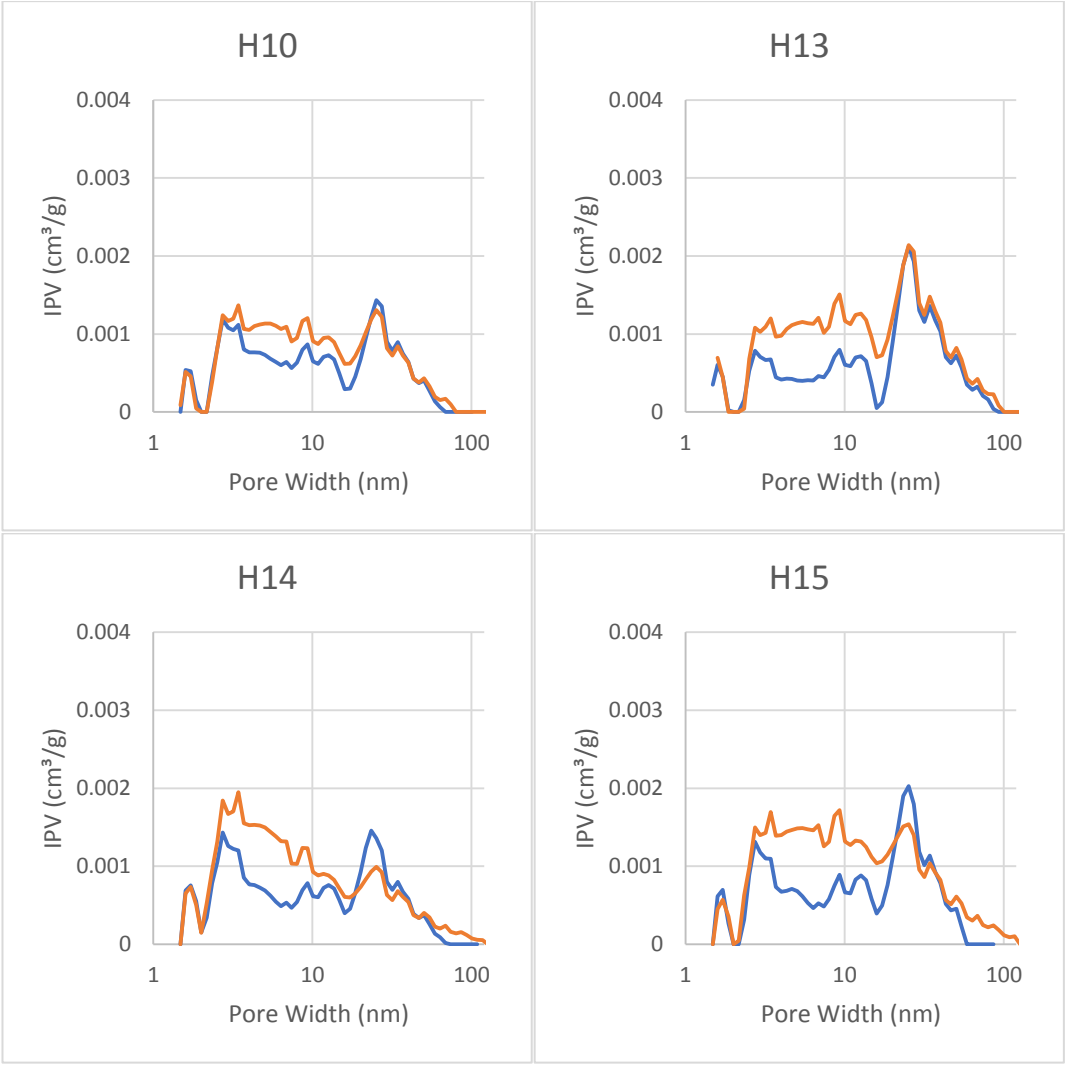
H10
0.004
0.003
0.002
0.001
0
IPV (cm³/g)
1
10
100
Pore Width (nm)
H13
0.004
0.003
0.002
0.001
0
IPV (cm³/g)
1
10
100
Pore Width (nm)
H14
0.004
0.003
0.002
0.001
0
IPV (cm³/g)
1
10
100
Pore Width (nm)
H15
0.004
0.003
0.002
0.001
0
IPV (cm³/g)
1
10
100
Pore Width (nm)

C. Incremental Surface Area (ISA) versus pore width

Blue and the red curves are for before and after exposure to $scCO_2$

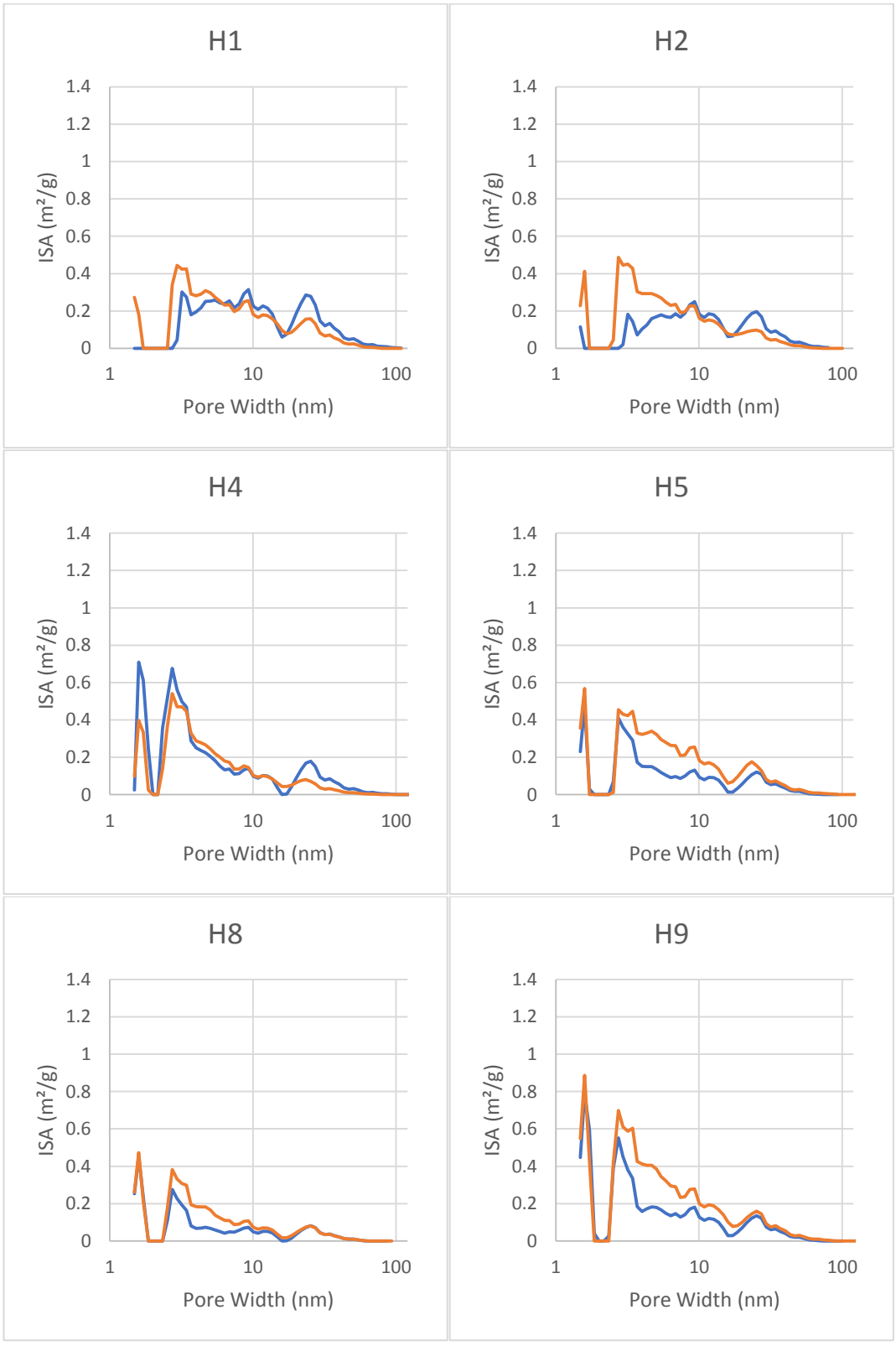

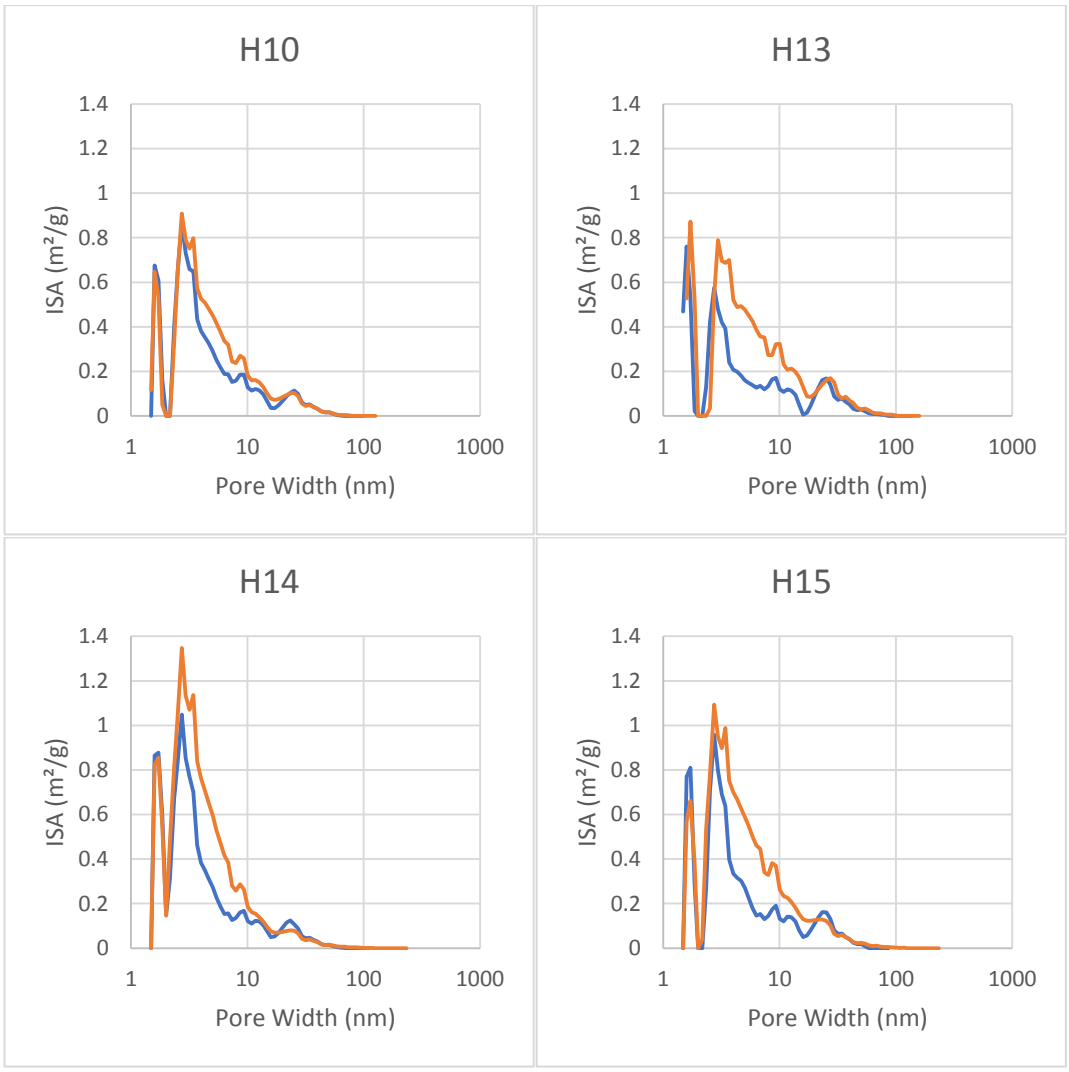
H10
H13
H14
H15
ISA (m²/g)
Pore Width (nm)
0
0.2
0.4
0.6
0.8
1
1.2
1.4
1
10
100
1000

D. Observation Samples

Incremental pore volume. Blue: Before, Red: After, Gray: Observed.

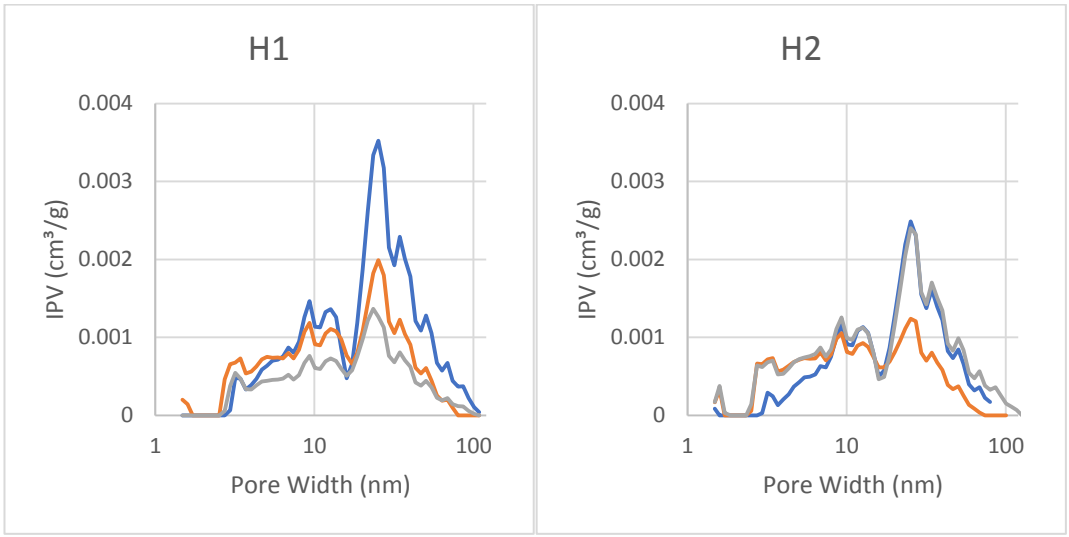

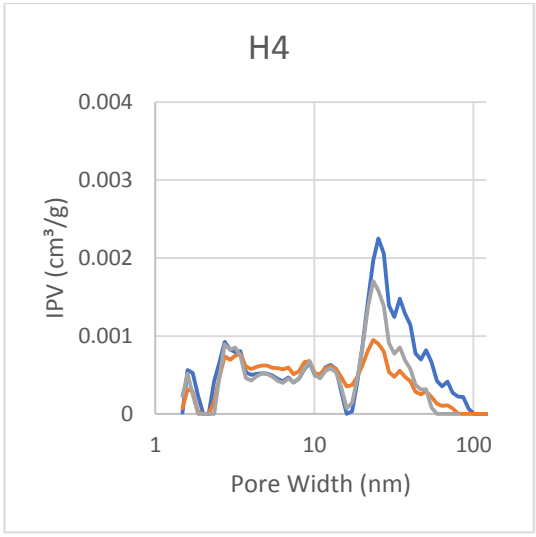

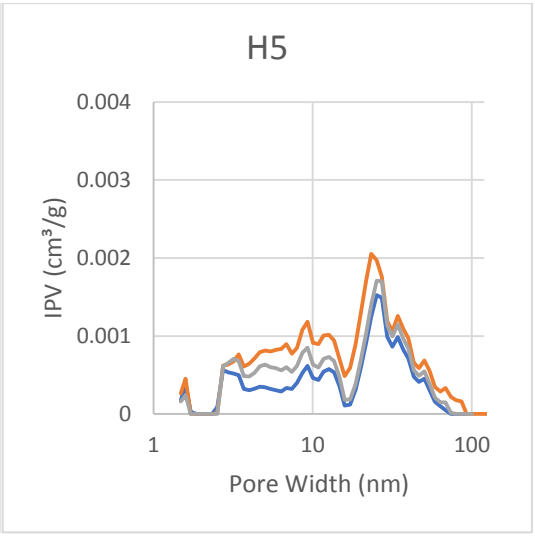

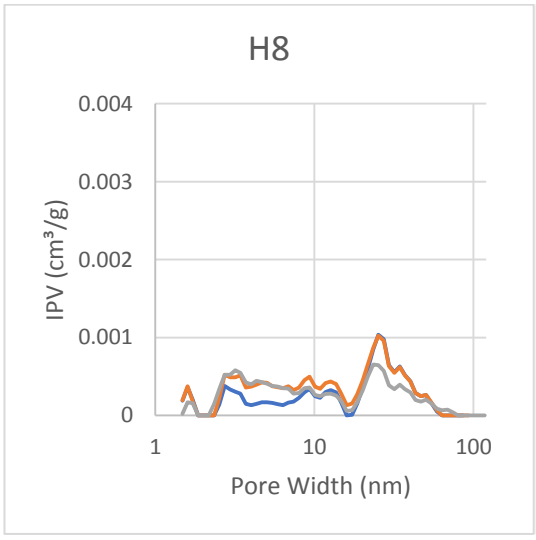

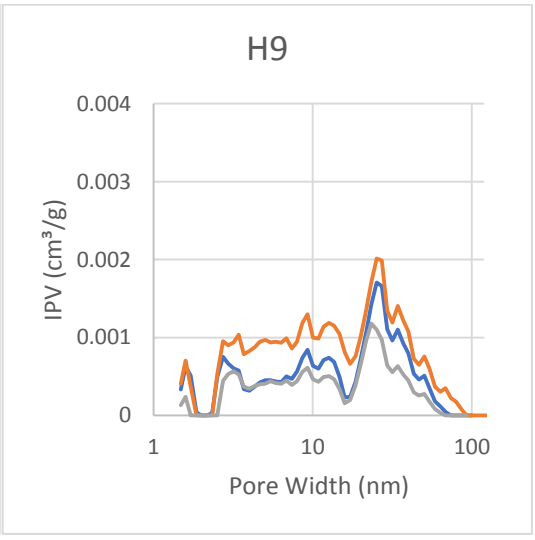

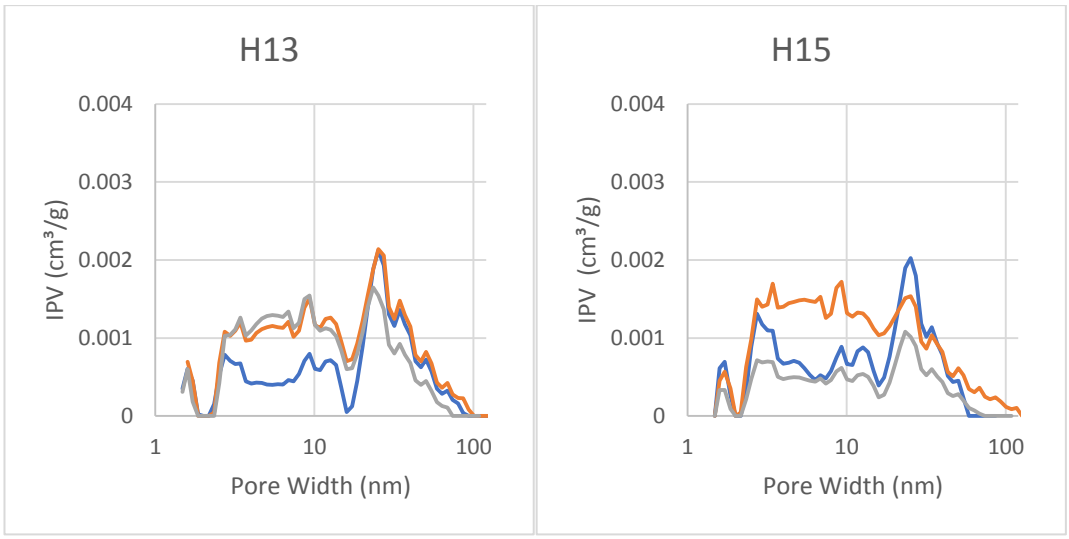
H13
0.004
0.003
0.002
0.001
0
IPV (cm³/g)
1
10
100
Pore Width (nm)
H15
0.004
0.003
0.002
0.001
0
IPV (cm³/g)
1
10
100
Pore Width (nm)

Incremental Surface Area. Blue: Pre-exposed, Red: Post exposed, Gray: Observed.

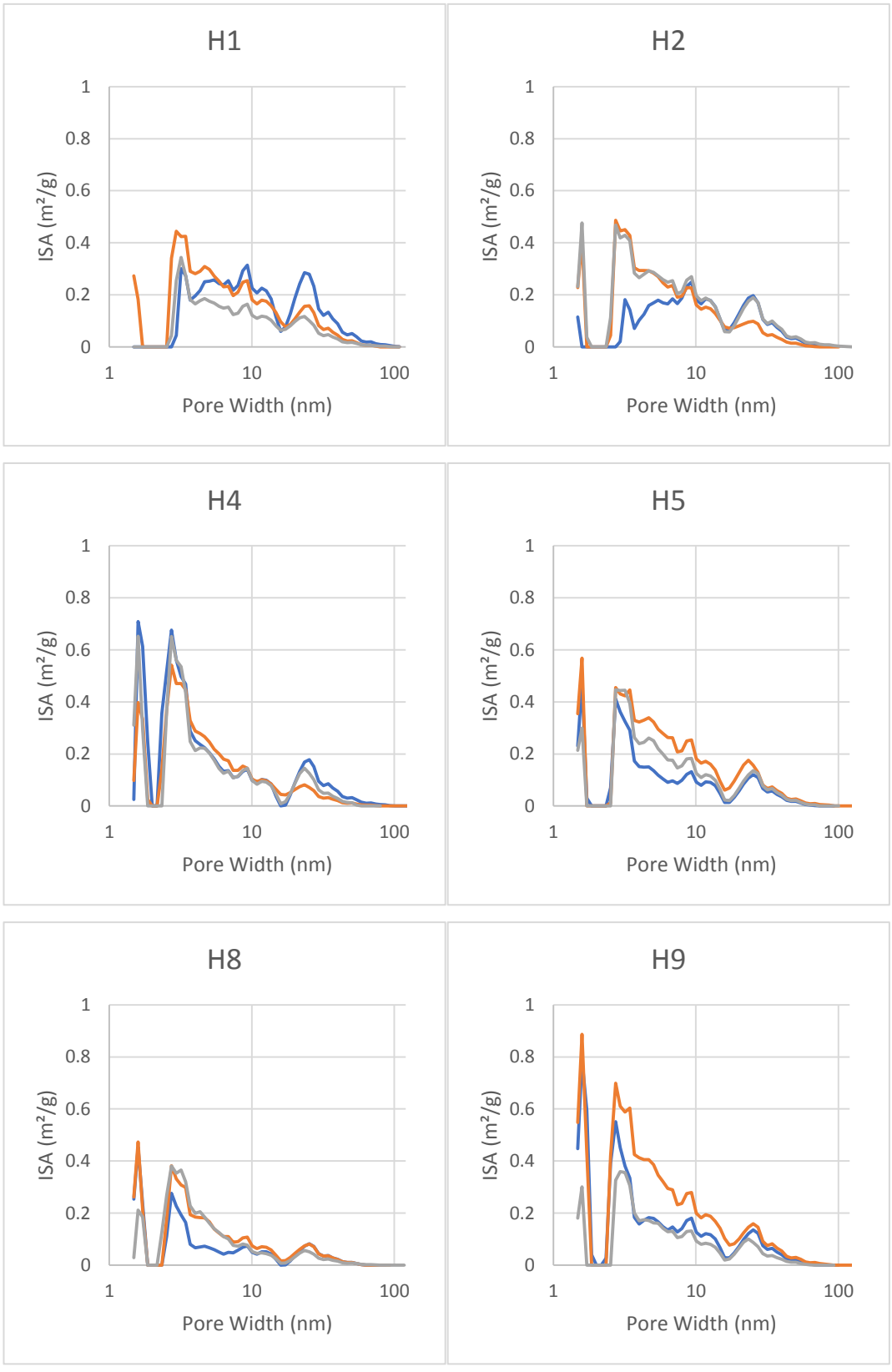

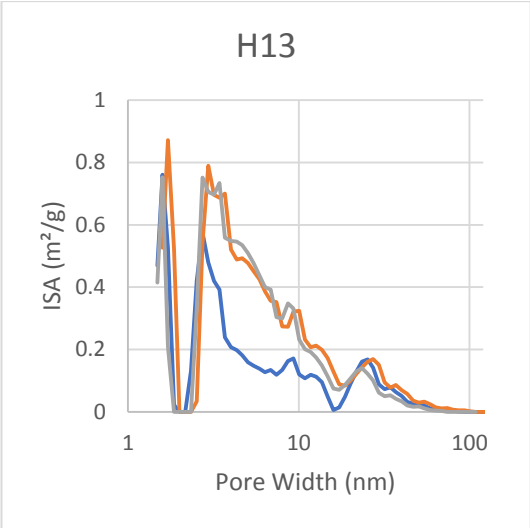
H13
ISA (m²/g)
1
0.8
0.6
0.4
0.2
0
1
10
100
Pore Width (nm)

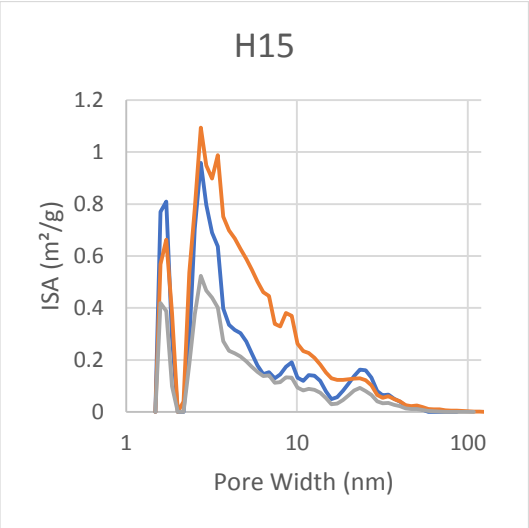
H15
ISA (m²/g)
1.2
1
0.8
0.6
0.4
0.2
0
1
10
100
Pore Width (nm)

Appendix VII. MICP

A. Capillary pressure curves from MICP intrusion vs. mercury saturation

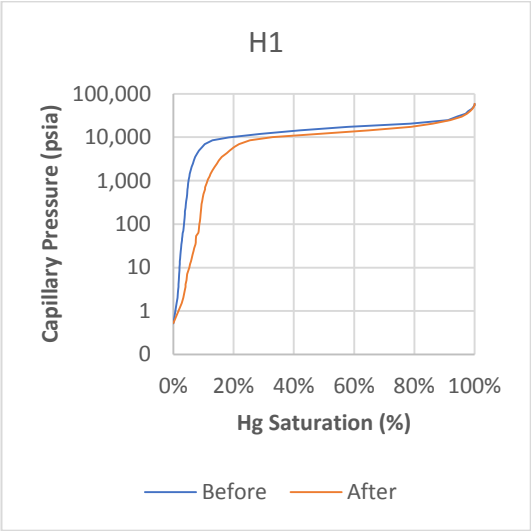

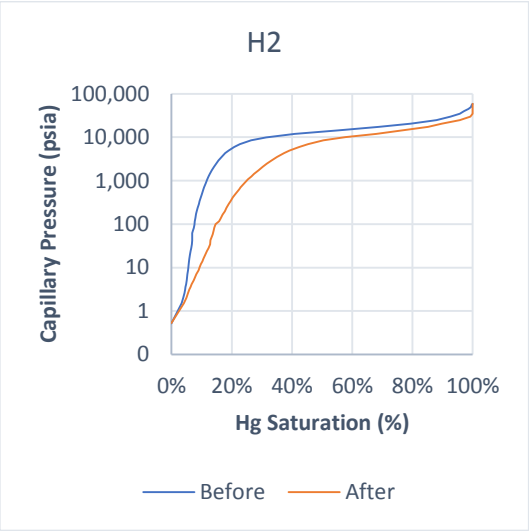

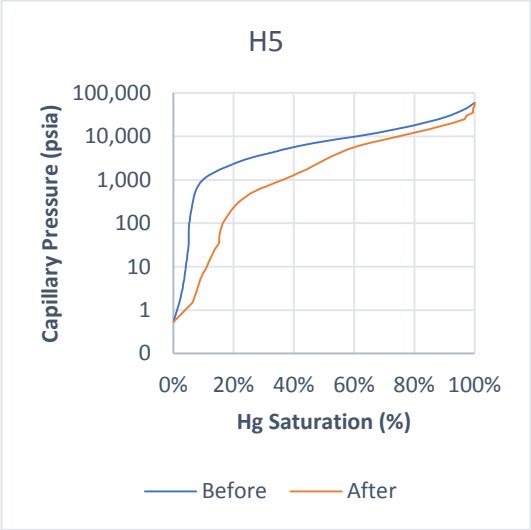

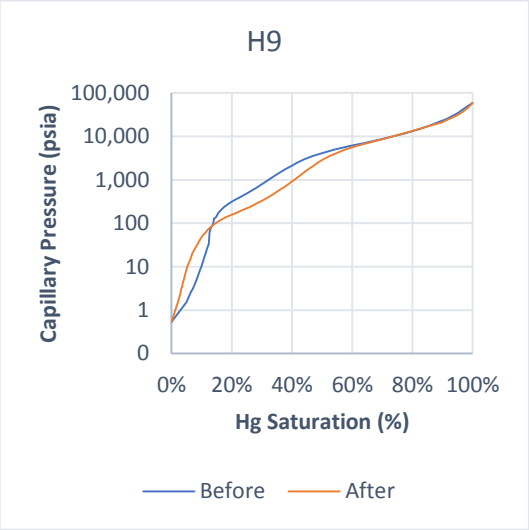

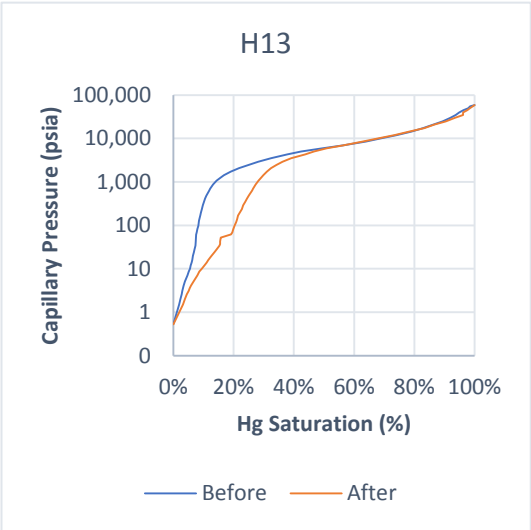

B. Incremental Intrusion vs Pore Size

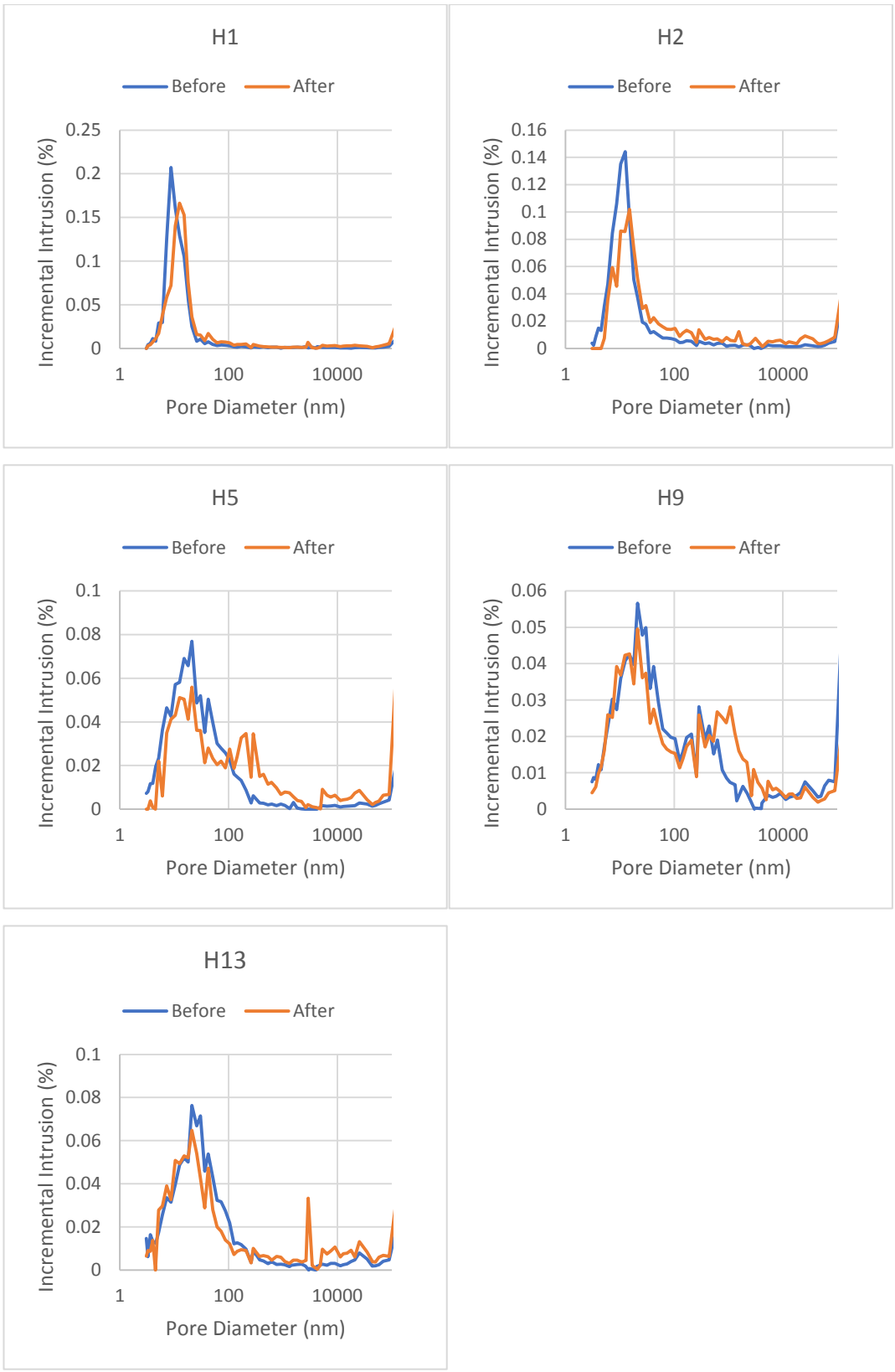

Appendix VIII. Reaction Path Modelling

A. Experimental condition

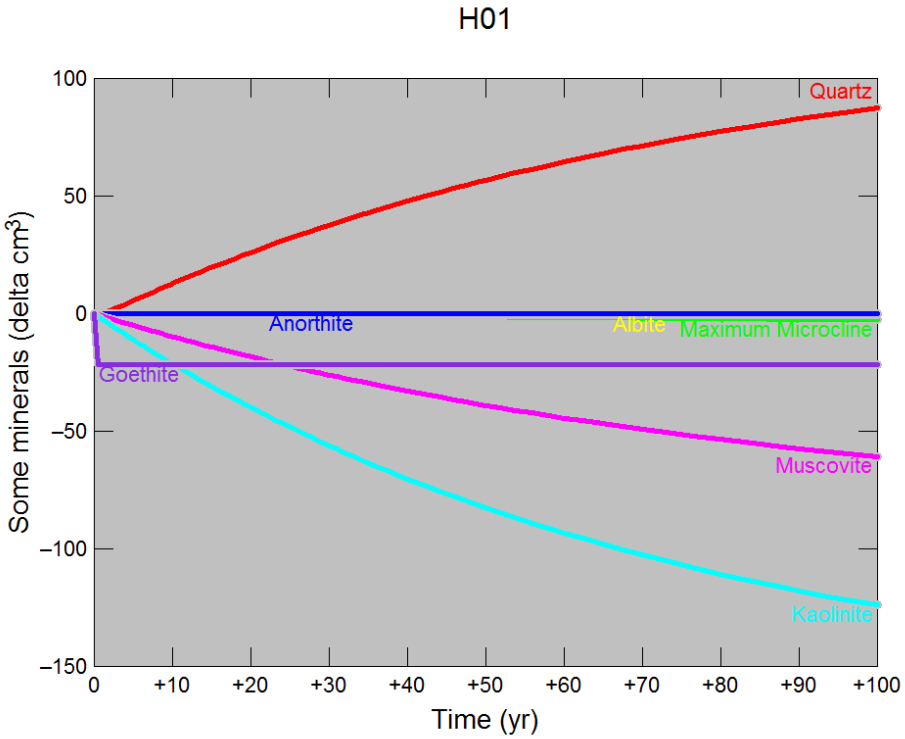

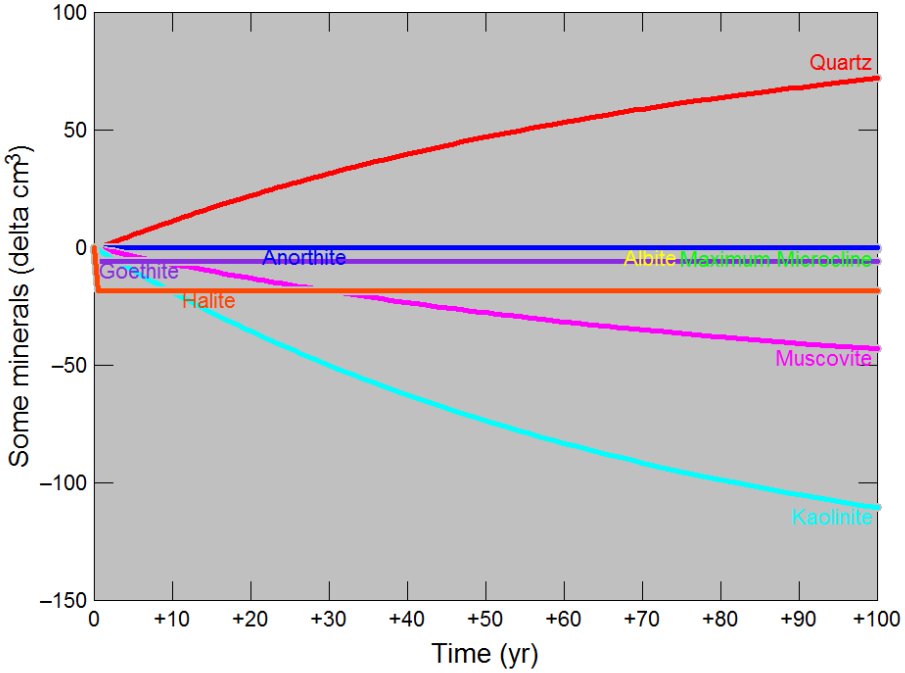

H03

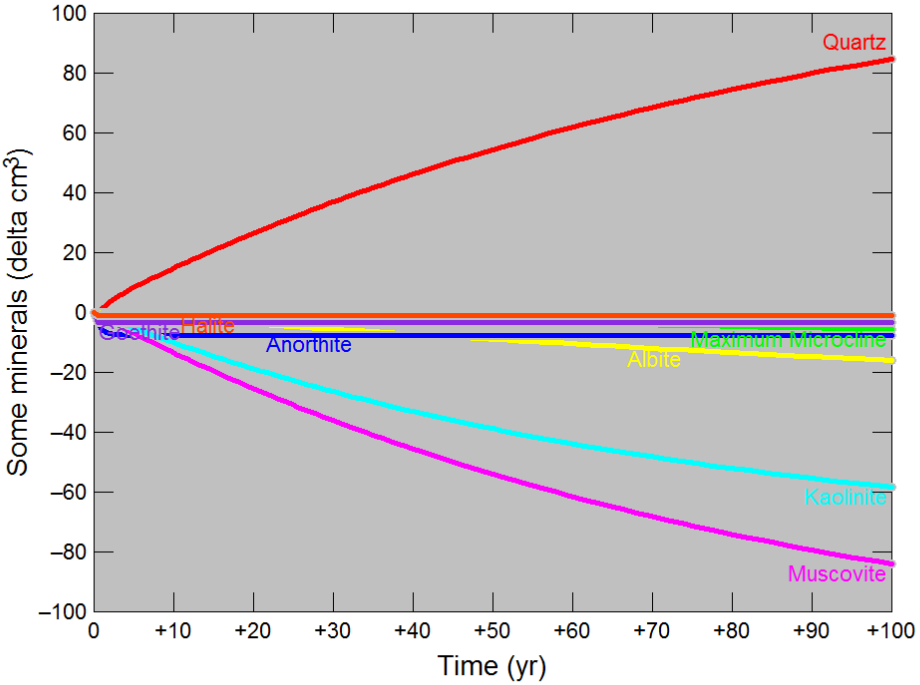
Some minerals (delta cm3)
Time (yr)
Quartz
Halite
Goethite
Anorthite
Maximum Microcline
Albite
Kaolinite
Muscovite

H04

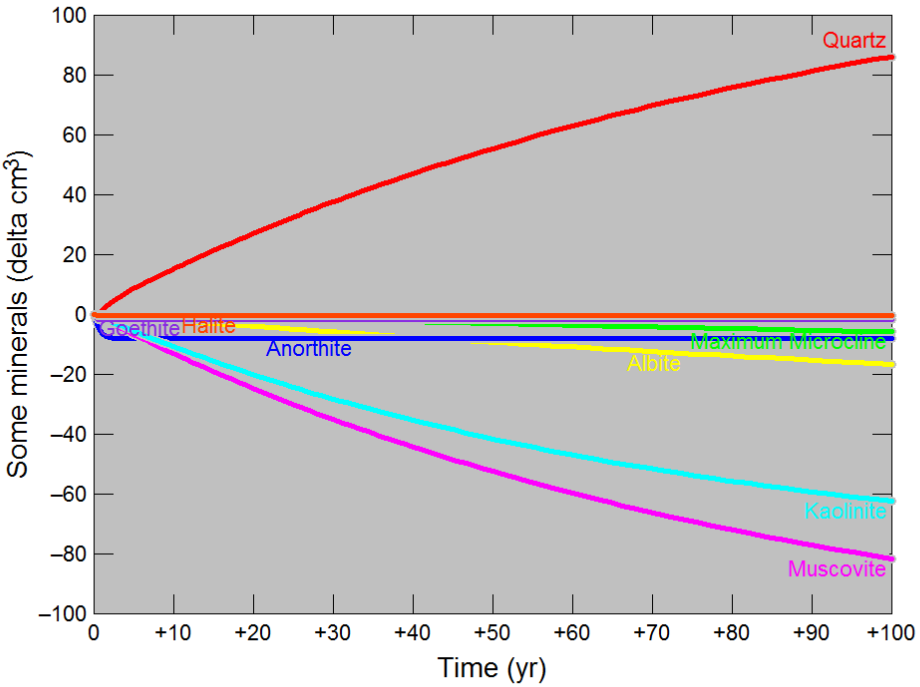
Some minerals (delta cm3)
Time (yr)
Quartz
Halite
Goethite
Anorthite
Maximum Microcline
Albite
Kaolinite
Muscovite

H05

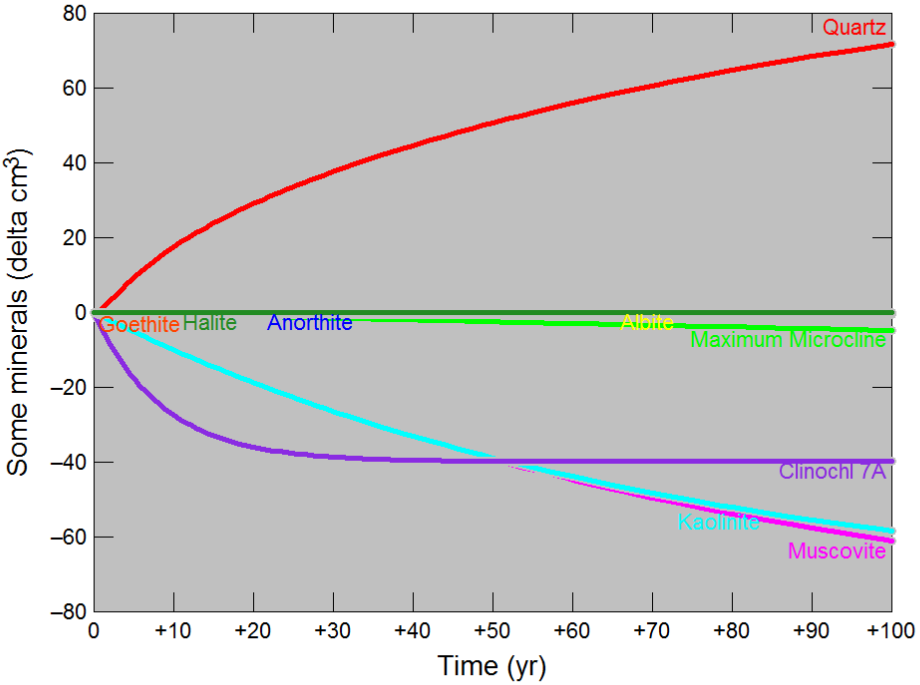
Some minerals (delta cm3)
Time (yr)
Quartz
Goethite
Halite
Anorthite
Albite
Maximum Microcline
Clinochl 7A
Kaolinite
Muscovite

H06

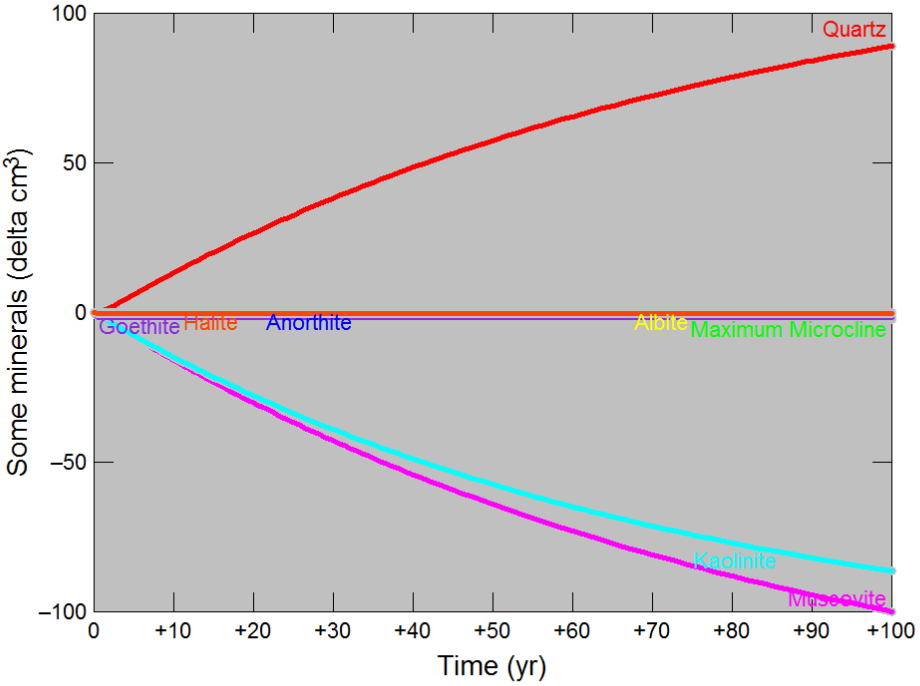
Some minerals (delta cm3)
Time (yr)
Quartz
Goethite
Halite
Anorthite
Albite
Maximum Microcline
Kaolinite
Muscovite

H07

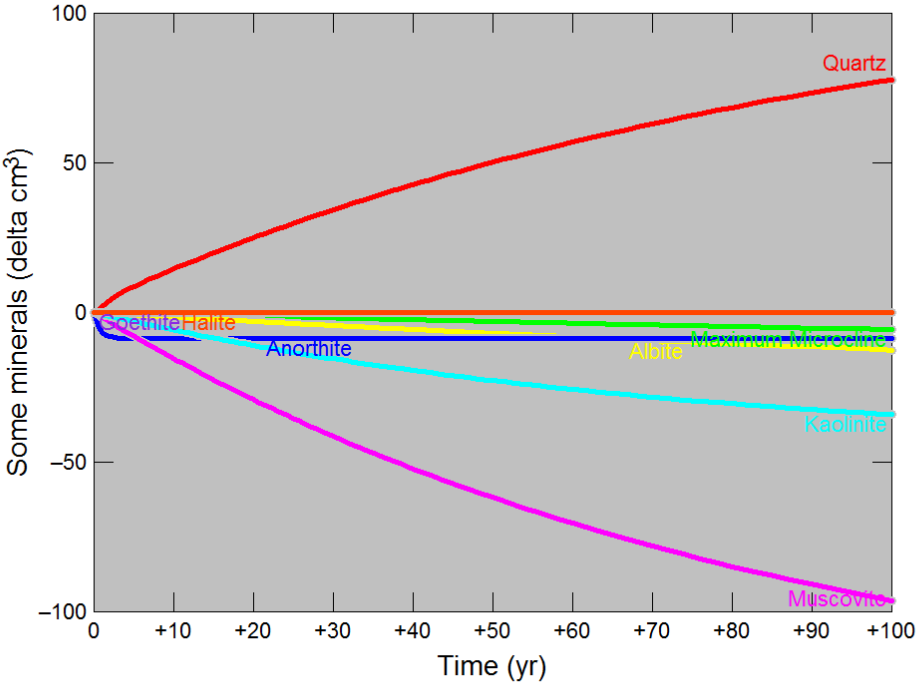
Some minerals (delta cm3)
Time (yr)
Quartz
Goethite
Halite
Anorthite
Albite
Maximum Microcline
Kaolinite
Muscovite

H08

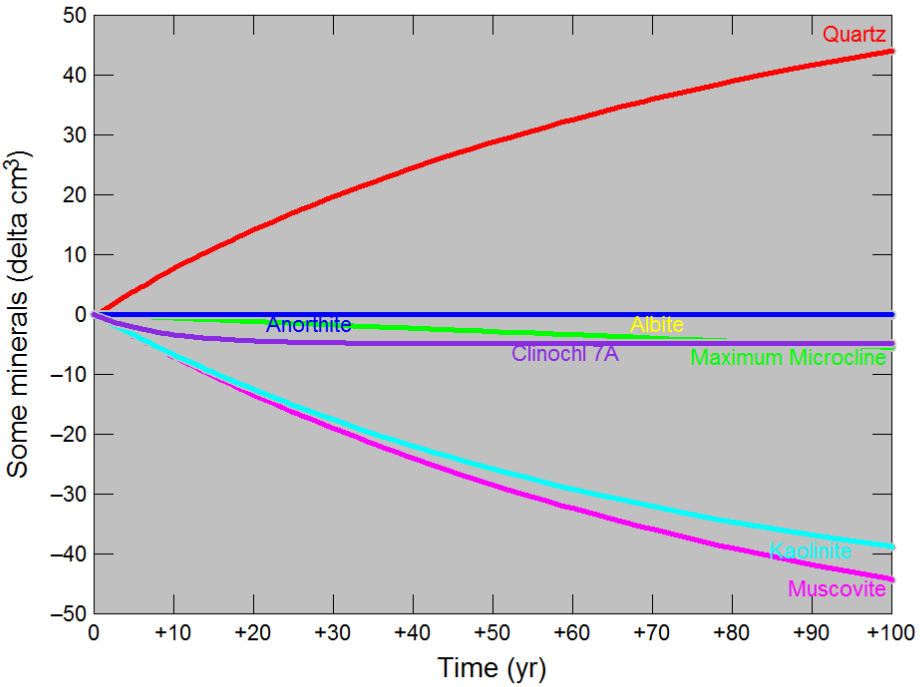
Some minerals (delta cm3)
Time (yr)
Quartz
Anorthite
Albite
Clinochl 7A
Maximum Microcline
Kaolinite
Muscovite

H09

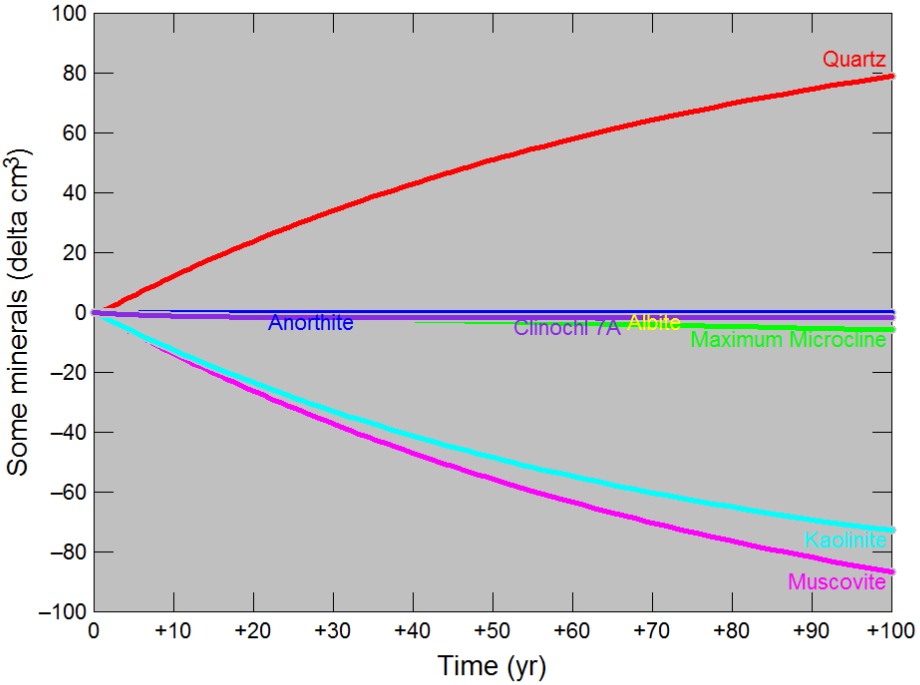
Some minerals (delta cm3)
Time (yr)
Quartz
Anorthite
Clinochl 7A
Albite
Maximum Microcline
Kaolinite
Muscovite

H10

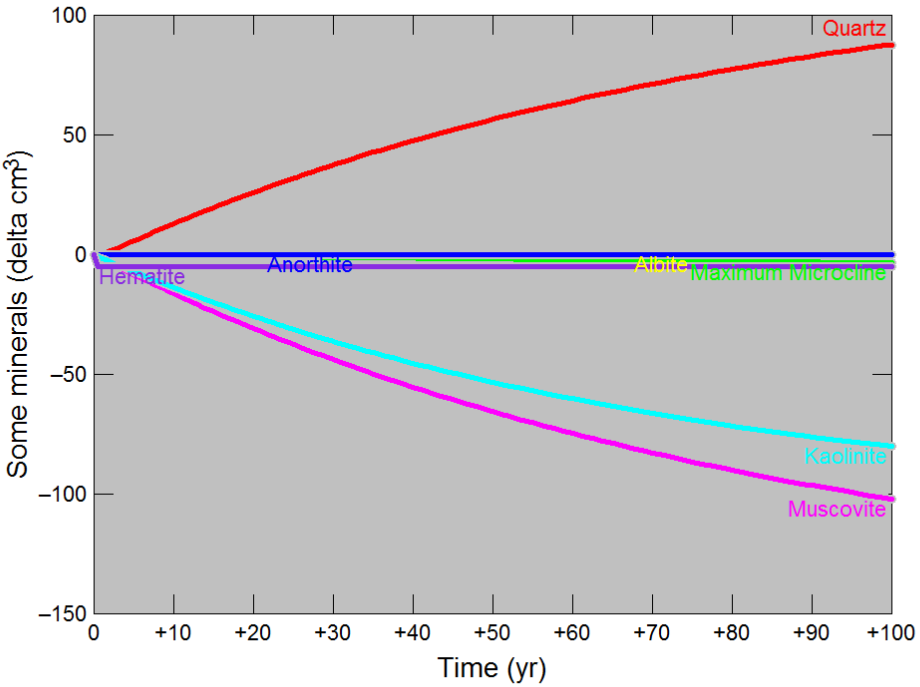
Some minerals (delta cm3)
Time (yr)
Quartz
Hematite
Anorthite
Albite
Maximum Microcline
Kaolinite
Muscovite

H11

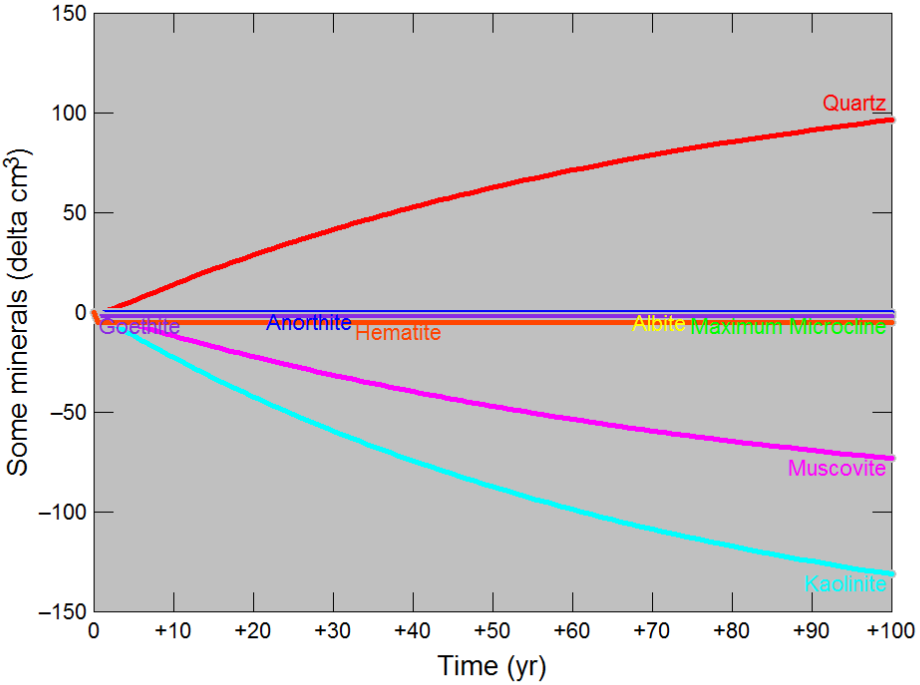
Some minerals (delta cm3)
Time (yr)
Quartz
Anorthite
Hematite
Albite
Maximum Microcline
Muscovite
Kaolinite
150
100
50
0
−50
−100
−150
0
+10
+20
+30
+40
+50
+60
+70
+80
+90
+100

H12

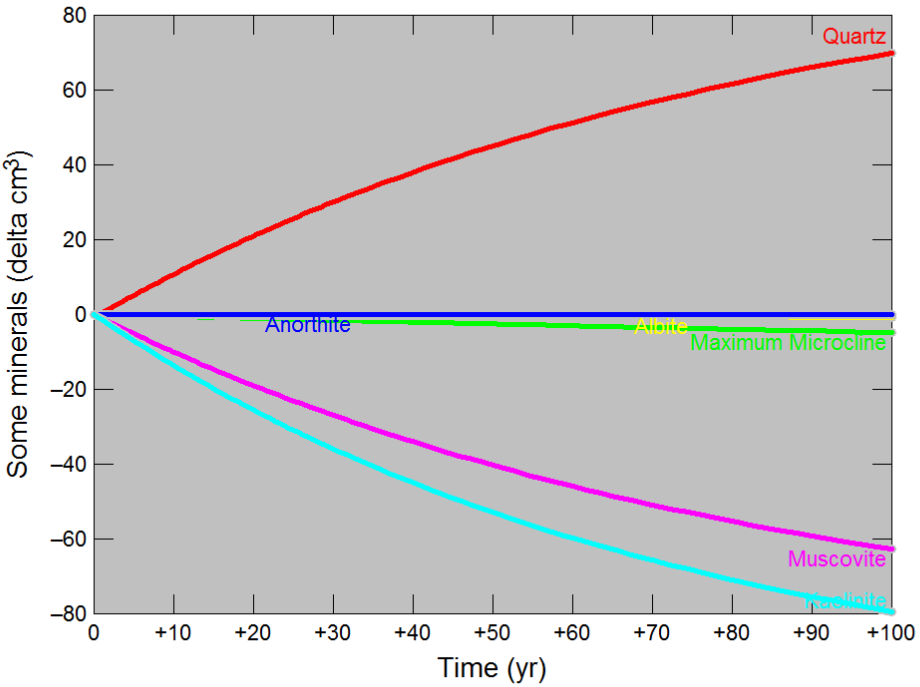
Some minerals (delta cm3)
Time (yr)
Quartz
Anorthite
Albite
Maximum Microcline
Muscovite
Kaolinite
80
60
40
20
0
−20
−40
−60
−80
0
+10
+20
+30
+40
+50
+60
+70
+80
+90
+100

H13

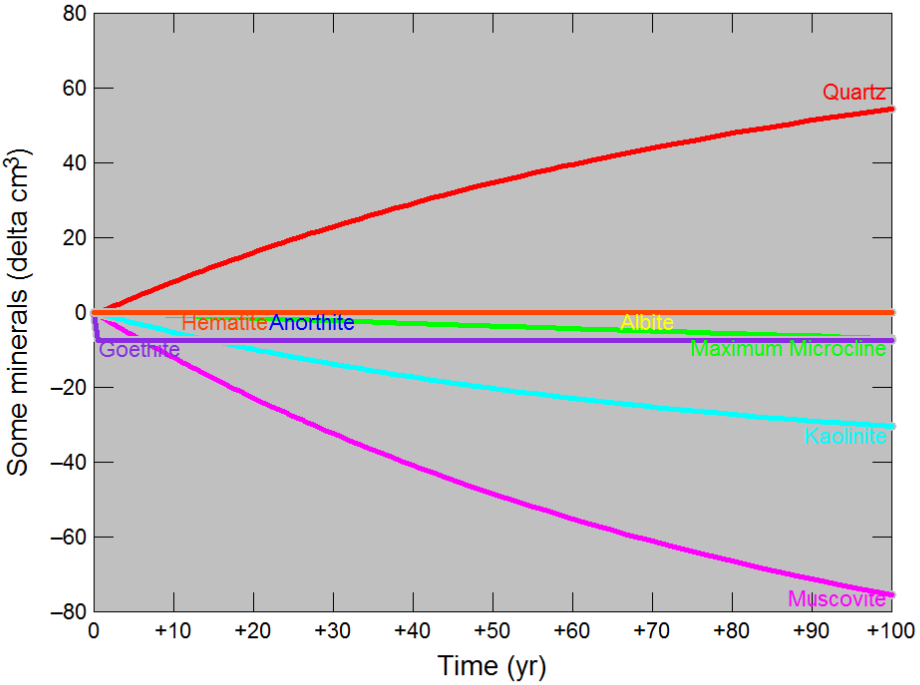
Some minerals (delta cm3)
Time (yr)
Quartz
Hematite
Anorthite
Albite
Goethite
Maximum Microcline
Kaolinite
Muscovite

H14

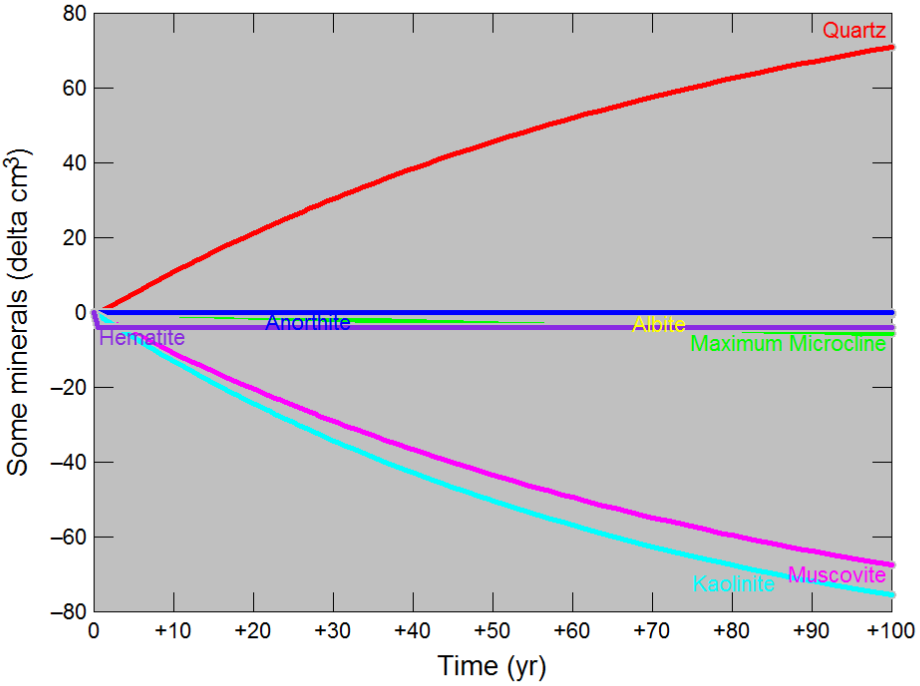
Some minerals (delta cm3)
Time (yr)
Quartz
Anorthite
Albite
Hematite
Maximum Microcline
Kaolinite
Muscovite

H15

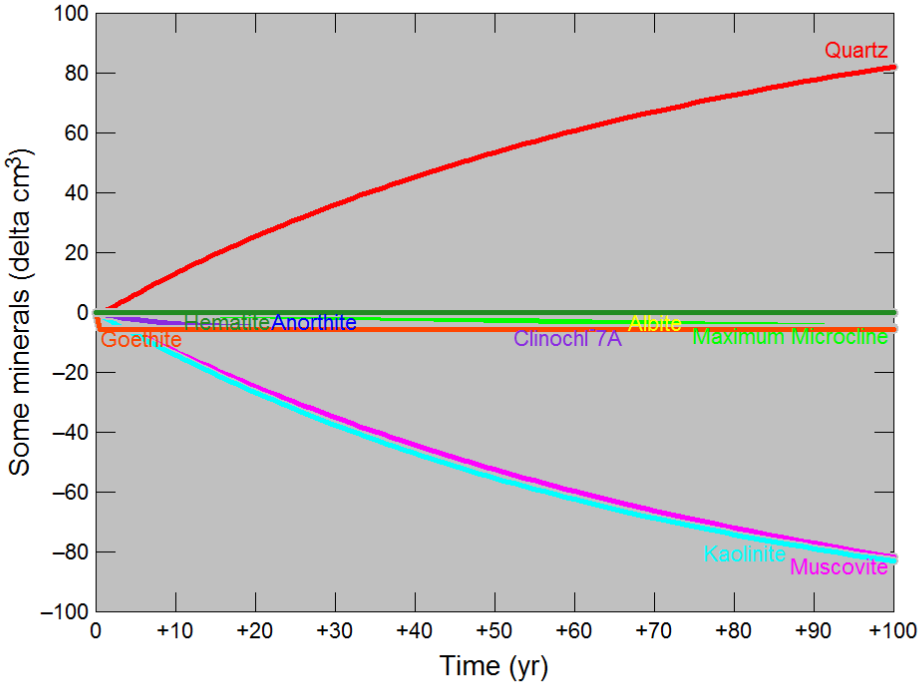
Some minerals (delta cm3)
Time (yr)
Quartz
Hematite
Anorthite
Albite
Goethite
Clinochl 7A
Maximum Microcline
Kaolinite
Muscovite

B. Reservoir condition

H01

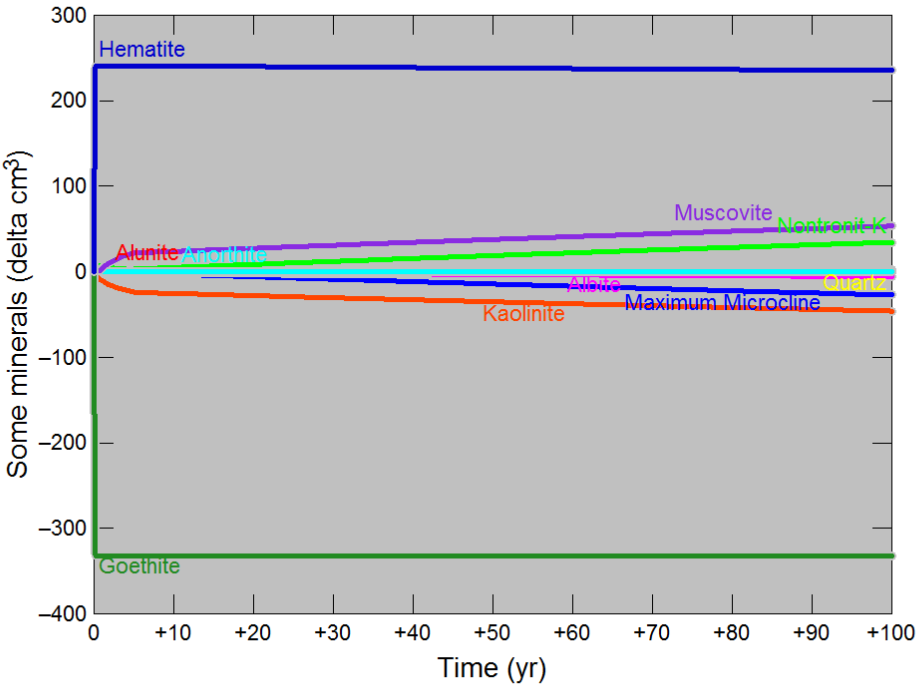

H02

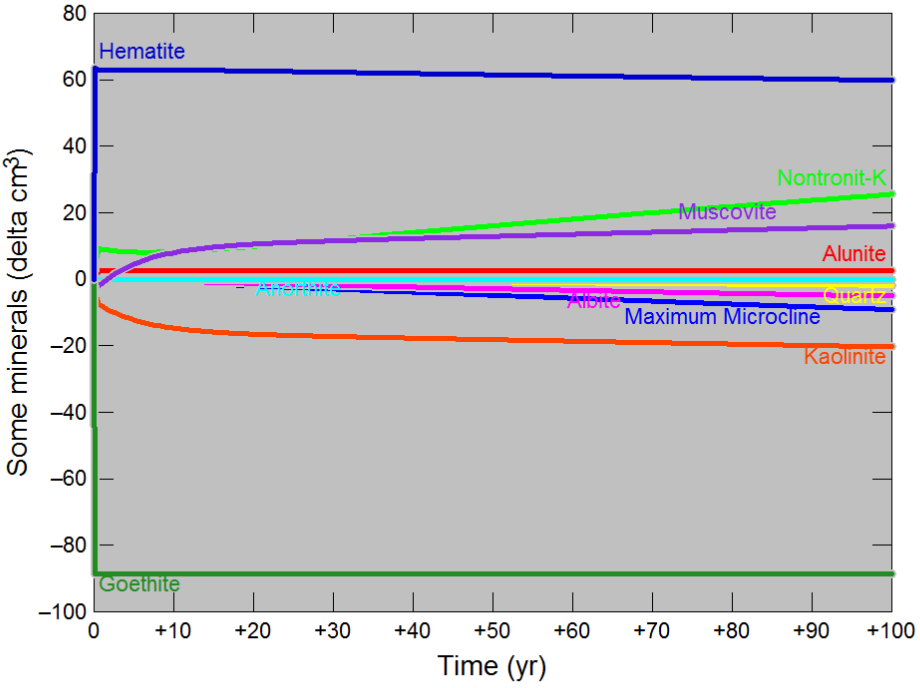

H03

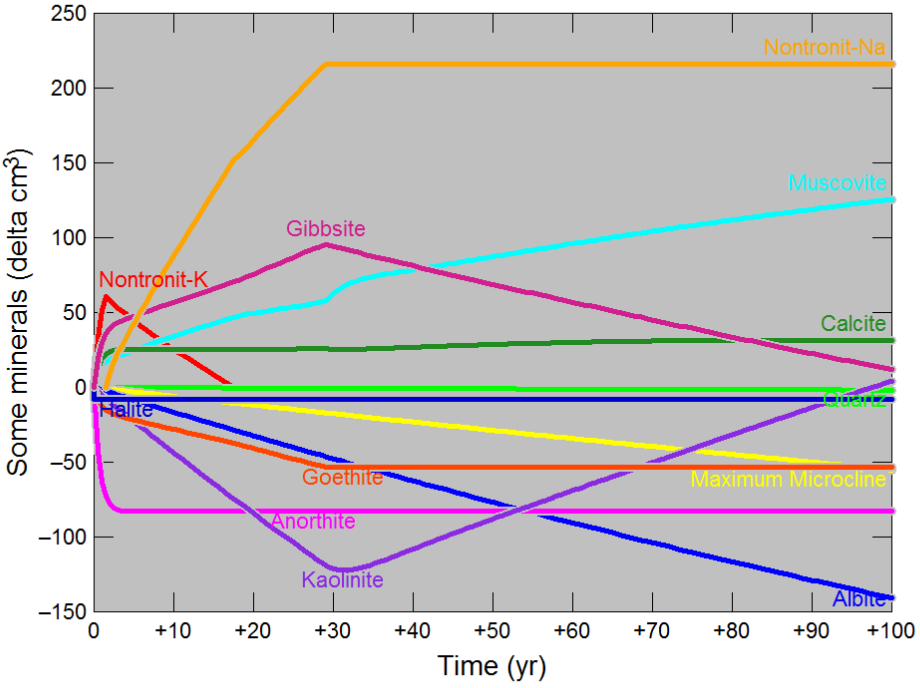
Some minerals (delta cm3)
Time (yr)
Nontronit-Na
Muscovite
Gibbsite
Nontronit-K
Calcite
Halite
Quartz
Goethite
Maximum Microcline
Anorthite
Kaolinite
Albite

H04

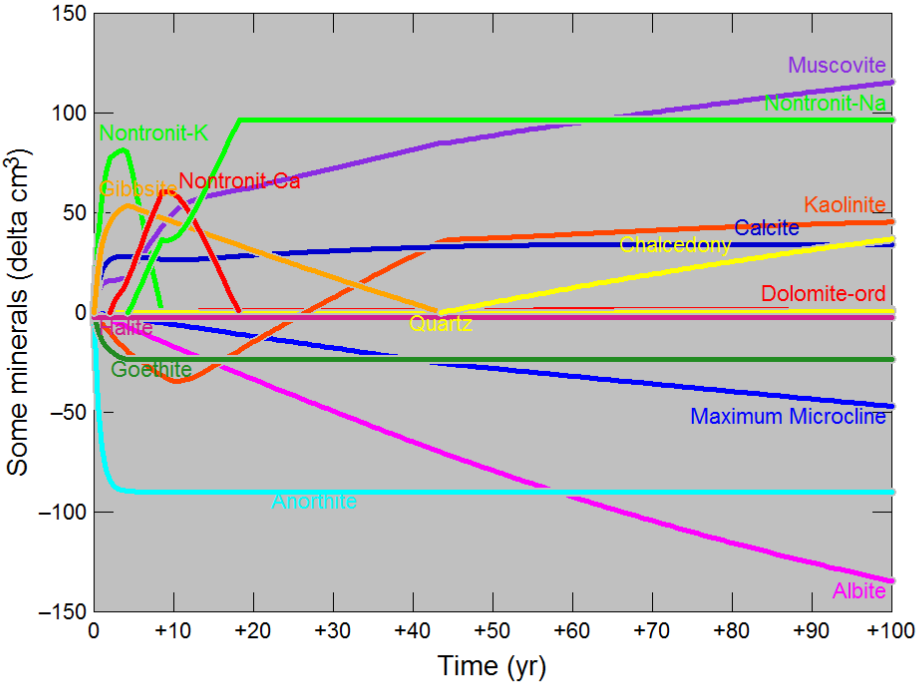
Some minerals (delta cm3)
Time (yr)
Muscovite
Nontronit-Na
Nontronit-K
Gibbsite
Nontronit-Ca
Kaolinite
Calcite
Chalcedony
Dolomite-ord
Halite
Quartz
Goethite
Maximum Microcline
Anorthite
Albite

H05

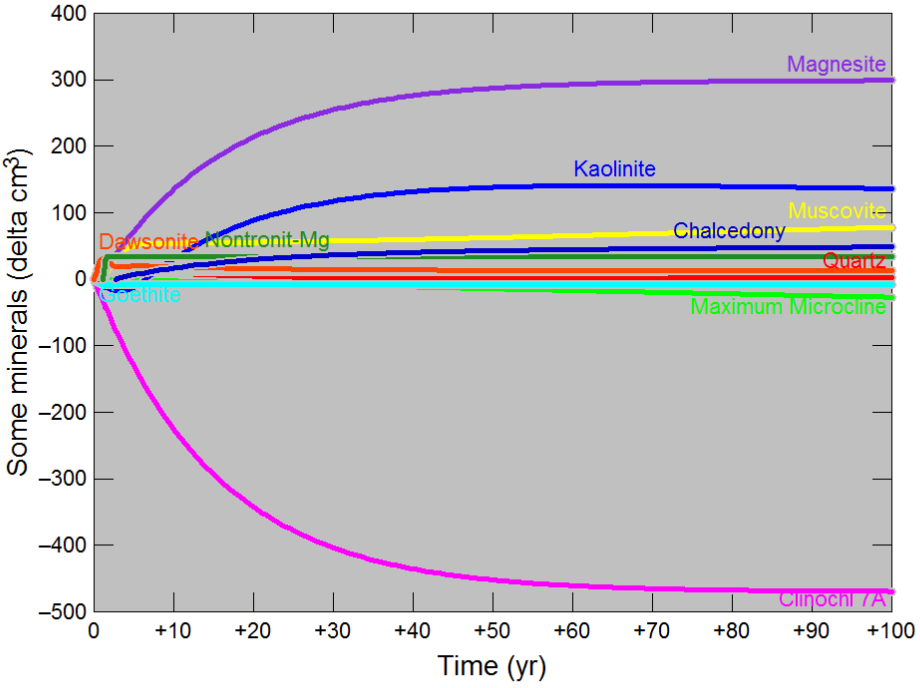
Some minerals (delta cm3)
Time (yr)
Magnesite
Kaolinite
Muscovite
Chalcedony
Dawsonite
Nontronit-Mg
Quartz
Goethite
Maximum Microcline
Clinochl 7A

H06

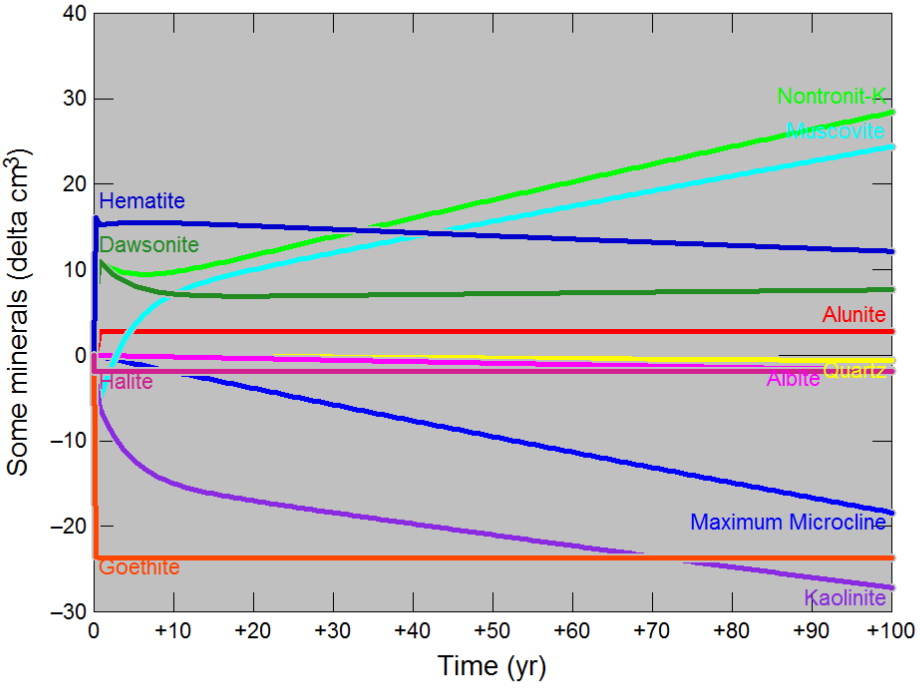
Some minerals (delta cm3)
Time (yr)
Nontronit-K
Muscovite
Hematite
Dawsonite
Alunite
Halite
Albite
Quartz
Maximum Microcline
Goethite
Kaolinite

H07

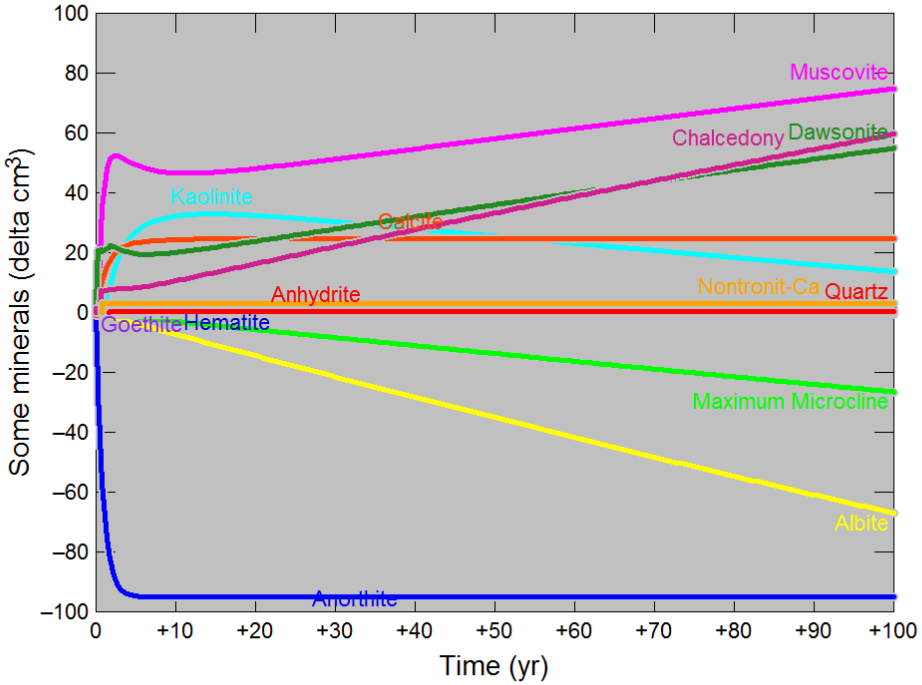
Some minerals (delta cm3)
Time (yr)
Muscovite
Chalcedony
Dawsonite
Kaolinite
Calcite
Nontronit-Ca
Quartz
Anhydrite
Goethite
Hematite
Maximum Microcline
Albite
Anorthite

H08

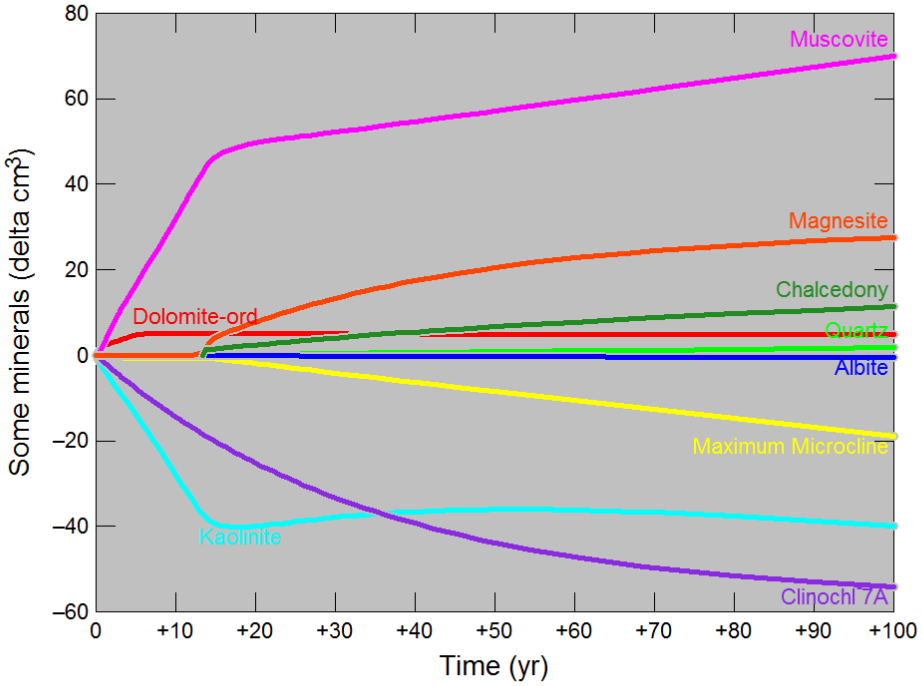
Some minerals (delta cm3)
Time (yr)
Muscovite
Magnesite
Chalcedony
Dolomite-ord
Quartz
Albite
Maximum Microcline
Kaolinite
Clinochl 7A

H09

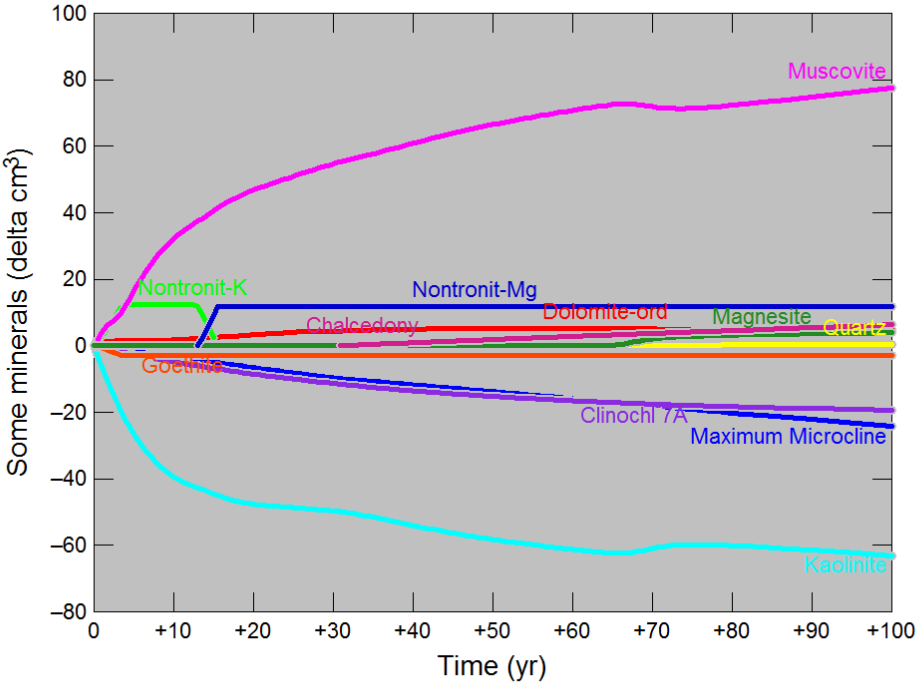
Some minerals (delta cm3)
Time (yr)
Muscovite
Nontronit-K
Nontronit-Mg
Dolomite-ord
Magnesite
Quartz
Chalcedony
Goethite
Clinochl 7A
Maximum Microcline
Kaolinite

H10

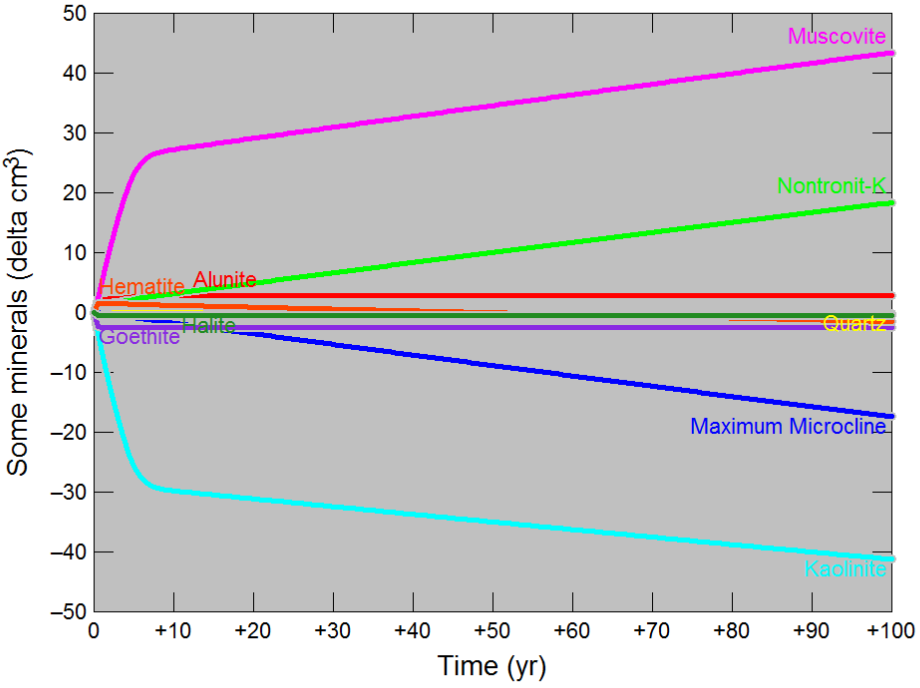
Some minerals (delta cm3)
Time (yr)
Muscovite
Nontronit-K
Hematite
Alunite
Quartz
Halite
Goethite
Maximum Microcline
Kaolinite

H11

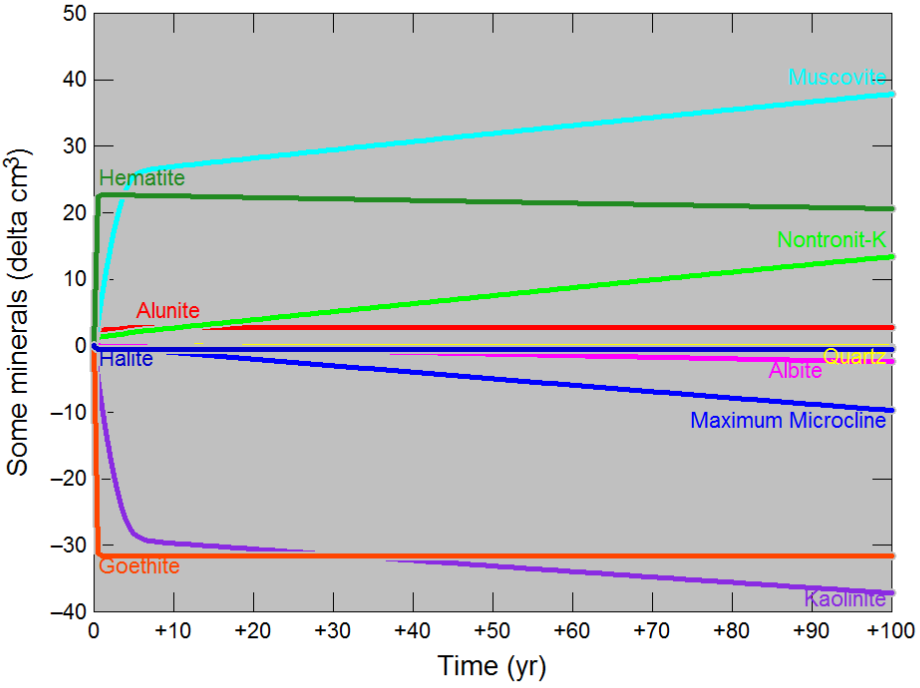
Some minerals (delta cm3)
Time (yr)
Muscovite
Hematite
Nontronit-K
Alunite
Halite
Quartz
Albite
Maximum Microcline
Goethite
Kaolinite

H12

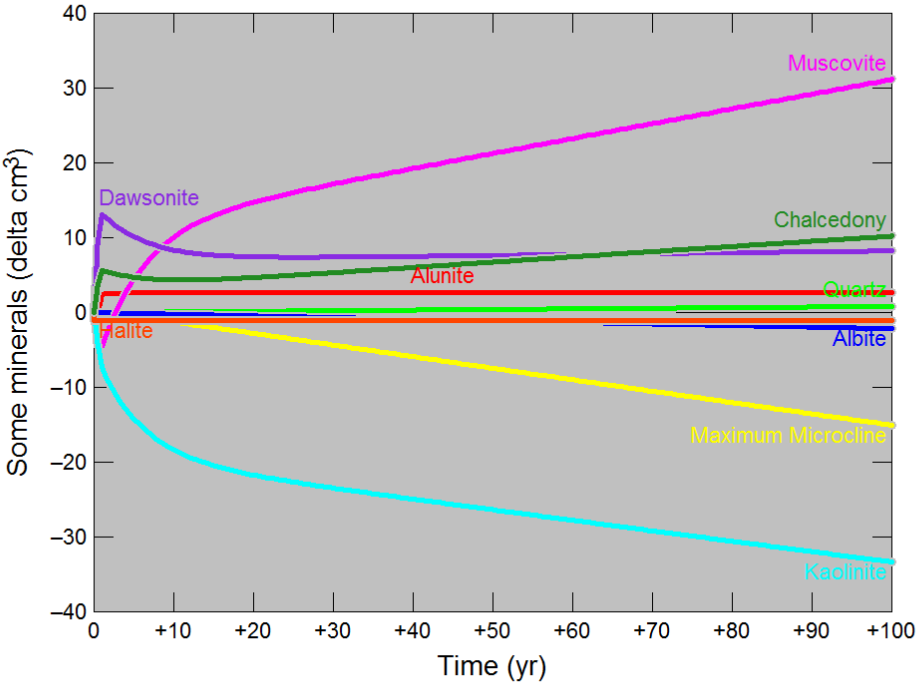
Some minerals (delta cm3)
Time (yr)
Muscovite
Dawsonite
Chalcedony
Alunite
Quartz
Halite
Albite
Maximum Microcline
Kaolinite

H13

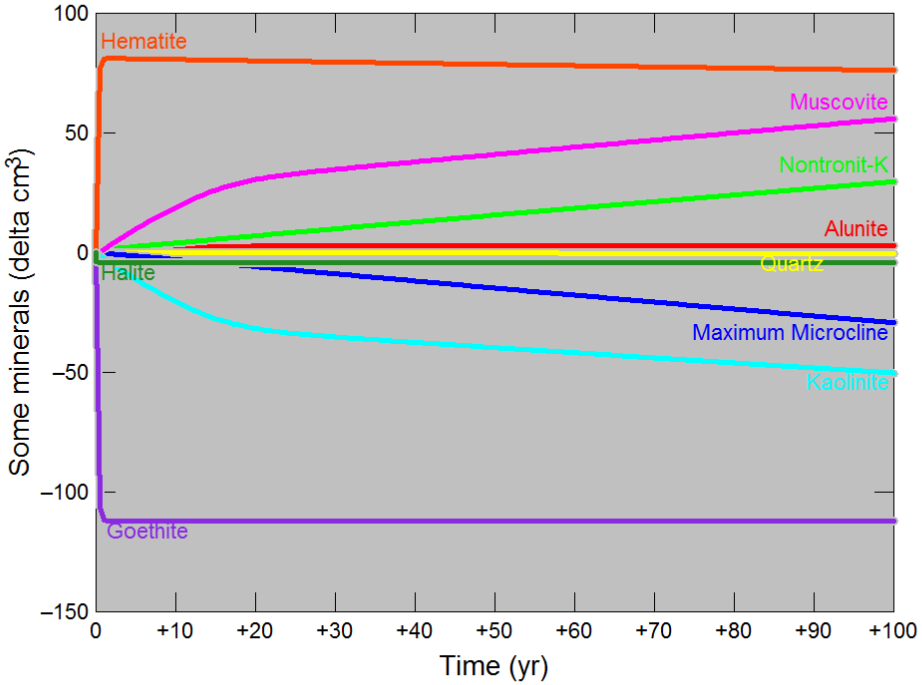
Hematite
Muscovite
Nontronit-K
Alunite
Quartz
Halite
Maximum Microcline
Kaolinite
Goethite
Some minerals (delta cm3)
Time (yr)
100
50
0
−50
−100
−150
0
+10
+20
+30
+40
+50
+60
+70
+80
+90
+100

H14

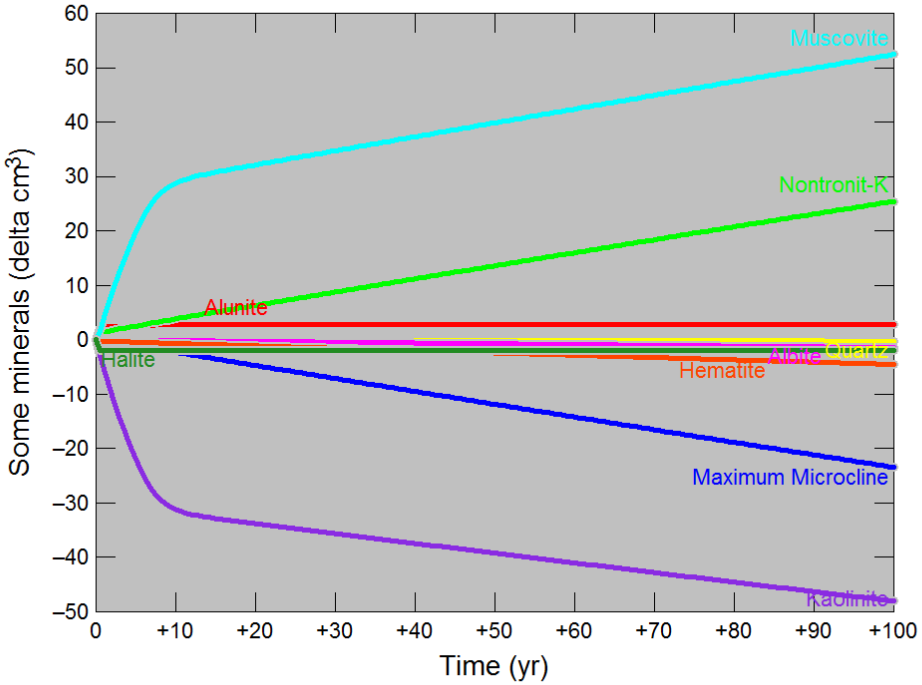
Muscovite
Nontronit-K
Alunite
Halite
Albite
Quartz
Hematite
Maximum Microcline
Kaolinite
Some minerals (delta cm3)
Time (yr)
60
50
40
30
20
10
0
−10
−20
−30
−40
−50
0
+10
+20
+30
+40
+50
+60
+70
+80
+90
+100

H15

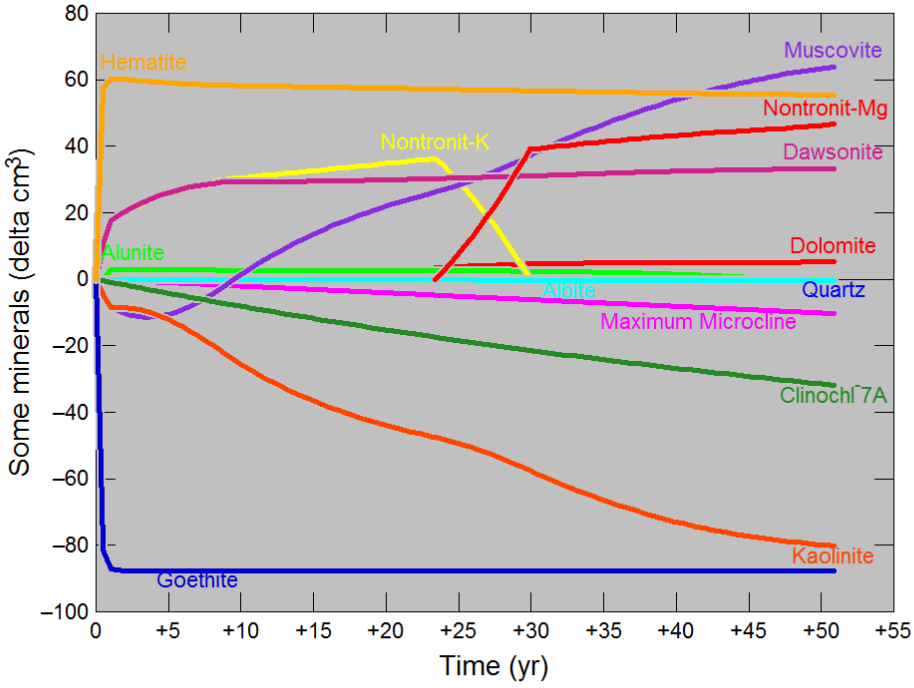
Some minerals (delta cm3)
Time (yr)
Hematite
Muscovite
Nontronit-Mg
Nontronit-K
Dawsonite
Alunite
Dolomite
Albite
Quartz
Maximum Microcline
Clinochl-7A
Kaolinite
Goethite
80
60
40
20
0
−20
−40
−60
−80
−100
0
+5
+10
+15
+20
+25
+30
+35
+40
+45
+50
+55

References

Aagaard, P., & Helgeson, H. C. (1982). Thermodynamic and kinetic constraints on reaction rates among minerals and aqueous solutions I, Theoretical considerations. *American Journal of Science, 282*(3), 237-285. doi: 10.2475/ajs.282.3.237

Alajmi, M. S. (2015). *Feasibility of seismic monitoring methods for Australian CO2 storage projects.* (Doctor of Philosophy), Curtin University.

Alemu, B. L., Aagaard, P., Munz, I. A., & Skurtveit, E. (2011). Caprock interaction with CO2: A laboratory study of reactivity of shale with supercritical CO2 and brine. *Applied Geochemistry, 26*(12), 1975-1989. doi: http://dx.doi.org/10.1016/j.apgeochem.2011.06.028

Amann, A., Waschbüsch, M., Bertier, P., Busch, A., Krooss, B. M., & Littke, R. (2011). Sealing rock characteristics under the influence of CO2. *Energy Procedia, 4*, 5170-5177. doi: http://dx.doi.org/10.1016/j.egypro.2011.02.494

Angeli, M., Soldal, M., Skurtveit, E., & Aker, E. (2009). Experimental percolation of supercritical CO2 through a caprock. *Energy Procedia, 1*(1), 3351-3358. doi: 10.1016/j.egypro.2009.02.123

Aplin, A. C., Matenaar, I. F., McCarty, D. K., & van der Pluijm, B. A. (2006). Influence of mechanical compaction and clay mineral diagenesis on the microfabric and pore-scale properties of deep-water Gulf of Mexico mudstones. *Clays and Clay Minerals, 54*(4), 500-514. doi: 10.1346/CCMN.2006.0540411

Armitage, P. J., Faulkner, D. R., & Worden, R. H. (2013). Caprock corrosion. *Nature Geoscience, 6*(2), 79-80. doi: 10.1038/ngeo1716

Audigane, P., Gaus, I., Czernichowski-Lauriol, I., Pruess, K., & Xu, T. (2007). Two-dimensional reactive transport modeling of CO2 injection in a saline aquifer at the Sleipner site, North Sea. *American Journal of Science, 307*(7), 974-1008. doi: 10.2475/07.2007.02

Bachu, S. (2002). Sequestration of CO2 in geological media in response to climate change: road map for site selection using the transform of the geological space into the CO2 phase space. *Energy Conversion & Management, 43*(1), 87-102.

Bachu, S. (2008). CO2 storage in geological media: Role, means, status and barriers to deployment. *Progress in Energy and Combustion Science, 34*(2), 254-273. doi: 10.1016/j.pecs.2007.10.001

Bachu, S., Gunter, W., & Perkins, E. (1994). Aquifer disposal of CO2: Hydrodynamic and mineral trapping. *Energy Conversion & Management, 35*(4), 269-279.

Berg, R. R. (1975). CAPILLARY PRESSURES IN STRATIGRAPHIC TRAPS. *AAPG Bulletin (American Association of Petroleum Geologists), 59*(6), 939-956.

Berner, R. A., Lasaga, A. C., & Garrels, R. M. (1983). The carbonate-silicate geochemical cycle and its effect on atmospheric carbon dioxide over the past 100 million years. *American Journal of Science, 283*(7), 641-683. doi: 10.2475/ajs.283.7.641

Berthe, G., Savoye, S., Wittebroodt, C., & Michelot, J. L. (2011). Effect of CO (sub 2) -enriched fluid on three argillite type caprocks (Vol. 75, pp. 523). London: London, United Kingdom: Mineralogical Society.

Bertier, P., Swennen, R., Laenen, B., Lagrou, D., & Dreesen, R. (2006). Experimental identification of CO2–water–rock interactions caused by sequestration of CO2 in Westphalian and Buntsandstein sandstones of the Campine Basin (NE-Belgium). *Journal of Geochemical Exploration, 89*(1-3), 10-14. doi: 10.1016/j.gexplo.2005.11.005

Bethke, C. M. (2010). *Geochemical and Biogeochemical Reaction Modeling* (2nd Edition ed.).

Bethke, C. M., & Yeakel, S. (2016). GWB Reaction Modeling Guide [Press release]

Brunauer, S., Emmett, P. H., & Teller, E. (1938). Adsorption of Gases in Multimolecular Layers. *Journal of the American Chemical Society, 60*(2), 309-319. doi: 10.1021/ja01269a023

Burrowes, O. G. (2001). Investigating CO2 storage potential of carbonate rocks during tertiary recovery from a billion barrel oil field, Weyburn, Saskatchewan

Part 2, Reservoir geology (IEA Weyburn CO2 Monitoring and Storage Project). In J. E. Christopher, C. F. Gilboy, F. M. Haidl, & L. K. Kreis (Eds.), (pp. 64-71). Regina, SK: Regina, SK, Canada: Saskatchewan Geological Survey.

Busch, A., Alles, S., Gensterblum, Y., Prinz, D., Dewhurst, D. N., Raven, M. D., . . . Krooss, B. M. (2008). Carbon dioxide storage potential of shales. *International Journal of Greenhouse Gas Control, 2*(3), 297-308. doi: http://dx.doi.org/10.1016/j.ijggc.2008.03.003

Busch, A., Alles, S., Krooss, B. M., Stanjek, H., & Dewhurst, D. (2009). Effects of physical sorption and chemical reactions of CO2 in shaly caprocks. *Energy Procedia, 1*(1), 3229-3235. doi: 10.1016/j.egypro.2009.02.107

Busch, A., & Müller, N. (2011). Determining CO2 /brine relative permeability and capillary threshold pressures for reservoir rocks and caprocks: Recommendations for development of standard laboratory protocols. *Energy Procedia, 4*, 6053-6060. doi: 10.1016/j.egypro.2011.02.610

Bustin, R. M., & Clarkson, C. R. (1998). Geological controls on coalbed methane reservoir capacity and gas content. *International Journal of Coal Geology, 38*(1-2), 3-26. doi: 10.1016/S0166-5162(98)00030-5

Castaneda-Herrera, C. A., Stevens, G. W., & Haese, R. R. (2018). Review of CO2 Leakage Mitigation and Remediation Technologies *Geological Carbon Storage* (pp. 327-337).

Celia, M. A., Bachu, S., Nordbotten, J. M., & Bandilla, K. W. (2015). Status of CO2 storage in deep saline aquifers with emphasis on modeling approaches and practical simulations. *Water Resources Research, 51*(9), 6846-6892. doi: 10.1002/2015WR017609

Chalbaud, C., Robin, M., Lombard, J. M., Martin, F., Egermann, P., & Bertin, H. (2009). Interfacial tension measurements and wettability evaluation for geological CO2 storage. *Advances in Water Resources, 32*(1), 98-109. doi: 10.1016/j.advwatres.2008.10.012

Comisky, J. T., Santiago, M., McCollom, B., Buddhala, A., & Newsham, K. E. (2011). Sample Size Effects on the Application of Mercury Injection Capillary Pressure for Determining the Storage Capacity of Tight Gas and Oil Shales.

Core Laboratories, I. (2015). Petrologic Analysis of Conventional Core Samples, GSWA Harvey 2, Harvey 3, and Harvey 4 Wells, Perth Basin, Australia: Australia Department of Mines and Petroleum.

Credoz, A., Bildstein, O., Jullien, M., Raynal, J., Pétronin, J.-C., Lillo, M., . . . Geniaut, G. (2009). Experimental and modeling study of geochemical reactivity between clayey caprocks and CO2 in geological storage conditions. *Energy Procedia, 1*(1), 3445-3452. doi: 10.1016/j.egypro.2009.02.135

Cubillas, P., Köhler, S., Prieto, M., Causserand, C., & Oelkers, E. H. (2005). How do mineral coatings affect dissolution rates? An experimental study of coupled CaCO3 dissolution—CdCO3 precipitation. *Geochimica et Cosmochimica Acta, 69*(23), 5459-5476. doi: 10.1016/j.gca.2005.07.016

Czernichowski-Lauriol, I., Rochelle, C., Gaus, I., Azaroual, M., Pearce, J., & Durst, P. (2006). Geochemical interactions between CO2, pore-waters and reservoir rocks - Lessons learned from laboratory experiments, field studies and computer simulations. *Advances in the Geological Storage of Carbon Dioxide: International Approaches to Reduce Anthropogenic Greenhouse Gas Emissions, 65*, 157-174.

Davis, M. C., Wesolowski, D. J., Rosenqvist, J. K., Brantley, S. L., & Mueller, K. T. (2011). Solubility and near-equilibrium dissolution rates of quartz in dilute NaCl solutions at

398-473 K under alkaline conditions. *Geochimica et Cosmochimica Acta, 75*(2). doi: 10.1016/j.gca.2010.10.023

Dawson, G. K. W., Sidiq, H., Pearce, J., Gao, J.-F., Golding, S. D., Rudolph, V., . . . Xing, H. (2013). ANLEC Project 3-1110-0101: Review of laboratory-scale geochemical and geomechanical experiments simulating geosequestration of CO2 in sandstone, and associated modelling studies (pp. 48). Manuka, ACT, Australia: Australian National Low Emissions Coal Research and Development.

De Silva, G. P. D., Ranjith, P. G., & Perera, M. S. A. (2015). Geochemical aspects of CO2 sequestration in deep saline aquifers: A review. *Fuel, 155*, 128-143. doi: http://dx.doi.org/10.1016/j.fuel.2015.03.045

Delle Piane, C., Olierook, H. K. H., Timms, N. E., Saeedi, A., Esteban, L., Rezaee, R., . . . Lebedev, M. (2013). Facies-based rock properties distribution along the Harvey 1 stratigraphic well: CSIRO Report Number EP133710.

Dethlefsen, F., Haase, C., Ebert, M., & Dahmke, A. (2012). Uncertainties of geochemical modeling during CO 2 sequestration applying batch equilibrium calculations. *Environmental Earth Sciences, 65*(4), 1105-1117. doi: 10.1007/s12665-011-1360-x

Dewhurst, D. N., Jones, R. M., & Raven, M. D. (2002). Microstructural and petrophysical characterization of Muderong Shale: application to top seal risking. *Petroleum Geoscience, 8*(4), 371-383. doi: DOI 10.1144/petgeo.8.4.371

Ennis-King, J., & Paterson, L. (2007). Coupling of geochemical reactions and convective mixing in the long-term geological storage of carbon dioxide. *International Journal of Greenhouse Gas Control, 1*(1), 86-93. doi: 10.1016/S1750-5836(07)00034-5

Falus, G., Székely, E., Király, C., Kónya, P., Udvardi, B., Freiler-Nagy, Á., . . . Szabó, Z. (2019). Geochemical reactions of Na-montmorillonite in dissolved scCO2 in relevance of modeling caprock behavior in CO2 geological storage. *Periodica Polytechnica Chemical Engineering, 63*(2), 318-327. doi: 10.3311/PPch.12850

Farquhar, S. M., Pearce, J. K., Dawson, G. K. W., Golab, A., Sommacal, S., Kirste, D., . . . Golding, S. D. (2015). A fresh approach to investigating CO 2 storage: Experimental CO 2 – water–rock interactions in a low-salinity reservoir system. *Chemical Geology, 399*, 98-122. doi: 10.1016/j.chemgeo.2014.10.006

Garrido, D. R. R., Lafortune, S., Souli, H., & Dubujet, P. (2013). Impact of supercritical CO2/water interaction on the caprock nanoporous structure. *Proceedings of the Fourteenth International Symposium on Water-Rock Interaction, Wri 14, 7*, 738-741. doi: 10.1016/j.proeps.2013.03.123

Gaus, I. (2010). Role and impact of CO2-rock interactions during CO2 storage in sedimentary rocks. *International Journal of Greenhouse Gas Control, 4*(1), 73-89. doi: http://dx.doi.org/10.1016/j.ijggc.2009.09.015

Gaus, I., Azaroual, M., & Czernichowski-Lauriol, I. (2005). Reactive transport modelling of the impact of CO2 injection on the clayey cap rock at Sleipner (North Sea). *Chemical Geology, 217*(3-4), 319-337. doi: 10.1016/j.chemgeo.2004.12.016

Gautier, J.-M., Oelkers, E. H., & Schott, J. (2001). Are quartz dissolution rates proportional to B.E.T. surface areas? *Geochimica et Cosmochimica Acta, 65*(7), 1059-1070. doi: 10.1016/S0016-7037(00)00570-6

Gherardi, F., Xu, T., & Pruess, K. (2007). Numerical modeling of self-limiting and self-enhancing caprock alteration induced by CO2 storage in a depleted gas reservoir. *Chemical Geology, 244*(1-2), 103-129. doi: 10.1016/j.chemgeo.2007.06.009

Gibson-Poole, C. M., Svendsen, L., Underschultz, J., Watson, M. N., Ennis-King, J., van Ruth, P. J., . . . Cinar, Y. (2007). Site characterisation of a basin-scale CO2 geological storage system: Gippsland Basin, southeast Australia. *Environmental Geology, 54*(8), 1583-1606. doi: 10.1007/s00254-007-0941-1

Giesche, H. (2006). Mercury Porosimetry: A General (Practical) Overview. *Particle & Particle Systems Characterization, 23*(1), 9-19. doi: 10.1002/ppsc.200601009

Griffith, C. A., Dzombak, D. A., & Lowry, G. V. (2011). Physical and chemical characteristics of potential seal strata in regions considered for demonstrating geological saline CO2 sequestration. *Environmental Earth Sciences, 64*(4), 925-948. doi: 10.1007/s12665-011-0911-5

Gunter, W. D., Bachu, S., & Benson, S. M. (2004). The role of hydrogeological and geochemical trapping in sedimentary basins for secure geological storage of carbon dioxide. *Geological Society Special Publications, 233*, 129-145.

Gunter, W. D., Perkins, E. H., & Hutcheon, I. (2000). Aquifer disposal of acid gases: modelling of water–rock reactions for trapping of acid wastes. *Applied Geochemistry, 15*(8), 1085-1095. doi: https://doi.org/10.1016/S0883-2927(99)00111-0

Gunter, W. D., Perkins, E. H., & McCann, T. J. (1993). Aquifer disposal of CO2-rich gases: Reaction design for added capacity. *Energy Conversion and Management, 34*(9-11), 941-948. doi: 10.1016/0196-8904(93)90040-H

Gunter, W. D., Wiwchar, B., & Perkins, E. H. (1997). Aquifer disposal of CO2-rich greenhouse gases: Extension of the time scale of experiment for CO2-sequestering reactions by geochemical modelling. *Mineralogy and Petrology, 59*(1-2), 121-140. doi: Doi 10.1007/Bf01163065

Hildenbrand, A., & Urai, J. L. (2003). Investigation of the morphology of pore space in mudstones—first results. *Marine and Petroleum Geology, 20*(10), 1185-1200. doi: 10.1016/j.marpetgeo.2003.07.001

Hinai, A. A., & Rezaee, R. (2015). Pore Geometry in Gas Shale Reservoirs *Fundamentals of Gas Shale Reservoirs* (pp. 89-116): John Wiley & Sons, Inc.

Holloway, S. (2001). STORAGE OF FOSSIL FUEL-DERIVED CARBON DIOXIDE BENEATH THE SURFACE OF THE EARTH. *Annual Review of Energy and the Environment, 26*(1), 145-166. doi: 10.1146/annurev.energy.26.1.145

IPCC. (2013). Climate Change 2013: The physical science basis. In T. Stocker, D. Qin, G.-K. Plattner, M. Tignor, S. Allen, J. Boschung, A. Nauels, Y. Xia, V. Bex, & P. Midgley (Eds.), *contribution of working group I to the fifth assessment report of the intergovernmental panel on climate change.* (pp. 1535). Cambridge, United Kingdom and New York, USA.

IPCC. (2014). Climate Change 2014: Synthesis Report. In Core Writing Team, R. K. Pachauri, & L. A. Meyer (Eds.), *Contribution of Working Groups I, II and III to the Fifth Assessment Report of the Intergovernmental Panel on Climate Change* (pp. 151). IPCC, Geneva, Switzerland.

IPCC Working Group III. (2005). IPCC Special Report on Carbon Dioxide Capture and Storage. In B. Prepared by Working Group III of the Intergovernmental Panel on Climate Change [Metz, O. Davidson, H. C. de Coninck, M. Loos, and L. A. Meyer (eds.)] (Ed.). Cambridge, United Kingdom and NewYork, NY, USA: Cambridge University Press.

Izgec, O., Demiral, B., Bertin, H., & Akin, S. (2008). CO2 injection into saline carbonate aquifer formations I: laboratory investigation. *Transport in Porous Media, 72*(1), 1-24. doi: 10.1007/s11242-007-9132-5

James W. Johnson, C. I. S. (2001). ABSTRACT: Reactive Transport Modeling of Geologic CO2 Sequestration to Identify Optimal Target Formations: Quantifying the Relative Effectiveness of Migration and Sequestration Processes as a Function of Reservoir Properties. *AAPG Bulletin, 85*. doi: 10.1306/8626E2B5-173B-11D7-8645000102C1865D

Jenkins, C. R., Cook, P. J., Ennis-King, J., Undershultz, J., Boreham, C., Dance, T., . . . Urosevic, M. (2012). Safe storage and effective monitoring of CO2 in depleted gas fields. *Proc Natl Acad Sci U S A, 109*(2), E35-41. doi: 10.1073/pnas.1107255108

Kampman, N., Bertier, P., Busch, A., Snippe, J., Harrington, J., Pipich, V., . . . Bickle, M. (2017). Validating Reactive Transport Models of CO2-brine-Rock Reactions in Caprocks Using Observations from a Natural CO2 Reservoir (Vol. 114, pp. 4902-4916): Elsevier Ltd.

Kaszuba, J. P., Janecky, D. R., & Snow, M. G. (2003). Carbon dioxide reaction processes in a model brine aquifer at 200 °C and 200 bars: implications for geologic sequestration of carbon. *Applied Geochemistry, 18*(7), 1065-1080. doi: 10.1016/S0883-2927(02)00239-1

Kaszuba, J. P., Janecky, D. R., & Snow, M. G. (2005). Experimental evaluation of mixed fluid reactions between supercritical carbon dioxide and NaCl brine: Relevance to the integrity of a geologic carbon repository. *Chemical Geology, 217*(3), 277-293. doi: 10.1016/j.chemgeo.2004.12.014

Kaszuba, J. P., Viswanathan, H. S., & Carey, J. W. (2011). Relative stability and significance of dawsonite and aluminum minerals in geologic carbon sequestration. *Geophysical Research Letters, 38*(8), n/a-n/a. doi: 10.1029/2011gl046845

Ketzer, J. M., Iglesias, R., Einloft, S., Dullius, J., Ligabue, R., & de Lima, V. (2009). Water–rock–CO2 interactions in saline aquifers aimed for carbon dioxide storage: Experimental and numerical modeling studies of the Rio Bonito Formation (Permian), southern Brazil. *Applied Geochemistry, 24*(5), 760-767. doi: 10.1016/j.apgeochem.2009.01.001

Kharaka, Y. K., & Cole, D. R. (2011). Geochemistry of Geologic Sequestration of Carbon Dioxide. In R. S. Harmon & A. Parker (Eds.), *Frontiers in Geochemistry, Contribution of Geochemistry to the Study of the Earth*.

Kharaka, Y. K., Cole, D. R., Thordsen, J. J., Kakouros, E., & Nance, H. S. (2006). Gas–water–rock interactions in sedimentary basins: CO2 sequestration in the Frio Formation, Texas, USA. *Journal of Geochemical Exploration, 89*(1-3), 183-186. doi: 10.1016/j.gexplo.2005.11.077

Khosrokhavar, R., Griffiths, S., & Wolf, K.-H. (2014). Shale Gas Formations and Their Potential for Carbon Storage: Opportunities and Outlook. *Environmental Processes, 1*(4), 595-611. doi: 10.1007/s40710-014-0036-4

Kirste, D. (2013). Geochemical modelling of selected seal rocks of the Gippsland Basin – final report (pp. 25). Canberra, Australia: Cooperative Research Centre for Greenhouse Gas Technologies.

Kirste, D., Pearce, J. K., Golding, S. D., & Dawson, G. K. W. (2019). Trace element mobility during CO2 storage: application of reactive transport modelling. *E3S web of conferences, 98*, 4007. doi: 10.1051/e3sconf/20199804007

Knauss, K. G., Johnson, J. W., & Steefel, C. I. (2005). Evaluation of the impact of CO2, co-contaminant gas, aqueous fluid and reservoir rock interactions on the geologic sequestration of CO2. *Chemical Geology, 217*(3-4), 339-350. doi: 10.1016/j.chemgeo.2004.12.017

Kohler, E., Parra, T., & Vidal, O. (2009). Clayey cap-rock behavior in H2O-CO2 media at low pressure and temperature conditions: an experimental approach. *Clays and Clay Minerals, 57*(5), 616-637. doi: 10.1346/CCMN.2009.0570509

Kreft, E., Bernstone, C., Meyer, R., May, F., Arts, R., Obdam, A., . . . Geel, C. (2007). "The Schweinrich structure", a potential site for industrial scale CO2 storage and a test case for safety assessment in Germany. *International Journal of Greenhouse Gas Control, 1*(1), 69-74. doi: 10.1016/S1750-5836(07)00009-6

Kuila, U., McCarty, D. K., Derkowski, A., Fischer, T. B., & Prasad, M. (2014). Total porosity measurement in gas shales by the water immersion porosimetry (WIP) method. *Fuel, 117*(PB), 1115-1129. doi: 10.1016/j.fuel.2013.09.073

Kuila, U., & Prasad, M. (2013). Specific surface area and pore-size distribution in clays and shales. *Geophysical Prospecting, 61*(2), 341-362. doi: 10.1111/1365-2478.12028

Kweon, H., & Deo, M. (2017). The impact of reactive surface area on brine-rock-carbon dioxide reactions in CO 2 sequestration. *Fuel, 188*, 39-49. doi: 10.1016/j.fuel.2016.10.010

Labani, M., & Rezaee, R. (2015). Petrophysical Evaluation of Gas Shale Reservoirs *Fundamentals of Gas Shale Reservoirs* (pp. 117-137): John Wiley & Sons, Inc.

Labani, M. M., Rezaee, R., Saeedi, A., & Hinai, A. A. (2013). Evaluation of pore size spectrum of gas shale reservoirs using low pressure nitrogen adsorption, gas expansion and mercury porosimetry: A case study from the Perth and Canning Basins, Western Australia. *Journal of Petroleum Science and Engineering, 112*, 7-16. doi: http://dx.doi.org/10.1016/j.petrol.2013.11.022

Labus, M., & Wertz, F. (2017). Identifying geochemical reactions on wellbore cement/caprock interface under sequestration conditions. *Environmental Earth Sciences, 76*(12), 1-13. doi: 10.1007/s12665-017-6771-x

Lagneau, V., Pipart, A., & Catalette, H. (2005). Reactive Transportmodelling and Long Term Behaviour of CO2 Sequestration in Saline Aquifers. *Oil & Gas Science and Technology - Rev. IFP, 60*(2), 231-247.

Lahann, R., Mastalerz, M., Rupp, J. A., & Drobniak, A. (2013). Influence of CO2 on New Albany Shale composition and pore structure. *International Journal of Coal Geology, 108*, 2-9. doi: http://dx.doi.org/10.1016/j.coal.2011.05.004

Lasaga, A. C., Kirkpatrick, R. J., & Mineralogical Society of, A. (1981). *Kinetics of geochemical processes / A.C. Lasaga & R.J. Kirkpatrick, editors*. Washington, D.C: Washington, D.C : Mineralogical Society of America.

Lasaga, A. C., Soler, J. M., Ganor, J., Burch, T. E., & Nagy, K. L. (1994). Chemical-Weathering Rate Laws and Global Geochemical Cycles. *Geochimica et Cosmochimica Acta, 58*(10), 2361-2386. doi: Doi 10.1016/0016-7037(94)90016-7

Law, D. H. S., & Bachu, S. (1996). Hydrogeological and numerical analysis of CO2 disposal in deep aquifers in the Alberta sedimentary basin. *Energy Conversion and Management, 37*(6), 1167-1174. doi: https://doi.org/10.1016/0196-8904(95)00315-0

Li, Q., Ma, X., Yang, G., Li, X., Yu, Y., Dong, J., & Kühn, M. (2019). Geochemical modeling of changes in caprock permeability caused by CO2–brine–rock interactions under the diffusion mechanism. *Oil & Gas Science and Technology – Revue d'IFP Energies nouvelles, 74*. doi: 10.2516/ogst/2019055

Li, Z., Dong, M., Li, S., & Huang, S. (2006). CO2 sequestration in depleted oil and gas reservoirs-caprock characterization and storage capacity. *Energy Conversion and Management, 47*(11-12), 1372-1382. doi: http://dx.doi.org/10.1016/j.enconman.2005.08.023

Lima, V. d., Einloft, S., Ketzer, J. M., Jullien, M., Bildstein, O., & Petronin, J.-C. (2011). CO2 Geological storage in saline aquifers: Paraná Basin caprock and reservoir chemical reactivity. *Energy Procedia, 4*, 5377-5384. doi: https://doi.org/10.1016/j.egypro.2011.02.521

Liu, F., Lu, P., Griffith, C., Hedges, S. W., Soong, Y., Hellevang, H., & Zhu, C. (2012). CO2–brine–caprock interaction: Reactivity experiments on Eau Claire shale and a review of relevant literature. *International Journal of Greenhouse Gas Control, 7*, 153-167. doi: 10.1016/j.ijggc.2012.01.012

Liu, F., Lu, P., Zhu, C., & Xiao, Y. (2011). Coupled reactive flow and transport modeling of CO2 sequestration in the Mt. Simon sandstone formation, Midwest U.S.A. *International Journal of Greenhouse Gas Control, 5*(2), 294-307. doi: https://doi.org/10.1016/j.ijggc.2010.08.008

Liu, M. (2013). *Behaviour of shale cap rock under exposure to supercritical CO2.* (Master of Science), University of Alberta, Edmonton, Alberta.

Lu, J., Kharaka, Y. K., Thordsen, J. J., Horita, J., Karamalidis, A., Griffith, C., . . . Hovorka, S. D. (2012). CO2–rock–brine interactions in Lower Tuscaloosa Formation at Cranfield CO2 sequestration site, Mississippi, U.S.A. *Chemical Geology, 291*, 269-277. doi: 10.1016/j.chemgeo.2011.10.020

Lu, P., Fu, Q., Seyfried, W. E., Hereford, A., & Zhu, C. (2011). Navajo Sandstone–brine–CO2 interaction: implications for geological carbon sequestration. *Environmental Earth Sciences, 62*(1), 101-118. doi: 10.1007/s12665-010-0501-y

Luigi, M. (2007a). Chapter 1 - Why We Should Care: The Impact of Anthropogenic Carbon Dioxide on the Carbon Cycle. In M. Luigi (Ed.), *Developments in Geochemistry* (Vol. Volume 11, pp. 1-14): Elsevier.

Luigi, M. (2007b). Chapter 3 - Carbon Dioxide and CO2–H2O Mixtures. In M. Luigi (Ed.), *Developments in Geochemistry* (Vol. Volume 11, pp. 27-51): Elsevier.

Luigi, M. (2007c). Chapter 4 - The Aqueous Electrolyte Solution. In M. Luigi (Ed.), *Developments in Geochemistry* (Vol. Volume 11, pp. 53-77): Elsevier.

Luigi, M. (2007d). Chapter 5 - The Product Solid Phases. In M. Luigi (Ed.), *Developments in Geochemistry* (Vol. Volume 11, pp. 79-167): Elsevier.

Luigi, M. (2007e). Chapter 7 - Reaction Path Modelling of Geological CO2 Sequestration. In M. Luigi (Ed.), *Developments in Geochemistry* (Vol. Volume 11, pp. 319-409): Elsevier.

Luigi, M. (2007f). *Geological Sequestration of Carbon Dioxide Thermodynamics, Kinetics, and Reaction Path Modeling* (Vol. Volume 11): Elsevier.

Manalo, F., Ding, M., Bryan, J., & Kantzas, A. (2003). *Separating the Signals from Clay Bound Water and Heavy Oil in NMR Spectra of Unconsolidated Samples*.

Marbler, H., Erickson, K. P., Schmidt, M., Lempp, C., & Pöllmann, H. (2013). Geomechanical and geochemical effects on sandstones caused by the reaction with supercritical CO2: an experimental approach to in situ conditions in deep geological reservoirs. *Environmental Earth Sciences, 69*(6), 1981-1998. doi: 10.1007/s12665-012-2033-0

Matteson, A., Tomanic, J. P., Herron, M. M., Allen, D. F., & Kenyon, W. E. (1998). *NMR Relaxation of Clay-Brine Mixtures*. Paper presented at the SPE Annual Technical Conference and Exhibition, 27-30 September, New Orleans, Louisiana.

McPhee, C., Reed, J., & Zubizarreta, I. (2015a). Capillary Pressure. *64*, 449-517. doi: 10.1016/b978-0-444-63533-4.00009-3

McPhee, C., Reed, J., & Zubizarreta, I. (2015b). Nuclear Magnetic Resonance (NMR) (Vol. 64, pp. 655-669).

Miller, Q. R. S., Wang, X., Kaszuba, J. P., Mouzakis, K. M., Navarre-Sitchler, A. K., Alvarado, V., . . . Heath, J. E. (2016). Experimental Study of Porosity Changes in Shale Caprocks Exposed to Carbon Dioxide-Saturated Brine II: Insights from Aqueous Geochemistry. *Environmental engineering science, 33*(10), 736-744. doi: 10.1089/ees.2015.0592

Mito, S., Xue, Z., & Ohsumi, T. (2008). Case study of geochemical reactions at the Nagaoka CO2 injection site, Japan. *International Journal of Greenhouse Gas Control, 2*(3), 309-318. doi: https://doi.org/10.1016/j.ijggc.2008.04.007

Moore, J., Adams, M., Allis, R., Lutz, S., & Rauzi, S. (2005). Mineralogical and geochemical consequences of the long-term presence of CO2 in natural reservoirs: An example from the Springerville–St. Johns Field, Arizona, and New Mexico, U.S.A. *Chemical Geology, 217*(3), 365-385. doi: https://doi.org/10.1016/j.chemgeo.2004.12.019

Mouzakis, K. M., Navarre-Sitchler, A. K., Rother, G., Bañuelos, J. L., Wang, X., Kaszuba, J. P., . . . McCray, J. E. (2016). Experimental Study of Porosity Changes in Shale Caprocks Exposed to CO2-Saturated Brines I: Evolution of Mineralogy, Pore Connectivity, Pore Size Distribution, and Surface Area. *Environmental engineering science, 33*(10), 725-735. doi: 10.1089/ees.2015.0588

National Geosequestration Laboratory. (2015). NGL report 2015 (pp. 24).

Navarre-Sitchler, A., Mouzakis, K., Heath, J., Dewers, T., Rother, G., Wang, X., . . . McCray, J. (2011). Changes to porosity and pore structure of mudstones resulting from reaction with CO (sub 2) and brine (Vol. 75, pp. 1527). London: London, United Kingdom: Mineralogical Society.

Naylor, M., Wilkinson, M., & Haszeldine, R. S. (2011). Calculation of CO2 column heights in depleted gas fields from known pre-production gas column heights. *Marine and Petroleum Geology, 28*(5), 1083-1093. doi: 10.1016/j.marpetgeo.2010.10.005

Nelson, C. R., Evans, J. M., Sorensen, J. A., Steadman, E. N., & Harju, J. A. (2005). Factors afecting the potential for Co2 leakage from geologic sinks *Plains CO2 Reduction (PCOR) Partnership* (pp. 36): Energy & Environmental Research Center.

Olabode, A. (2012). *EXPERIMENTAL INVESTIGATIONS IN CO2 SEQUESTRATION AND SHALE CAPROCK INTEGRITY.* (Master of Science i), Louisiana State University.

Olabode, A., & Radonjic, M. (2017). Geochemical Markers in Shale-CO2 Experiment at Core Scale (Vol. 114, pp. 3840-3854): Elsevier Ltd.

Olabode, A. O., Du, H., & Radonjic, M. (2017). Diagenetic Fluid Transport in Fractured Shale using Laboratory Rock/Fluid Interactions Data to Analyze Sealing Potential: American Rock Mechanics Association.

Oldenburg, C. M., Unger, A. J. A., Hepple, R. P., & Jordan, P. D. (2002). On leakage and seepage from geological carbon sequestration sites (U. S. D. o. Energy, Trans.) (pp. 60). Berkeley, CA (US): Ernest Orlando Lawrence Berkeley National Laboratory.

Olierook, H. K. H., Delle Piane, C., Timms, N. E., Esteban, L., Rezaee, R., Mory, A. J., & Hancock, L. (2014). Facies-based rock properties characterization for CO2 sequestration: GSWA Harvey 1 well, Western Australia. *Marine and Petroleum Geology, 50*, 83-102. doi: 10.1016/j.marpetgeo.2013.11.002

Palandri, J. L., & Kharaka, Y. K. (2004). A Compilation of Rate Parameters of Water-Mineral Interaction Kinetics for Application to Geochemical Modeling (pp. 64): U.S. GEOLOGICAL SURVEY.

Palandri, J. L., & Kharaka, Y. K. (2005). Ferric iron-bearing sediments as a mineral trap for CO2 sequestration: Iron reduction using sulfur-bearing waste gas. *Chemical Geology, 217*(3), 351-364. doi: https://doi.org/10.1016/j.chemgeo.2004.12.018

Pan, Y., Hui, D., Luo, P., Zhang, Y., Sun, L., & Wang, K. (2018). Experimental Investigation of the Geochemical Interactions between Supercritical CO2 and Shale: Implications for CO2 Storage in Gas-bearing Shale Formations. *Energy & Fuels, 32*(2). doi: 10.1021/acs.energyfuels.7b03074

Pearce, J., & Dawson, G. (2018). Experimental Determination of Impure CO2 Alteration of Calcite Cemented Cap-Rock, and Long Term Predictions of Cap-Rock Reactivity. *Geosciences, 8*(7), 241. doi: 10.3390/geosciences8070241

Pearce, J. K., Dawson, G. K. W., Blach, T. P., Bahadur, J., Melnichenko, Y. B., & Golding, S. D. (2018). Impure CO2 reaction of feldspar, clay, and organic matter rich cap-rocks: Decreases in the fraction of accessible mesopores measured by SANS. *International Journal of Coal Geology, 185*, 79-90. doi: 10.1016/j.coal.2017.11.011

Pearce, J. K., Dawson, G. K. W., Golab, A., Knuefing, L., Sommacal, S., Rudolph, V., & Golding, S. D. (2019). A combined geochemical and µCT study on the CO2 reactivity of Surat Basin reservoir and cap-rock cores: Porosity changes, mineral dissolution and fines migration. *International Journal of Greenhouse Gas Control, 80*, 10-24. doi: 10.1016/j.ijggc.2018.11.010

Pearce, J. K., Golab, A., Dawson, G. K. W., Knuefing, L., Goodwin, C., & Golding, S. D. (2016). Mineralogical controls on porosity and water chemistry during O2-SO2-CO2 reaction of CO2 storage reservoir and cap-rock core. *Applied Geochemistry, 75*, 152-168. doi: 10.1016/j.apgeochem.2016.11.002

Pearce, J. K., Kirste, D. M., Dawson, G. K. W., Rudolph, V., & Golding, S. D. (2019). Geochemical modelling of experimental O2–SO2–CO2 reactions of reservoir, cap-rock, and overlying cores. *Applied Geochemistry, 109*, 104400. doi: 10.1016/j.apgeochem.2019.104400

Pearce, J. K., La Croix, A. D., Underschultz, J. R., & Golding, S. D. (2020). Long term reactivity of CO2 in a low salinity reservoir-seal complex. *Applied Geochemistry, 114*, 104529. doi: 10.1016/j.apgeochem.2020.104529

Pearce, J. M., Holloway, S., Wacker, H., Nelis, M. K., Rochelle, C., & Bateman, K. (1996). Natural occurrences as analogues for the geological disposal of carbon dioxide. *Energy Conversion and Management, 37*(6), 1123-1128. doi: 10.1016/0196-8904(95)00309-6

Perera, M. S. A., Ranjith, P. G., Airey, D. W., & Choi, S. K. (2011). Sub- and super-critical carbon dioxide flow behavior in naturally fractured black coal: An experimental study. *Fuel, 90*(11), 3390-3397. doi: 10.1016/j.fuel.2011.05.016

Pham, V. T. H., Lu, P., Aagaard, P., Zhu, C., & Hellevang, H. (2011). On the potential of CO2–water–rock interactions for CO2 storage using a modified kinetic model. *International Journal of Greenhouse Gas Control, 5*(4), 1002-1015. doi: 10.1016/j.ijggc.2010.12.002

Piane, C. D., Bourdet, J., Dautriat, J., Esteban, L., Kager, S., Lebedev, M., . . . Yurikov2, A. (2018). The Lesueur: Deposition, Rocks, Facies, Properties ANLEC Project 7-0115-0240 Final report. CSIRO Report Number EP133710.

Prammer, M. G., Drack, E. D., Bouton, J. C., Gardner, J. S., Coates, G. R., Chandler, R. N., & Miller, M. N. (1996). *Measurements of Clay-Bound Water and Total Porosity by Magnetic Resonance Logging*. Paper presented at the SPE Annual Technical Conference and Exhibition, Denver, Colorado, USA.

Preston, B. L., Jones, R.N. (2006). *Climate Change Impacts on Australia and the Benefits of Early Action to Reduce Global Greenhouse Gas Emissions* Australia: CSIRO.

Ranganathan, P., van Hemert, P., Rudolph, E. S. J., & Zitha, P. Z. J. (2011). Numerical modeling of CO2 mineralisation during storage in deep saline aquifers. *Energy Procedia, 4*, 4538-4545. doi: https://doi.org/10.1016/j.egypro.2011.02.411

Rathnaweera, T. D., Ranjith, P. G., & Perera, M. S. A. (2016). Experimental investigation of geochemical and mineralogical effects of CO2 sequestration on flow characteristics of reservoir rock in deep saline aquifers. *Scientific Reports, 6*. doi: 10.1038/srep19362

Rathnaweera, T. D., Ranjith, P. G., Perera, M. S. A., & Haque, A. (2016). Influence of CO 2 – Brine Co-injection on CO 2 Storage Capacity Enhancement in Deep Saline Aquifers: An Experimental Study on Hawkesbury Sandstone Formation. *Energy & Fuels, 30*(5), 4229-4243. doi: 10.1021/acs.energyfuels.6b00113

Rezaee, R. (2014). Shale alteration after exposure to supercritical CO2. *Applied polymer science*.

Rezaee, R., Saeedi, A., Iglauer, S., & Evans, B. (2013). CarbonNet Dynamic Seal Capacity (pp. 97). Canberra, Australia: Cooperative Research Centre for Greenhouse Gas Technologies

Rezaee, R., Saeedi, A., Iglauer, S., & Evans, B. (2017). Shale alteration after exposure to supercritical CO2. *International Journal of Greenhouse Gas Control, 62*, 91-99. doi: 10.1016/j.ijggc.2017.04.004

Rimmelé, G., Barlet-Gouédard, V., & Renard, F. (2010). Evolution of the Petrophysical and Mineralogical Properties of Two Reservoir Rocks Under Thermodynamic Conditions Relevant for CO2 Geological Storage at 3 km Depth. *Oil Gas Sci. Technol. – Rev. IFP, 65*(4), 565-580.

Rimstidt, J. D., & Barnes, H. L. (1980). The Kinetics of Silica-Water Reactions. *Geochimica et Cosmochimica Acta, 44*(11), 1683-1699. doi: Doi 10.1016/0016-7037(80)90220-3

Rochelle, C., Bateman, K., & Pearce, J. M. (1996). *Fluid-rock interactions resulting from the underground disposal of carbon dioxide.* Paper presented at the 4th Int. Symp. Gochem. Earth's Surf., University of Leeds, Dept. of Earth Sciences, Leeds.

Rockwater. (2015). Harvey 3 Lesueur Formation Fluid Sampling *Southwesthub Geosequestration Project* (pp. 24). Western Australia: Department Of Mines And Petroleum.

Rosenbauer, R. J., Koksalan, T., & Palandri, J. L. (2005). Experimental investigation of CO2–brine–rock interactions at elevated temperature and pressure: Implications for CO2 sequestration in deep-saline aquifers. *Fuel Processing Technology, 86*(14-15), 1581-1597. doi: 10.1016/j.fuproc.2005.01.011

Rouquerol, J., Avnir, D., Fairbridge, C., H. Everett, D., M. Haynes, J., Pernicone, N., . . . Unger, K. (1994). *Recommendations for the Characterization of Porous Solids* (Vol. 66).

Rutqvist, J., Vasco, D. W., & Myer, L. (2009). Coupled reservoir-geomechanical analysis of CO2 injection at In Salah, Algeria. *Energy Procedia, 1*(1), 1847-1854. doi: 10.1016/j.egypro.2009.01.241

Sass, B. M., Gupta, N., Ickes, J. A., Engelhard, M. H., Baer, D. R., Bergman, P., & Byrer, C. (2001). Interaction of rock minerals with carbon dioxide and brine

a hydrothermal investigation.

Schlomer, S., & Krooss, B. M. (1997). Experimental characterisation of the hydrocarbon sealing efficiency of cap rocks. *Marine and Petroleum Geology, 14*(5), 563-578.

Schowalter, T. T. (1979). MECHANICS OF SECONDARY HYDROCARBON MIGRATION AND ENTRAPMENT. *AAPG Bull, 63*(5), 723-760.

Sharma, S., Cook, P., Jenkins, C., Steeper, T., Lees, M., & Ranasinghe, N. (2011). The CO2CRC Otway Project: Leveraging experience and exploiting new opportunities at Australia's first CCS project site. *Energy Procedia, 4*, 5447-5454. doi: https://doi.org/10.1016/j.egypro.2011.02.530

Sharma, S., & Gent, D. V. (2018). *The Australian South West Hub Project: Developing confidence in Migration Assisted Trapping in a saline aquifer – understanding uncertainty boundaries through scenarios that stress the models*. Paper presented at the 14th International Conference on Greenhouse Gas Control Technologies, GHGT-14, Melbourne, Australia.

Shiraki, R., & Dunn, T. L. (2000). Experimental study on water–rock interactions during CO2 flooding in the Tensleep Formation, Wyoming, USA. *Applied Geochemistry, 15*(3), 265-279. doi: https://doi.org/10.1016/S0883-2927(99)00048-7

Shukla, R., Ranjith, P., Haque, A., & Choi, X. (2010). A review of studies on CO2 sequestration and caprock integrity. *Fuel, 89*(10), 2651-2664. doi: 10.1016/j.fuel.2010.05.012

Shukla, R., Ranjith, P. G., Haque, S. K., & Choi, A. (2011). Study of caprock integrity in geosequestration of carbon dioxide. *International Journal of Geomechanics, 11*(4), 294-301. doi: 10.1061/(ASCE)GM.1943-5622.0000015

Sing, K. S. W., Everett, D. H., Haul, R. A. W., Moscou, L., Pierotti, R. A., Rouquerol, J., & Siemieniewska, T. (1985). Reporting Physisorption Data for Gas/Solid Systems with Special Reference to the Determination of Surface Area and Porosity. *Pure and Applied Chemistry, 57*, 603–619.

Soldal, M. (2008). *Caprock interaction with CO2 Geomechanical and geochemical effects.* (Master Thesis in Geosciences), UNIVERSITY OF OSLO.

Soong, Y., Goodman, A. L., McCarthy-Jones, J. R., & Baltrus, J. P. (2004). Experimental and simulation studies on mineral trapping of CO2 with brine. *Energy Conversion and Management, 45*(11-12), 1845-1859. doi: 10.1016/j.enconman.2003.09.029

Szabó, Z., Hellevang, H., Király, C., Sendula, E., Kónya, P., Falus, G., . . . Szabó, C. (2016). Experimental-modelling geochemical study of potential CCS caprocks in brine and CO2-saturated brine. *International Journal of Greenhouse Gas Control, 44*, 262-275. doi: 10.1016/j.ijggc.2015.11.027

Tester, J. W., Worley, W. G., Robinson, B. A., Grigsby, C. O., & Feerer, J. L. (1994). Correlating quartz dissolution kinetics in pure water from 25 to 625°C. *Geochimica et Cosmochimica Acta, 58*(11), 2407-2420. doi: 10.1016/0016-7037(94)90020-5

Wang, K., Xu, T., Wang, F., & Tian, H. (2016). Experimental study of CO2–brine–rock interaction during CO2 sequestration in deep coal seams. *International Journal of Coal Geology, 154-155*, 265-274. doi: https://doi.org/10.1016/j.coal.2016.01.010

Wang, S., Liu, K., Han, J., Ling, K., Wang, H., & Jia, B. (2019). Investigation of Properties Alternation during Super-Critical CO2 Injection in Shale. *Applied Sciences, 9*(8), 1686. doi: 10.3390/app9081686

Washburn, E. W. (1921). Note on a Method of Determining the Distribution of Pore Sizes in a Porous Material. *Proceedings of the National Academy of Sciences of the United States of America, 7*(4), 115. doi: 10.1073/pnas.7.4.115

White, A. F., Brantley, S. L., & Mineralogical Society of, A. (1995). *Chemical weathering rates of silicate minerals / A. F. White & S. L. Brantley, editors*. Washington, D.C: Washington, D.C : Mineralogical Society of America.

White, A. F., & Peterson, M. L. (1990). Role of Reactive-Surface-Area Characterization in Geochemical Kinetic Models. *416*, 461-475. doi: 10.1021/bk-1990-0416.ch035

White, S. P., Allis, R. G., Moore, J., Chidsey, T., Morgan, C., Gwynn, W., & Adams, M. (2005). Simulation of reactive transport of injected CO2 on the Colorado Plateau, Utah, USA. *Chemical Geology, 217*(3-4), 387-405. doi: 10.1016/j.chemgeo.2004.12.020

Wigand, M., Carey, J. W., Schutta, H., Spangenberg, E., & Erzinger, J. (2008). Geochemical effects of CO2 sequestration in sandstones under simulated in situ conditions of deep saline aquifers. *Appl. Geochem., 23*(9), 2735-2745. doi: 10.1016/j.apgeochem.2008.06.006

Wollenweber, J., Alles, S., Busch, A., Krooss, B. M., Stanjek, H., & Littke, R. (2010). Experimental investigation of the CO2 sealing efficiency of caprocks. *International Journal of Greenhouse Gas Control, 4*(2), 231-241. doi: 10.1016/j.ijggc.2010.01.003

Wollenweber, J., Alles, S. a., Kronimus, A., Busch, A., Stanjek, H., & Krooss, B. M. (2009). Caprock and overburden processes in geological CO2 storage: An experimental study on sealing efficiency and mineral alterations. *Energy Procedia, 1*(1), 3469-3476. doi: 10.1016/j.egypro.2009.02.138

Xu, T., Apps, J., Pruess, K., & Yamamoto, H. (2007). Numerical modeling of injection and mineral trapping Of CO2 with H2S and SO2 in a sandstone formation. *Chem. Geol., 242*(3-4), 319-346. doi: 10.1016/j.chemgeo.2007.03.022

Xu, T., Apps, J. A., & Pruess, K. (2000a). *Analysis of mineral trapping for CO2 disposal in deep aquifers*, Washington, DC.

Xu, T., Apps, J. A., & Pruess, K. (2000b). Analysis of mineral trapping for CO2 disposal in deep aquifers (Vol. 81, pp. 253). Washington, DC: Washington, DC, United States: American Geophysical Union.

Xu, T., Apps, J. A., & Pruess, K. (2003). Reactive geochemical transport simulation to study mineral trapping for CO2disposal in deep arenaceous formations. *Journal of Geophysical Research: Solid Earth, 108*(B2). doi: 10.1029/2002jb001979

Xu, T., Apps, J. A., & Pruess, K. (2004). Numerical simulation of CO2 disposal by mineral trapping in deep aquifers. *Applied Geochemistry, 19*(6), 917-936. doi: 10.1016/j.apgeochem.2003.11.003

Xu, T., Apps, J. A., & Pruess, K. (2005). Mineral sequestration of carbon dioxide in a sandstone–shale system. *Chemical Geology, 217*(3), 295-318. doi: 10.1016/j.chemgeo.2004.12.015

Xu, X., Chen, S., & Zhang, D. (2006). Convective stability analysis of the long-term storage of carbon dioxide in deep saline aquifers. *Advances in Water Resources, 29*(3), 397-407. doi: 10.1016/j.advwatres.2005.05.008

Yang, F., Bai, B., Tang, D., Shari, D.-N., & David, W. (2010). Characteristics of CO2 sequestration in saline aquifers. *Petroleum Science, 7*(1), 83-92. doi: 10.1007/s12182-010-0010-3

Yang, H., Xu, Z., Fan, M., Gupta, R., Slimane, R. B., Bland, A. E., & Wright, I. (2008). Progress in carbon dioxide separation and capture: A review. *Journal of Environmental Sciences, 20*(1), 14-27. doi: http://dx.doi.org/10.1016/S1001-0742(08)60002-9

Yin, H., Zhou, J., Jiang, Y., Xian, X., & Liu, Q. (2016). Physical and structural changes in shale associated with supercritical CO2 exposure. *Fuel, 184*, 289-303. doi: 10.1016/j.fuel.2016.07.028

Yu, Z., Liu, L., Yang, S., Li, S., & Yang, Y. (2012). An experimental study of CO2–brine–rock interaction at in situ pressure–temperature reservoir conditions. *Chemical Geology, 326-327*, 88-101. doi: 10.1016/j.chemgeo.2012.07.030

Zhu, C., Veblen, D. R., Blum, A. E., & Chipera, S. J. (2006). Naturally weathered feldspar surfaces in the Navajo Sandstone aquifer, Black Mesa, Arizona: Electron microscopic characterization. *Geochimica et Cosmochimica Acta, 70*(18), 4600-4616. doi: 10.1016/j.gca.2006.07.013